

Status of Solar Energy Potential, Development and Application in Myanmar

Hla Myo Aung
Renewable Energy Research
Department, Department of
Research and Innovation,
Yangon, Myanmar

Zaw Min Naing
Department of Research and
Innovation, Yangon, Myanmar

Thi Thi Soe
Renewable Energy Research
Department, Department of
Research and Innovation,
Yangon, Myanmar

Abstract: Myanmar has abundant of renewable energy resources through the country. Among the renewable energy available, the potential of solar energy is one of the great interests in Myanmar. The government of Myanmar has set a plan to electrify the whole county in 2030. On the other hand, ASEAN has a target that is to increase 23% of Renewable Energy in ASEAN generation mix by 2025. For the time being, Myanmar has mainly relied on hydropower system for the electricity generation. Due to lack of water in summer season in Myanmar, Solar Energy will be a vital role in Electricity generation because of the high sunshine hours for that time. Therefore, the government of Myanmar is trying to increase the utilization of solar energy for the rural electrification. In this respect, the seventy percent of population are living in rural area where they cannot access the electricity. For the off-grid area, Myanmar has mainly emphasis on solar home system and mini-grid system to be sustainable, affordable and environmental friendly. This paper aims to describe the high potential of solar energy, current situation of solar energy implementations and the important of Renewable Energy of Myanmar respectively. This paper is also intends to know good opportunity for international investors and developers concerning solar energy. This paper presents Hence, The current status, future potentials of solar energy sector and solar energy development in Myanmar are presented in this context. In this paper, also up to date information is provided for the solar energy sector of the country.

Keywords: solar energy, renewable energy, rural electrification, off-grid area, mini-grid system, environmental friendly

1. INTRODUCTION

Myanmar is Located between the Himalaya in the north and the Andaman Sea to the south, and roughly shaped like a diamond. The landscape of Myanmar is as diverse as it is intriguing .Wedged between China to the east and India to the west. Myanmar also shares borders with Thailand, Laos and Bangladesh. Stretched over 676,578sq km, it is the 40thlargest in South-east Asia, behind Indonesia. The coastline stretches out 2832 km, with the Bay of Bengal on the south-west coast and the Andaman Sea to the south-west coast and the Andaman Sea to the south-east.

Myanmar is the member of ASEAN, located in South East Asia and with a population of more than 51m Scattered across 14 states/ regions with 412 townships/sub- townships, Myanmar is the 12th most populous country in Asia and the fifth in South- east Asia, behind Indonesia, the Philippines, Vietnam and Thailand. The three main cities are the business capital of Yangon, with a population of more than 7.3m; followed by the second business capital of Mandalay, with 1.73m people, and the administrative capital of Naypyidaw, which has approximately 1.16m inhabitants.[1]

2. ENERGY SECTOR AND SOLAR POTENTIAL IN MYANMAR

Overall, Myanmar’s total final energy consumption increased between 2000 and 2013 by an average 2.3% annually, from 11 Mtoe to 14.3 Mtoe. Over this period energy consumption by the industrial has doubled, the consumption by the commercial sector grew three times as much, whereas energy use in transport sector has not increased generally. Residential consumption increased only by 1.3% annually but, it remains by far the largest consumer of energy due to exclusive use of biomass (fuel wood and charcoal).[2]

The existing electricity capacity and infrastructure can only meet about 50% of the current electricity demand resulting in regular load shedding and challenges in electricity supply management. In total electricity installed capacity in Myanmar, hydroelectric power 64.37% and 31.31%, 2.4%, 1.83% and 0.09% of electricity generation installed by gas, coal, diesel and biomass as shown in Figure 1.[3]

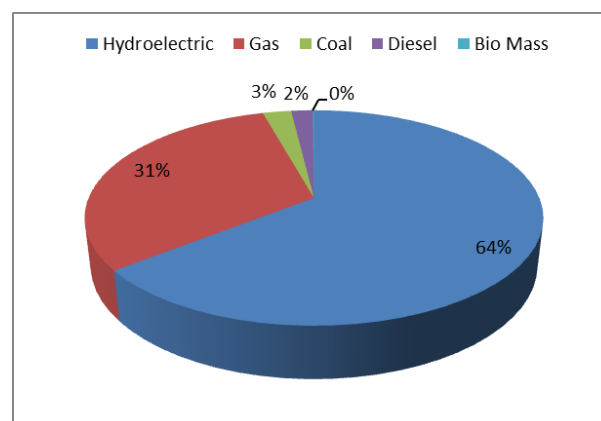


Figure.1 Installed Generation Capacity as in 2016 (June)

POTENTIAL OF SOLAR ENERGY IN MYANMAR: In Myanmar, it enjoys abundant sunshine all year round, especially in the Central Myanmar Dry Zone Area. Potential available solar energy of Myanmar is around 51973.8 TWh/year in accordance with NEDO surveying data in 2003. On average, daily global solar radiation in Myanmar varies from the value of 15 MJ/m²-day in the north and the east to 20 MJ/m²-day in the west as shown in Figure 2. High solar radiation (>20 MJ/m²-day) is observed mostly in the fertile plains including the areas of Magway, Mandalay and Sagaing Regions. In the north, low solar radiation (14 MJ/m²-day) is observed as a result of cloudy skies generated from the cold

front system. On the other hand, the pattern of low solar radiation (16-18 MJ/m²-day) is also seen in the east and the south regions. This is because of the monsoons, which bring heavy rains and clouds. In contrast, high solar radiation (20-22 MJ/m²-day) is seen over the areas of Mandalay, Magway and Sagaing Regions.

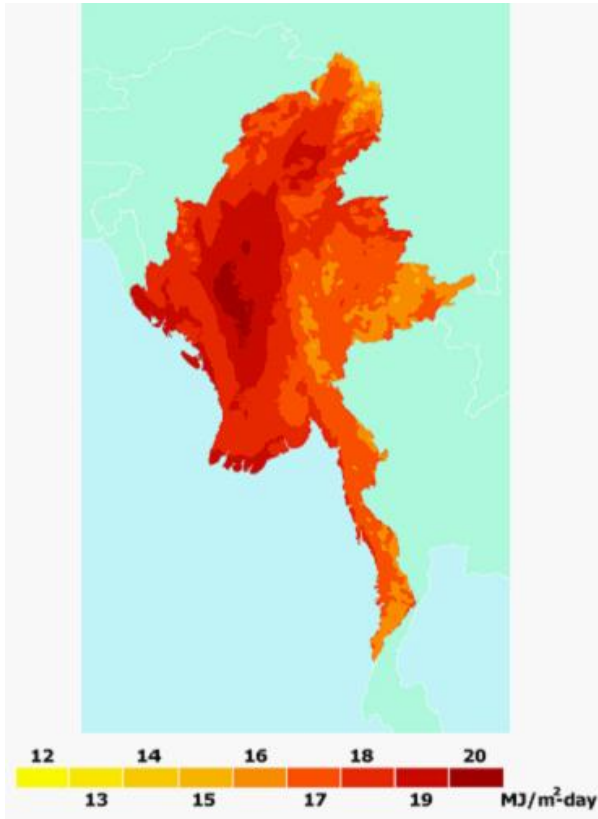


Figure. 2 Yearly average of daily global radiation over Myanmar

The year average solar radiation of Myanmar is found to be 18.3 MJ/m²-day, when averaged over the country. The annual maximum solar irradiation is in February and the minimum in July-August.[4]

3. RELATED POLICY AND INSTITUTION FRAMEWORK FOR ENERGY SECTOR

Myanmar lacks a unified policy for promoting the development and use of its renewable energy resources. The government has not yet officially established renewable energy targets. The national grid infrastructure is not reliable to accept the renewable energy generating sources. Electricity Law was legislated by the Union Parliament in Oct, 2004 and formulation of by laws are also ongoing. National Electricity master Plan (final draft II) was prepared by JICA and submitted to Ministry in Aug, 2014. In the National Electricity Master Plan, renewable energy (only solar and wind) share would be 9% (2000MW) of installed capacity by 2030[5]. Followed by ASEAN target, the component of renewable energy will be increased to 23% by 2025 in the ASEAN Energy Mix [6]. The Myanmar National Electrification Plan (NEP) aims to electrify 100% of Myanmar's households by 2030[3]. However, institutional and regulatory framework is still fragmented in renewable

energy sector. There are two National plans regarding energy sector in our country. They are National Energy Master Plan has been finalized by the management of National Energy Management Committee (NEMC), under the Ministry of Energy during the previous government.

3.1. National Energy Master Plan

The National Energy Master Plan had been accomplished by the assistance of ADB in December 2015. Among these nine policies, renewable energy is;

- (i) To implement programs on a wider scale, utilizing renewable energy resources such as wind, solar, hydro, geothermal and bio-energy for the sustainable energy development in Myanmar [2]

By mid-2014, Renewable Energy Research Department under the Department of Research and Innovation (DRI), Ministry of Science and Technology has completely formulated Renewable Energy Policy, Strategy and Roadmap Myanmar (First Draft) which covers the proposed activities in the key sectors and the road map for implementation of the RE Policy.

The first draft was contributed to the concerned Ministries and organization to fill up the existing and implementation plan for future trend of Renewable Energy to meet 27% target of Renewable Energy development until 2030. In accordance with the comments and suggestions from the concerned Ministries, finally the second draft of RE policy had been completed in January, 2016. In the formulation of RE policy First draft, it has targeted to fulfill the RE final goal of 27% in total installed capacity, the certain amount from four types of renewable energy sources will be allocated such as hydropower power 1.3%, solar 17.8% (on grid) 3.7 % (off grid), biomass 1%, bio gasification 0.02% and bio-fuel 5% by comparing with existing and demand & find the way as adder. The draft Renewable Energy Policy is presented to the Parliament for consideration. The focus is on the development of the following:

- A. Domestic Energy (improve cooking stove)
- B. Thermal Energy (Solar water heating, waste heating utilization plants, training and education of efficient solar thermal uses)
- C. Grid Connected Renewable Energy (the most attention and investment of RET are wind, solar and biomass and RET offer a valuable contribution to the national electricity production and to energy security)
- D. Off-Grid Renewable Energy (GOM will apply in Off-grid RE delivery models with the advantages of learning from international experience in order to achieve the rural electrification targets)
- E. Energy Research (conduct research on improving existing technologies and emerging viable and marketable technologies)

3.2. National Electrification Plan (NEP)

The Department of Rural Development (DRD) of the MOAI therefore has embarked on the renewable energy based national electrification program. The main objective of the NEP is to achieve universal access to electricity in Myanmar by 2030. With technical assistance from World Bank Group, the Government developed a National Electrification Plan in 2014 to accomplish this rapid increase through a two-pronged, sector-wide approach: an ambitious extension of the national grid plus off-grid electrification for communities that would otherwise have to wait for years for grid access. NEP aims to

support from different stakeholders with the implementation program for achieving national access targets as the following:

- i. Dense areas require less MV per connection and will be connected first.
- ii. Remote communities require more and will be connected later.
- iii. Major areas for Pre electrification have higher cost per connections, thus to be connected in the final phases.

The total cost of National Electrification Program is estimated at US \$ 5.8 billion (grid and off-grid) till 2030. NEP aims to electrify 7.2 million households and achieve universal access to electricity by 2030 as shown in Figure 3.[3]

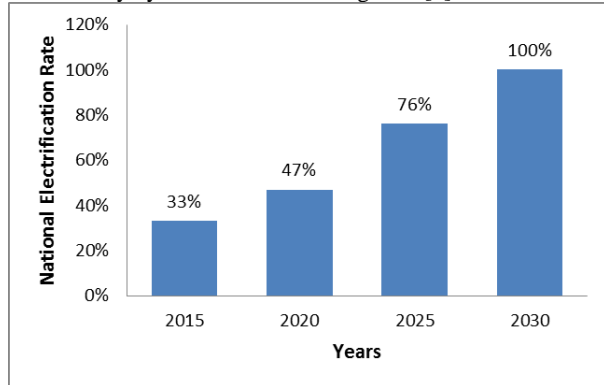


Figure. 3 National Electrification Plan (NEP)

3.3. Institutional Framework for Energy Sector of Myanmar

The structure of energy sector in Myanmar is very fragmented and the responsibilities for various aspects of energy development in Myanmar. For the time being, Ministry of Electricity and Energy (MoEE) is responsible for the overall focal point for energy policy, coordination and international cooperation and also the oil and gas sector for developing, operating, and maintaining all large hydropower and coal-fired thermal plants; for developing and maintaining the transmission and distribution systems throughout the country, and for operating gas-fired thermal plants and mini hydropower plants. In addition, Ministry of Agriculture and Irrigation (MoAI) is take the lead in the development of biofuels, micro-hydropower (with installed capacity of up to 10 MW), bioenergy from agricultural residues, and biogas. Ministry of Education (MoE) is one of the energy concerned Ministry that conducts for the research and development of Renewable Energy technologies and promotion of renewable energy sector in Myanmar. And also Ministry of Natural Resource and Environmental Conservation regulates the use of biomass from forest resources for energy purposes and climate change issues. Finally, Ministry of Industry (MoI) is undertaking the formulation of Energy Efficiency and Conservation policy and also leading role on the development and implementation of Energy Efficiency and Consecration sector in Myanmar.

4. DEVELOPMENT AND APPLICATION OF SOLAR ENERGY IN MYANMAR

The Government of the Republic of the Union of Myanmar (GoM) has a policy to support to the utilization of renewable energy and private investment in the electricity sector. The draft Power Generation Development Plan (PGDP) proposed

by JICA financed electricity sector master plan study sets a target of renewable of solar, wind, biomass and geothermal to be developed by 2,000 MW, which is equivalent to 10% of the power supply capacity at 2030 as assumed in the draft document. A Memorandum of Understanding was recently signed between MoEE and US investors of a solar PV project to Myanmar. The project consists of two 150 MW facilities, one in Nabuai and the other in Wundwin, both locations in Mandalay Region. The published project cost is 480 m\$, equal to 1,600 \$/kW. The targeted commissioning of the project is in 2016. Also a Thai company has been pursuing a 220 MW solar power plant in Minbu in Magway Region as shown in Figure 4. The cost assumptions made here are 2,100 \$/kW for a solar PV plant operating on average at 20% capacity factor.

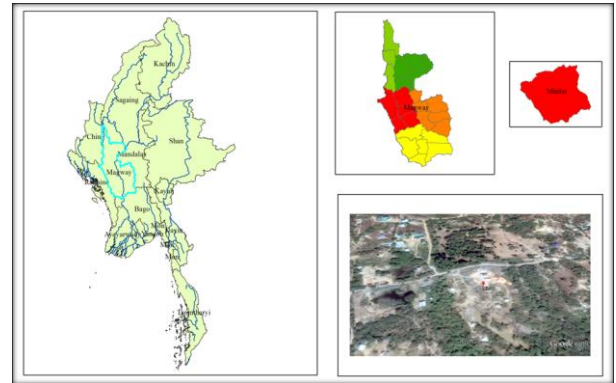


Figure. 4 Project Location (Magway Division, Minbu District, Sagu Township)

Green Earth Power (Myanmar) Co., Ltd (GEP) appointed Shwe Kyun Gyi Construction Co., Ltd (SKG) to start preliminary civil work since July, 2015. They have completed 100% of site clearing and construction of compacted gravel soil road (access road) at the site. At the moment, they started grading phase one areas, substation areas and office areas. Minbu Solar Power Project is located in Minbu district, Magwe region and the capacity is approximately 220MW (Phase I 50MW, Phase II 50MW, Phase III 50MW and Phase IV 70MW) respectively. On the other hand, Myanmar Electric Power Enterprise (MEPE) completed in the construction of the 30kV of National transmission line by April, 2016. Project land area has about 836 acres wide and lease hold from Government. Myanmar Electric Power Enterprise under the Ministry of Electricity and Energy will be off taker. The electricity tariff will be 0.1275 US\$/kWh and the project life is 30 years plan. The project construction time will take totally 48 months (Phase 1 complete in 12 months, Phase II in 24 months, Phase III in 36 months and Phase IV in 48 months).[7]

4.1. Off-grid Solar Power Generating System for Rural Area

In recent years, following off-grid solar power generating systems have been rapidly developed in Myanmar.

- i. Solar water pumping system
- ii. Industry, Telecommunications & Public service
- iii. Solar Lighting for streets, gardens and public transportation stops
- iv. Solar refrigeration system for Health
- v. Solar Home system for Residential (especially in lighting for houses)

Solar Home System (SHS) is divided by three categories for off-grid rural electrification in Myanmar. They are small (capacity range 30kW), medium (45W) and large scale (60W) respectively in as described in Table 1.[8]

Table 1. solar home system for off-grid rural electrification

Solar Panel peak wattage (Wp)	30W	45W	60W
Load consumption	Three LED lights, a cell phone	Four LED lights, a cell phone and TV	Five LED lights, a cell phone and TV

In Myanmar, There are four types of Solar photovoltaic (PV) application in public institution system and implemented by Department of Rural Development (DRD), under the Ministry of Agriculture and Irrigation (MoAI). These are primary, middle and high school, rural health Centre, religious building and street light as shown in Table 2.[8]

Table 2. Application of Solar PV system

Application	Solar Peak Power (Wp)	Load
Primary School	120	9 LED lights, Tablet and Cell phone
Middle School	375	20 LED lights, Tablet and Cell phone
High School	475	26 LED lights, Tablet and Cell phone
Rural Health Center	180	6 LED lights, Cell phone and small appliance
Religious Building	120	9 LED lights
Street light	70	1 LED light

4.2. Research & Development (R&D) and Human Resource Development (HRD) for Solar Energy Technology

DRI under MOE has been involved as the leading department for the formulation of RE policy. Researchers from DRI have been conducting researches in the field of Renewable Energy, particularly biogas, rice rush gasifier, wind turbine, solar and micro hydro power projects. For the solar technology, design models and solutions are contributed for utilization of solar energy to the village people in Myanmar. In addition, training courses on renewable energy technology and application including solar energy technology have been disseminated by DRI starting from 2014.

The Renewable Energy research department under the DRI is doing research for renewable energy technologies (especially Solar, Wind, Hydro, Gasifier and Biogas). Regarding international cooperation, DRI signed in MoU with Ministry of New and Renewable Energy in India for the cooperation on development of new and renewable energy technologies focusing on solar energy, bio-energy and wind

energy in August, 2016. Currently, DRI is trying to be able to sign in MoU with Asia Air Survey (Japan) company for research and development on renewable energy. Moreover, DRI have cooperated with ADB, UNIDO, and GIZ. DRI also co-operate with Renewable Energy Association in Myanmar (REAM), Green Energy Green Growth (GEGG) and Myanmar Engineering Society (MES) to enhance the development of renewable energy sector. The summary Training and Awareness Program on Renewable Energy (Solar, Wind, Hydro, Gasifier and Biogas) has being provided by DRI as shown in Figure 5.

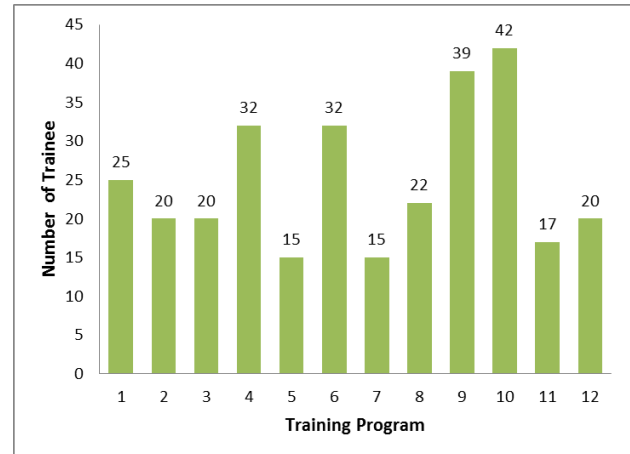


Figure. 5 Training and Awareness Program on RE technologies provided by DRI

5. RESULT AND DISCUSSION

For the time being, Government of Myanmar considers to increase the utilization of Renewable Energy to reduce the environmental impact and for increasing of electricity demand. Most of the state and region have become implement the large scale solar power project. For example, the 30MW solar project will be implemented in Maubin Township, Irrewaddy region, Myanmar. The high authorized people consider the wide range of solar power plant application in energy master plan.

There are many challenges in the development of renewable energy sector. Renewable Energy is often considered as non-viable energy solution compared to the subsidized conventional energy generation and also lack of consumer awareness on benefits and opportunities of renewable energy. There is still need for renewable energy development in our country. Moreover, regarding development of solar energy, advanced technologies such as design of solar panels, solar energy conversion, processing technologies, modeling, simulation and engineering of solar plants are important issues in Myanmar.

Above challenges can be effectively overcome through the following recommendation:

- i. RE policy, strategy and roadmap need to be finalized to ensure RE contributes significantly to the energy mix and enhance public awareness on benefits & opportunities of RE
- ii. The Government of Myanmar would have in place an appropriate legal and regulatory frame work with enforcement mechanism
- iii. It is necessary to strengthen training and capacity building for local technical officers and mini-grid project developers

- iv. Related organizations need to provide transparent information on energy costs, resource availability, subsidies, RE policies, and roadmap to project developers

International support (funding, capacity building, and technology transfer) to help Myanmar implemented RE policy to meet the target of ASEAN renewable energy.

6. CONCLUSION

Myanmar has very weak of cooperation and collaboration within and between various concerned ministries,

7. ACKNOWLEDGMENTS

Our thanks to the experts who have contributed towards development of the template. The author would like to express special thanks to Dr. Zaw Min Naing, Deputy Director General and Head, Renewable Energy and Electronic Technology Research Center, Department of Research and Innovation, for his effective suggestions and valuable ideas. The author is deeply grateful to Dr. Thi Thi Soe, Deputy Director, Renewable Energy Research Department, Department of Research and Innovation, for his invaluable support, suggestions and sharing experience in the research period.

8. REFERENCES

- [1] August 2014, ADB report, Renewable Energy Developments and potential in the Greater Mekong Sub-region. .
- [2] 19 December 2014, MYANMAR ENERGY MASTER PLAN, the Asian Development Bank and the Myanmar Ministry of Energy.

development partners, private sectors, institutes, universities and other stakeholders for the progress in RE development. In this paper we studied current status and policy development of renewable energy in Myanmar. In fact, according to discussion the condition of solar energy resource is good potential in Myanmar but requires additional attention for better development of solar energy source.

- [3] September 2014, Myanmar National Electrification Program (NEP) Roadmap and Investment Prospectus: Final road map and investment prospectus
- [4] September, 2009, Assessment of Solar Energy Potentials for Myanmar, Solar Energy Research Laboratory, Department of Physics, Faculty of Science, Silpakorn University, Thailand.
- [5] Forman, G. 2003. An extensive empirical study of feature selection metrics for text classification. *J. Mach. Learn. Res.* 3 (Mar. 2003), 1289-1305.
- [6] Brown, L. D., Hua, H., and Gao, C. 2003. A widget framework for augmented interaction in SCAPE.
- [7] Y.T. Yu, M.F. Lau, "A comparison of MC/DC, MUMCUT and several other coverage criteria for logical decisions", *Journal of Systems and Software*, 2005, in press.
- [8] Spector, A. Z. 1989. Achieving application requirements. In *Distributed Systems*, S. Mullender

Automatic Sorting Machine

Moe Win Khaing
Department of Electronic
Engineering
Technological University
Thanlyin, Myanmar

Dr. Aye Mya Win
Department of Electronic
Engineering
Technological University
Thanlyin, Myanmar

Daw Thida Aye
Department of Electronic
Engineering
Technological University
Thanlyin, Myanmar

Abstract: The automatic sorting system has been reported to be complex. Programmable logic controller used for the operation and the control of an industrial unnamed system, namely conveyor, pneumatic cylinders, solenoids. Thus, we have developed a system for sorting object with any metallic impurities using sensor and motor controlled by Programmable Logic Controller (PLC) and the conveyor in the system passes the object through sensors and hence sorting logic is decided. The research obtained shows that metals and red colors wood were sorted into their respective and correct position. The system can be implemented by choosing the desire colors which depend on the setup of the color sensor.

Keywords: plc, automation, cylinders, solenoids; color sensors

1. INTRODUCTION

Sorting is very important in any type of industry such as manufacturing processes. The main system is to sort the products manufactured in the Industry. The purpose of this research paper is to save the time and to reduce the human efforts in industry. An automatic sorting machine has main operation of sorting components according to the metals, nonmetals and colors. This consist of conveyor belt, proximity sensor, and color sensor, Pneumatic Cylinders and Solenoids, which reduces the efforts of material handling. A sorting machine is more practical and economical method of automation.

The design is quite simple and of flexible use, means only conveyor used for material handling. In this research work, we have developed a cost-effective automation system for sorting for any metallic impurity. The whole process is automatically with the help of PLC. Cylinders are used for pushing the object from the conveyor belt into the box. Conveyor belt brings the objects near the sensor and PLC is decided for select the materials and colors. The system consists of proximity sensor, color sensor, Omron sysmac PLC CP1E and conveyor belt. The metal defect is detected with the help of the proximity sensor. DC motor used for running the conveyor. The motor is interfaced with the PLC through relay cards. Sensor are above the conveyor. One sensor is mounted on the placing mechanism of the stacker lift. This sensor will detect the metal blocks and color blocks and then choose metals and colors blocks are kept in the box by the cylinder working with image processing, on the other hands, the database collection is the most challenging task. For database collection, it is necessary to collect the basic information about the crop and its diseases as the important task. Therefore, a detail study should be done on the types of disease, their symptoms on crop and the patterns of disease. By observing the patterns of disease, the system will get designed. The mainly occurring diseases on leaf are Bacterial disease, Fungal disease, Viral disease and diseases due to insects. The paper gives the detailing of these diseases [3].

2. COMPONENTS

2.1 Programmable Logic Controller System

A programmable logic controller (PLC) is an industrial computerized control system that continuously monitors the state of input devices and makes decisions based upon a custom program to control system the states of output devices. A fixed PLC is usually small, has little memory, and a limited number of input and outputs, or I/O as typically referred to Figure 1. The CPU, power supply, and I/O system are all constructed as a single entity [3].



Figure 1. PLC CP1E

The input sensing devices is fed to the input module which acts like an optical isolation. What is connected to the main device CPU and memory data. The monitor who acts like a programming device where it displays the given. This research paper is mainly device is used PLC controller because nowadays manufacturing products are very plentiful and more and more producing. Then the entire system is

connected to the output block where the output are the lamp, motor, etc [3].

2.2 Sensors

A metal sensor is an electronic instrument which detects the presence of metal nearby. Metal detectors are useful for finding metal inclusions hidden within the objects. The proximity sensor is shown in Fig. 2.



Figure 2. Proximity Sensor

Proximity (Metal) sensors are generally with four main elements:

- A coil and ferrite core assembly,
- An oscillator,
- A convertor/trigger circuit (detector), and
- Output device.

This sensor is used to differentiate between two colors red and green. The model of the sensor is E3FA DN12. This sensor is more useful than another color sensors because it system can be choice the desired colors depend on the position adjustment of the distance. The object is moving on the conveyor line is sensed by this sensor and it sent the signal to the PLC according to the wavelength produced by the reflected wave. The object is further sorted on the basic of the colors. The color sensor is shown in Figure 3.



Figure 3. E3FA DN12 Color Sensor

2.3 Geared DC Motor

65 RPM Side Shaft compact DC motor is suitable for small automation systems. Motor runs smoothly 18V and gives 65 RPM at 27W. Motor has 6m diameter, 13.5m length drive shaft with D shape for excellent coupling. This motor is suitable for this design because PLC controller is used 24 V DC. This voltage can reduced by using voltage regulator.

2.4 Pneumatics

In a pneumatic system, energy is stored in a potential state under the form of compressed air. Working energy (kinetic energy and pressure) results in a pneumatic system when the compressed air is allowed to expand. To perform any applicable amount of work then, a device is needed which can supply an air tank with a sufficient amount of air at a desired pressure. There are many different cylinder types [4].The cylinders used in this paper are listed below:

- Single acting spring return cylinder,
- Double acting cylinder,
- Directional control valves, and
- Four way valve.

The pneumatic cylinder is as shown in Figure 4.



Figure 4. Pneumatic Cylinder

2.5 Solenoid

A solenoid is a type electromagnet when the purpose is to generate a controlled magnetic field. If the purpose of the solenoid is instead to impede changes in the electric current, a solenoid can be more specially classified as an inductor rather than and electromagnetic [4]. The way pneumatic solenoid valve is shown in Figure 5.



Figure 5. 5/2 Way Pneumatic Solenoid Valve

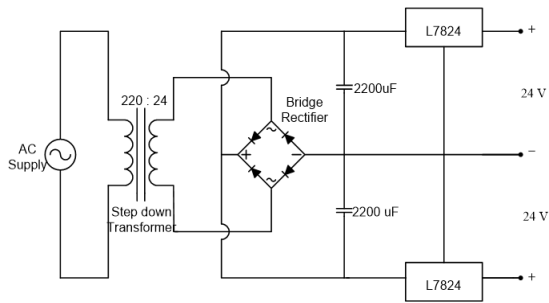


Figure 6. Power supply of the solenoids

2.6 Circuit Function

The 5/2 way pneumatic valve has five connection ports and two states. It has one pressure port (P,1), two ports (A,2) and (B,4) that connect to the device that needs to be controlled, and two exhaust ports (EA,3) and (EB,5). The two states of the valve are [4]:

- Pressure port (P,1) connects to port (A,2), while port (B,4) vents through exhaust port (EB,5)
- Pressure port (P,1) connects to port (B,4), while port (A,2) vents through port (EA,3).

2.7 Design of Automatic Conveyor System

The main objective of the system is automatic sorting of materials which can be applied to industries. Here, by operating push button switch the conveyor starts to move and the items are being sorted. Design of the automatic sorting system is shown in Figure 7.



Figure 7. Design of the Automatic Sorting System

The color sensor and inductive proximity (metal) sensor are mounted on the model and are connected to the Omron PLC kit. When the objects are detected by the color sensor the signal is sent to the PLC kit where according to the program ladder logic the conditions are analyzed and the output is given to pneumatic valves which activates pistons for sorting.

The metal detector is connected to Omron PLC kit. The objects that contain hidden metal in them are detected and signal is sent to the PLC where according to the ladder logic, the objects are selected and put in the box from the conveyor by activating the pistons and hence carrying out the sorting mechanisms. We can consider the color of the objects, green, red and etc.

3. PROGRAMMING, OPERATIONS AND SEQUENCES

The flow chart of design automatic sorting machine for metals, non-metals and colors using PLC is shown in Figure 8. The block diagram is shown in Figure 9.

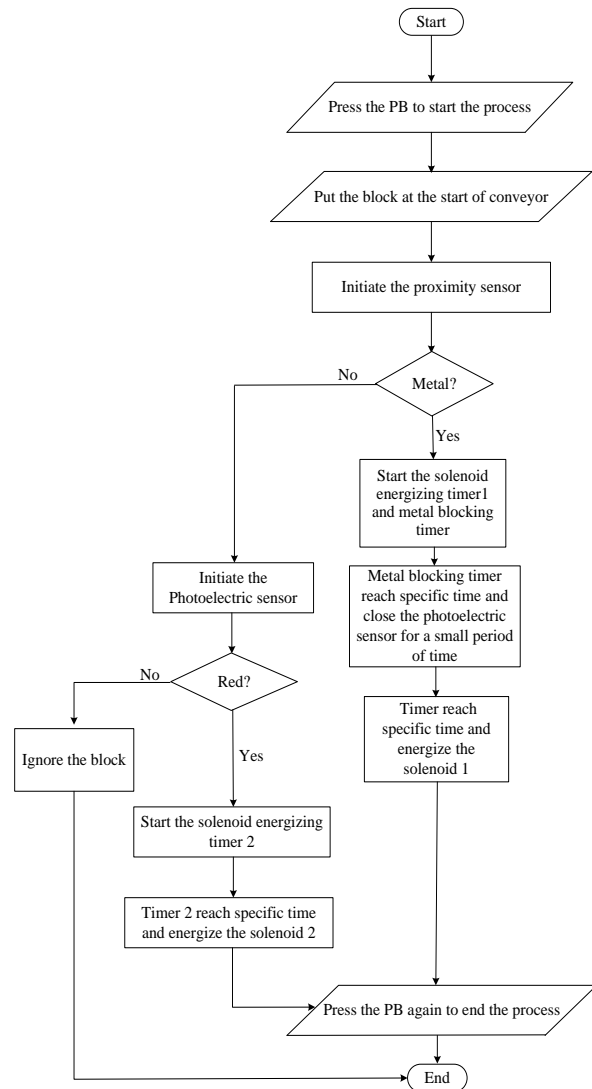


Figure 1. Block Diagram of the System

Figure 8. Flow Chart of Automatic Sorting Machine for Metals, Non-metals and Colors using PLC

In the following, for each device, are shown the programmed steps within the PLC.

- The conveyor belt is initiated, carried by the DC motor.
- Put the blocks of metals and wood color blocks, the machining piece are ejected by the cylinder on to the belt and conveyed.
- The metal sensor will detect any type of pieces traveling on the belt.
- And then the color sensor will detect the any color of wood travelling on the belt.
- The conveyor unit is initiated, by carrying the received piece towards the sorting chute.
- The machining piece is transported under two sensors.
- Type A pieces are detected by the metal sensor which triggers the nearby piston, pushing the block.
- Type B pieces are detected by the color sensor which triggers the near the piston, pushing the piece down to slit 2.

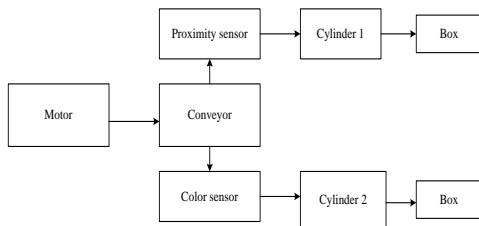


Figure 9. The Block Diagram of System

4. CONTROL UNIT

The control unit is composed of one push button for N.O and also use for N.C use by green color. All these items are shown in Fig. They are power supply, Omron PLC (CP1E), Connection, Relays and Cables. Although this structure is complexed, operation is good condition. This box is constructed by hollow pipe of aluminium and optical fiber. The control board of system is shown in Figure 10. The circuit diagram of system is shown in Figure 11. The hardware configuration of the system is shown in Figure 12.

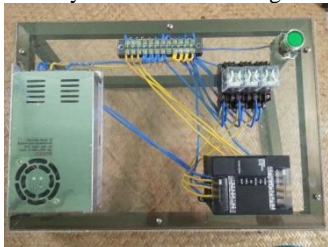


Figure 10. The Control Board of System

The operation of the control unit is the following.

- By pressing the green button, the conveyor unit initiates and the DC motor begins to rotate.
- By pressing this green button, the conveyor unit will stop.

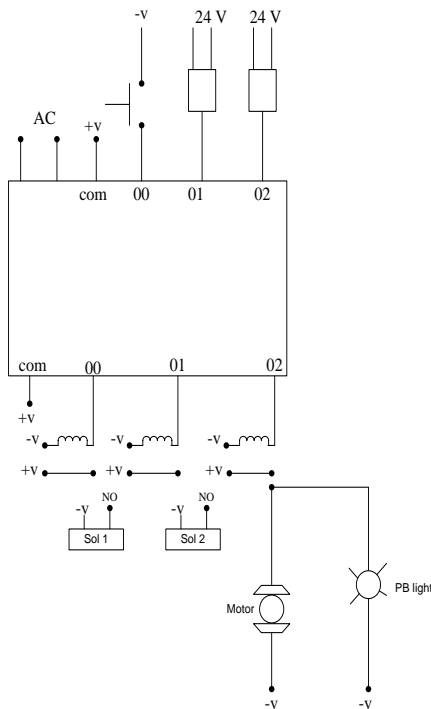


Figure 11. The Circuit Diagram of System

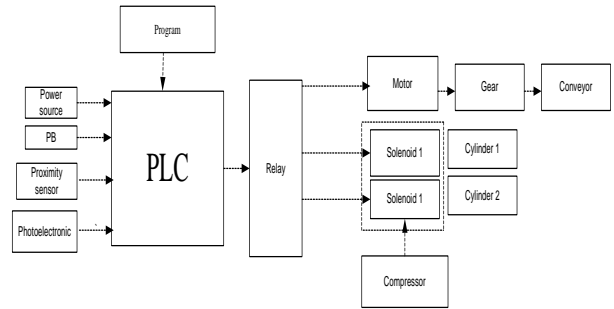


Figure 12. The Hardware Configuration of System

5. PLC'S INPUT AND OUTPUT DESIGNATION

A complete analysis of the assembly, the necessary inputs were identified, thus setting the required number of controlled outputs of the PLC. Table 1 shows the designation of each inputs and that are used to collect data from its operation. Having established each input for the PLC, the program inside the controller was molded into altering the outputs according to the sequence of inputs received. Each step of the program is initiated by a certain input, or a consecutive set of inputs [5].

Table 1. Table captions should be placed above the table

Process symbol	PLC input	Description
S0	I 0.00	Push button Start/Stop the process
S1	I 0.01	Proximity sensor sense the metal object.
S2	I 0.02	Photoelectric sensor sense the color

Table 2. Table captions should be placed above the table

Process symbol	PLC input	Description
K0	Q 100.00	Run the motor
Y1	Q 100.01	Active solenoid 1 and cylinder 1 push the metal block
Y2	Q 100.02	Active solenoid 2 and cylinder 2 push the desired color block

6. SOFTWARE REQUIREMENTS

The main software is CX programmer software from the product of Omron trend. This software is cheaper than other PLC kit such as Siemens, Deltas. Easy to use and can choose suitable I/O ports. Among them the research paper is used CP1E model consists of 6 input ports and 4 output ports. This model is suitable and cost effective for any researcher. This software is shown in Figure 13.

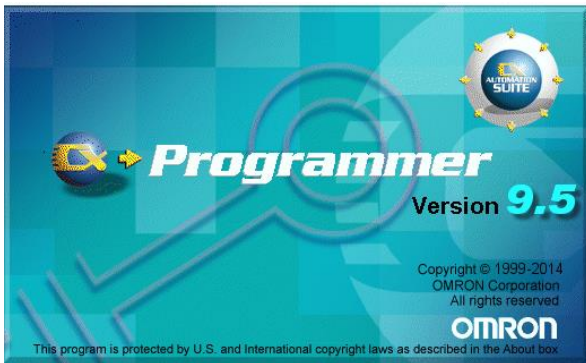


Figure 13. The Software of the CX Programmer

7. CONCLUSION

The research work presents a conveyor controlled unit application using a programmable logic controller. During the operation such a system is continuously changing its state due to various events that can be appeared. For a design engineer it is very important to identify all the possible states of the system in order to correctly program the behavior of the system in order to minimize the time needed to restore the operation [6]. We have proposed a system which would increase the production rate and accuracy of material handling systems. The system should segregate objects based on their type i.e metal or non-metal, color as required by the user. PLC with the frame of logic gates will make program modification easy and thus, we can modify the system according to the requirement [7].

8. ACKNOWLEDGMENT

Firstly, the author would like to acknowledge Dr. Thein Gi, Rector of Technological University (Thanlyin), for her kind permission to carry out this research work. The authors would like to thank many colleagues from digital image processing research group of Department of Electronic Engineering of Technological University (Thanlyin). The author particularly wishes to acknowledge all the teachers from Department of Electronic Engineering, Technological University (Thanlyin), for their support, encouragement and invaluable guidance in preparation of this research. The authors would like to express their thanks to all persons who have given support during the preparation period of this research work.

9. REFERENCES

- [1] SIEMENS, SIMATIC S7-200 Programmable logic Controller George Alexandru SMEU, Faculty of Electrical Engineering, University POLITEHNICA of Bucharest, Romania georg.semuc@com, May 23-25, 2013.
- [2] Prof. Dhaval Tailor, Vivek Kamani, Ankit Ghetiya, "PLC Object Sorting and Stacking Automation with PLC" Department of Electrical Engineering A.D Patel Institute of Technology, New VV Nagar, India.

- [3] Y V Aruna et al. Int. Journal of Engineering Research and Applications "Automatic convey or system with In-Process Sorting Mechanism using PLC and HMI System" Department of Electrical & Electronics Engg., Cambridge Institute Of Technology, Banqalore-36).
- [4] Solenoid-Wikipedia <https://en.m.wikipedia.org/wiki/Solenoid>.
- [5] Sorting of Objects Based on Colour, Weight and Type on A Conveyor Line Using PLC S. V. Rautu, A. P. Shinde, N. R. Darda, A. V. Vaghule, C. B. Meshram, S.S. Sarawade (Department of Mechanical Engineering, M.E.S. College of Engineering, Pune, S.P. Pune University, India).
- [6] Prof. Nilima Bargal, Aditya Deshpande, Rucha Kulkarni, Rucha Moghe, PLC based Object Sorting Automation, International Research Journal Of Engineering & Technology, ISSN (Online): 2395-0056, July 2016.
- [7] Sheela S, Shivaram. K. R, Meghashree S, Monica L, Prathima A, Shriya M. Kumar, Low Cost Automation for Sorting of Objects on Conveyor Belt, International Journal Of Innovative Research in Science, Engineering & Technology, ISSN (Online): 2319-8753, May 2016 .

Support Vector Machine Based Classification of Leaf Diseases

Ko Ko Zaw
Department of Electronic
Engineering
Technological University
Thanlyin, Myanmar

Dr. Zin Ma Ma Myo
Department of Electronic
Engineering
Technological University
Thanlyin, Myanmar

Daw Thae Hsu Thoug
Department of Electronic
Engineering
Technological University
Thanlyin, Myanmar

Abstract: Myanmar is well known for agricultural country; wherein about 65% of the labor force depends on agriculture. Since the leaf diseases are microscopic organism, cannot be detected normal human eyes. Leaves are special indicator to distinguish the diseases because the image information of the leaf are changed when the leaf surf the diseases. So, the image processing techniques can be used in agricultural sector. The research work presents a support vector machine classifier algorithm by using MATLAB R2017a for the classification of leaf diseases such as Alternaria Alternata, Cercospora leaf spot, Bacterial Blight and so on. In this research work, RGB color space is converted into HSI (Hue Saturation Intensity) color space. In segmentation step, k-means clustering is used to select the defected area, and it is extracted the features by using GLCM (Gray Level Co-occurrence Matrix). Prior to the features extraction, the median filter is used for getting noise free feature results. Finally, the leaf disease is classified by using support vector machine (SVM) and computes the accuracy. From the obtained results, the maximum accuracy of the system is 83%.

Keywords: leaf diseases; median filter; k-means clustering; gray level co-occurrence matrix; support vector machine

1. INTRODUCTION

Most of the diseases symptoms are found in leaves, stem and fruit. The image processing can be used in the leaf diseases detection and classification system. The common diseases of leaf are Bacterial Blight, Anthracnose, Alternaria Alternata, and so on. Such diseases are commonly found on mango, rice, watermelon, and others leaf. Leaf diseases can decrease the yield. These diseases may cause by pathogen such as fungi and bacterial. These diseases can be automatically detected and classified by using multiclass support vector machine (multiclass SVM). The main purpose of this research work is to design, implement and evaluate an image processing based software solution for classification of leaf diseases. The diseases of leaf features are as follow.

1. Alternaria Alternata: small reddish brown circular spots appear on the leaves.
2. Anthracnose: Appears as small regular or irregular dull violet or black leaf spots with yellowish halos. Leaves turn yellow and fall out.
3. Bacterial Blight: Appearance of one to several small water soaked, dark colored irregular spots on leaf.
4. Cercospora: Leaf spots are minute, brown with yellow halo. Spots are scattered, circular or irregular and become dark brown with age [1].

2. LITERATURE REVIEW

Some papers are describing to detection leaf disease using various methods suggesting the various implementation ways as follow. Visual Analysis, Image Processing and Optical Sensor are mainly implemented in three ways as the disease detection method. By using these three methods, the system can be developed to detect the disease earlier and that can overcome the challenges and disadvantages. By means of the methods comparison, disease detection by using visual analysis does not give the accurate output while in case of optical sensor, the system is not easy to implement and costly. So, image processing is the only way to build the simple,

robust and accurate disease detection system [2]. While working with image processing, on the other hands, the database collection is the most challenging task. For database collection, it is necessary to collect the basic information about the crop and its diseases as the important task. Therefore, a detail study should be done on the types of disease, their symptoms on crop and the patterns of disease. By observing the patterns of disease, the system will get designed. The mainly occurring diseases on leaf are Bacterial disease, Fungal disease, Viral disease and diseases due to insects. The paper gives the detailing of these diseases [3].

3. METHODOLOGY

The methodology of the research work can be divided into four stages such as image preprocessing, image segmentation, feature extraction, and disease detection and classification. Block diagram of the system is shown in Figure 1 [4].

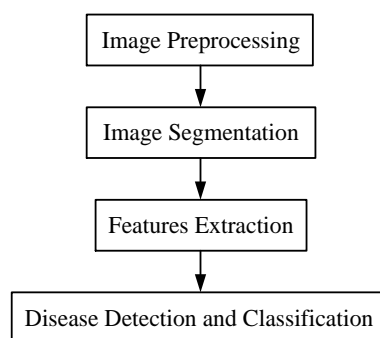


Figure 1. Block Diagram of the System

The flow chart of the leaf diseases detection and classification system is shown in Figure 2 [5].

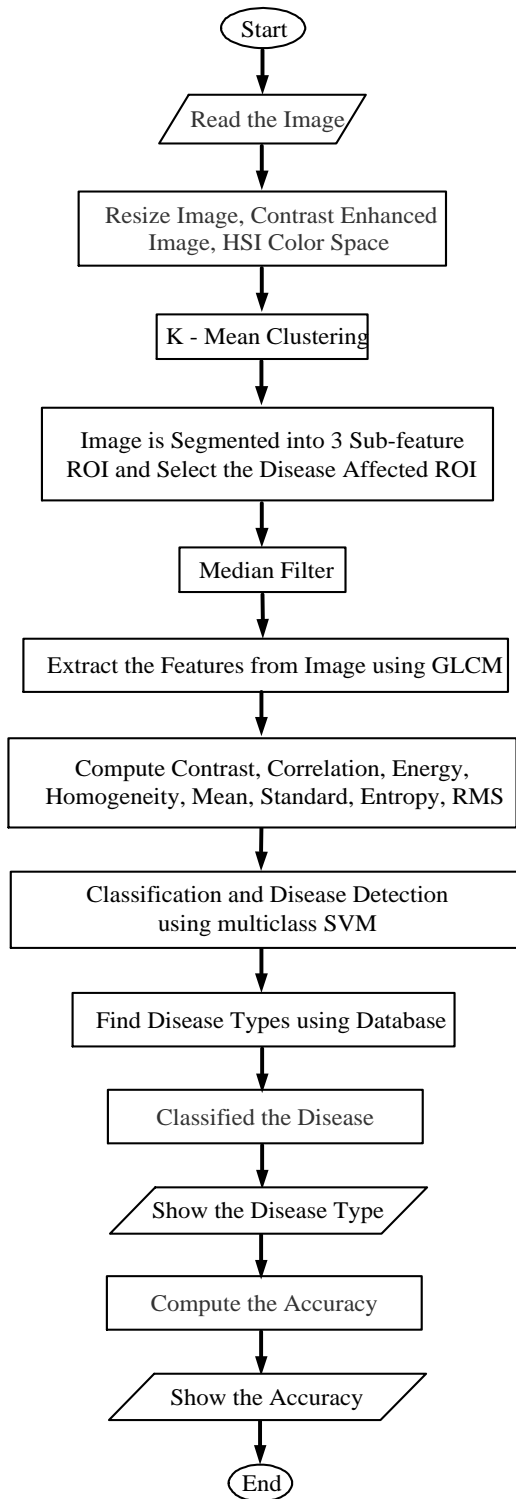


Figure 2. The Flow Chart of Leaf Diseases Classification System

The purposes and the advantages using image analysis are as follow [6].

1. To identify diseased leaf,
2. To measure affected area by disease,
3. To find the boundaries of the affected area,
4. To find out the color of the affected area,
5. To identify the diseases correctly.

The procedure of leaf diseases detection and classification system is the following.

1. Read input image.
2. Resize image.
3. The resized image is contrasted enhancement.
4. Converted RGB color space to HSI color space.
5. Apply k-mean clustering operation.
6. Image is segmented into three sub-features.
7. Select the disease affected area.
8. Filter the image by using median filter.
9. Extract the feature from the image using Gray-Level Co-occurrence Matrix (GLCM).
10. Compute contrast, correlation, energy, homogeneity, mean standard, entropy, root mean square.
11. Classify the diseases using multiclass support vector machine.
12. Compute the accuracy.
13. Show the accuracy.

3.1 HSI Color Space

HSI model is proposed to improve the RGB model. The Hue Saturation Intensity (HSI) color model closely resembles the color sensing properties of human vision. The HSI color space was developed to be 'intuitive' in manipulating color and was designed to approximate the way humans perceive and interpret color. HLS (Hue, Lightness, and Saturation) color space is similar to the HSI, the term light is rather than intensity. HSI color space is best for traditional image processing functions such as convolution, equalization, histogram and so on, which operate by the manipulation of brightness values since I is equally dependent on R,G, and B. The arccos function to compute H, arccos always gives you a value between 0 and 180 degrees.

However, H can assume values between 0 and 360 degrees. If $B > G$, then H must be greater than 180 degrees. Therefore, if $B > G$, just compute H as before and then take $(360 \text{ degrees} - H)$ as the actual hue value. The saturation is the distance on the triangle in the rgb-subspace from white relative to the distance from white to the fully saturated color with the same hue. Fully saturated colors are on the edges of the triangle. Hue is a color attribute that describes a pure color (pure yellow, orange or red), whereas a saturation gives a measure of degree to which a pure color is diluted by white light.

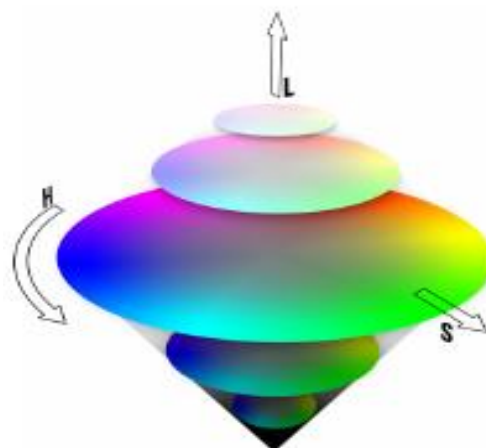


Figure 3. HSI Color Space

Table 1. Some Colors and Three HIS Intensity Value

Color	H	S	I
Red	60°	1	0.375
Green	120°	1	0.375
Blue	240°	1	0.375
Yellow	60°	1	0.375
Cyan	180°	1	0.375
Magenta	300°	1	0.375
White	-	0	0.75
Black	-	0	0

The HSI color model owes its usefulness to two principle facts. Firstly, the intensity component, I, is decoupled from the color information in the image. Secondly, the hue and saturation components are intimately to the way in which human being perceive color. HSI color space is shown in Figure 3 [7] and HSI intensity of some colors is shown in Table 1 [8].

4. TEST AND RESULTS

In this section, tests and results of automated leaf diseases detection and classification system using gray-level co-occurrence matrix (GLCM) and multiclass support vector machine (multiclass SVM) are expressed. The performance of the algorithm as a whole is analyzed and discussed. Tests were carried out to find the best segmentation result, so that the error measurement is minimized, and to confirm that leaf diseases detection and classification can perform accurately. As were as confirming that the system provides accurate detection, experiments were also conducted in order to confirm the detection by extracting the properties of the images. In the image preprocessing step consist of three parts such as read the image, resize image and contrast enhanced image. The image preprocessing is shown in Figure 4.



(a)



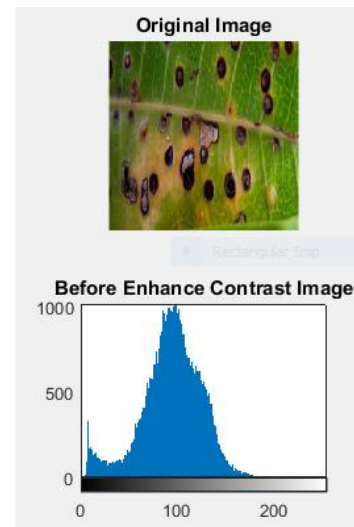
(b)



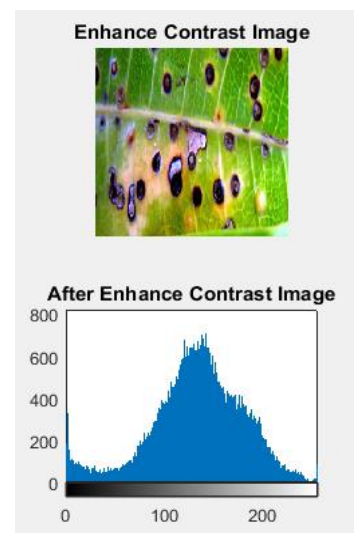
(c)

Figure 4. Image Preprocessing (a) Original Image, (b) Resize Image, and (c) Contrast Enhanced Image

Histogram equalization is a consideration for the image enhancement. It is a traditional approach of image contrast adjustment then the histogram equalization is shown in Figure 5.



(a)

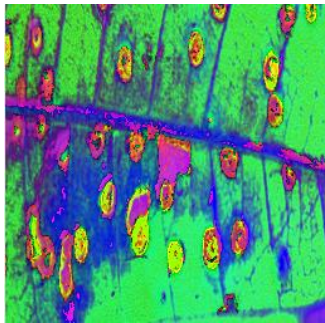


(b)

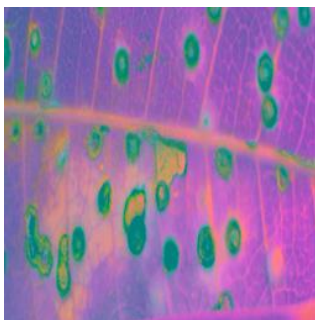
Figure 5. Histogram Equalization Image (a) before contrast enhancement, (b) after contrast enhancement

After making the preprocessing, the RGB color space is converted into HSI and L*a*b (a luminosity layer 'L*',

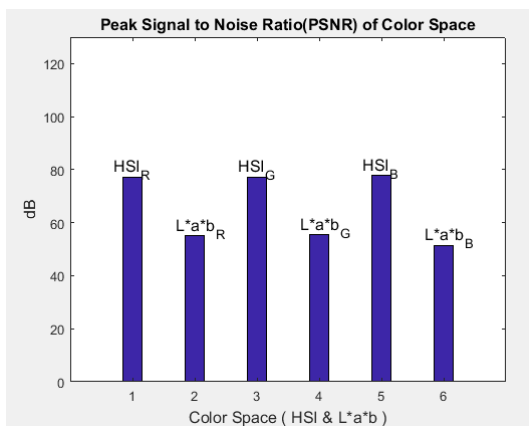
chromaticity-layer 'a*' and 'b*'). The HSI color space is higher peak signal to noise ratio than L*a*b color space. The results are shown in Figure 6.



(a)



(b)



(c)

Figure 6. Color Space (a) HIS Color Space, (b) L*a*b Color Space, and (c) Peak Signal to Noise Ratio (PSNR) of Color Space

The image is segmented into three sub-features by using k-mean clustering. And then, select the disease affected area. The results are shown in Figure 7.



Figure 7. k-mean clustering

In the feature extraction, the segmented image is converted into gray scale image, then filter by using median filter and GLCM is used to extract the feature [9]. The segmented image is as shown in Figure 8. The gray scale image and median filter image are shown in Figure 9 and Figure 10. After that, the affected area of leaf can be calculated. The affected area of leaf is shown in Figure 11. Finally, the leaf diseases can be classified by using multiclass support vector machine. The disease type is shown in Figure 12. The accuracy is shown in Figure 13.

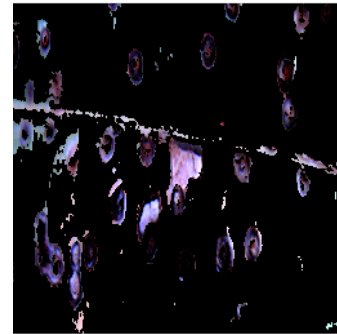


Figure 8. Segmented Image

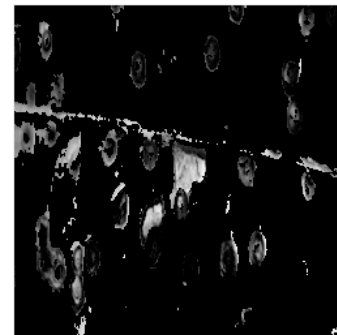


Figure 9. Gray Scale Image

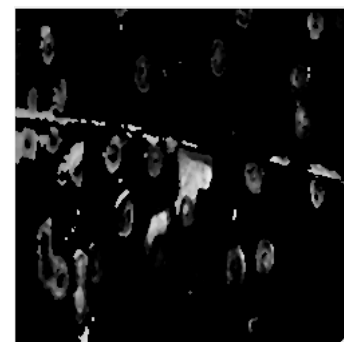


Figure 10. Median Filter Image

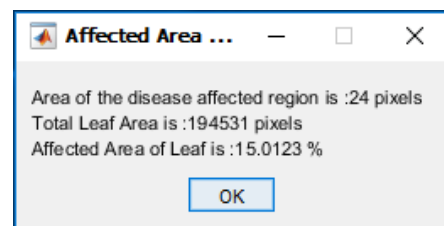


Figure 11. Affected Area of Leaf

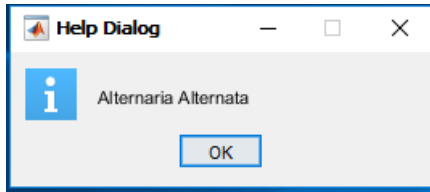


Figure 12. Disease Type of Leaf

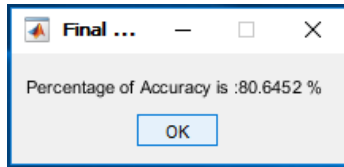


Figure 12. Disease Type of Leaf

This system elaborates the evaluated results with proper discussion. Windows 10 based system 4GB DDR4 Memory, 1TB of HDD, Core i5 is used for conduction the experiments. And then, MATLAB R2017a is used for the simulation of work. The total program execution time is shown in Figure 14.

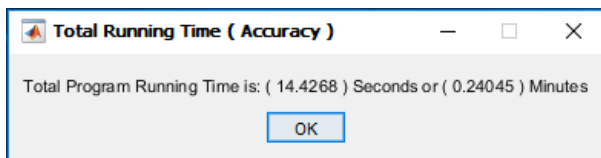


Figure 14. The Total Program Execution Time

Accuracy is defined as the ratio of the number of correctly recognized samples to the total number of test samples [10]. The percentage values of accuracy of each disease are shown in Table 2.

Table 2. The percentage values of accuracy of each disease

Sr. No	Disease Type	Percentage of Accuracy
1.	Alternaria Alternata	80.6452 %
2.	Anthraco nose	82.2581 %
3.	Bacterial Blight	80.6452 %
4.	Cercosporal Leaf Spot	82.2581 %
5.	Healthy Leaf	83.8710 %

5. CONCLUSION

From the results shown in above, the total program execution time takes 0.24045 minute and the maximum accuracy is 83.8710%. Furthermore, this system can be applied for the other leaf diseases to get the peak signal to noise ratio. When the total program execution time is less, the system can be assigned the higher performance.

6. ACKNOWLEDGEMENTS

Firstly, the author would like to acknowledge Dr. Thein Gi, Rector of Technological University (Thanlyin), for her kind permission to carry out this research work. The authors would

like to thank many colleagues from digital image processing research group of Department of Electronic Engineering of Technological University (Thanlyin). The author particularly wishes to acknowledge all the teachers from Department of Electronic Engineering, Technological University (Thanlyin), for their support, encouragement and invaluable guidance in preparation of this research. The authors would like to express their thanks to all persons who have given support during the preparation period of this research work.

7. REFERENCES

- [1] Ko Ko Zaw, Zin Ma Ma Myo, and Wah Wah Hlaing. 2018. "Multiclass Support Vector Machine Based Detection and Classification of Leaf Diseases", 11th National Conference on Science and Engineering, YTU, Yangon, Myanmar
- [2] A. Miyatra, S. Solanki. 2014. "Disease and Nutrient Deficiency Detection in Cotton Plant," International Journal of Engineering Development and Research, vol. 2, no 2, pp. 2801-2804.
- [3] V. A. Gulhane, A. A. Gurjar. 2011. "Detection of disease on cotton Leaves and Its Possible Diagnosis", International Journal of Image Processing (IJIP), vol. 5 : no 5 : pp. 590-598.
- [4] S. S. Panchal, R. Sonar. 2016. "Pomegranate Leaf Disease Detection Using Support Vector Machine," International Journal of Engineering and Computer Science, vol. 5, no 6, pp. 16815-16818.
- [5] V. M. Tiwari, T. Gupta. 2017. "Plant Leaf Disease Analysis using Image Processing Technique with Modified SVM-CS Classifier," International Journal of Engineering and Management Technology, vol. 5, no. 1, pp. 11-17.
- [6] A. N. Rathod , B. A. Tanawala, V. H. Shah. 2014. "Leaf disease detection using image processing and neural network", IJAERD vol. 1, no. 6, June, pp. 1-10.
- [7] S. Jayaraman, S. Esakkirajan , and T. Veerakumar. 2009. Digital Image Processing. U.S.A.: McGraw Hill Co.,
- [8] Myo Myo Han. 2017. "Analysis on Detection Improvement of Textile Fabric Defects using Gray Level Co-occurrence Matrix for automatic system," M.E. thesis, Dept. Electronic Eng., Yangon Technological University., Yangon, Myanmar.
- [9] D. Gadkari. 2004. "Image Quality Analysis Using GLCM," M.E. thesis, University of Central Florida, Orlando, Florida.
- [10] S. S. Patki, G. S. Sable. 2016. "Cotton Leaf Disease Detection & Classification using Multi SVM," International Journal of Advanced Research in Computer and Communication Engineering, vol. 5, no. 10, pp. 165-168.

3D Modeling of Five Speed Manual Transmission System for Teaching Aid Vehicles

Swe Zin Nyunt
Department of Mechanical
Engineering,
Technological University
Thanlyin, Myanmar

Theingi
Technological University
Thanlyin, Myanmar

Aung Hein Latt
Government Technical
Institute, Myanmar

Abstract: Additive manufacturing education is becoming to widespread adoption. Additive manufacturing is also the manufacturing technology. It is used by multiple industry subsectors, including motor vehicles, aerospace, machinery, electronics, and medical products. It can facilitate the customized production of strong light-weight 3D modeling. This paper describes 3D modeling of five speed transmission is designed and constructed by using AutoCAD software, 3D Mesh software, MakerBot 3D printer and digitizer. This 3D modeling of five speed transmission is good quality through lighter part, can demonstrate easily. The teacher can take 3D modeling of transmission and teach the operations of transmission in the classroom. It can produce the gears, fork, cover and synchronizer sleeves with different color. Many beautiful colors are interested to the students. So, it can use as teaching aids for the engineering students. In this transmission, five forward speed gears are helical type whereas reverse gears are spur type. Design consideration of spur gear and helical gears and shafts are included in this paper. In gear design, the number of teeth, face width, gear tooth features and pitch diameter are calculated. The shafts are designed according to the point of view of the strength.

Keywords: Gear, Teeth, Transmission, 3D Modeling, Additive Manufacturing

1. INTRODUCTION

A gear is a component that is used to transfer torque from a rotating input. It uses teeth to mesh together with other gears in order to transmit movement; usually gears that mesh together have identical type of teeth. Two gears together will form a transmission that is capable of changing speed, torque, and direction of the power source. A desired output of speed and torque can be obtained by controlling different geometry sizes between two gears. The transmission has the capability to enable the engine turning effect and its rotational speed output to be adjusted by choosing a range of under and overdrive gear ratios. So the vehicle responds to the driver's requirements within the limits of the various road conditions. There are two types of transmission, manual and automatic. Both do the same job. Manual transmission consists of cast iron or aluminum housing, shafts, bearings, gears, synchronizing devices and shifting mechanisms. Automatic transmission includes a torque converter, compound planetary gear set, two or more disc clutches and one or more bands.[7]



Figure 1. 3D Modeling of Toyota Transmission

Additive manufacturing is a new and innovative method used to manufacture solid objects. It allows the user to make the complicated 3D model using a method of manufacturing for a part is made by adding layer after layer of a heated material that cools and solidifies almost instantly. These 3D shapes are initially created on a computer using solid modeling software, which can be downloaded into the printer. Depending on shape, material, series volume and other criteria, series production is economically possible using metal additive manufacturing.[6] Additive manufacturing system is a process by which digital 3D design data is used to build up a component in layers by depositing material. A range of different metals, plastic and composite materials may be used in additive manufacturing system. In this paper, 3D modelling transmission for Toyota 22RE engine produced by using additive manufacturing method is shown in Figure (1). A five-speed manual transmission includes five forward gears and one reverse gear, applying advanced monolithic structure of the intermediate shaft and the shift lock ring-type synchronizer. The transmission possesses a compact structure, a small size, high transmission efficiency, and a larger ratio range, with good economy and dynamic performance. Each process is limited to one type of material and only few are able to process more than one material e.g. thermoplastics of different color. [5]

2. LITERATURE REVIEW

A typical transmission consists of housing, shafts, bearings, gears, synchronizing devices and shifting mechanisms. Shafts and bearings are related in their relative positions in the housing. The five-speed transmission includes five forward gears and one reverse gear, applying advanced monolithic structure of the intermediate shaft and the shift lock ring-type synchronizer. The gear positions are described as follows.

2.1 Neutral Gear Position

With the gears in neutral as shown in Figure (2) and the car stationary, the transmission main shaft is not turning. When the clutch is engaged and the engine is running, the clutch shaft gear drives the counter shaft driven gear.

This turns the counter shaft and the other gears on the counter shaft. In this position, the transmitted power from engine output passes through the clutch shaft or input shaft of transmission and then directly through fourth gear or main drive gear on counter shaft[4].

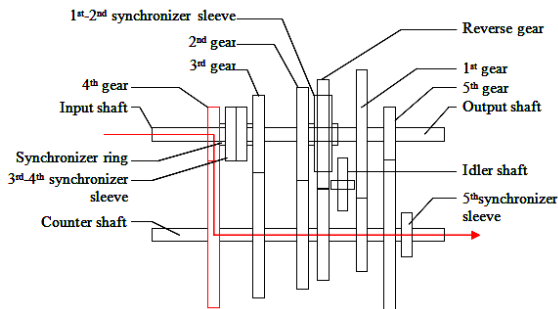


Figure 2. Neutral Gear Position

2.2 First Gear Position

When the clutch is depressed, the clutch disc is released and the gear shift lever is moved into 1st position. Movement of the gear shift lever causes the linkage to select the 1st-2nd synchronizer sleeve and move it to the right. When the clutch is engaged, the power flows through transmission as shown in Figure (3). The power trends in this position, the transmitted power passes through the main drive gear of input shaft and constant mesh counter gear to the first gear on counter shaft and then to first gear on main shaft.[4]

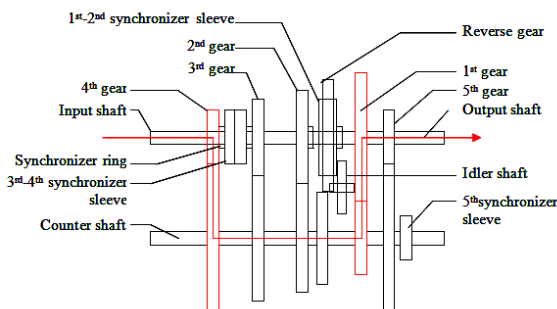


Figure 3. First Gear Position

2.3 Second Gear Position

The 1st-2nd synchronizer sleeve has been moved to the left so that its internal teeth engage the external teeth on the 2nd speed gear. The power flows through the clutch gear to drive the counter gear assembly. The medium size gear on the counter shaft drives the second speed gear through the synchronizer to the second speed gear on the main shaft [4].

2.4 Third Gear Position

When the gear shift lever is moved into 3rd position, movement of the gear shift lever causes the linkage to select the 3rd synchronizer sleeve and move it to the right. The 1st-2nd synchronizer sleeve must be moved to its center position. The power flows through the main drive gear of the input shaft, constant mesh counter gear and then to the third gear on the counter shaft, finally to the transmission main shaft.[4]

2.5 Fourth Gear Position

In this gear, the 3rd-4th synchronizer sleeve has been moved to the left so its internal teeth engage the external teeth of the clutch gear. This gear is a direct drive and the gear ratio is 1:1.

The power trends directly to the drive shaft and there is no speed reduction in this case [4].

2.6 Fifth Gear Position

This speed gear is actually an overdrive. That is, the output shaft turns faster or overdrives, than the input shaft. The purpose of overdrive is to reduce engine wear, engine noise and fuel consumption. The advantage of overdrive is that it reduces engine speed around 30 percent while still maintaining the same road speed. When the transmission is shifted into overdrive, the clutch synchronizer sleeve locks the overdrive gear to the main shaft. The 5th speed gear on counter shaft is larger than the overdrive gear on the main shaft. Thus, increased gear ratio can be provided.[4]

2.7 Reverse Gear Position

To achieve reverse gear, an extra gear is inserted into gear train. This gear is called the reverse idler gear. When the shift lever is moved to reverse, the reverse idler gear is meshed with reverse gears on the counter shaft and main shaft. In reverse, both synchronizer sleeves are in neutral. The flow of power through the transmission is as shown in Figure (4). Because of the reverse idler gear, the main shaft turns in the reverse direction. The wheels turn in the reverse direction and the car moves backward.[4]

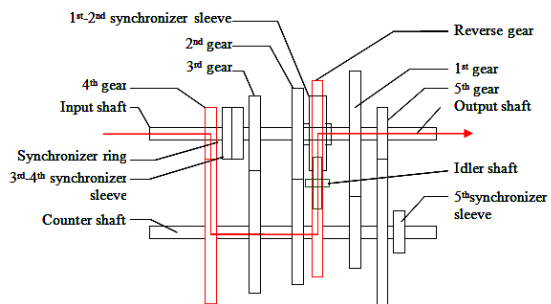


Figure 4. Reverse Gear Position

2.8 Synchronizing Device

To avoid the clashing of gears during shifting, and to simplify the shifting action for the driver, synchronizing devices are used in transmission. Its job is to move ahead of the unit that is to be meshed, seize the other unit and bring the rotational speed of both units together. Once both units are rotating at the same speed, they may be meshed. This type splines the hub to the shaft but does not permit end movement of the hub. The clutch sleeve is shifted forward or backward on the hub. This action forces (by means of inserts) the blocking rings to equalize gear speeds before the clutch sleeve engages the other gear to lock gear to hub through clutch sleeve. All forward gears are synchronized. There are several types of synchronizer units used today. All use a cone (blocking ring) that precedes the movement of either the clutch hub or clutch sleeve. The cone engages a tapered surface on the part to be engaged to synchronize the speed before meshing. The power can be transmitted quickly and smoothly without damaging the gears [7].

2.9 Shifting Mechanisms

The transmission is shifted by means of shifter forks that ride in a groove cut into the clutch sleeve and sliding gear. The forks are attached to the clutch to a cam and shaft assembly. Spring loaded steel balls pop into notches cut in the cam assembly to hold the shift mechanism into whatever gear is selected. The shafts pass through the hold the shift mechanism into whatever gear is selected. The shafts pass through the

hosing or housing cover and are fastened to shift levers. Shift forks are made of die-cast aluminum. Gear shift levers on manual transmissions are located either on the steering column or on the floor board. With either location, the operation of gearshift lever does two things. First, it selects the gear assembly to be engaged. Second, it shifts or moves the gear to provide the desired gear position.[7]

3. DESIGN OF TRANSMISSION

Design theory of gears and shafts are described.

3.1 Design of Gear

The velocity ratio (V.R) is

$$V.R = \omega_p / \omega_g = N_p / N_g = n_g / n_p = D_g / D_p \quad (1)$$

where ω = Angular velocity (rad/sec) and

N = Rotational speed (rev/min). The transmitted force F_t , acts at the pitch line with a velocity, $v = \frac{\pi D_p N_p}{60}$ (2)

where D_p is the pinion diameter in meter, V is the pitch line velocity in meter per second and N_p is the rotational speed of the pinion in rpm. . If the torque (M_t) is Newton-meter, the transmitted force is $F_t = M_t / r_p$ (3)

the radial force (F_r) can be computed $F_r = F_t \tan \psi$ (4)

where ψ is the pressure angle of the tooth form. For spur gear, the normal force (F_n) can be computed

$$F_n = \frac{F_t}{\cos \phi} \quad (5)$$

For helical gear, the normal force (F_n) can be computed

$$F_n = \frac{F_t}{\cos \phi_n \cos \psi} \quad (6)$$

where ϕ_n is the normal pressure angle of the tooth form and is ψ the helix angle of the tooth form[3]. The axial force directed parallel to the axis of the shaft carrying the gear and is also called thrust force. The axial force is computed by:

$$F_a = F_t \tan \psi \quad (7)$$

Stresses in Gear Teeth, Lewis equation may be used.

$$\left(\frac{1}{m^2 y} \right)_{all} = \frac{S_{all} k \pi^2}{F_t} \quad (8)$$

$$S_{all} = \frac{2 M_1}{m^3 k \pi^2 y n} \quad (9)$$

where M_1 = Torque on weaker gear and
 n = Number of teeth on weaker gear.

The endurance load is calculated by the following equations.

The endurance load equations for spur and helical gears are

For spur gear, $F_o = S_o B y \pi m$ (10)

For helical gear, $F_o = S_o B y \pi m \cos \psi$ (11)

The limiting endurance load must be equal to or greater than the dynamic load (F_d).[3]

The wear load F_w for spur gear, $F_w = D_p B K_w Q$ (12)

For helical gear, $F_w = \frac{D_p B K_w Q}{\cos^2 \psi}$ (13)

Where D_p =Pitch diameter or smaller gear(pinion),m,
 D_g =Pitch diameter of larger gear (gear), m,
 K_w =Load stress factor for fatigue, N/m²,
 n_p =Number of teeth on pinion,

n_g =Number of teeth on gear and

Q =Ratio factor

BHN = Average brinell hardness number of gears.

The wear load F_w is an allowable load and must be equal to or greater than the dynamic load F_d [3]. The dynamic analysis, as proposed by

$$\text{For spur gear, } F_d = \frac{21 \times V (BC + F_t)}{21 \times V + \sqrt{(BC + F_t)}} + F_t \quad (14)$$

For helical gear,

$$F_d = \frac{21 \times V (BC \cos^2 \psi + F_t) \cos \psi}{21 \times V + \sqrt{(BC \cos^2 \psi + F_t)}} + F_t \quad (15)$$

where C = Dynamic factor, N/m.

3.2 Design of Counter Shaft

A shaft is the component of mechanical devices that transmits rotational motion and power from one place to another. The power is delivered to the shaft by some tangential force and the resultant torque or torsional moment. The torsional moment (M_t) acting on the shaft can be determined from this equation.[3]

$$M_t = \frac{9550 \times KW}{rpm} \quad (16)$$

For a gear drive, the torque is found from this equation.

$$M_t = F_t \times (D/2) \quad (17)$$

where F_t = Tangential force at the pitch radius, N and
 D = Pitch diameter, m.

The ASME Code equations are described as follows. For a solid shaft with axial loading, the Code equation is:

$$d^3 = \frac{16}{\pi S_s} \sqrt{\left[K_b M_b + \frac{\alpha F_a d}{8} \right]^2 + (K_t M_t)^2} \quad (18)$$

For a solid shaft having little or no axial loading, the Code equation reduces to:

$$d^3 = \frac{16}{\pi S_s} \times \sqrt{(K_b \times M_b)^2 + (K_t \times M_t)^2} \quad (19)$$

where M_t = Torsional moment, Nm,
 M_b = Bending moment, Nm,
 d = Shaft diameter, m,
 K_t = Combined shock and fatigue factor applied to torsional moment.

ASME Code states for steel purchased under definite specifications, the permissible shear stress may also be taken as 30% of the elastic limit in tension but not more than 18% of the ultimate tensile strength for shafts without keyways. These values are to be reduced by 25% if keyways are present [3]. The shaft diameter is taken as follows.

- (1) Up to 25mm in 0.5mm increment
- (2) 25mm to 50mm in 1mm increment
- (3) 50mm to 100mm in 2mm increment
- (4) 100mm to 200 mm in 5mm increment.

4. DESIGN OF TRANSMISSION

To design the transmission of Toyota, the required data are collected from the existing transmission and assumptions are extracted from the theory of automobile.

Max: power 65 kW at 4600 rpm
Max: torque 162 Nm at 2400 rpm
Transmission 5 speed manual
Transmission type Rear wheel drive

The design consideration and calculation of transmission are mostly dependent upon the maximum torque of the input speed from the engine. In gear design, choose 6150 OQT 400 material which has brinell hardness 601, yield stress 1860 MPa and ultimate stress 2170 MPa. The gears are designed to transmit power and satisfy the dynamic check. In gear design, the number of teeth, face width, gear tooth features and pitch diameter are calculated.

The calculated results for gear pairs are described in Table 1.

Table 1. Calculated results for gears

Gear pair	Input Gear Pair	1 st	2 nd	3 rd	4 th	5 th	R
Pitch dia:	93/55	104/44	86/62	68/80	55/93	51/97	108/87/40
Gear ratio	-	3.996	2.345	1.437	1.0000	0.889	4.565
No.of teeth	-	35/15	29/21	28/32	28/47	26/49	31/25/12
Face width	-	30	20	19	21	21	32
F _t (N)	-	12450	8836	6848	5891	5647.4	13695
Torque(Nm)	-	647.4/ 273.9	379.9/ 273.9	232.8/ 273.9	162/ 273.9	144/ 273.9	739.5/595.7 /273.9
F _r (N)	-	19203	13931	11923	-	10367	19852
F _a (N)	-	18019	13997	13567	-	13636	21052
F _d (N)	-	17490	13619	11424	-	10123	19274

The shafts are designed according to the point of view of the strength. In the strength shaft design, the shaft diameters for variety of speeds have to be calculated by using the ASME code equation.

The calculated results for shafts are described in Table 2.

Table 2. Calculated results for shafts

Type of Shaft	Material	S _u (MPa)	S _y (MPa)	Dia (mm)	Length (mm)
Input Shaft	6150 OQT 400	2170	1860	25	218
Output Shaft	6150 OQT400	2170	1860	30	395
Counter Shaft	6150 OQT400	2170	1860	35	320
Idler Shaft	6150OQT400	2170	1860	30	170

5. 3D MODELING OF TRANSMISSION

3D modeling is used in various industries like films, animation and gaming, interior designing and architecture. They are also used in the medical industry for the interactive representations of anatomy. A wide number of 3D software is also used in constructing digital representation of mechanical models or parts before they are actually manufactured. CAD/CAM related software are used in such fields, and with these software, not only can you construct the parts, but also assemble them, and observe their functionality. 3D modeling is also used in the field of industrial design, wherein products are 3D modeled before representing them to the clients. 3D models, which is suitable for indexing and retrieval of 3D models by features such as geometry, dimensions, material, texture, diffuse reflection, etc..[11] 3D Solid models can be tested in different ways depending on what is needed by using simulation, mechanism design, and analysis. For example; a

pool pump would need a simulation ran of the water running through the pump to see how the water flows through the pump. These tests verify if a product is developed correctly or if it needs to modify its requirements.[5]

The minimum wall thickness or feature size necessary in order to be built and self-supporting is 1 mm with a tolerance of +/- 0.05mm. Depending on what material is being used, undercuts or angles under 40° will need to be supported. The supports are generated in secondary CAD programs in many different forms such as lattice or grid work structures with each column only as thick as the laser beam in order to facilitate easier removal.[5]

Firstly, the gears and components of transmission are drawn with 1:2 scales by using CAD software and Autodesk 3D Mesh software.

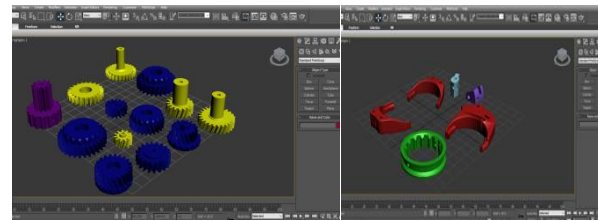


Figure 5. Gears and Forks

Secondly, the settings for each component are done by using MakerBot software. And then, the parts of transmission are printed by MakerBot 3D printer. Finally, these parts are installed and operated successfully.

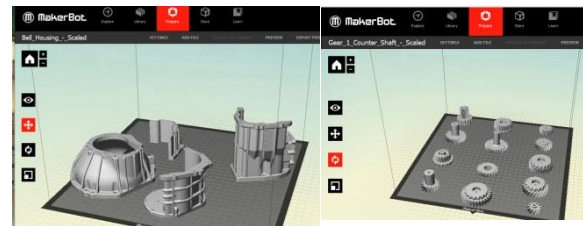


Figure 6. Covers and Gears

For all of the components, Z resolution was used because that showed good finish of the product and there was no need for higher resolution, which will mean longer printing time. The quality of the print was always the highest due to the fact that good precision is needed for functional gears.[14]



Figure 7. Makerbot 3D Printer and Digitizer

The results demonstrate that the total time of printing all of the components from the transmission is 8 hours and 25 minutes, which is no long and it can be decreased if more than

one component is printed at the same time. The material cost to print the gearbox including the raft, support material used is depending upon the time.

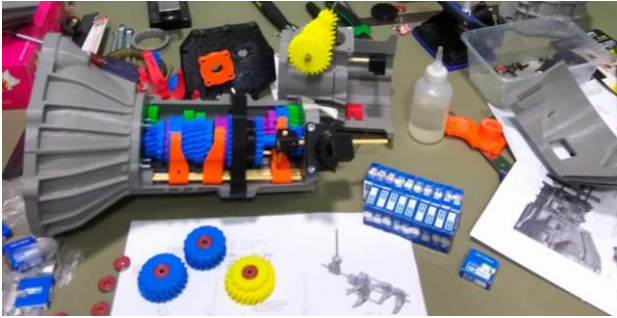


Figure 8. Installing of Prototype Transmission

6. CONCLUSIONS

In this transmission, there are all together five forward speed and one reverse. Among the five forward speeds, the fourth drive is the direct drive and the final drive is the overdrive. The design calculation is based on maximum tangential load at 1st speed range. Gears and shafts are designed with 6150 OQT 400 heat treated alloy steel, which has brinell hardness 601, yield stress 1860 MPa and ultimate stress 2170 MPa. The design of spur gears, helical gears and shaft designs are calculated in this paper. The required design calculation of spur and helical gears can also be calculated through both strength and dynamic check. The gear ratios are 3.996, 2.345, 1.437, 1.000, 0.889 and 4.565. The shafts are designed according to the point of view of the strength. In the strength shaft design, the shaft diameters for variety of speeds have to be calculated by using the ASME code equation. Diameters of output, counter, idler and input shaft are 40, 35, 30 and 25 mm respectively. In many instances, the cost of producing a 3D model using additive manufacturing processes exceeds that of traditional methods. 3D printing is a quick, simple and relatively cheap method for production of models for automobile teaching aids. As it presents a wide range of materials and technologies with various features and parameters are available. This enables a potential researcher to choose the right technology fitting exactly the needs and fulfilling the requirements of prepared experiment. Thin-walled and tough models have been successfully manufactured. In this design, structural rigidity combined with lightness must always be the first consideration for the durability of the wearing parts and smoothness of running. Develop environmental impact profiles for major additive finishing processes. Investigate work piece pretreatment, acid cleaning, and rinsing sub-processes contributions toward the environmental impact of additive finishing processes. It can facilitate the customized production of strong light-weight 3D modeling. So, the teachers can take this transmission to the classroom. And then, they can explain about the operations and can demonstrate this 3D model transmission.

7. ACKNOWLEDGMENTS

The author thanks to Colleagues from Department of Additive Manufacturing and Reverse Engineering, Automotive Technology Research Institute (PyinOoLwin) and Department of Mechanical Engineering, Technological University (Thanlyin), for their supports.

8. REFERENCES

[1] Baldinger M, Duchi A. High Value Manufacturing. In: da Silva Bartolo PJ, editors. High Value Manufacturing:

Advanced Research in Virtual and Rapid Prototyping: Proceedings of the 6th International Conference on Advanced Research in Virtual and Rapid Prototyping.

- [2] Cort L. Miller and Michale W. Washo, 1987, Marks' Standard Handbook, 9th Edition, McGraw. Hill Book Company.
- [3] Hall, Hollow enho, Laughlin, 1961. Theory and Problem of Machine Design, SOS series SchoumPublishing Co; New York.
- [4] Hiller, V.A.W, 1979. "Motor Vehicle Basic Principles, Hatchinson & Co., Ltd. London".
- [5] <http://en.wikipedia.org/w/index.php>
- [6] Klahn C, Leutenecker B, Meboldt M. Design for Additive Manufacturing – Supporting the Substitution of Components in Series Products. Procedia CIRP 2014;21:138–43.
- [7] Martin W. Stocket, 1969. "Auto Mechanics Fundamentals"
- [8] Nannan G and Ming C L 2013 Additive manufacturing: technology, applications and research needs *Front. Mech. Eng.* 8(3): (Higher Education Press and Springer-Verlag Berlin Heidelberg)
- [9] Robert L. Mott, P.E, 1985, "Machine Elements in Mechanical Design", Charles E. Merrill Publishing Company.
- [10] Willaim H. Crouse, 1981, "Automotive Mechanics, 8th Edition", Tata McGraw Hill Publishing Company, Ltd.
- [11] Wohlers T, editor. Wohlers Report 2013 - Additive Manufacturing and 3D Printing State of the Industry - Annual Worldwide Progress Report. 18th ed. Fort Collins, CO: Wohlers Associates; 2013.
- [12] Wright Douglas, 2001. "Design and Analysis of Machine Elements". May 2005.
- [13] Yang, S., and Zhao, Y., 2015, "Additive manufacturing-enabled design theory and methodology: a critical review," *The International Journal of Advanced Manufacturing Technology*.
- [14] www.additivemanufacturing.com/basics/
- [15] www.instructables.com

Benchmark Evaluation & Proposed Electrical Architecture for a 12V BSG Vehicle

Priyamvad Mishra
Adaptation Responsible, Vehicle Integration Dept
FCA Engineering India Pvt Ltd,
India

K. Phaneendra Varma
Senior Engineer, Electrical & Electronics Dept
FCA Engineering India Pvt Ltd,
India

Abstract: This paper makes an effort to define an optimal electrical architecture for a 12V BSG system for a mid- sized diesel engine, with the help of functional validation tests and specific test cases developed by the authors. The first few sections of the paper explain various modes of a 12V BSG hybrid operations namely-ESS, torque assist and recuperation on a reference vehicle. Set of test cases have been developed to explain 12V BSG behavior as a DC motor during ESS and torque- assist mode of operation and as a 3-phase generator during regenerative coasting mode. In the final section, an optimized electrical architecture of 12V BSG system is proposed for mid-sized diesel engine with manual transmission, based on objective measurement of test cases and a Pugh Comparison matrix of various feasible architectures.

Keywords: Belt Driven Starter Generator (BSG) System; 12V enhanced flooded battery; Voltage Stabilization Module; BSG architecture

1. INTRODUCTION

Due to increase in the CO₂ Emissions [1], we are currently facing the problem of Global Warming [2]. To overcome the same, automobile OEM'S are searching for the alternatives to conventional Internal Combustion Engine (ICE) and working towards hybridization of vehicle powertrain, to reduce the CO₂ Emissions. This also helps for improvement in Fuel Economy without any de-gradation in vehicle performance.

Basically, there are 5 different levels of powertrain hybridization depending on hybrid function capabilities, capacity of electric motor or the machine capacity, energy savings expressed in terms of km/l used in the vehicle. Table 1 elaborates on different hybridization levels [3].

This paper concentrates on the electrical architecture of a Micro-Mild Hybrid segment, which is capable of providing hybrid functions e.g. ESS, torque assist and recuperation. For this a literature survey has been done, based on various Mild hybrid systems available in the market:

- 1) Low voltage (12V) start stop/ micro hybrids [4].
- 2) BSG mild hybrid, system voltage $12V \leq V_{system} \leq 48V$ [5, 6].
- 3) ISG mild hybrid, system voltage $V_{system} > 60V$.

However, cost impact, architectural complexities, high voltage system hazard [8] and other packaging constraints such as size limitations) limits the usage [6] of ISG in passenger vehicle segment.

This paper focuses on 12V and 48V hybrid systems [5, 6, and 8] which are getting popular worldwide. There are fewer hybrid vehicles operating with 48V BSG, but are not getting as popular as compared with 12V BSG, in particular for India market. This is due to lot of other factors like packaging, architectural modifications and requirement of dedicated DC-DC converter for stepping down 48V to 12V, for vehicle accessories apart from 48V BSG unit [3, 9]. In this paper, a 12V BSG system has been proposed and analyzed taking into consideration, for a bumper to bumper congested traffic with vehicle halts in excess of 90 seconds. The 12V BSG architecture proves a very economical and relatively maintenance free solution for above transit operations, for Indian urban city drive conditions.

The paper is organized into four sections: section I explains the circuit configuration. Section II provides the operating principle of a 12V BSG system. Section III evaluates the primary BSG functions with aid of special test cases. Section IV discusses the proposed EE architecture for a BSG system on a mid-sized Diesel Powertrain, followed by the conclusion of the work.

Table 1: Various Hybridization Levels Available in Global Market [Energy Saving benefits are measured on NEDC cycle [12]; for a pure Electric Vehicle Energy Savings is considered 100% in absence of secondary power source, primarily an IC engine]

Functions	Micro & Micro-Mild hybrid	Mild Hybrid	Full Hybrid	Plug in hybrid (PHEV)	EV
Start/Stop	✓	✓	✓	✓	✓
Regenerate braking	✓ (micro-mild only)	✓	✓	✓	✓
Additional electric power for few seconds	✓ (micro-mild only)	✓	✓	✓	✓
Electric power for mild distance (city)			✓	✓	✓
Electric power for long distance & recharge on grid				✓	✓
Energy Savings	5-10% (upto 25% in city traffic)	10-25%	25-40%	50-100%	100%
Electric Power	1.5-10KW	5-20kW	30-75kW	70-100kW	30-100kW
Car Examples	PSA C2	Honda Civic	Toyota Prius	GM Volt	Nissan leaf

2. CIRCUIT CONFIGURATION AND OPERATION OF A 12V BSG SYSTEM

Fig.1 illustrates the electrical architecture of key low voltage components for a 12V BSG reference vehicle. The BSG unit functions both as a motor and an alternator with modes of operation being controlled by Engine Control Unit (ECU). BSG replaces the conventional alternator and it is directly driven by the Front End Accessory Drive (FEAD) belt of engine.

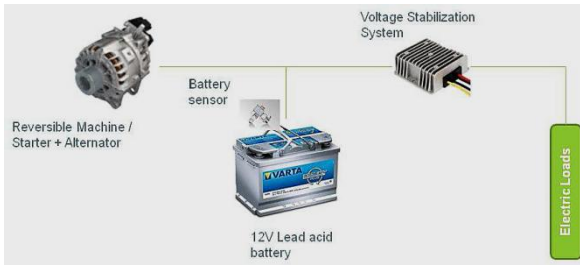


Figure 1: Electrical Architecture 12V BSG System

Hence this type of hybrid system is also known as Belt Driven Starter Generator (BSG). BSG unit primarily consists of an e-motor coupled with power control module which acts as two-way rectifier, AC to DC & Vice versa.

The Intelligent Battery Sensor (IBS) broadcasts critical battery parameters to ECU on a dedicated Local Interconnect Network (LIN), between ECU and vehicle 12V battery. IBS will communicate all the parameters like battery Voltage, battery current, Battery State of Charge (SOC) etc. Based on the driver inputs it will command the BSG system to provide various functions, based on battery state of Charge, expressed as % of full charge. Engine Control Unit which also acts as master gateway for ESS operation, also controls energy flow to & from BSG unit to battery/ engine output shaft, thus commanding BSG to switch from motor to alternator mode of operation.

A Voltage Stabilization Module (VSM) is used in the reference vehicle to supply un-interrupted 12V supply to critical electrical loads in the vehicle i.e. all vehicle control units, radio & navigation systems in this vehicle.

There are three modes of hybrid operations typically for a 12V BSG system, these are as follows:

- Mode I: ESS Mode (Engine Start Stop).
- Mode II: Torque assist Mode.
- Mode III: Recuperation Mode.

2.1 Mode-I: ESS Mode

As shown in Figure 2, in this mode BSG unit operates as motor and it will crank the Engine. This crank is also called as warm crank, as this is post 1st cranking operation which is always via the starter motor of the vehicle. The current required during BSG crank event is relatively less as compared to the starter motor crank. This is because the starter must engage the crankshaft ring gear to overcome higher engine frictional forces under cold start. The BSG unit being part of Front End Accessory Drive (FEAD), cranks the engine by overcoming FEAD belt drive inertia of both engine & belt tensioner, which is relatively lower in magnitude when compared with crankshaft inertia. Also frictional forces to be overcome are lower on account of warmed up engine. Considering the sizing of BSG unit which is limited to 4 kW max output, it is not capable to support power equivalent for starter motor crank. Figure 2 depicts energy flow between BSG system and engine under Engine Start Stop (ESS) event via BSG crank. It is observed that the BSG operating in motor during event of engine crank/ESS, draws the maximum current from the battery as compared to torque assist mode. At the same time vehicle battery also needs to support 12V uninterrupted energy demand, to critical vehicle loads.

Hence a VSM module is connected in series between 12V battery and critical vehicle loads. Though it is not defined but BSG supports engine stop. Further BSG unit is capable of engine stall assistance, provided all conditions for ESS enable; which are discussed in next section are available prior to next BSG crank event.

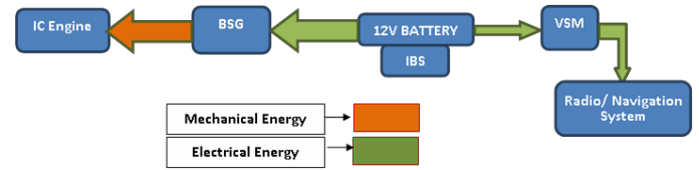


Figure 2: Energy flow during the ESS Mode

2.2 Mode II: Torque assist

In this mode, the BSG unit operates as motor and supplements ICE torque, thus reducing the energy demand from the engine during this phase. This assist is limited due to size of e-motor & battery capacity, but it helps to improve the fuel economy and CO₂ emissions of vehicle. Figure 3 shows energy flow during torque assist. During torque assist mode BSG unit acts as draws relatively lower magnitude of current to provide required assist, while the critical loads functions as explained in Mode-I.

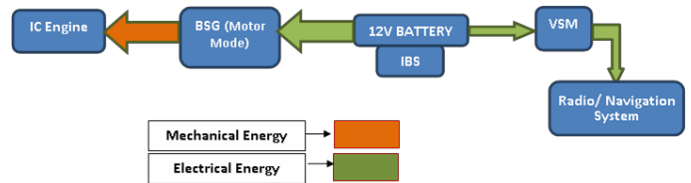


Figure 3: Energy flow during Torque Assist mode

2.3 Mode III: Recuperation Mode

In this mode, the BSG unit will act as alternator driven by ICE torque. The electrical output from BSG unit is used to charge vehicle battery and run all 12V electrical loads in vehicle. Figure 4 depicts the energy flow during the Recuperation mode. During recuperation BSG unit is driven by the ICE residual torque (during vehicle deceleration, while in gear coasting), this torque is used by BSG unit to charge the 12V vehicle batteries as a smart alternator.

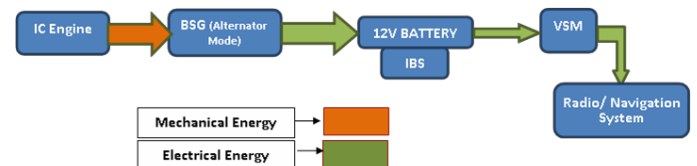


Figure 4: Energy flow during Recuperation Mode

3. OPERATING PRINCIPLE FOR 12V BSG SYSTEM OF A REFERENCE VEHICLE

Jen-Chiun Guan et al [7], has illustrated various hybrid operating modes of BSG, using MATLAB Simulink models to represent driver, engine, vehicle, CVT, BSG and battery. This paper defines a power split ratio PSR [10, 11] used to evaluate BSG mode of operation i.e. motor and alternator mode.

$$PSR = P_{eng} / P_{req}, \text{ Where}$$

P_{eng} = engine power and P_{BSG} = BSG motor output power

P_{req} = Power Request from driver, $P_{req} = P_{eng} + P_{BSG}$.

1) When $(0 < PSR < 1)$ BSG unit operates in motor mode.

2) If $PSR = 1$, i.e. $P_{req} = P_{eng}$, BSG unit operates in engine mode.

3) If $PSR > 1$, i.e. P_{BSG} is negative, BSG unit is in alternator mode charging the battery.

The authors in this section have attempted to explain these primary hybrid functions of a 12V BSG system, by developing of unique Design Validation Plan & Requirements (DVP&R) or test cases, exclusively for a 12V BSG system. The various BSG functions were defined in a simplified way using combination of test cases on a reference vehicle.

Figure 5 shows the schematic diagram of the Electrical load management in reference vehicle. All the electrical loads are connected in parallel to the vehicle battery. Fuse 1 provides protection to the BSG unit against heavy ingress current at time of cranking the engine. Typically, its rating is ~ 450A. Fuse 2 (100A) is a common fuse for protection of all electrical loads except the starter motor and the BSG. The starter motor will have the protection only for its solenoid but not for the armature of the starter motor which will draw ~500A at the time of the starting. A 30A fuse is connected for protection of starter motor solenoid.

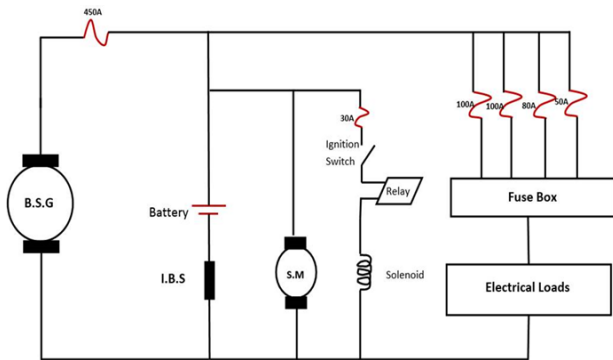


Figure 5: Schematic diagram of BSG system on reference vehicle

Table 2 (More detail is provided in Appendix at the end of paper) shows the Engine Start-Stop (ESS) logic matrix in the reference vehicle and discusses the inputs required for the activation of the BSG system [4]. The ESS Logic matrix is derived from the reference vehicle, by set of functional validation tests undertaken by enabling and disabling certain inputs which are as below:

- 1) Driver Detection.
- 2) Driver Door Detection.
- 3) Hood latch Detection (The hood latch switch needs to be normally closed during all conditions for ESS crank to be enabled, hence this input is not depicted exclusively in the logic diagram).

It is observed from these tests that BSG prompted/ enabled engine crank operation, better known as ESS function is available only when above listed input combinations are available as per Logic sequence explained below. This condition holds good irrespective of whether the engine is in stall condition, or engine comes to an auto-stop, while in forward or reverse motion of vehicle.

The above ESS operational matrix has been represented by the author in a simplified form using logic gates, as seen in Fig.6.

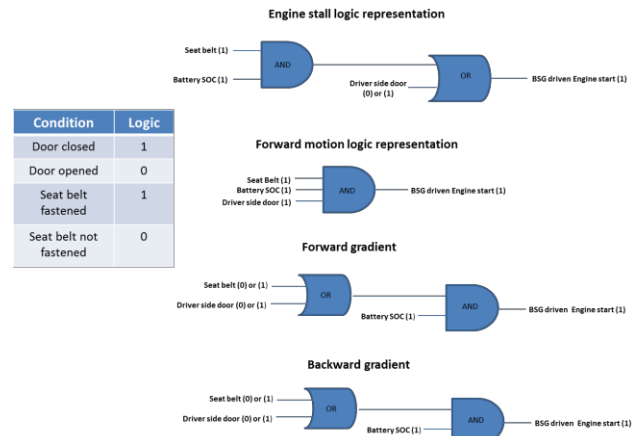


Figure 6: Logical representation of ESS logic in reference vehicle

Note: Hood latch switch is always closed during all conditions [Priyamvad Mishra & Phaneendra Varma, 27-Feb-18]

4. EVALUATION OF BSG FUNCTIONALITY WITH SPECIAL TEST CASES

In this section primary BSG functions has been explained using system parameters viz.: battery current, battery voltage, engine RPM, along with inputs required for BSG functionality activation like accelerator and brake pedal inputs on reference vehicle are discussed.

The primary functions have been tested at different operating conditions like AC ON/OFF and ESS enable/disable during these test cases as listed below:

- 1) Starter motor crank or first cranking operation.
- 2) BSG prompted engine crank or warm crank.
- 3) Torque assist when accelerating in low rpm ranges from 1st thru 4th gears.
- 4) Recuperation available when vehicle is coasting.

The drive cycle for these test cases is a standard urban India drive cycle which is the heavy urban section of NEDC drive cycle.

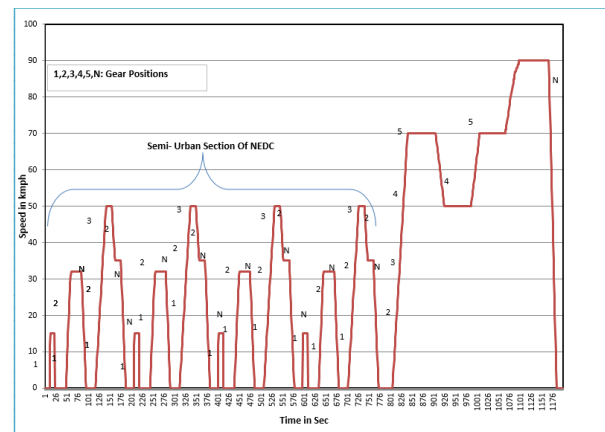


Figure 7: Drive cycle for evaluation for BSG functions

The average vehicle speed is 15 km/h and no of stops per km is 3 to 5. The test cases have been undertaken with various load conditions, viz AC load and ESS Signal enabled or disabled, with their significance as explained below:

- a) AC ON ESS ON: AC load impacts the duration for which vehicle remains in auto stop condition i.e. the lower temperature set point, the lesser time vehicle is in auto stop

condition, this is to maintain cabin comfort which takes precedence with AC ON.

b) AC OFF ESS ON: During this test scenario the duration for auto stop is maximum as there is no cabin load preference here.

c) AC ON ESS OFF: With ESS signal disabled in this scenario there is no start stop event possible.

Measurement of system parameters:

- Battery Voltage: Shunt load placed in series with battery & BSG unit.
- Engine Speed, Vehicle Speed: L350 Optical sensor & CAN data logger.
- Accelerator input: potentiometer
- A CAN signal is tapped referred as hybrid system sensor signal to indicate ESS, torque assist & recuperation modes of operation.

Figures 7 and 8 explain the comparison between cranking profiles of a conventional starter motor crank and a BSG prompted crank events.

4.1 Starter crank or Cold crank:

The 1st cranking operation of vehicles equipped with BSG is always through starter. Reason for same is explained in earlier section. Since this is the first crank operation of vehicle it is referred as cold crank. Figure 7 shows changes in battery system parameters like Battery voltage, battery current, battery SOC (State of Charge) during the starter motor crank, plotted against cranking time interval in seconds.

During this period, significantly high current (~550A) is drawn from the battery, because starter motor pinion is directly engaging the crankshaft ring gear and must overcome engine static friction higher moment of inertia of crankshaft. It is also evident from significantly higher voltage drop (~2.9V) during starter motor crank.

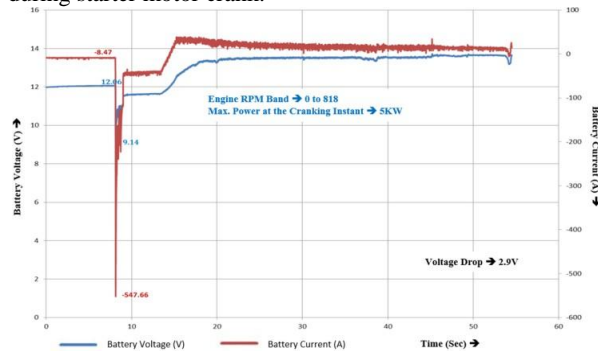


Figure 8: System parameters during starter motor crank event

Table 3: Test case of starter motor crank (cold start)

System Parameters		Cold start (@ 23°C)
Battery Voltage (V)	Maximum	12.06
	Minimum	9.14
Battery Current (A)	Minimum	0
	Maximum	-547
Engine rpm	Minimum	0
	Maximum	818

4.2 BSG crank or warm crank:

All the subsequent cranks for a warmed up engine from initial starter motor crank is via BSG. From Table 4, it is seen that there is a significant drop in battery voltage during the BSG crank when AC is in ON condition, 12.2V ~9.71V. Hence a VSM is provided to protect in vehicle sensitive loads like

radio, navigation, ECU units, from rapid surges in current during BSG crank event and provide constant voltage supply.

Table 4: Test case of BSG crank (Hot start)

System Parameters		AC ON & ESS ON	AC OFF & ESS ON
Battery Voltage (V)	Maximum	12.21	12.62
	Minimum	9.71	10.28
Battery Current (A)	Minimum	-19.64	0
	Maximum	-420	-414
Engine rpm	Minimum	0	0
	Maximum	1022.3	956.0

Figure 8 shows changes in the system parameters during the BSG crank. It is observed that during this period the current drawn by BSG is relatively lower (~400A) as compared to the starter motor crank. The negative sign indicates the current drawn by BSG in motor mode to crank the engine. Duration of BSG start is almost 1/3rd of the starter motor start operation Table 9 (Refer Appendix at end for details).

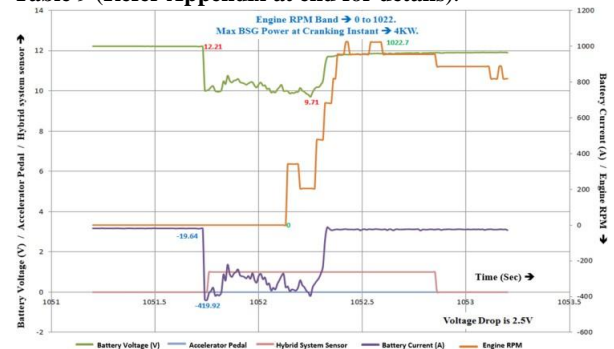


Figure 9: System parameters during BSG Prompted crank Event

4.3 Torque assist:

When the driver presses the accelerator pedal with pedal travel < 40% of total travel. With a good battery SOC %, a supplementary torque from BSG is addition to engine output torque.

This gives a sporty feel and a peppy responsive accelerator response which is clearly limited. Table 5 depicts torque assist event, during which a minor drop in the battery voltage can be observed. Also, there is a significant increase in the battery current, indicating BSG unit functions in motor mode.

Table 5: Test case of torque assist event

System Parameters		AC On ESS On	AC Off ESS On	AC On ESS Off
Battery Voltage (V)	Maximum	14.22	14.08	13.08
	Minimum	12.44	11.91	12.02
Battery Current (A)	Minimum	4.70	14.92	26.26
	Maximum	-80.1	-75.9	-83.0
Engine rpm	Minimum	1084	955	814
	Maximum	1893	1505	1819
Accelerator pedal Travel (%)	Minimum	0	0	0
	Maximum	38	22	24

Figure 9 shows changes in the system parameters during the torque assist event. In a torque assist function, BSG unit supplements the engine torque for a certain engine rpm range in each gear, starting from 1st to 4th gear. The energy required for torque assist is provided by the vehicle battery,

which is for a very short burst of time. It can also be seen that the torque assist is available for accelerator pedal travel less than 40% and engine rpm between 1050rpm to 1900rpm.

4.4 Recuperation:

During the Recuperation period vehicle is decelerating when coasting in gear without acceleration input, the battery is charged by the BSG unit, which now functions as a generator. Fig.10 shows the changes in the system parameters during recuperation mode.

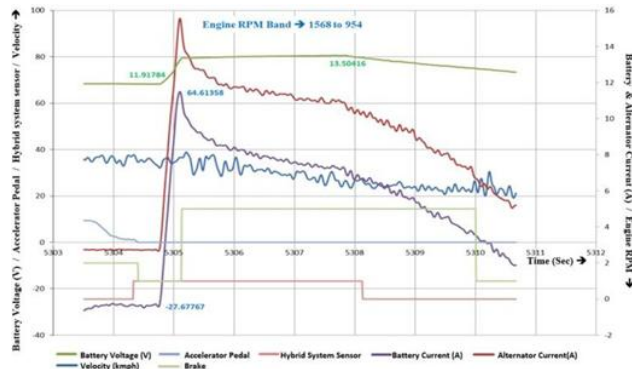


Figure 11: System parameters during recuperation mode

From Figures 8, 9 and 10, it can be summarized that the BSG unit operates as a bi-directional DC motor as well as AC generator, based on vehicle operating condition, battery SOC conservation principle or strategy. BSG unit acts as DC motor and supplements the engine torque during the torque assist mode. Also during the ESS event, BSG unit meets the energy demand to crank the engine via a belt driven starter mode of operation.

The BSG unit, also behaves as a 3-phase generator during recuperation event, generating AC current which is converted to 12V DC input to charge vehicle, through in-built rectification.

Table 6: Test Case of Recuperation Event in the Vehicle

System Parameters		AC On ESS On	AC Off ESS On	AC On ESS Off
Battery Voltage (V)	Maximum	13.61	14.16	13.5
	Minimum	12.31	12.12	11.91
Battery Current (A)	Minimum	0	-69.7	-27.7
	Maximum	61.12	71.0	64.6
Engine rpm	Minimum	1226	886	954
	Maximum	1662	1368	1568

With driver foot off accelerator pedal, coasting condition Table 6 shows test case for recuperation event, during which BSG unit can charges the battery, in smart alternator mode(SAM) during the coast down. SAM behavior is alternator mode of operation where the alternator is not charging to a fixed set point, rather there is floating reference voltage based on the engine load and electrical load demand. SAM strategy requires a continuous monitoring of battery's state of charge (IBS sensor) and a LIN communication protocol, to control the alternator. It thus aids in decreasing the fuel consumption as well as the overall emissions produced by the vehicle. SAM strategy is applicable in

vehicles equipped with Intelligent Battery Sensor (IBS) and LIN communication interface through which the desired operating conditions are transmitted to the alternator.

Table 7: Fuel consumption comparison of base vehicle & reference vehicle

Variant	AC ON	AC OFF
BSG	19.5 km/l	21.40 km/l
Non-BSG	18.15 km/l	19.3 km/l

Based on Fuel economy comparison between 2 vehicles measured back to back on standard NEDC drive cycle:

- 1st is base vehicle equipped with conventional powertrain.
- 2nd is reference vehicle having same vehicle configuration as base vehicle, but equipped with BSG.

From Table 7, it is can be seen that BSG unit helps reduce fuel consumption by ~7-10%, on account of combined benefit of SAM strategy and ESS functionality. These benefits further magnify when tested in bumper to bumper traffic with frequent stop start operations.

5. PROPOSED 12V BSG ELECTRICAL ARCHITECTURE FOR A MID-SIZED DIESEL MANUAL TRANSMISSION

Referring to comparative study of 12V versus 48V BSG systems done by previous teams [7, 4, and 5] and by authors [8], 12V BSG architecture is shortlisted for the current scope of work. The key merits for going to a 12V system over 48V system for a stop start traffic with lots of traffic signals, are listed below:

- Need of DC-DC converter to connect 48V grid to 12V.
- Simple adaptation in absence of any major modifications needed.
- Depending on battery size, separate battery cooling arrangement is required for 48V system.
- Packaging constraints to house additional batteries, DC to DC converter and a battery cooling system.

The subject vehicle under proposal is equipped with a mid-sized Diesel BS4 Engine with 6 speed manual transmission.

Table 8 (Refer Appendix at end for details) compares various possible combinations of electrical architectures suited for a Micro Mild Hybrid vehicle, equipped with a 12V Belt Driven Starter Generator. Further by application of Pugh Matrix optimization methodology based on selective parameters, it is clearly seen that single battery/ single VSM is an optimized proposal for subject 12V BSG architecture.

- It is comparatively cost effective with limited voltage stabilization provision available for supporting uninterrupted power supply to sensitive in-vehicle electrical loads.
- VSM scores over a dedicated DC to DC converter for a stop start traffic conditions, which requires low voltage surge issues only during cranking operations.
- DC to DC converter is more viable when there is perceived voltage loss to some of heavy vehicle load demands like headlamp and interior lights. Also a DC- DC is continuous in

operation unlike a VSM which comes in operation only during cranking.

6. Conclusion and Future Scope

Based on the architectural study, special test cases evaluation on reference vehicle, a 12V single battery (with single Voltage Stabilizer for Radio/ Navigation unit) is proposed for a diesel powertrain of subject vehicle. The objective of the proposed work has been achieved with a BSG system, achieving CO₂ emissions reduction of 0.136gms/km and improvement in fuel economy by ~7.5%, over a non-BSG variant. This has been achieved without de-gradation in overall performance and NVH characteristics of the base vehicle or non-BSG variant [Fig 12 & Table 10- refer Appendix at end for more details]. Further adaptation of a 12V BSG on base vehicle requires with minimal architectural changes at a lower cost.

In accordance with rapid developments in design of e-motors, battery technology for hybrid vehicles, it's possible to target for even lower Carbon footprint for these vehicles by use of:

- ✓ More efficient electric motor (operating with $\eta > 90\%$).
- ✓ Superior next generation battery technologies like AGM, Enhanced flooded and Li-ion batteries [11].
- ✓ Increasing the level of hybridization: Full Hybrids (Series, Parallel or Split HEVs), Plug in HEVs.

References

1. Ipsita Banerjee, "CO₂ Emissions from Land Transport in India: Scenarios of the Uncertain", Civil & Environmental Engineering, University of California, Berkeley, Page 3-8.
2. Matthew E. Caire, "Global Warming: Is it Real?", Honor thesis, 05-May-17, Page: 8-18.
3. Roberto Capata and Antonino Coccia Roberto Capata and Antonino Coccia, "Procedure for the Design of a Hybrid-Series Vehicle and the Hybridization Degree Choice", www.mdpi.com/journal/energies, 15-Mar-2010, Page: 451-458.
4. Anand Kishor Asekar, "Stop-Start system using Micro-hybrid technology for increasing fuel efficiency", International Journal of Mechanical & Prod Engg, Vol-1, Issue-6, Dec-2013, and Page: 20-23.
5. Aditya Kumawat, Amrit Kumar Thakur, "A Comprehensive study of Automotive 48-Volt Technology", SSRG- IJME- Vol4, Issue5, May-2017, and Page: 13, 15-18.
6. Marc Angelo Z. Amador, Marc Anthony C. Lina, Alexyz G. Aquino, Filipe A. Gutteres, et al "Design and Implementation of Power Management System Utilizing Super capacitors for Hybrid Vehicles", International Journal of Scientific Engineering and Technology, Volume No.3, Issue No.8, Page: 1074 – 1077.

7. Jen-Chiuan Guan, Bo-Chiuan Chen, Yin-Dar-Huang, Yu-Jen Chiu, "Adaptive Power Management Strategy for Hybrid Electric Vehicle with Belt-driven Starter Generator", Proceedings of 2015 IEEE 12th International Conference on Networking, Sensing and Control Howard Civil Service International House, Taipei, Taiwan, April 9-11, 2015, Page: 503, 506 & 507.

8. Saurabh Belsare, HP Khainar, Priyamvad Mishra, "Benchmarking, Target setting & Evaluation of a Belt Driven Starter Generator (BSG) for 2.0 L Diesel Engine", International Journal of Recent Trends in Engineering & Research Vol 3 Issue 6 Jun-2017, Page: 318-320.

9. Luke A. DeBruin, "Energy and Feasibility Analysis of Gasoline Engine Start/Stop Technology" https://kb.osu.edu/dspace/bitstream/handle/1811/54555/Start-stop_Thesis.pdf.

10. Chan-Chiao Lin, Huei Peng, Jessy W. Grizzle, Fellow, IEEE, and Jun-Mo Kang, "Power Management Strategy for a Parallel Hybrid Electric Truck", IEEE Control systems, Vol-11, No.6, Nov-2003, Page: 839-845.

11. Alan Soltis and Xiang Chen, "A New Control Strategy for Hybrid Electric Vehicles", University of Windsor, Proceedings of the American Control Conference Denver, Colorado June 4-6, 2003, Page: 1398-1399.

12. "Impact of Worldwide Test Procedures on Advanced Technology Fuel Efficiency Benefits"- A. Rousseau, Yi Ding, EVS27 Barcelona, Spain, November 17–20, 2013, Page: 1-8.

Acknowledgments

- The authors would like to thank FCA Engineering India Pvt Ltd, in particular Mr. Ramesh Gogineni and Mr. Pankaj Dahad (APAC – Engg), for providing a challenging opportunity and guidance during course of work.

- Authors also like to express their gratitude towards Mr. Ed Kirk, Mr. Velu Saravana Kumar & Mr. Shane Berger (From FCA Engg Ltd); for their efforts to define and refine a robust and unique functional objective document for a 12V BSG Hybrid vehicle for mid-sized Diesel powertrain with Single battery & Single VSM."

Definitions/Abbreviations

BSG	Belt-driven starter generator
ISG	Integrated starter generator
HEV	Hybrid electric vehicle
IBS	Intelligent battery sensor
ESS	Engine auto start-stop
VSM	voltage stabilization module
ECU	Engine control unit
BCM	Body control module
FEAD	front-end accessory drive
ICE	Internal combustion engine
SOC	State Of Charge
AGM	Absorbent glass Material
EFB	Enhanced flooded battery

Reference Vehicle It is a compact C-segment Diesel sedan class mild hybrid. It is equipped with 5 speed manual transmission, a 12V BSG (4 kW peak output power) with 70Ah Enhanced Flooded battery. It combines the capability to provide torque assist of around 5 Nm and limited regenerative charging capability.

Kerb weight = 1135kg
Max available torque = 200Nm

7. Appendix

Table 2: Reference vehicle ESS Matrix

	Door	Seat Belt	Result	Remarks	Conclusion
Engine Stall	Closed	Closed	ESS Functional	BSG start available	The BSG driven start will be available if and only if seat belt is fastened. This is an input to the logic of driver occupancy.BSG will work if seat belt is fastened and driver side door open or closed irrespective of it.
	Open	Open	ESS Not Functional	BSG start not available	
	Open	Closed	ESS Functional	BSG start available	
	Closed	Open	ESS Not Functional	BSG start not available	
	Closed	Open	ESS Not Functional	BSG start not available	
Forward motion	Closed	Closed	ESS functional	BSG start available	BSG driven start will be available only when driver side door is closed and driver side seat belt is fastened while considering forward motion.
	Open	Open	ESS not functional	BSG start not available	
	Open	Closed	ESS not functional	BSG start not available	
	Closed	Open	ESS not functional	BSG start not available	
	Closed	Open	ESS not functional	BSG start not available	
Forward Gradient	Closed	Closed	ESS functional	BSG start available	BSG driven start will be available for all combinations of door and seat belt except for when door is open and at the same time seat belt is not fastened. This is because engine activation is needed for powering up the EPS module and having sufficient brake pressure. Safety and ability to maneuver on slope is given priority.
	Closed	Open	ESS functional	BSG start available	
	Open	Closed	ESS functional	BSG start available	
	Open	Open	ESS not functional	BSG start not available	
	Open	Open	ESS not functional	BSG start not available	
Backward Gradient	Closed	Closed	ESS Functional	BSG start available	BSG driven start will be available for all combinations of door and seat belt except for when door is open and at the same time seat belt is not fastened. This is because engine activation is needed for powering up the EPS module and having sufficient brake pressure. Safety and ability to maneuver on slope is given priority
	Closed	Open	ESS Functional	BSG start available	
	Open	Closed	ESS Functional	BSG start available	
	Open	Open	ESS not functional	BSG start not available	
	Open	Open	ESS not functional	BSG start not available	

Table 8: Evaluation of Possible 12V BSG System Architectures Using Pugh Matrix Optimization Method
 [© Priyamvad Mishra & Phaneendra Varma, 27-Feb-18]

Comparative Parameters	12V Standalone Lead-acid Battery	12V Standalone Lead Acid Battery + Voltage Stabilizer	12V Standalone Lead Acid Battery + DC: DC converter	Dual Lead Acid Battery
Packaging	0	-	-	--
Vehicle Electric Architecture Impact	0	-	-	--
Maintenance	0	0	0	--
Cold Cranking capability	+	+	+	++
Torque Assist capability	+	+	+	+
Regeneration Performance	Limited energy recovering	Limited energy recovering	Limited energy recovering	Optimized energy recovering
Voltage regulation	Oscillation on Voltage net	Sensitive loads voltage stabilized for less than 1 sec	Sensitive loads voltage stabilized for less than 5 sec	Loads voltage stabilized
Loads Impacted	All loads	Inductive loads and rest of loads after 1 sec	Inductive loads and rest of loads after 5 sec	None of the loads
Costs (USD for annual volume: 53k)	AGM battery 60Ah: \$70 Total: \$70	AGM battery 60Ah: \$70 VSM 200W: \$19 Total: \$89	AGM battery 60Ah: \$70 DC: DC CONV 450W: \$100 Total: \$170	AGM battery 1 (60Ah): \$70 AGM battery 2 (20Ah): \$46 Solid State Switch: \$29 Total: \$145
Electrical diagram				

- Architecture Proposal for 12V μHybrid Vehicle
 - The DC/DC converter costs can vary depending of the level of sensitive loads

Table 9: Cranking profile comparison of Starter motor & BSG crank

System Parameters	Conventional crank (By starter motor)	Auto Start (By BSG)
Peak current	800A	500A
Cranking current	220A	300A
Max voltage dip	3.5V	2V
Crank duration	0.9sec	0.5Sec

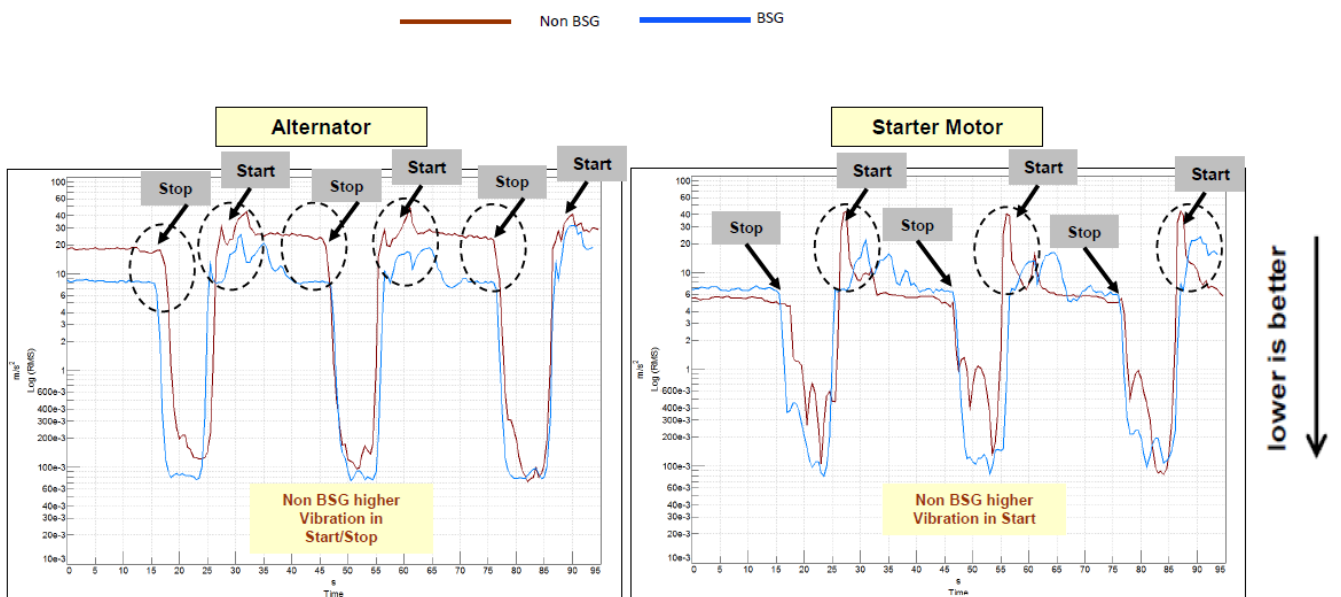


Fig12: NVH characteristics of base vehicle (non-BSG) & BSG variant

As compared to base vehicle,

- Vibration level is lesser on Alternator & starter motor locations in BSG vehicle during both Start and Stop Events

Table 11: Performance Comparison of base vehicle (non-BSG) & BSG variant

Acceleration Performance	AC ON (Time in Second)			AC OFF (Time in Second)		
	BSG Vehicle	Non BSG	BSG improvement as compared to Non BSG (%)	BSG Vehicle	Non BSG	BSG improvement as compared to Non BSG (%)
0-60 kmph	6.0 sec	6.2 sec	3.2 %	6.0 sec	5.9 sec	-1.7 %
0-100 kmph	14.5 sec	14.9 sec	2.7 %	14.5 sec	14.8 sec	2.7 %
0-120 kmph	20.1 sec	20.6 sec	2.4 %	20.0 sec	20.4 sec	2.0 %
0-400 m	19.5 sec	19.7 sec	1.0 %	19.7 sec	19.8 sec	0.5 %
0-1000 m	35.4 sec	35.8 sec	1.1 %	35.3 sec	36.0 sec	1.9 %

Dehydration of Aqueous Ethanol Mixtures By Extractive Distillation

Thu Zar Thein
Chemical Engineering
Technological University
Ministry of Education
Thanlyin, Myanmar

Wai Mar Htway
Chemical Engineering
Technological University
Ministry of Education
Thanlyin, Myanmar

Win Ei Ei Tun
Chemical Engineering
Technological University
Ministry of Education
Thanlyin, Myanmar

Abstract: This paper investigate the dehydration of ethanol by extractive distillation process with salt in solvent and also without salt. There are many sources to produce ethanol. It can be obtained from plants and agricultural wastes as well as olefins from cracking units of petroleum refining. Because the methods of ethanol production are the hydration method and fermentation, water molecules are present in ethanol. It has to be dehydrated to use as a fuel in automobile engines and other applications. There are many methods to separate water from ethanol to improved concentration. In this paper, the dehydration of ethanol is carried out by extractive distillation process and use ethylene glycol as a separating agent with calcium chloride as salt in order to improve the concentration of ethanol. Different ratios of ethanol-water and ethylene glycol such as (1:1:0, 1:1:0.25, 1:1:0.25 (20% of solvent)) were tested to obtain the best result of concentration percent. The maximum ethanol concentration was 92 vol% which obtained from 52 vol% ethanol in feed mixture.

Keywords: anhydrous ethanol; ethylene glycol; calcium chloride; extractive distillation; concentration

1. INTRODUCTION

Ethanol or ethyl alcohol (C_2H_5OH) is a clear colorless liquid which is biodegradable, low in toxicity and causes little environmental pollution if split [1]. Ethanol burns to produce carbon dioxide and water. It is reduces pollution associated with petroleum products such as SO_x and NO_x . Ethanol is a high octane fuel and has replaced lead as an octane enhancer in petrol [2]. Bioethanol and biodiesel are the alternative fuels that can be used. The production of alternative is due to the realization that crude oil stocks are limited, hence the swing towards more renewable sources of energy. Bioethanol and biodiesel have received increasing attention as excellent alternative fuels and have virtually limitless potential for growth [3].

Anhydrous ethanol is used as chemical reagent, organic solvent and raw materials for many important chemicals and intermediates for drugs, plastics, lacquers, polishes, plasticizers, cosmetics. It is also used in pharmaceutical formulations, production of biodiesel (fatty acid ethyl esters), electronic and military industries [3]. Anhydrous ethanol is considered to be an excellent alternative clean-burning fuel to gasoline. In properly designed automotive systems, ethanol has the potential to achieve very low emission levels. Pure 100% ethanol is not generally used as a motor fuel; instead, a percentage of ethanol is combined with unleaded gasoline. This is beneficial because the ethanol decreases the fuel's cost, increases the fuel's octane rating, and decreases gasoline's harmful emissions [4].

However the main challenge facing bioethanol production is the separation of high purity bioethanol, because bioethanol contains water. The separation of ethanol from water is

difficult because of the existence of an azeotrope in the mixture. Since ethanol-water solution forms a minimum-boiling azeotropes of composition of 89.4 mol% ethanol and 10.6 mol% of water at 78.28°C and standard atmospheric pressure, the dilute ethanol–water solutions produced by fermentation process can be continuously rectified to give at best solutions containing 89.4mol% ethanol at standard atmospheric pressure [5]. Therefore, special purpose for removal of the remaining water is required for manufacture of anhydrous ethanol. Various processes for producing anhydrous ethanol have been used. The two traditional methods of high purity ethanol separation are: Extractive distillation and Azeotropic distillation. Other three emerging techniques are: salt distillation, pressure swing distillation and pervaporation.

Extractive distillation is commonly applied in industry, and is becoming an important separation method in chemical engineering. Extractive distillation is a distillation in the presence of a miscible, high boiling, relatively non-volatile component, and the solvent that forms no azeotrope with the other components in the mixture. The method is used for mixtures having a low value of relative volatility, nearing unity. The method of extractive distillation uses a separation solvent, which is generally non-volatile, has a high boiling point and is miscible with the mixture, but doesn't form an azeotropic mixture. The solvent interact differently with the components of the mixture, thereby causing their relative volatilities to change. This enables the new three-part mixture to be separated by normal distillation. The solvent should be easily separable from the bottom product, and should not react chemically with the components or the mixture, or cause

corrosion in the equipment. The solvent plays an important role in design of extractive distillation and selection of suitable solvent/salt is fundamental to ensure an effective and economical design [5].

2. MATERIALS

2.1. Raw Materials

Ethanol was obtained from local market. The measured concentration of ethanol by alcohol-meter was 98 volume percent. Ethylene glycol was used as a solvent in this method. Calcium chloride was also used as a dissolved salt in solvent. And then, water was used as cooling water for condenser as well as solvent to get different concentrations of ethanol and it has the pH grade of 7. Ethylene glycol, calcium chloride and water can be obtained from local market.

3. EXPERIMENTAL PRODECURE

Three samples of experiment were tested in this paper. Experiment 1 was carried out by simple distillation method and 2, 3 were accomplished by extractive distillation method with solvent and then dissolved salt in solvent (20% of solvent). In these experiment were carried out by using simple batch distillation apparatus that operated bottom temperature in flask at 79°C, water flow rate of condenser 67.16 ml/sec, condenser water-in at 23°C and condenser water-out at 32°C. The initial concentration of ethanol and the final concentration of ethanol were determined by using hydrometer.

Table-1. Operating Conditions for Experiment 1

Parameter	Experiment 1
Ethanol-water - ethylene glycol feed ratio	1:1:0
Volume of ethanol	200 ml
Volume of water	200 ml
Ethanol volume concentration in feed	52%

According to the Table-1, ethanol and water are fully mixed and stirred in beaker and then determined the ethanol concentration of feed using alcohol meter. It was heated on heating mantle at least 40 minutes and then simple bath distillation method was carried out. Finally, the volume concentration of the purified product was determined by using hydrometer.

Table-2. Operating Conditions for Experiment 2

Parameter	Experiment 2
Ethanol-water-ethylene glycol feed ratio	1:1:0.25
Volume of ethanol	200 ml
Volume of water	200 ml
Volume of ethylene glycol	50 ml
Mass of salt	-
Ethanol volume concentration in feed	52%

In experiment 2, ethylene glycol was used as a solvent and it was added to mixture of ethanol-water. That was heated on heating mantle at least 40 minutes. It was carried out extractive distillation process by using solvent.

Table-3. Operating Conditions for Experiment 3

Parameter	Experiment 3
Ethanol- water - ethylene glycol feed ratio	1:1:0.25
Mass of ethanol	200 ml
Mass of water	200 ml
Mass of ethylene glycol	50 ml
Mass of salt (20% of solvent)	11.1g
Ethanol volume concentration in feed	52%

In the experiment 3, 11.1 grams of calcium chloride was weighed and crushed with pestle to get the powder form. The powder of CaCl₂ was mixed with ethylene glycol in the beaker. The ratio of ethanol, water and ethylene glycol (1:1: 0.25) were completely mixed with stirrer. The final mixture was heated on a heating mantle at 79°C for at least 2 hours. Finally, the ethanol concentration of product was measured by using alcohol meter. Each experiments were carried out at least three times and collected the data.



Figure 1 -Testing of simple bath distillation

4. RESULTS AND DISCUSSIONS

Table-4. Results of Experimental Testing

Test	Ethanol-water-ethylene glycol feed ratio	Mass of salt	Final Results of Ethanol (vol%)
Experiment 1	1:1:0	-	82%
Experiment 2	1:1:0.25	-	88%
Experiment 3	1:1:0.25	11.1g	92%

According to the experimental testing of Tabe-4, the result of experiment 1 was obtained the ethanol concentration of 82 vol% and it was simple distillation which separate ethanol and water based on their boiling point. Anhydrous ethanol could not be obtained in experiment 1.

In experiment 2, extractive distillation was carried out and ethylene glycol was used as a separating agent. The concentration of ethanol improved to 88 vol% was obtained in this experiment.

In the experiment 3, the resulting ethanol concentrations were more improved to 92 vol% in the top product from 52 vol% concentration of ethanol in the feed mixture. This experiment integrates the advantages of liquid solvent (easy solvent) and solid salt (high separation ability). It improves the performance of solvent. The amount of maximum ethanol concentration was obtained in this experiment because extractive distillation was carried out by using solvent in which CaCl_2 was used as salt.

5. CONCLUSION AND RECOMMENDATION

5.1 Conclusion

In this paper, the main purpose is obtainable ethanol from the local market to be dehydrated by one of purifying processes.

Among them, the extractive distillation with ethylene glycol solvent was used to purify ethanol-water mixtures in either with dissolved salt or without salt. According to the literature, a simple distillation process can produce maximum concentration of 95.6 vol% and the extractive distillation with dissolved salt in solvent enable to purify ethanol-water almost anhydrous (above 99.99 vol% ethanol). The extractive distillation with salt in solvent improves the performance of solvent, reduce the number of theoretical plates, the energy consumption and cost of equipment. This process has high efficiency and low solvent wastage.

The advantages of this process are (1) to complete nonvolatile, exist only in the liquid phase (2) the overhead product will be completed free of separating agent (3) require lesser energy (4) require lesser separating agent. The number of theoretical plates in liquid solvent extractive distillation is more than salt dissolved in liquid solvent extractive distillation. The most important parameters of the distillation such as the number of theoretical plates vary with the reflux ratio and the concentration of the desired component in the feed.

In the practical testing, the ethanol products were not pure because of some difficulties during the operation, such as controlling the temperature of the heating mental. However, ethanol concentration of 82 vol% was produced from the concentration of 52 vol% ethanol in feed mixture by a simple bath distillation method. That of about 88 vol% ethanol was accomplished from 52 vol% ethanol in feed mixture by an extractive distillation with ethylene glycol solvent. The ethanol concentration of 92 vol% was done from 52 vol% ethanol in feed mixture by extractive distillation with dissolved salt (CaCl_2) in solvent.

5.2 Recommendation

In this study, further experiment is needed to be done even though the experimental results of ethanol products are satisfied. The ethanol concentration will be more improved (1) if the heating mental can be controlled stable at the desired temperature and (2) if the distillation column with plates or trays can be used in extractive distillation.

6. ACKNOWLEDGEMENT

The author would like to express her deepest gratitude to Dr. Win Ei Ei Tun, Professor and Head, Department of Chemical Engineering, Technological University, Thanlyin for her valuable guidance and suggestions for this paper. The author also like to thanks to all teachers from Department of Chemical Engineering who were directly or indirectly involved in the successful completion of this paper. Finally the author would like to express her indebtedness and deep gratitude to her beloved parents for their kind support and understanding during the whole course of this work.

7. REFERENCES

- [1] D. J. O'Brien, J. C. Craig Jr. "Ethanol Production in a Continuous Fermentation/Membrane Pervaporation System", U.S. Department of Agriculture, Eastern Research Center, Philadelphia, USA, 1996.

- [2] Avinash K. Agarwal. Ashok Pandey Ashwani K. Gupta. Suresh K. Aggarwal Abhijit Kushari Editors, "Novel Combustion Concepts for Sustainable Energy Development", Springer India 2014.
- [3] Walker, Graeme M., "Bioethanol: Science and Publishing Aps, (2010).
- [4] Jones, J.C., "Atmospheric Pollution, "Ventus Publishing Aps,(2008)
- [5] Tassios D. P., "Extractive and Azeotropic Distillation, "American Chemical Society, Washington, D.C, 1972.
- [6] Badger W. L., Banchero Julius T.," Introduction to Chemical Engineering," International Student Edition, McGraw-Hill Book Company, Inc, 1955
- [7] Jones, J.C., "Hydrocarbons: Physical Properties and their Relevance to Utilization, "Jones & Ventus Publishing Aps, (2010)
- [8] Krell Erich., "Handbook of laboratory Distillation," Elsevier Scientific Publishing Company, Amsterdam, 1982.
- [9] Wikipedia., "Ethanol,"<http://en.wikipedia.org/wiki/Ethanol> Fuel.
- [10] Wikipedia., "Ethanol Fuel,"
<http://en.wikipedia.org/wiki/Ethanol> Fuel
- [11] Wikipedia., "Gasoline,"<http://en.wikipedia.org/wiki/Gasoline>.
- [12] Wikipedia., "Number of plates,"
[http://en.wikipedia.org/wiki/Number of Plates](http://en.wikipedia.org/wiki/Number_of_Plates).
- [13] Wikipedia., "McCabe Thiele Method,"
[http://en.wikipedia.org/wiki/ McCabeThiele Method](http://en.wikipedia.org/wiki/McCabeThiele_Method).
- [14] Wikipedia., "Reflux,""<http://en.wikipedia.org/wiki/Reflux>.

Bioethanol Production from Office Waste Paper

Wai Mar Htway
Chemical Engineering
Technological University
Ministry of Education
Thanlyin, Myanmar

Thu Zar Thein
Chemical Engineering
Technological University
Ministry of Education
Thanlyin, Myanmar

Ye Myat Phone Hlaing
Technological University
Thanlyin, Myanmar
ymph8395@gmail.com

Abstract: In this study, office waste paper was utilized as the raw material for production of bioethanol. Experimental studies have been carried out cellulose to sugar by acid hydrolysis. Acid hydrolysis of waste paper to sugar was carried out 121°C with 5%(v/v) sulfuric acid with the volume of 100ml, 200ml and 5,10,15 g of office waste paper to obtain the best yield of hydrolysate. After adjustment of pH with 5M of sodium hydroxide solution, fermentation was investigated using *Saccharomyces Cerevisiae* to convert sugar to bioethanol and produced 0.033 g/ml of maximum sugar with 150 rpm for overnight at room temperature. The viability of cell was not the only factor influencing fermentation. The operation time for hydrolysis, adjustment of pH, amount of yeast and rate of aeration during fermentation was a key interactive factor resulting in ethanol accumulation.

Keywords: office waste paper, acid hydrolysis, bioethanol, *Saccharomyces Cerevisia*

1. INTRODUCTION

In this study, bioethanol from office waste paper is produced from renewable source. Production from second generation is more benefit because of the consumption of waste residues. Office waste paper from office and photocopy service waste is readily available. Therefore it is attractive for producing second generation bioethanol. The conversion of office waste paper into ethanol is more useful because it is rich in carbohydrate.(1)

2. LITERATURE REVIEW

Since consumption of paper was increasing for a long time, and the amount of paper going into landfills was increased. And then has become a severe problem for disposal in developed and developing countries.. Bioethanol can be produced from sugar source, starch source and cellulose source. Paper is cellulose source, which is sustainable, renewable source and reduce the landfill problem.(4)

The technology for bioethanol production includes acid hydrolysis or enzymatic hydrolysis, pH adjustment, fermentation and distillation. The hydrolysis of office waste paper with enzyme is difficult because of consisting of hemicelluloses and lignin. Dilute acid hydrolysis is fast, easy and acid losses are not important.(1) The present research is based on bioethanol production from waste office paper. This feedstock results to be attractive for bioethanol production due to its availability. Despite of recycling efforts have been strengthened in the last years, the recycling rate is about a 65%, since the quality of the paper decreases with the recycling process. Then, waste office paper could be a suitable raw material for obtaining bioethanol.

3. EXPERIMENTAL

3.1 Yeast Activity Test

Activity of yeast was determined in 250 ml of Erlenmeyer flasks with sugar solution. After *Saccharomyces*

Cerevisia was transferred into the sugar solution with 150 rpm at room temperature, carbon dioxide gas was appeared within 15 minutes.

3.2 Hydrolysis with Dilute Sulfuric Acid

Waste office paper collected from office and photocopiers was used. The paper was cut into pieces. The 5% of sulphuric acid 100 mL solution was poured into 250 mL Erlenmeyer flasks which the 10 g of paper was put. The samples of flasks were placed into autoclaves. At the temperature of 121°C, the hydrolysis was carried out various reaction time, acid concentration, and paper weight. The product take out from the autoclave was cool and then filtered by filter paper to separate the liquid and solid. The product from hydrolysis was measured by refractor meter for sugar content and by pH meter for pH value.

3.3 Addition of NaOH Solution

After filtration all the samples were neutralized by adding 5M of Sodium hydroxide solution to obtain pH range 4.5 to 5 at room temperature.

3.4 Fermentation

For fermentation, the strain of *Saccharomyces cerevisiae* were added in the different condition 0.5 g,1g, 1.5g, 2g,2.5 g respectively at 30° C and 150 rpm for overnight. After one night, the product was measured for ethanol content, pH value and density.

4. Result and Discussion

The complex experimental results are shown in Table1. The result suggests that the sugar information depends on the effect of concentration of acid and paper weight in the hydrolysis. The optimized condition for production of bioethanol was 10g of office paper,5% H₂SO₄ 100mL,at 121°C and 60 minutes of content time. By using Response Surface Method(RSM), the increase of sugar brix and amount of yeast led to the increase of ethanol yield. On the other hand, the temperature of distillation also affected the purity of ethanol

As shown in figure(2) the response of surface diagram, the increase of temperature and sugar brix % achieved to the increase of the percentage of ethanol. The highest yield percentage of ethanol was obtained with sugar brix 10.2 % at the amount of yeast 2g.

Model Summary

S	R-sq	R-sq(adj)	R-sq(pred)
1.99307	97.36%	92.62%	57.82%

The R² values for the two models are 97.36% and 92.62%, indicating that the three factors accounted for over 95% of the variation of sugar Brix%, amount of yeast(g) and temperature of distillation (°C). This indicates that the fitted model is adequate. The use of graphical representations of the empirical models shown in figure (1) to facilitate interpretation of factor effects on three factors and $\alpha=0.05$.

The initial concentration of sugar brix was about 0.1062 g of sugar per mL of solution, the pH was 0.92. The adjustment of hydrolysate with 5M of NaOH solution was increased the pH of solution. The amount of NaOH solution was resulted on sugar content. Since the percentage of ethanol obtained by the fermentation of high content sugar brix with

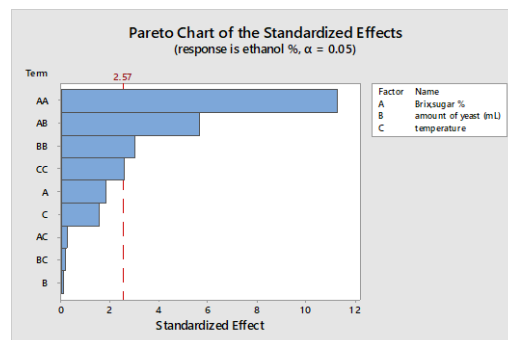


Figure 1. Parto Chart of the Standardized Effects

sample	Paper wt(g)	5% H ₂ SO ₄ (mL)	Sugar%, Brix	Sp.gr	g of sugar/ml of solution	pH	Amount of yeast(g)	Ethanol % after fermentation for 24 hr
1	5	100	9.6	1.0384	0.0997	1	1.5	7
2	5	100	9.6	1.0384	0.0997	1	2	13.7
3	5	100	9.6	1.0384	0.0997	1	2.5	17.7
4	5	200	3.5	1.0137	0.0354	0.87	1.5	1.8
5	5	200	3.5	1.0137	0.0354	0.89	2	2
6	5	200	3.5	1.0137	0.0354	0.89	2.5	2
7	10	100	10	1.04	0.104	0.93	1.5	7
8	10	100	8	1.0318	0.0825	0.96	2	6
9	10	100	10	1.04	0.104	0.93	2.5	18.9
10	10	100	10.2	1.0409	0.1062	0.92	1.5	9
11	10	100	10.2	1.0409	0.1062	0.92	2	19.5
12	10	100	10	1.04	0.104	0.92	2.5	19
13	10	100	10	1.04	0.104	0.93	1.5	9.3
14	10	100	9.7	1.0388	0.1001	0.95	2	18.6
15	10	100	10.1	1.0404	0.1051	0.93	2.5	13
16	10	100	10	1.04	0.104	0.93	1.5	7.1
17	10	100	10.1	1.0404	0.1051	0.93	2	18.3
18	20	200	4	1.0157	0.0406	1.23	1.5	2
19	20	200	3.9	1.0153	0.039	1.22	2	1.2
20	20	200	4	1.0157	0.0406	1.25	2.5	2

Table 1. Experimental results for ethanol production

amount of yeast in the optimized culture medium, the amount of yeast was varied within 1.5 g to 2.5 g range. There was chosen for the best fermentation with 2 g of yeast.

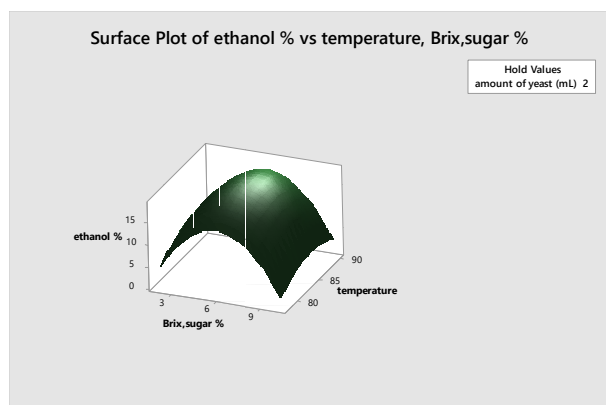


Figure 2.Surface Plot of ethanol% vs temperature,Sugar Brix%

5. CONCLUSION

This production showed that relatively high concentrations of sugars can be obtained by hydrolysis of 10 g of waste office paper using 5 % sulfuric acid during 60 minutes. The reaction time did not exert any significant effect for either sugar brix. The fermentation of hydrolysate with different amount of yeast to produce the ethanol *Saccharomyces cerevisiae* is the microorganism for fermenting lignocelluloses hydrolysis. However, the cellulose of waste paper is somehow difficult to hydrolyze enzymatically because it is associated with hemicelluloses and lignin. Therefore dilute-acid hydrolysis is a fast and easy way to pretreat lignocellulosic materials. The cost of this production is lowest because of waste paper. The cost of sulfuric acid ,yeast and sodium hydroxide were low cost compared with ethanol price.

The results of production predicted that the office waste paper is the most beneficial as a raw material for bioethanol production.

6. ACKNOWLEDGMENTS

The authors acknowledge, Dr.Win Ei Ei Tun, Professor and Head of Chemical Department, Dr.Su Lin Thu, Professor , Daw Thuzar Thein, Lecturer, Chemical Engineering

Department, Thanlyin Technological University, U Aung Myint Myat, Managing Director, U Thein Naing , Factory director ,San Chein Alcohol Plant, Aywarwaddy Region,Myanmar.

7. REFERENCES

- [1] David A. Lima,Rafaela L.N Deluna, C.Martin and Easter R.Gouveia. 2014. Comparison of Bioethanol Production from Acid Hydrolysis of Waste Office Paper using *Saccharomyces Cerevisiae* and *Spathaspora Passalidarum*. Federal University of Pernambuco.
- [2] K.M.Dombek and L.O.Ingram.1987. Ethanol Production during Batch Fermentation with *Saccharomyces Cerevisiae*: Changes in Glycolytic Enzymes and Internal pH. University of Florida.
- [3] Gulden Izmirliglu and Ali Demirci. 2012. Ethanol Production from Waste Patato Mash by Using *Saccharomyces Cerevisiae*. Pennsylvania State University, University Park.
- [4] Shruti A.Byadgi and P.B.Kalburgi. 2016. Production of Bioethanol from Waste Newspaper. Basaveshwar Engineering College.
- [5] R. Maceiras, V. Alfonsín and J.E. Poole. Journal of Environmental Science.Bioethanol Production from Waste Office Paper. Centro Universitario
- [6] Charles Louis Loyalty Robus. 2013.Production of Bioethanol from Paper Sludge using Simultaneous Saccharification and Fermentation. Stellenbosch University
- [7] Bibi Zainab* and Aslam Fakhra. 2014. Production of Ethanol by fermentation process by using Yeast *Saccharomyces cerevisiae*. Lahore College for Women University
- [8] Pooja Raj Chansoliya, Rahul An and Sunita Sharma. 2016. Analysis of Bioethanol production from Newspaper by *Saccharomyces cerevisiae* and *Zymomonasmobilis*. Madhav Institute of Technology and Science,

Experimental and Numerical Computational Fluid Dynamics Analysis on the Flow at Pelton Turbine Nozzle with Various Opening Settings

Zar Chi Thuang
Department of Mechanical
Engineering,
Technological University
Thanlyin, Myanmar

Theingi
Rector,
Technological University
Thanlyin, Myanmar

Kyi Kyi Swe
Department of Mechanical
Engineering,
Technological University
Thanlyin, Myanmar

Abstract: This paper refers to the flow analysis of nozzle with spear for different nozzle opening of Pelton turbine. Experimental test was performed by using model turbine to find out the parameters during testing period. The flow rate, head and the rotational speed on the turbine shaft are measured for various nozzle openings covering a wide operation range. The best efficiency is 86% and output power of the model turbine is 110W. For water flow simulation of nozzle with spear by applying Computational Fluid Dynamics (CFD) software ANSYS CFX-14.5 are presented. The pressure and velocity distribution have also been obtained to study the effect of nozzle on flow pattern. The flow simulation has been carried out the standard $k - \epsilon$ turbulence model. And then, CFD simulation results with experimental value have been compared in this research.

Keywords: nozzle with spear, Pelton turbine, pressure, velocity, experimental test, CFD software

1. INTRODUCTION

Pelton turbine is the most commonly used impulse turbines in modern hydropower system. It is also called the constant-pressure turbine and there is no pressure drop across the buckets. It is regulated by decreasing or increasing the diameter of the jet and this is affected by means of a needle or spear which closes or opens the throat of the nozzle [1].

A nozzle transforms water under a high head into a powerful jet. The jet leaving the nozzle is surrounded by air [2]. The momentum of this jet is destroyed by striking the runner, which absorbs the resulting force. If the velocity of water leaving the runner is nearly zero, all the kinetic energy of the jet is has been transformed into mechanical energy, so the efficiency is high. The nozzle must be spaced so closely that water issued from one jet spared after striking the runner interferences with another jet. A Pelton turbine has one more nozzles discharging jets of water which strike a series of buckets mounted on the periphery of a circular disc [3, 4].

2. TESTING PROCEDURE OF MODEL PELTON TURBINE

The main purpose of this performance is to measure the power output and efficiency variation with rotational speed for different openings of the nozzle and to compare this to the CFD software ANSYS-14.5.

2.1 Experimental Set-Up

Experimental set-up consists of Pelton turbine, inlet pressure gauge, centrifugal pump, tachometer, calibrated orifice meter connected to mercury manometer, brake drum dynamometer with rope and mass loading arrangement.

2.2 Operation of Model Pelton Turbine

The model turbine is located in the Renewable laboratory at Mechanical Engineering Department which is situated in Mandalay Technological University. A schematic view of the experimental setup is shown in Figure 1. In this case, the nozzle opening position is five conditions for the whole test.

They are 20%, 40%, 60%, 80% and 100% nozzle opening position. Turbine is tested as a pump storage type of plant.

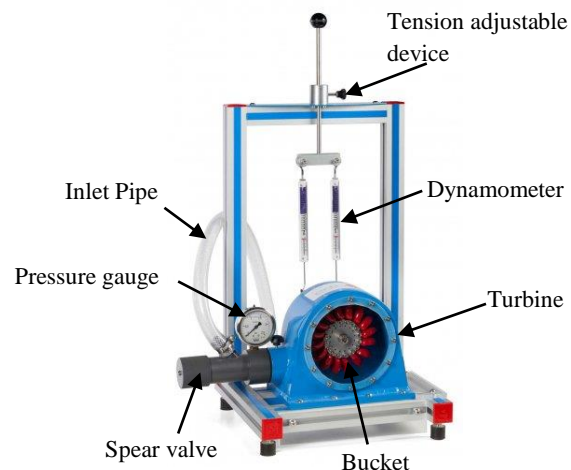


Figure 1. Schematic diagram of model turbine

The resource of required water is carried from the ground tank. It is pumped to the artificial water way by using the pump. The required jet opening is set by turning the hand wheel in anti-clockwise direction. The inlet pressure is read by using a pressure gauge. A pressure gage is attached to the water pipe entering the turbine for reading the available water head. The speed of the turbine is measured by using a tachometer. The rectangular iron box is used to measure the flow rate. The volume of the container is known and the flow rate is obtained simply by the ratio of the volume and the filling time.

A band brake connected to two dynamometers allows varying the load given to the turbine by means of a connection device. The rotational shaft speed is measured by a digital tachometer counting the frequency of the marking on the surface of the brake drum on the back side of the turbine. Energy is extracted from the turbine using an assembly comprising friction plates centered on the turbine shaft [5].

3. EXPERIMENTAL TEST OF MODEL TURBINE

The pressure gauge reading, the speed of turbine and load are read during the test. After reading the data, efficiency of Pelton turbine is calculated in various nozzle opening. The specifications of model turbine are described as follows;

Table 1. The specifications of model turbine

Descriptions	Symbols	Value	Units
Diameter of runner	D_r	96	mm
Nozzle inlet pipe diameter	D_i	16	mm
Diameter of nozzle	D_n	10	mm
Center to center distance from the rotor axis	C	110	mm
Distance between jet and bucket	X_{nb}	20	mm
Number of bucket	Z	16	-
Number of jet	n_j	1	-
Coefficient of velocity	C_v	0.985	-

3.1 Calculation of Effective Head and Efficiency

Firstly, the required 20% nozzle opening is set by turning the hand wheel in anti-clockwise direction and adjust the inlet pressure (at 1.37 bar indicated by a Bourdan tube pressure gauge) by operating the bypass line valve. Keep on loading the Pelton turbine by adding masses from no load up to until the Pelton wheel stops. At each loading, note down the rotational speed of the turbine using a tachometer. After that, 40%, 60%, 80% and 100% nozzle opening for each run have been done above procedure.

The primary feature of the impulse turbine is the power production as the jet is deflected by the moving buckets. Negligible head loss at the nozzle and at the impact with the buckets (assuming that the entire available head is converted into jet velocity). Jet velocity can be calculated by using Equation 1;

$$Q = A_j \cdot V_j \cdot n_j \quad (1)$$

The velocity of the water jet is a function of the pressure difference, when viscosity is absent;

$$V_j = C_v \sqrt{\frac{2p_{out}}{\rho_w}} \quad (2)$$

The theoretical power is a function of the bucket speed and the jet speed. The bucket speed is;

$$V_b = R_r \cdot \omega \quad (3)$$

The effective head at inlet to the turbine can be measured through use of the following Bernoulli equation;

$$H_{available} = \frac{p_{in}}{\rho_w g} + \frac{V^2}{2g} + Z \quad (4)$$

The energy equation applied to the control volume provides the power extracted from the available head by the turbine;

$$P_{available} = \rho g Q H_{available} \quad (5)$$

By applying the angular momentum equation to the same control volume about the axis of the turbine shaft of the power developed by the turbine can be written as

$$P_o = T \omega \quad (6)$$

And then, the efficiency of the turbine is defined as the ratio between the power developed by the turbine to the available water power can be obtained by using the equation 7[5, 6]. The result table of different nozzle position for model turbine is illustrated in Table 2.

$$\eta_t = \frac{P_o}{P_{available}} \quad (7)$$

Table 2. Results data for model turbine

Descriptions	Nozzle Opening (%)				
	20	40	60	80	100
N (rpm)	1583	1380	1255	1200	1075
$Q \times 10^{-4}$ (m ³ /s)	5.08	5.17	5.22	5.28	5.32
V_{in} (m/s)	2.6	2.57	2.52	2.49	2.47
V_{out} (m/s)	15.9	15	14.85	14.6	14.4
p_{in} (Bar)	1.37	1.33	1.23	1.2	1.1
p_{out} (Bar)	1.3	1.16	1.14	1.1	1.07
H_{avail} (m)	26.9	25	23.8	23	21.8
P_o (W)	108	110	85	68	61
η (%)	80	86	70	57	53

4. NUMERICAL APPROACH

In general, a numerical analysis procedure involves the following steps: (i) development of governing equations for the flow physics; (ii) discretising the equations in both time and space, (iii) discretising the flow domain (meshing); (iv) solving the discretised equations using a computerised solver (or program) and (v) post-processing of the results using a computerised program. It is necessary to justify the numerical results by comparing them with experimental or theoretical results. As stated already, numerical analysis is currently the standard way of designing turbines in the industry.

Numerical analysis for predicting the performance of impulse turbine runners poses a special challenge because of complexity of the flow physics. In impulse turbines like Pelton turbine, the jet flow in the runner is intermittent and there is a movable free surface boundary between the jet and surrounding air. This means that the actual flow is unsteady and two phase with a movable free surface. Two approaches are being used to numerically analyze such a flow. These approaches are particle tracking method and a classical CFD method [7, 8].

Some previous investigators have attempted to numerically study the flow through the nozzle and bucket of Pelton turbine. Mack et al. used Eulerian CFD methods for simulating the flow at the distributor of a multi-jet Pelton turbine. Also they used the volume of fluid model to study the effects of secondary flows, due to pipe bends, on the quality of the jet formed at a Pelton turbine nozzle [9].

4.1 Governing Equation

Computational Fluid Dynamics (CFD) is concerned with numerical solution of differential equations governing transport of mass, momentum and energy in moving fluids [10]. Methods of CFD assume computation of liquid and gas flows by numerical solution of Navier – Stokes and continuity equations (for turbulent flows – Reynolds equations) which describe the most general case of movement of fluid medium. The correspondent sequence of actions from creation of a geometrical model and specifying boundary conditions to analysis of computation results is described in the paper [11].

The equations used in this numerical flow analysis are the Reynolds Averaged Navier Stokes (RANS) equation with turbulence models based on eddy viscosity concept [12]. RANS for the continuity and momentum equations are given in equation (8) and (9)

$$\frac{\partial \rho}{\partial t} + \nabla \cdot (\rho V) = 0 \tag{8}$$

$$\frac{\partial \rho V}{\partial t} + \nabla \cdot (\rho V \otimes V) - \nabla \cdot (\mu_{eff} \nabla V) = -\nabla p' + \nabla \cdot (\mu_{eff} \nabla V)^T + F \tag{9}$$

$$\mu_{eff} = \mu + \mu_t \tag{10}$$

where, F = the sum of body forces

p = the modified pressure

μ_{eff} = the effective viscosity accounting for turbulence

V = vector of velocity

5. METHODOLOGY

The numerical analysis for this study was performed in ANSYS Workbench 14.5 where ANSYS CFX Project with its subprograms, namely: Geometry, Mesh, ANSYS CFX-Pre, ANSYS CFX solver and ANSYS Post-processing, is used as presented in Figure 2. As stated already, numerical analysis require coming up with a flow domain which has to be discretized (or meshed) in space and time (for unsteady state analysis) [13].

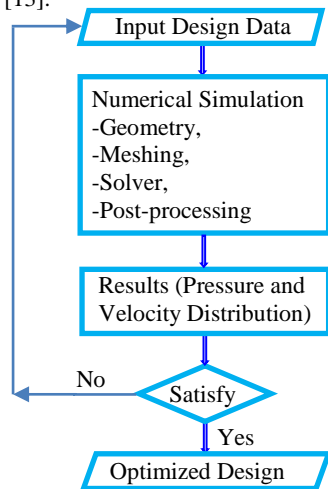


Figure 2. Flow chart for simulation procedure

5.1 Geometric Modeling

The flow domain Figure 3 is designed in “Geometry” sub-program using the ANSYS Design Modeler. The flow domain

consists of the nozzle with spear and jet [14]. The jet is designed in ANSYS Design Modeler while the nozzle with spear in SolidWorks 2012. The numerical problem can be solved by using the “multiple frame of reference” as detailed in ANSYS Theory Guide of 14.5 [15].

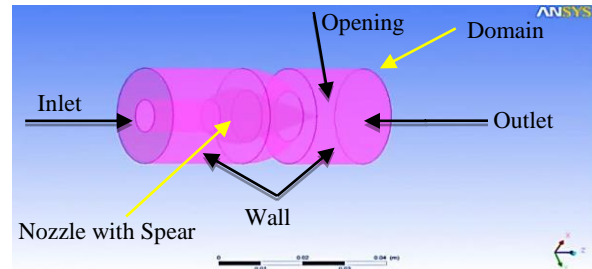


Figure 3. Three dimensional view of nozzle with spear

5.2 Mesh Generation

The geometry is divided into small sub parts for CFD analysis called mesh and the process is called meshing. The shape of the mesh elements can be triangular, quadrilateral, tetrahedral, hexahedral or prism depending upon the size and shape of the geometry. The shape and size of the mesh elements can be varied and are kept according to the dimension of the geometry, accuracy required, computational power of the system and memory [14].

The meshing of nozzle and spear domain has been done at spear shapes and the meshing of nozzle with spear domain for fillet spear shape [16]. As shown in Figure 4, the meshing of the fluid domain was divided into two standalone meshing components, one for the nozzle domain and one for the opening domain.

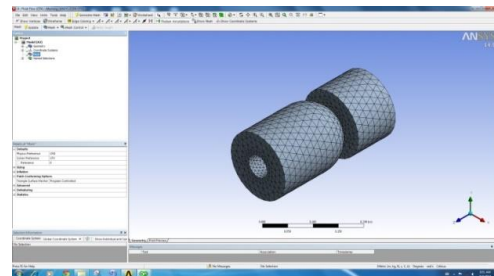


Figure 4. Meshing of flow domain for 100% nozzle opening

The main reason for this was that the nozzle domain was meshed with an advanced size function. The fluid domain was meshed with the advanced size function and consists mostly of triangular elements around the jet core and jet domain. Sweeping gives a high degree of structure in a mesh and this method was used on the jet and the surrounding domain. ANSYS Meshing 14.5 actually does a great job meshing the large part automatically. The summary of meshing data for each surface has been described in Table 3.

Table 3. Mesh information for nozzle with spear domain

Domain	Nodes	Elements
Nozzle	11181	61282

5.2.1 Domain and Interface Properties

The mesh is converted into the required format and is imported to ANSYS CFX-14.5 software. In ANSYS CFX-Pre the properties of the domains and fluid are defined along with their interface properties. The summary of the domain properties are given in Table 4.

Table 4. Domain physics for CFX in nozzle

Component	Feature	Details
Design Modeler		Geometry Creation
		Named Selection
CFX-Pre	User Mode	Quick Setup Wizard
	Location	Fluid
	Domain type	Fluid Domain
	Fluid list	Water
	Reference pressure	1 [atm]
	Buoyancy model	Not Buoyant
	Domain motion option	Stationary
	Turbulence option	k-Epsilon
	Coordinate Frame	Coord 0

5.2.2 Boundary Conditions

The flow parameters like pressure and velocity or mass flow rate are to be specified in the form of inlet and outlet boundary conditions to obtain numerical simulation and the nature of the boundary condition affects the accuracy of numerical solution. The boundary conditions were prescribed at inlet, outlet, wall and interface locations of the nozzle as shown in Table 5.

Table 5. Boundary physics for CFX

Domain	Boundaries	
Domain 1	Boundary - inlet	
	Location	inlet
	Flow Regime	Subsonic
	Mass Flow Rate	5.17e-01 [kg s ⁻¹]
	Turbulence	Medium Intensity and Eddy Viscosity Ratio
	Boundary – opening	
	Location	opening
	Flow Direction	Normal to Boundary Condition
	Flow Regime	Subsonic
	Mass And Momentum	Opening Pressure and Direction
	Relative Pressure	1.0000e+00 [atm]
	Turbulence	Medium Intensity and Eddy Viscosity Ratio
	Boundary – outlet	
	Location	outlet
	Flow Regime	Subsonic
	Relative Pressure	1 [atm]
	Pressure Averaging	Average Over Whole Outlet
	Boundary - wall	
	Location	wall
	Mass And Momentum	No Slip Wall
Wall Roughness	Smooth Wall	

6. GRAPHICAL PLOTS FOR NOZZLE

Pressure contours and velocity stream lines are achieved using insert contour and streamline commands of menu bar in

ANSYS CFX-Post. Pressure contours and velocity stream lines for geometry at different nozzle openings have been shown below.

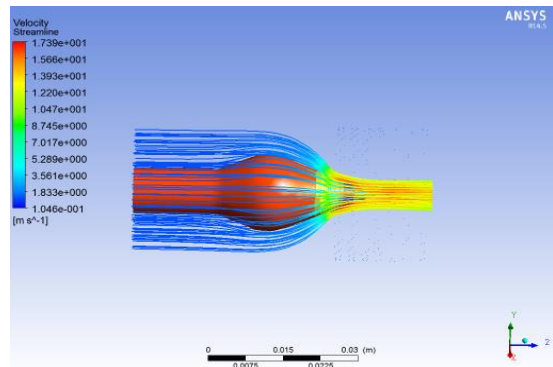


Figure 5. Velocity distribution in geometry with 20 % nozzle opening

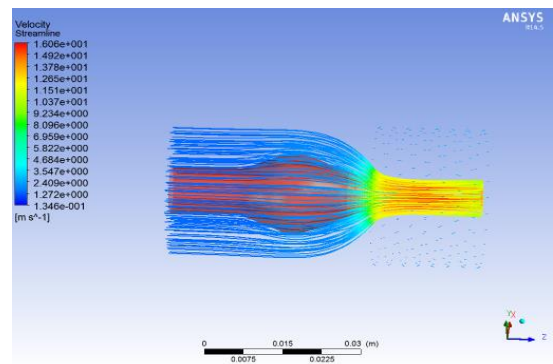


Figure 6. Velocity distribution in geometry with 40 % nozzle opening

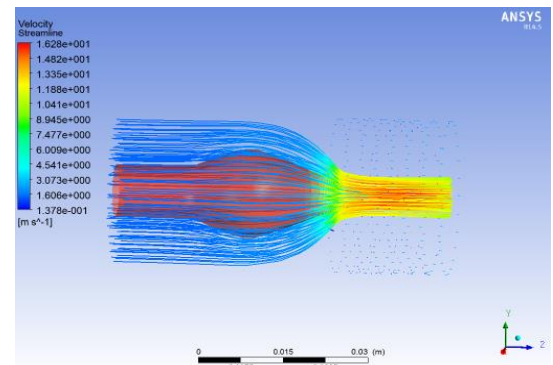


Figure 7. Velocity distribution in geometry with 60 % nozzle opening

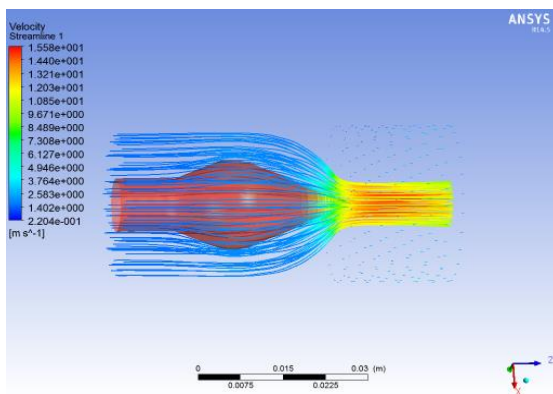


Figure 8. Velocity distribution in geometry with 80 % nozzle opening

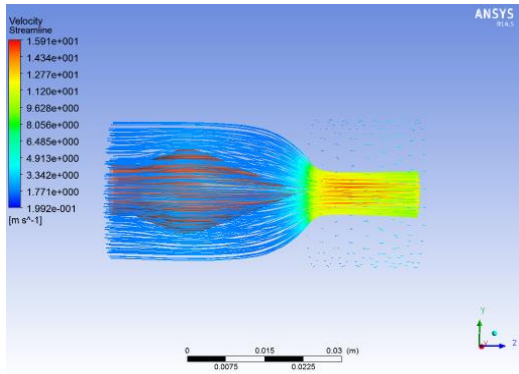


Figure 9. Velocity distribution in geometry with 100 % nozzle opening

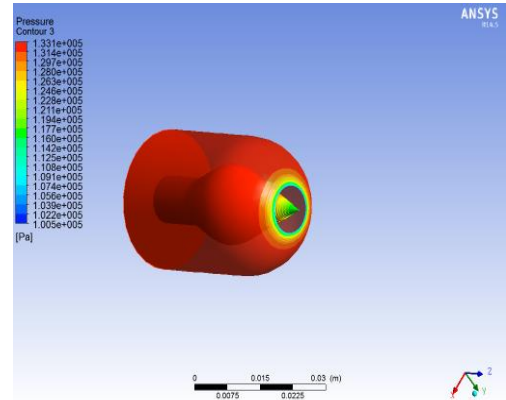


Figure 13. Pressure distribution in geometry with 60 % nozzle opening

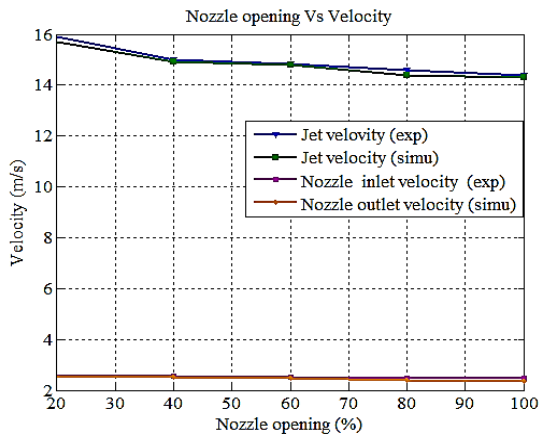


Figure 10. Relationship between nozzle opening and velocities

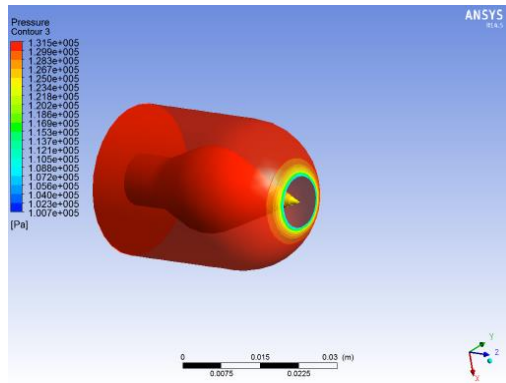


Figure 14. Pressure distribution in geometry with 80 % nozzle opening

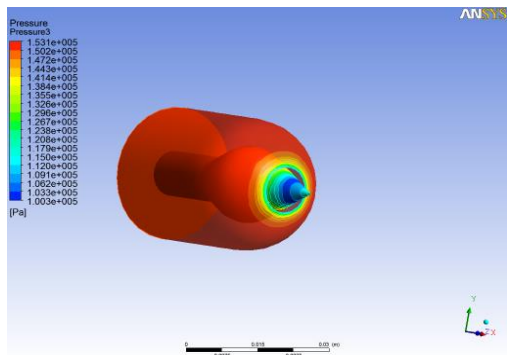


Figure 11. Pressure distribution in geometry with 20 % nozzle opening

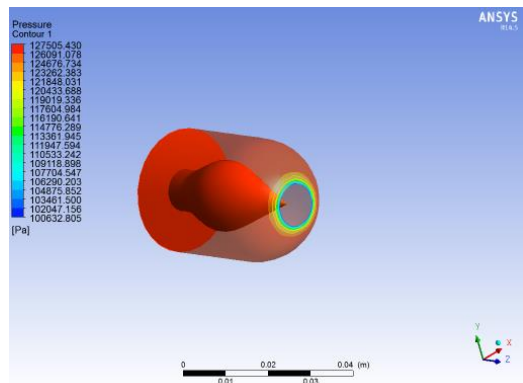


Figure 15. Pressure distribution in geometry with 100 % nozzle opening

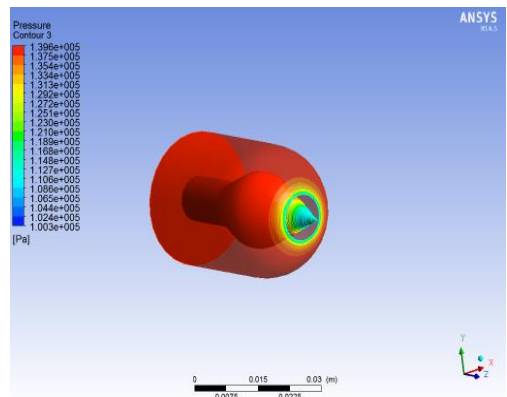


Figure 12. Pressure distribution in geometry with 40 % nozzle opening

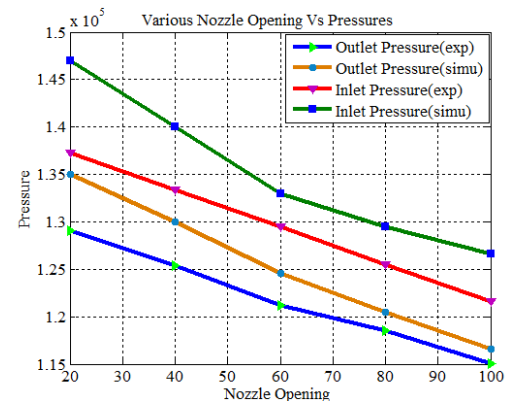


Figure 16. Relationship between nozzle Opening and pressures

7. SIMULATION RESULTS FOR NOZZLE

The flow simulation has been carried out for constant cross-sectional area of the jet and mass flow rate. The velocity obtained from numerical simulation for model turbine is close to experimental value. The streamlines in jet are parallel before striking the plate and spreads after strike of jet to the plate. As the outlet angle of the plate increases, the thickness of the water sheet decreases due to flow over the larger area of the plate before exit. Also this leads to reduction in water jet velocity at the outlet. The results are analyzed for water volume fraction iso-surfaces, pressure distribution within the flow domains. The distance between jet and bucket (20 mm) is also kept same in all cases for model turbine. The root mean square (RMS) residual is set to 10^{-7} for the termination of iterations. The solver was run for 200 iterations. The comparison between the theoretical and numerical results is given in Table 6.

Table 6. Comparison results between experimental with simulation of model turbine

Description	Experimental Results	Simulation Results	Units
Inlet Velocity	2.53	2.598	m/s
Outlet Velocity	15.84	16.793	m/s
Inlet Pressure	137293.1	142800	Pa
Outlet Pressure	125400	130900	Pa

8. CONCLUSION

In this research, the experiment of Model Pelton turbine has been carried out. Five position of nozzle are placed with the various speeds during the test. Relationship between speed and efficiency curve are obtained from the experiment results of model turbine. According to experimental results, the maximum efficiency occurs 40% nozzle opening. At 20% nozzle opening position, the efficiency decreases immediately because the area of nozzle is too small. At 60%, 80% and fully open position of nozzle, the efficiency decrease because of the cross-sectional area of nozzle is inversely proportional to the pressure. The best operating point is obtained at the maximum efficiency of turbine. In this point, the efficiency of model turbine is 86 %, speed ratio is 0.46 and the flow rate is $5.17 \times 10^{-4} \text{ m}^3/\text{sec}$ at the speed of the turbine is 1380 rpm.

The variation of pressure and velocity distribution using pressure contours and velocity streamlines on the surface of the nozzle have been observed. According to numerical results, the pressure at the jet outlet is nearly equal to atmospheric pressure because the jet issued freely in air. The outlet velocity of the jet is higher than the inlet velocity of the fluid which shows that the pressure energy is being converted into kinetic energy. Finally, experimental results are verified by comparing with simulation results.

NOMENCLATURE

Q	- Discharge of the Incoming Jet	[m ³ /s]
N	- Rotational Speed	[rpm]
T	- Torque acting on the turbine Shaft	[N-m]
V _j	- Velocity of Jet	[m/s]
H _{avai}	- Available Head	[m]

p _{in}	- Nozzle Inlet Pressure	[Pa]
p _{out}	- Nozzle Outlet Pressure	[Pa]
P _{avai}	- Available Power	[W]
P _o	- Power Output of the Turbine	[W]
η _t	- Efficiency of the Turbine	[%]

9. ACKNOWLEDGMENT

The author is deeply gratitude to Dr. Theingi, Rector, Technological University (Thanlyin), for her encouragement and kindly advice. The author's special thanks are sent to her parents, for their guidance from childhood till now.

10. REFERENCES

- [1] Anil Kumar, Numerical Simulation of Pelton Turbine Nozzle for Different Shapes of Spear, Maulana Azad National Institute of Technology, Bhopal, June 2011.
- [2] Vishal Gupta, Vishnu Prasad, Numerical Modeling for Hydro Energy Convertor, Impulse Turbine, ICGSEE, 2013.
- [3] Bansal R.K, A Text Book of Fluid Mechanics and Hydraulic Machines, 2009.
- [4] Anonymous, Micro - Hydropower Systems. A Buyer's guide, 2005.
- [5] Robertson, J.A. and Crowe, C.T, Engineering Fluid Mechanics, 5th edition, Houghton Mifflin, Boston, MA, 1993.
- [6] White, F.M., Fluid Mechanics, 3rd edition, McGraw-Hill, Inc., New York, NY, 1994.
- [7] Patel K, Patel B, Yadav V, and Foggia T.: Development of Pelton turbine using numerical simulation, 25th IAHR Symposium on Hydraulic Machinery and Systems IOP Publishing IOP Conf. Series: Earth and Environmental Science 12 ,2010.
- [8] Alexandre Perrig, Hydrodynamics of the Free Surface Flow in Pelton Turbine Buckets. PhD thesis, University of Lausanne, 2007.
- [9] Angehrn, R., Rettich, J., and Schärer, C.: Pelton runner design based on measured unsteady pressure distributions in the bucket, Hydropower & Dams, 1999.
- [10] Anil W. Date, Introduction to Computational Fluid Dynamics, Cambridge University Press, 2005.
- [11] Kochevsky A. N., Nanya V. G. Contemporary Approach for Simulation and Computation of Fluid Flows in Centrifugal Hydro machines // Bulletin of Sumy State University, 2003.
- [12] Chiyembekezo S. Kaunda, Cuthbert Z. Kimambo, A numerical investigation of flow profile and performance of a low cost Crossflow turbine, Volume 5, Issue 3, 2014.
- [13] Xirouchakis Prof. P., president du jury Prof. F. Avelan: Hydrodynamics of The Free Surface Flow in Pelton Turbine Buckets, Lausanne, EPFL 2007.
- [14] Abhishek Sharma, Prashant Sharma, Numerical Simulation for Pressure Distribution in Pelton Turbine Nozzle for the Different Shapes of Spear, IJETA, Vol.1, Issue 4, 2012.
- [15] ANSYS. CFX Modeling / Theory Guide 14.5, (2010).
- [16] Abhishek Sharma, Numerical Simulation and CFD Analysis for Energy Loss Computation in Fully Open Geometry of Pelton Turbine, 2013.

Speech to Text Conversion System for Myanmar Alphabet

Zaw Win Aung
Technological University (Loikaw)
Loikaw, Myanmar

Abstract: This paper is aimed to implement the speech to text conversion system for Myanmar alphabet. The Myanmar alphabet consists of 33 characters from ‘ka’ to ‘ah’. The proposed system is software architecture which allows the user to speak against the computer in Myanmar language and the corresponding character is printed on the screen in the Microsoft Office Word Document Format. The system is emphasized on Speaker Independent Isolated Word Recognition System. The proposed system directly acquires and converts speech to text. This system contains two main modules: feature extraction and feature matching. Mel Frequency Cepstrum Coefficients (MFCC) is applied for feature extraction which extracts a small amount of data from the voice signal that can later be used to represent each character. Feature matching involves the actual procedure to identify the unknown character by comparing extracted features from the voice inputs of a set of known characters. In this system, Vector Quantization (VQ) approach using Linde, Buzo and Gray (LBG) clustering algorithm, which reduces the amount of data and complexity, is applied for feature matching. To implement this system MATLAB programming language is used.

Keywords: Speech to text; Myanmar alphabet; isolated word recognition; Myanmar character; Myanmar language

1. INTRODUCTION

There is a widespread need for transcription services converting audio files into written text for various purposes: meeting minutes, court reports, medical records, interviews, videos, speeches, and so on. Written text is easier to analyze and store than audio files, and apart from this, there are many circumstances one could imagine for needing to transcribe human speech: those who are deaf still need to listen to certain audio files; people with limited ability to type, such as those who are paralyzed or suffer from Carpal Tunnel Syndrome, still need to draft documents; and so on. Speech-to-Text (STT) system is a system for conversion of speech into text. It takes speech as input and divides it into small segments. These small segments are sounds, known as monophones. It extracts the feature vectors of the monophones and matches them with stored feature vectors and most likely or higher matched character is returned to the editor for printing.

A System-on-Programmable-Chip (SOPC) based Speech-to-Text architecture has been proposed by Murugan and Balaji[1]. This speech-to-text system uses isolated word recognition with a vocabulary of ten words (digits 0 to 9) and statistical modeling (HMM) for machine speech recognition. They used Matlab tool for recording speech in this process. The training steps have been performed using PC-based C programs. The resulting HMM models are loaded onto a Field programmable gate array (FPGA) for the recognition phase. The uttered word is recognized based on maximum likelihood estimation.

An architecture for Hindi Speech Recognition System using Hidden Markov Model Toolkit (HTK) has been proposed by Kumar and Aggarwal[2]. The proposed system was built as a speech recognition system for Hindi language. Hidden Markov Model Toolkit has been used to develop the system. The proposed architecture has four phases, namely, preprocessing, feature extraction, model generation and pattern classification. The system recognizes the isolated words using acoustic word model. The system was trained for

30 Hindi words. Training data was collected from eight speakers. The developer reported the accuracy of 94.63%.

Phonetic Speech Analysis for Speech to Text Conversion has been given by Bapat, and Nagalkar[3]. Their work aimed in generating phonetic codes of the uttered speech in training-less, human independent manner. The proposed system has four phases, namely, end point detection, segmenting speech into phonemes, phoneme class identification and phoneme variant identification in the class identified. The proposed system uses differentiation, zero-crossing calculation and FFT operations.

2. IMPLEMENTATION

The proposed speech to text conversion system is simulated in MATLAB with speech signal as input and produces the corresponding text as output. The database consists of 165 speech samples which were collected from the same speaker. Each speech sample is about 1 second long. The speaker is asked to utter Myanmar character from ‘ka’ to ‘ah’ five times in a training session and one time in a testing session later on. The same microphone is used for all recordings. Speech signals are sampled at 8000 Hz.

In the training phase, feature vectors are calculated from the input speech signal by MFCC feature extraction algorithm. Finally, the codebook or reference model for each speech signal is constructed from the MFCC feature vectors using LBG clustering algorithm and store it in the database. In the identification phase, the input speech signal is compared with the stored reference models in the database and the distance between them is calculated using Euclidean distance. And then, the system outputs the speech ID which has minimum distance as identification result and the corresponding character is printed on the screen in the Microsoft Office Word Document Format. Figure 1 and Figure 2 show the training and testing phases of speech to text conversion system.

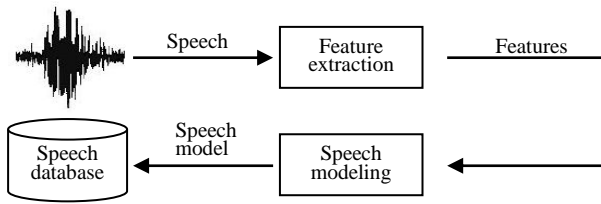


Figure 1. Training phase of speech to text system

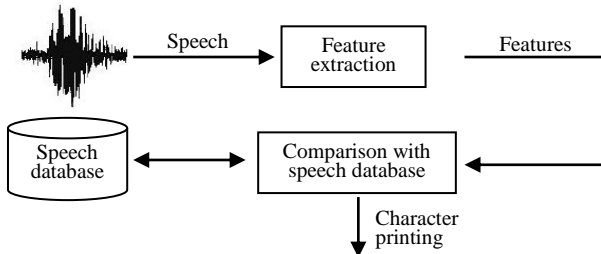


Figure 2. Testing phase of speech to text system

3. EXPERIMENTAL RESULT

This section describes the results of experiments carried out in different database sizes. In order to show the effectiveness of the proposed system, the computation time as well as accuracy of the system is computed. The training times taken by the system are shown in Table 1. The computation times and accuracy of the system are shown in Table 2.

Table 1. Computation time taken by the system in training phase

No	No: of Trained Samples	Time taken (seconds)
1	33 sample	1.67
2	66 samples	3.16
3	99 samples	4.66
4	132 samples	6.14
5	165 samples	7.67

Table 2. Computation time and accuracy of the system in testing phase

No	No: of Test Samples	No: of Samples in the Database	Time taken (seconds)	Accuracy (percent)
1	33	33	0.73	91%
2	33	66	1.89	97%
3	33	99	2.78	100%
4	33	132	5.52	100%
5	33	165	6.67	100%

4. RESULT ANALYSIS

In the training phase, including feature extraction and codebook construction, total length of training time is about 7.67 seconds for all 165 speech samples. The system is also tested with 33, 66, 99 and 132 speech samples in the database and it takes 1.67 seconds, 3.16 seconds, 4.66 seconds and 6.14 seconds respectively for training.

In the testing phase, when the system is tested by 165 speech samples in the database, the computation time taken by the system is 6.67 seconds for testing all 33 characters. On the other hand, the accuracy of the system is exactly 100 percent. In the experiments of testing by 33, 66, 99 and 132 speech samples in the database, it is found that the computation times is 0.73 seconds, 1.89 seconds, 2.78 seconds and 5.52 seconds respectively for testing all 33 characters. In the case of accuracy, the system achieves 91 percent, 97 percent, 100 percent and 100 percent respectively.

According to the experiments, it was found that most of the errors occurred among 'Ka Gyi', 'Gha Gyi', 'Na Gyi' and 'La Gyi' because these characters produce quite similar sound in Myanmar Language. The error also occurred between 'Ah' and 'Ha'. When the accuracy is taken into account, the larger the size of the database is, the higher the accuracy of the system is.

5. CONCLUSION

From this work it can be concluded that the system is reliable to use in real world applications and it is reasonably fast for working in real-time.

6. ACKNOWLEDGMENTS

The author would like to take the opportunity to thank all of his colleagues who have given him support and encouragement during the period of the research. The author also would like to express his indebtedness and deep gratitude to his beloved parents, wife and son for their kindness, support and understanding during the whole course of this work and encouragement to attain his ambition without any trouble.

7. REFERENCES

- [1] Bala Murugan M.T, Balaji .M, "SOPC-Based Speech-to-Text Conversion", Nios II Embedded Processor Design Contest—Outstanding Designs 2006, Second Prize, National Institute of Technology, Trichy, 2006.
- [2] Kumar Kuldeep and Aggarwal R.K., "Hindi Speech Recognition System using HTK", J. of International Journal of Computing and Business Research, vol. 2, pp. 3-7, 2011.
- [3] Bapat Abhijit V., Nagalkar Lalit K., "Phonetic Speech Analysis for Speech to Text Conversion", in IEEE Region 10 Colloquium and the Third International Conference on Industrial and Information Systems, Kharagpur, India, 2008, pp. 1-4.

A Versatile Automatic Weight Changer For Mass Comparators

Kyi Kyi Swe

Department of Mechanical
Engineering,
Technological University
Thanlyin, Myanmar

Kyaw Myat Moe

Department of Mechanical
Engineering,
Yangon Technological
University, Myanmar

Zar Chi Thaug

Department of Mechanical
Engineering,
Technological University
Thanlyin, Myanmar

Abstract: This paper describes an automatic weight changer for changing weights on the pan of a mass comparator. The weight changer is easy to use, and is designed to be readily fitted to most common types of top-loading mass comparators and balances of maximum capacity 20 g to 200 g. The versatility of the weight changer is demonstrated by its use in improving the efficiency of routine mass calibration and by its use to compare weights in an evacuated chamber. In each instance the repeatability achieved is 20% or less of the resolution of the balance. The weight changer currently allows up to five weights (or groups of weights) to be automatically compared, but is easily modified to allow comparison of more weights.

Keywords:

1. INTRODUCTION

The requirement for National Metrology Institutes to carry out routine calibration of high accuracy weights has meant that there has been continuing interest in improving the efficiency of such calibrations. Over the past century, research has been carried out on suitable design schemes for calibrating sets of weights, and the favoured schemes are those in which each weight is involved in more than one comparison, both alone and as part of a group of weights 1,2. In addition, the choice of a method of mass comparison is not trivial. Repeated loadings of weights are required to reduce or establish the uncertainty in the result, or to allow compensation or correction for any drift in the comparator zero 3. Research into methods of mass comparison has shown that the best performance is obtained when 3 to 5 weights (or groups of weights) are involved in a cyclic comparison sequence 3.

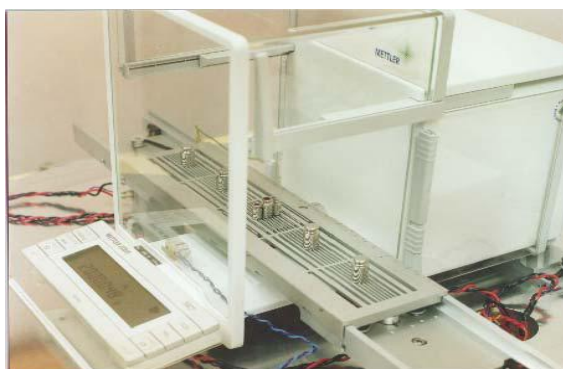


Figure 1. The automatic weight changer fitted to a mass comparator of 200 g capacity

Recent developments in mass comparator technology have also contributed much to the improvement in efficiency of mass calibrations. Top-performance commercially-available mass comparators have weight changers that operate under computer control to automatically load weights on and off the weighing pan.

Comparator readings are also sent to the computer, so that mass comparisons may be carried out under full computer

control. This makes such comparators ideally suited to comparison methods that require repeated interchange of weights. These comparators provide consistent loading of weights, and eliminate tedious, time-consuming manual loading by an operator. In addition, these comparators allow mass comparisons to be carried out without operator disturbances and at times when environmental influences (such as vibration from traffic) are least.

However, these top performance comparators are intended for the highest accuracy comparisons and aspects of their operation make them unsuitable for the routine calibration of weights. Firstly, considerable care is required in loading weights onto the changer. These comparators have self-centering pans, and weights must be accurately centered in each changer position to reduce the amount of movement of the pan on loading and to avoid collision between the pan and the changer. In some cases the pan consists of a thin strip of metal and careful loading is required to prevent weights from falling over. Secondly, the design of the changer and pan on these comparators severely limits the combinations of weights that may be used in a group, so that most common weighing design schemes cannot be implemented. Some comparators require special disk weights to allow combinations of weights to be used, but in such cases the possible combinations of weights (other than disk weights) are even more limited. These comparators have rotating weight changers which restrict the number of weights that can be compared at one time to four (in some cases two). Thirdly, these highest accuracy comparators require long waiting times (~ 1 minute) to reach stability each time the pan is loaded.

Here we describe a weight changer that has all the advantages of automatic operation and that is ideally suited for routine high accuracy calibration. One feature of the design of the changer is that it may be fitted to most types of top-loading mass comparators (of similar capacity) with minimal effort. (We use the word comparator to also mean a balance that is used for mass comparison). A second feature of the weight changer is that it can be used to implement most design schemes as there are practically no restrictions on the combinations of weights that may be loaded onto it. Weights

(or groups of weights) may be loaded onto the changer with no more effort than is normally required to ensure weights are sufficiently centred to avoid significant pan position (eccentricity) error. A third feature is that the speed of the weight changer may be varied to suit the type of weighing. We give examples of the versatility and performance of the weight changer through its use in routine mass calibration and in comparing weights inside an evacuated chamber.

2. DESCRIPTION

Figure 1 shows the automatic weight changer fitted to a comparator of 200 g capacity. The changer consists of a weight carrier with linear movement that fits over the pan of the comparator. The carrier is moved vertically (to load and unload the weights) or horizontally (to change weights). In the configuration shown, the carrier has positions for 5 weights (or groups of weights), but is easily modified to allow comparisons of up to 10 or 15 weights (or groups of weights). As the doors of the comparator weighing chamber must be left open, the carrier and comparator are enclosed in a draught shield during use (not shown in Figure 1).

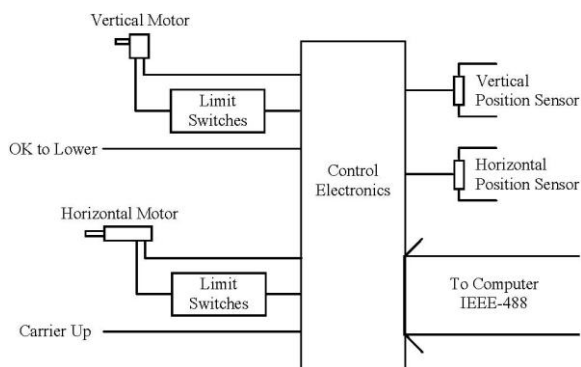


Figure 2. Schematic diagram of the weight changer control electronics

The only modification required of the comparator is that the weighing pan be replaced by a custom-made pan consisting of “fins”, for supporting the weights, that fit into slits in the weight carrier. The tops of the fins can be seen in Figure 1 protruding through the slits in the carrier, as the carrier is being lowered and the fins are just starting to pick up the three weights. With this design, we believe the changer may be easily adapted to common types of top loading comparators of 20 g to 200 g capacity. We are currently able to use the weight changer with a 200 g capacity Mettler AT201 balance and a 50 g capacity Sartorius C50 comparator, both of which are used routinely to calibrate weights from 5 g up to 200 g, and a Mettler AE 200 balance which is used for vacuum weighing applications.

The current weight carrier has slits 3 mm apart in the centre and is designed for weights with diameters from 6 mm to over 60 mm. It will carry standard weights as small as 1 or 2 g. The largest load that the carrier will support is currently limited by the vertical drive motor to a total capacity of about 1 kg.

The weight changer and comparator are mounted on a 700 mm diameter 25 mm thick aluminium base, supported by three adjustable feet at 120° spacing and of sufficient height to allow space for the drive motors which are attached underneath the base. Toothed belts couple the drive motors to the horizontal and vertical movements and ensure repeatable positioning. On top of the base are three adjustable V-groove slots (in a Yconfiguration) which allow secure and accurate positioning of the comparator. To assemble the system, the

comparator is first placed in position on the base, and the carrier is then placed over the weighing pan and secured to the base. The base shown in Figure 1 is also the bottom of a chamber that encloses the comparator for mass comparisons in vacuum. This base has vacuum feed throughs for electrical connections and the motor drive shafts. When using the automatic weighing system in ambient air, the only requirement is for a base of sufficient rigidity to allow suitable performance of the comparator.

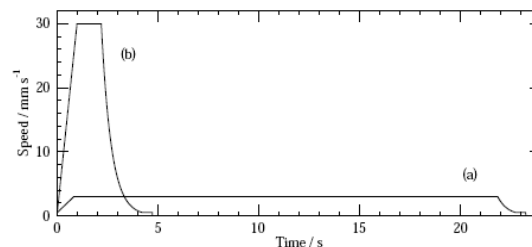


Figure 3. Typical speed profiles for the horizontal movement of the weight carrier. (a) profile with a maximum speed of 3 mm s⁻¹, (b) profile with a maximum speed of 30 mm s⁻¹

The design of the control electronics (Figure 2) is a major factor in the versatility of the weight changer. Two programmable speed dc motors are used to move the weight carrier horizontally and vertically, so that the computer has full control over the speed and positioning of the weight carrier. Weights can be moved by the carrier at horizontal speeds from 0.25 to 50 mm s⁻¹, and at vertical speeds from 0.01 to 1.20 mm s⁻¹. Position sensors (potentiometers) on the vertical and horizontal movements provide position information for the computer. In addition, two sensors are used to prevent undesirable movement. One sensor checks that the carrier is up before horizontal movement can commence, and the other checks that the carrier is in one of the five positions suitable for lowering. The horizontal and vertical movements have limit switches at their allowable extremes and each motor has an over-torque cut-out.

Communication with the controlling computer is provided through an IEEE-488 interface with listen and talk capabilities.

Limited local operation from the front panel of the controller is also available, including two speed horizontal and one speed vertical movement. The control electronics are custombuilt but could be assembled using commercially available motor controllers.

Computer software routines for positioning and moving the carrier (vertically or horizontally) may be incorporated into any computer program written for a specific application of the weight changer. Figure 3 shows typical programmed speed profiles for moving the carrier horizontally from one weighing position to the next adjacent position (a distance of 66 mm). Figure 3 (a) is a profile used for routine weighings in air, in which weights are moved slowly (maximum speed 3 mm s⁻¹) to minimise air currents. The profile of Figure 3 (b) gives faster movement (maximum speed 30 mm s⁻¹) and is used for weighings in vacuum (see later). The feature of each profile is the exponential slowing down to a set minimum speed as the target position is approached, in order to allow reproducible positioning of the carrier to well within 0.5 mm. Software routines are also used during initial setting up of the changer to establish potentiometer readings corresponding to the weighing positions and to the carrier-up and carrier-down positions.

During the initial setting up of the changer it is necessary to ensure that the top of the carrier is parallel to the top of weighing pan, to prevent the weights from ‘walking’ during mass comparisons. The tendency for the weights to walk increases with the number of repeat loadings in the given application, and also apparently with the diameter of the weights and the height of the centre of mass of the weights. The best alignment is achieved by observing the projection onto a screen of a laser beam reflected vertically from a mirror placed on the weighing pan. The carrier-pan alignment is adjusted to minimise the movement of the projection as the mirror is just lifted off the pan by the weight changer. With the carrier aligned by this method, trials using 46 mm diameter 85 g weights showed that after 80 repeat loadings of the weights, the weights had only moved by about 0.5 mm.

For routine calibration work using standard weights, alignment by levelling both the weighing pan and the carrier using a bubble level is sufficient. With the system aligned by this method the alignment error was less than 0.003 radians. Trials with 200 g weights showed that after 80 consecutive loadings of each weight, the weights had moved by 4 mm or less. The amount of movement was progressively less for smaller weights of the same diameter. For routine comparisons typically carried out in our laboratory, this rate of movement does not cause significant pan position error.

Table 1. Results of comparisons of reference standards using the weight changer with a Mettler AT201 balance.

Nominal mass / g	Measured difference - calibration difference $\Delta m_c - \Delta m_m$ / μg	Std. uncertainty of measured difference / μg	Std. uncertainty of calibration difference / μg	t
100	1.88	1.00 $v=8$	1.40 $v=23$	1.09 $v_{\text{eff}}=30$
100	2.58	1.62 $v=9$	1.40 $v=23$	1.21 $v_{\text{eff}}=22$
50	-0.67	1.15 $v=8$	1.00 $v=22$	0.44 $v_{\text{eff}}=20$
50	3.02	1.34 $v=9$	1.00 $v=22$	1.80 $v_{\text{eff}}=19$
30	1.00	1.42 $v=9$	0.88 $v=22$	0.60 $v_{\text{eff}}=16$
20	-2.13	1.77 $v=8$	0.57 $v=22$	1.14 $v_{\text{eff}}=9$
20	-0.66	1.23 $v=9$	0.57 $v=22$	0.48 $v_{\text{eff}}=13$
10	0.29	0.59 $v=8$	0.73 $v=22$	0.31 $v_{\text{eff}}=27$
10	-5.23	0.97 $v=9$	0.73 $v=22$	4.32 $v_{\text{eff}}=19$
10	3.05	1.68 $v=8$	0.73 $v=22$	1.66 $v_{\text{eff}}=11$
5	1.72	1.42 $v=9$	0.96 $v=22$	1.01 $v_{\text{eff}}=17$

3. APPLICATIONS

Routine Calibration of Weights

The weight changer is currently being used with a 200 g capacity Mettler AT201 balance (resolution = 10 μg) for routine calibration of weights ranging in nominal mass from 200 g to 5 g, to accuracies of 5 parts in 10^7 (with a lower limit of 10 μg). In OIML terms [4], such accuracies are suitable for the calibration of Class E₂ weights. Ongoing assessment of the performance of the comparator and changer is being carried out in conjunction with its use, and involves the inclusion of two calibrated reference standards in positions on the carrier during each weighing. These reference standards have been recently calibrated using a more accurate comparator. The measured difference Δm_m in the mass of these two standards is compared with the difference Δm_c obtained from their calibration. A typical weighing at (for example) 20 g, and which utilises all five positions on the carrier, consists of comparisons in the following cyclic sequence: 20, 20s, 20's, 20', (10+10s), where 's' denotes a reference standard. In this case a weighing consists of 3 cyclic repeats of the sequence to give 15 readings in total. The mass differences are calculated by a least squares method assuming linear drift in the comparator zero [3]. For the purposes of assessing the performance of the comparator and changer, a weighing is repeated 9 or 10 times, taking a total time of 2.5 to 3 hours.

Table 1 shows the results obtained for all comparisons of the reference standards during a two month trial of the

comparator and weight changer. The quantity listed in the second column of Table 1 is the difference between the measured difference Δm_m in mass of the two reference standards (the mean of the results of the 9 or 10 repeat weightings), and the ‘calibration difference’ Δm_c . This quantity gives an indication of the performance of the comparator and weight changer combination. Corresponding standard uncertainties and degrees of freedom ν are tabulated in the third and fourth columns of Table 1.

The most striking feature of these results is that the standard deviations in measured mass differences are all below 18 % of the resolution of the comparator. We cannot achieve this level of performance by manually loading the comparator. For a mass comparison where the uncertainty is due only to the resolution r of the comparator, the standard uncertainty r_3 in a measured mass difference is $r\sqrt{2}/\sqrt{12}$, that is, 41% of the resolution. Clearly, there is sufficient variability in the comparator readings so that using the weight changer reduces the limitations of the comparator resolution.

Assuming that the tabulated uncertainties are dominated by Type A [5] components, we may use the t-test [6] for significance in the tabulated differences. Calculated t values and effective degrees of freedom ν_{eff} (see Table 1) indicate

that, with only one exception (that for which $t = 4.32$), the differences are not significant at a 95 % level of confidence.

3.1 Weighing In Vacuum

The weight changer was originally designed for weighing the floating elements of gas pressure balances in vacuum [7]. It is the mass in vacuum of these floating elements that determines the pressure generated by an absolute mode pressure balance. Conventional weightings in air and in water could not be used to accurately determine the true masses of the floating elements because of their complex structure and internal cavities.

The balance used for these weightings in vacuum is a special version of the 200 g capacity Mettler AE 200 that has the weighing cell and display module in two separate units, allowing the display module to be outside the vacuum chamber. This Mettler AE-SE 200 has a resolution of 100 μg . Prior to the weightings, the pan and carrier were aligned using a laser, as described earlier, because the base of the floating elements is about 46 mm in diameter, so they are prone to ‘walking’ with repeated loading and unloading.

A typical weighing in vacuum uses all five carrier positions with two reference standards S1, S2 and three floating elements FE1, FE2, FE3 loaded three times in the sequence S1, FE1, S2, FE2, FE3. The floating element masses are either 85 g or 170 g. Each three cycle weighting is performed within 10 minutes to allow changes in mass after evacuation to be monitored. This short weighing time is achieved by changing the masses at a maximum horizontal speed of 30 mm s⁻¹ (see Figure 3 (b)).

As with the application to routine weight calibration, the accuracies achieved in the automatic weightings in vacuum are well within the resolution of the balance. The performance was checked by comparing the difference between the calibrated mass values for two 85 g reference standards with the difference measured in a typical vacuum weighing. The average measured difference between the two 85 g standards obtained from six weightings in vacuum was 714 μg with a standard uncertainty of 20 μg , compared with their calibration difference of 707 μg . The measured difference minus the

calibration difference is only 7 μg and the 20 μg standard uncertainty is just 20 % of the resolution. In this case, the drift in the balance zero of 8 μg per reading (on average) contributed to reducing the standard uncertainty to below the 41 μg resolution limit.

4. CONCLUSION

We have described an automatic weight changer that may be readily fitted to common types of top-loading mass comparators and balances, and we have given examples of its use in routine calibration of weights and in a vacuum weighing application. We have demonstrated the effectiveness of the weight changer through its versatility, and through its ability to allow optimal mass comparator performance to be achieved, all of which make it well suited for use in a mass standards laboratory of a National Metrology Institute.

5. ACKNOWLEDGMENT

The preferred spelling of the word “acknowledgment” in American English is without an “e” after the “g.” Use the singular heading even if you have many acknowledgments. Avoid expressions such as “One of us (S.B.A.) would like to thank” Instead, write “F. A. Author thanks” Sponsor and financial support acknowledgments are placed in the unnumbered footnote on the first page.

6. REFERENCES

- [1] S. Chen, B. Mulgrew, and P. M. Grant, “A clustering technique for digital communications channel equalization using radial basis function networks,” *IEEE Trans. on Neural Networks*, vol. 4, pp. 570-578, July 1993.
- [2] J. U. Duncombe, “Infrared navigation—Part I: An assessment of feasibility,” *IEEE Trans. Electron Devices*, vol. ED-11, pp. 34-39, Jan. 1959. C. Y. Lin, M. Wu, J. A. Bloom, I. J. Cox, and M. Miller, “Rotation, scale, and translation resilient public watermarking for images,” *IEEE Trans. Image Process.*, vol. 10, no. 5, pp. 767-782, May 2001.
- [3] J. M. Cameron, M. C. Croarkin, and R. C. Raybold, *Designs for the Calibration of Standards of Mass*, NBS Technical Note 952, U.S. Government Printing Office, Washington D.C., 1977. 2. F. Kohlrausch, *Praktische Physik*, Band 1, Mary S. Rosenberg, New York, 1947
- [4] C. M. Sutton and M. T. Clarkson, “A General Approach to Comparisons in the Presence of Drift,” *Metrologia*, Vol. 30, No. 5, pp. 487-493, 1993/94.
- [5] Organisation Internationale de Métrologie Légale, *Weights of classes E1, E2, F1, F2, M1, M2, M3*, International Recommendation R 111, 1994.
- [6] ISO/IEC/OIML/BIPM publication, *Guide to the Expression of Uncertainty in Measurement*, 1993.
- [7] C. F. Dietrich, *Uncertainty, Calibration and Probability*, Adam Hilger, London, 1973.
- [8] C. M. Sutton, “The Pressure Balance as an Absolute Pressure Standard,” *Metrologia*, Vol. 30, No. 6, pp. 591-594, 1993/94.

Design Consideration of Permanent Magnet Synchronous Reluctance Motor by Finite Element Method

Zaw Htet Myint

Department of Electrical Power Engineering
Mandalay Technological University
Mandalay, Myanmar

Abstract: A synchronous reluctance motor (SynRM) which uses a sinusoidal wave to drive a rotor constructed with several flux barriers. The stator winding of this motor is the same specifications as that used in an induction motor or a brushless motor which utilizes permanent magnet. This paper presents the design of synchronous reluctance motor with assistant of permanent magnet for 8kg washing machine. At the beginning of the design, main dimension of stator and number of stator slots are calculated. Rotors design parameters such as flux barriers, different insulation, magnet position are considered after calculating the number of stator slot. The rotor design process is considered to determine the best value for maximum average torque and minimum torque ripple. Permanent magnets are placed inside the flux barriers and results are verified by using finite element method (FEM).

Keywords: synchronous reluctance motor, permanent magnet, NdFeB, magnetic flux distribution, finite element method (FEM), washing machine

1. INTRODUCTION

Washing machine is the electronic home appliance used to wash the various type of clothes without applying any physical efforts. With washing machine people don't have to rub the clothes with hand or squeeze them to remove the water. The washing machine washes the clothes automatically without having to supervise its operation. The washing machine automatically takes the required amount of water and detergent. It also automatically sets the timer for washing, rinsing and drying as per the selected mode of operation. There are many types of washing machines varying in mechanical construction, motor type driving a drum, a control system of motor control part, human interface, semi-automatic type, level of energy efficiency, washing performance, drying performance and water consumption. Many types of washing machines are horizontal type and vertical type based on drum position, front loading and top loading washing machines based on drum loading, belt driven and direct drive based on drive construction.

Washing machine is mainly operated by a motor, which is connected to the agitator through a unit called a transmission. The motor and transmission are near the bottom of the machine, while the agitator extends up through the middle of the machine. The motor is coupled to the agitator or the disc and produces its rotator motion. These are multispeed motors, whose speed can be changed as per the requirement. In the fully automatic washing machine the speed of the motor i.e. the agitator changes automatically as per the load on the washing machine. In fact, it is the motor which accelerates the process of washing. Therefore, it is a very important component of a washing machine.

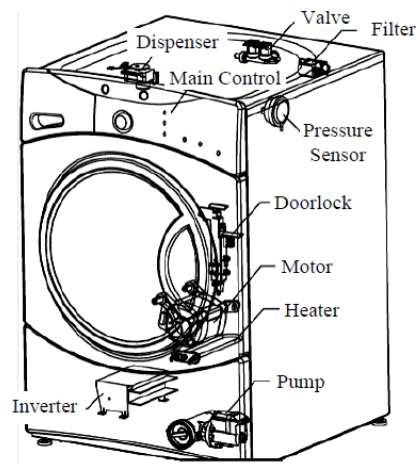


Figure 1. Inside a front-loading washing machine

Most of the Washing machine runs with the help of induction motor and universal motor. Moreover, modern motor construction such as synchronous motors are also used in washing machine. Nowadays, direct drive washing machines utilizing PM motor is increasing due to the mechanical simplicity, high performance and efficiency of the system. Induction motors are the wide used motors in industrial and civil applications, due to the simple realization, the robustness and the possibility to be supplied directly by the sinusoidal main without the necessity of a static power supply with related control system. If the application requires speed regulation, motor different from the induction motor type can be adopted. In the last years, among the electric motors available for variable speed drives, the synchronous reluctance motors (transvers rotor lamination type) have gained consistent market quotes. Synchronous reluctance

motor has a higher rated torque compared with induction motor because of the absence of the rotor losses. The comparison between SynRM and IM at the same torque at the same frame size is the induction motor is hotter than the reluctance one. As a consequence, with the same power dissipation, (the same temperature of the stator windings), the reluctance motor is able to produce a higher torque than the induction motor. In this paper, synchronous reluctance motor is considered to use in washing machine. Some specifications of the washing machine for the research is as shown in Table 1.

Table 1. Specifications of washing machine

Voltage	220-240 V
Current	10 A
Frequency	50 Hz
Wash capacity	8 kg
Speed	1400 rpm
Power	400 W
Water consumption	64 liters

2. SYNCHRONOUS RELUCTANCE MOTOR

The Synchronous Reluctance machines were discovered many years ago, around the early 60's, even if the theory of anisotropic filed structure go back to the 1923 where Doherty and Nickle published a paper. Kusko in 1926 shows a first design of synchronous reluctance motor with multi barriers structure. Honsinger in 1957 developed some of the first consistent theory on the design of multi barrier synchronous reluctance machines.

2.1 Types of Synchronous Reluctance Rotors

The major types of synchronous reluctance rotors are the simple salient pole rotor, the axially laminated rotor and the transverse laminated rotor. They are depicted in Figure 2. The salient pole rotor design has a simple and rigid structure but a low saliency ratio and consequently poor performance. However, the rigid structure creates the possibility of using the salient pole rotor design in high-speed and extremely high-speed machines. The axially laminated rotor design has a good saliency ratio and performance, but the eddy current losses as a result of the axial lamination are large. However, the mechanical design is extremely complex for industrial manufacturing, at least for four-pole machines, where the sheets have to be bent and connected with bolts. However, a two-pole axially laminated machine is easier to manufacture because the electrical sheets are straight. The transverse laminated rotor has similar sheets that can easily be punched and iron losses in the rotor are reduced compared to the axially laminated structure. Therefore, the transverse

laminated structure is the best choice for industrial manufacturing.

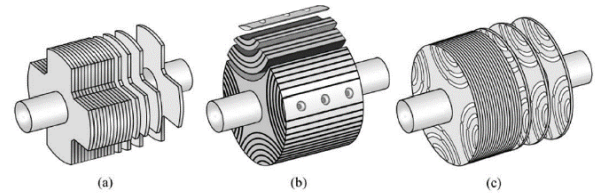


Figure 2. Schematics of (a) simple salient pole; (b) axially laminated; (c) transverse laminated rotors

The structure of reluctance motor is same as that of salient pole synchronous machine. The rotor does not have any field winding. The stator has three phase symmetrical winding, which creates sinusoidal rotating magnetic field in the air gap, and the reluctance torque is developed because the induced magnetic field in the rotor has a tendency to cause the rotor to align with the stator field at a minimum reluctance position. The rotor of the modern reluctance machine is designed with iron laminations in the axial direction separated by non-magnetic material. The performance of the reluctance motor may approach that of induction machine.

2.2 Basic Theory of synchronous reluctance motor

The synchronous reluctance machine (SynRM) utilizes the reluctance concept and rotating sinusoidal MMF, which can be produced by the traditional IM stator, for torque production. The main idea can be explained by Figure 3. A magnetic field (Ψ) which is applied to the anisotropic object is producing torque if there is an angle difference between the d-axis and the field. It is obvious that if the d-axis of object is not aligned with the field, it will introduce a field distortion in the main field. The main direction of this distortion field is aligned along the q-axis of the object. In the SynRM (Ψ) is produced by a sinusoidally distributed winding in a slotted and it links the stator and rotor through a small air gap, exactly as in a slotted and it links the stator and rotor through a small air gap, exactly as in a traditional IM. The field is rotating at synchronous speed and can be assumed to have a sinusoidal distribution. In this situation there will always be a torque which acts to reduce the whole system potential energy by reducing the distortion field in the q-axis. If load angle is kept constant, for example by control or applying a load torque, then electromagnetic energy will be continuously converted to mechanical energy. The stator current is responsible for both the magnetization and the torque production which is trying to reduce the field distortion, this can be done by controlling the current angle, which is the angle between the current vector to the stator winding the rotor d-axis in synchronous reference frame.

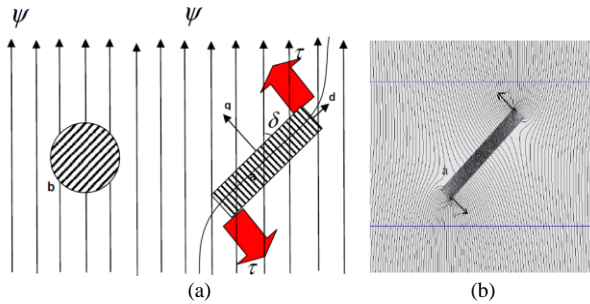


Figure 3. An object with anisotropic geometry (a) and isotropic geometry (b) in a magnetic field Ψ and torque production mechanism

Synchronous reluctance motor has two rotor paths for the flux. One is a high permeability path, the flux lines flowing in rotor iron paths, parallel to the flux-barriers. It is commonly referred to as the d-axis path. The second is a low permeability path, the flux lines have to cross the rotor flux barriers. It is commonly referred to as the q-axis path. The final dq reference frame is obtained. The rotor is designed with several flux barriers, in order to obstacle the flux along the q-axis. And, to achieve a high saliency ratio, that is, a high reluctance torque component. The iron bridges (at the ends and sometimes in the middle of each barriers) sustain the rotor parts. A portion of q-axis flux flows through these bridges, with a consequence reduction of the torque. The diagrams of a SynRM geometry with their d- and q- axes flux lines are shown in Figure 4.

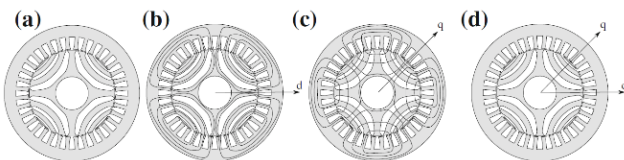


Figure 4. Sketch of a synchronous reluctance motor with (a) geometry, (b) d-axis flux lines, (c) q-axis flux lines, and (d) reference frame

3. DESIGN CONSIDERATION OF SYNCHRONOUS RELUCTANCE MOTOR

There are three main classes of parameter classification for SynRM.

- Design parameters of stator geometry
- Design variables or microscopic parameters
- Target variables

The first group includes the parameters of stator geometry such as number of slots, poles, outer diameter and inter diameter of stator, etc. the second group includes variables that are mainly based on the rotor geometry. The third group and rotor geometry (second) should be calculated from finite element method in order to obtain accurate results. The stator structure of transversally laminated type is essentially the same with other machines such as induction machines, so, the main performance difference comes from rotor structure.

The SynRM can be built putting a reluctance rotor inside stators extracted from the induction production line.

3.1. Design Specifications of SynRM Rating

The specifications of the proposed synchronous reluctance motor is described in Table 2.

Table 2. Specifications of SynRM

Voltage	220V
Current	4.2A
Frequency	50Hz
Speed	1500rpm
Output Power	400W
Efficiency	68%
Power Factor	0.65
Number of poles	4

3.2. Design consideration for stator geometry

The output power equation is

$$KVA = VI \times 10^{-3} \quad (1)$$

where V=rated voltage

I=full load current

$$V = 4.44k_w f \phi T_m \quad (2)$$

where ϕ =flux per pole

K_w =winding factor

F=frequency

T_m =number of turns of main winding

$$\phi = B_{av} \frac{\pi D}{p} L \quad (3)$$

where B_{av} =average value of flux density in air gap

p=number of pole

D= stator bore diameter

L=stator core length

$$ac = \frac{2T_m I}{\pi D} \quad (4)$$

where ac=ampere conductor per meter pf arm periphery

$$KVA = 4.44k_w f \phi T_m \times 10^{-3}$$

$$KVA = (1.11\pi^2 k_w B_{av} ac \times 10^{-3}) D^2 L n_s \quad (5)$$

$$C_0 = 1.11\pi^2 k_w B_{av} ac \times 10^{-3}$$

where, C_0 =output coefficient

$$KVA = c_0 D^2 L n_s \quad (6)$$

If the rating is horse power, it can be changed in KVA.

$$KVA = \frac{hp \times 0.746}{\eta \times \cos \phi} \quad (7)$$

where, η =full load efficiency

$\cos \phi$ =full load power factor

Main dimension is

$$D^2 L = \frac{hp \times 0.746}{\eta \cos \phi C_0 n_s} \quad (8)$$

To separate D and L from $D^2 L$

$$L \cong \tau_p \quad (9)$$

$$\text{pole pitch, } \tau_p = \frac{\pi D}{p} \quad (10)$$

Depth of stator core is

$$d_{c1} = \frac{B_t}{B_c} \times \frac{S_1 \times b_{t1}}{\pi p} \quad (11)$$

Width of the teeth is

$$b_{t1} = \frac{(1.27 + 0.035 D_i) D_i}{S_i} \quad (12)$$

Width of the slot at top section is

Assuming parallel sided teeth and trapezoidal slots with flat bottom, the width of the slot at the mouth is given by,

$$b_{11} = \frac{\pi(D_i + 2(h_{10} + h_{11}))}{S_1} - b_{t1} \quad (13)$$

Depth of the slot below the mouth is

$$h_{14} = 0.5(D_0 - D_i) - (h_{10} + h_{11} + d_{c1}) \quad (14)$$

Width of the slot at bottom is

$$b_{13} = b_{11} + 2h_{14} \tan \alpha \quad (15)$$

Length of Air Gap is

$$l_g = 0.013 + \frac{0.0042 D_i}{\sqrt{p}} \quad (16)$$

Winding distribution factor

$$k_w = \frac{k_{p1} T_1 + k_{p2} T_2 + k_{p3} T_3 + \dots}{T_1 + T_2 + T_3 + \dots} \quad (17)$$

Current carried by main winding,

$$I = \frac{hp \times 0.746}{V \cdot \eta \cdot \cos \phi} \quad (18)$$

Area of cross section of conductor,

$$a_m = \frac{I}{\delta_m} \quad (19)$$

The useful slot height, teeth area per pole, depth of stator core, depth of slot below the mouth and width of tooth can be calculated from the above equations.

3.3. Design results for stator geometry

The calculated design results are shown in Table 3 and the geometrical diagram of the stator is depicted in Figure 5.

Table 3. Result data of stator geometry

Name	Symbol	Result
Outer diameter	D_0	18cm
Inner diameter	D_i	11cm
Core length	L	7cm
Number of stator slots	S_1	24
Slot opening	b_{10}	0.26cm
Depth of tip	h_{10}	0.07cm
Depth of mouth	h_{11}	0.09cm
Width of tooth	b_{t1}	0.76cm
Stator core depth	d_{c1}	1.74cm
Width of slot at the top section	b_{11}	0.72cm
Length of air gap	l_g	0.036cm
Depth of slot below the mouth	h_{14}	1.6cm
Width of the slot at the bottom	b_{13}	1.41cm

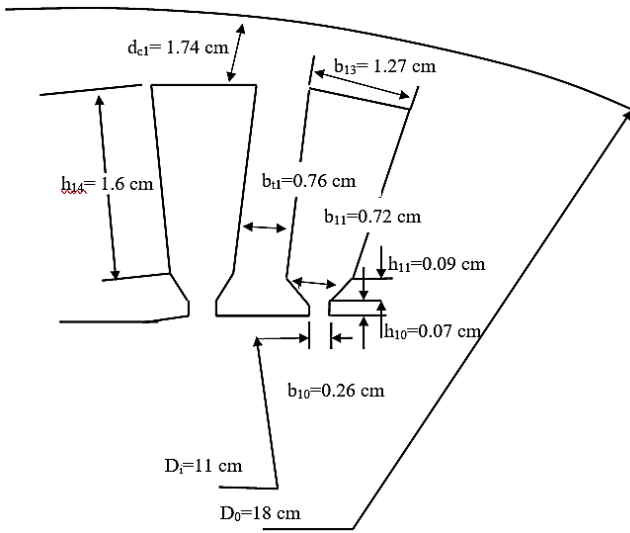


Figure 5. Stator Slot Geometry

4. PERFORMANCE ANALYSIS OF SYNCHRONOUS RELUCTANCE MOTOR

The finite element method (FEM) is an important tool for the design and analysis of electric machine. The rotor structure of synchronous reluctance motor is made of laminated iron. There are three flux barriers per pole in this design. Permanent magnets are inserted in them. The running condition by NdFeB32MGOe is depicted in Figure 6.

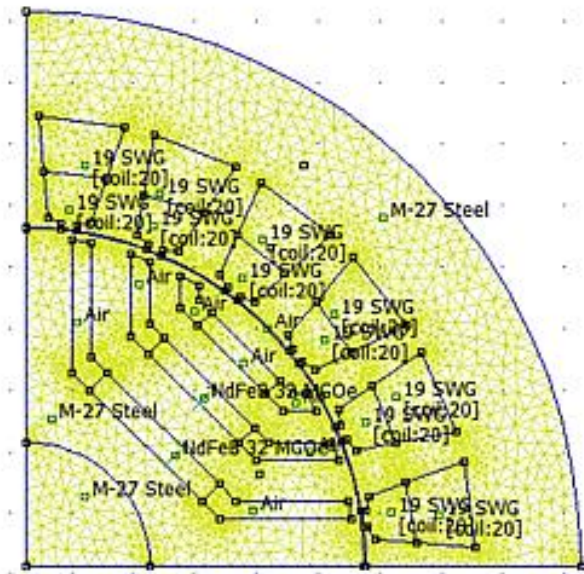


Figure 6. Running condition by NdFeB32MGOe

Figure 7 shows the magnetic flux density values for SynRM per pole result output, flux density which can be plotted as a colour density plot.

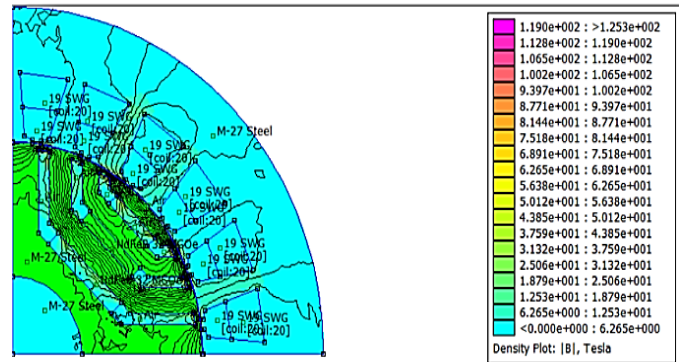


Figure 7. Magnetic flux density for SynRM per pole

Figure 8 shows the magnitude of magnetic flux density for one pole of SynRM by using finite element method (FEM) software.

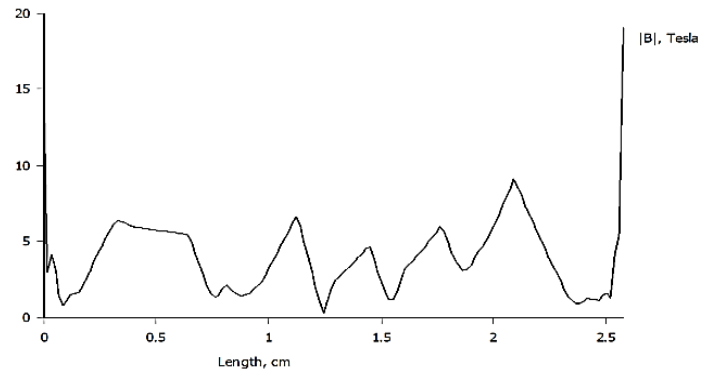


Figure 8. The magnitude of magnetic flux density for one pole

5. CONCLUSION

The simulation of stator slot number, rotor flux barriers number, insulation ratio and permanent magnet position of a synchronous reluctance motor is investigated. The design process has been carried out by using analytic calculation. Moreover, the finite element method was used to calculate the flux density in the motor components. In this design, stator slot dimensions are calculated by sizing equation and then rotor structure is analyzed with finite element method. In this paper, Synchronous reluctance motor is designed for 8kg washing machine which rated power 400W.

6. REFERENCES

- [1] Takayoshi Matsuo, Thomas A. Lipo, “Rotor Design Optimization of Synchronous Reluctance Machine”, IEEE Transactions on Energy Conversion, Vol.9.No2, June 1994
- [2]R.RMoghaddam, “Synchronous Reluctance Machine (SynRM) Design,” M.S. Thesis, Dept. of Elec. Eng. , KTH Royal Institute of Technology, Stockholm, Sweden,2007
- [3]Alfredo Vagati, “Design of Low-Torque_Ripple Synchronous Reluctance Motors,”IEEE, Michele Pastorelli, Giovanni Franceschini, and Stefan Cornal Petrache 1998
- [4]Aldo Boglietti,“Induction and synchronous reluctance motors comparison,” Senior IEEE, Michele Pastorelli, Italy2008
- [5]Cruickshank, A.J.O; Anderson, A.F; Menzies, R.W.,”Theory and performance of reluctance motors with axially laminated anisotropic rotors,”Electrical Ehineers, Proc. Of the Instiyute of , vol.42, no.11, pp.1162,1168,Nov.1923

Design of a Microcontroller Based Automatic Voltage Stabilizer with Toroidal Transformer

Thet Htun Aung

Department of Electrical Power Engineering
Mandalay Technological University
Myanmar

Abstract- Every electrical and electronic appliance is designed to work perfectly at a certain input voltage. In Myanmar, household electrical and electronic appliances are designed to work properly at 220VAC, 50Hz and most of the times the voltage supplied from distribution companies are as low as 130VAC making this appliances to work under threat of low voltage supply. This low supply voltage causes these appliances to malfunction and in most cases damage them. Since the electric power supply/distribution companies are unable to provide the consistent adequate voltage level (220VAC) demanded by these sensitive appliances, therefore there is need for consumers to protect the appliances from damage and ensure their safe operation, hence the use of automatic voltage stabilizers to improve the situation. In this research work, a PIC16F877A microcontroller was programmed to monitor the input voltage from distribution companies and if voltage level is between 130 VAC and 250VAC, it gives a constant output voltage of nearly 220VAC required by the appliance. The model parameter calculated from the design information.

Keywords – Myanmar, Household Electrical, Stabilizer, Input And Output Voltage, Electric Power Supply, Distribution, Microcontroller.

I. INTRODUCTION

The development of any country is largely hinged on the availability of undisturbed and regulated power supply. In Myanmar, electricity is generated by turbine driven synchronous generators at 50Hz at a standard minimum voltage of 11kV. The generated voltage is then stepped up to the primary or secondary Grid voltage of 132kV to reduce power losses during transmission. The generated power then travels from the generating stations to the point of utilization via high voltage Transmission lines, most of which are suspended overhead. However due to the uneven power demand at the load end and the complexity of the consumer network, a third party is required to ensure that the generated electricity is properly distributed according to the load demand, while taking into consideration the necessary geographic and economic factors as they affect the overall socio-economic growth of the nation. In Distribution, electrical power is stepped down at distribution sub-stations of various levels to a final voltage of 400 V (phase to phase) and 230V (phase to neutral) which is directly consumed by most electrical load. Voltage is the most important parameter in electrical power [1] system and it is necessary to be maintained a constant output voltage because, it is the driving force that pushes current through the conductor. Voltage stability is vital for safety and optimal performance of electrical appliances. Most electrical appliances are designed for optimal operation, maximum length of service and safety if the power rating of the appliance is maintained.

The automatic voltage stabilizer presented in this research aim at designing a suitable Automatic Voltage Stabilizer rated 15 kVA with output 220 VAC, when the input voltage is varying between 130 VAC and 250 VAC.

II. MATHEMATICAL EQUATIONS OF TOROIDAL TRANSFORMER

The rating of the servo motor automatic voltage stabilizer is mainly depended on the transformer rating. The circuit diagram of the servo motor automatic voltage stabilizer including variable autotransformer. The simplest device for regulating the voltage applied to a load is the variable auto-transformer. One of the best known types is the “Variac”. The core consists of a deep stack of ring-shaped laminations. The insulation is removed from a circular track around the upper horizontal face of the winding and a carbon brush carried on a rotating arm makes contact with any desired turn on the winding. For the input fluctuation -40% , $+10\%$ toroidal transformer must be withstand the variation of the maximum input voltage is $242\text{ V} \approx 250\text{ V}$ and the minimum input voltage is $132\text{ V} \approx 130\text{ V}$. The output voltage must be nearly 220 V . Variable transformer type of this AVS is toroidal transformer. The capacity of automatic voltage stabilizer is 15 kVA (single-phase). The output voltage regulation is $\pm 5\%$.

A. Design Equation

Equations such as e.m.f. equation, e.m.f. per turn in terms of output and output equation are needed to design

of the magnetic circuit (main dimensions of core, yoke and window).

B. E.M.F. Equation

When the alternating voltage is applied across the primary of the transformer, it takes a magnetizing current and a flux; ϕ is established in the transformer core. The flux, ϕ is uniformly distributed over the transformer core section and is linked with all the turns of primary and secondary windings. The main flux, ϕ established in the core is alternating in nature.

Hence an e.m.f. is induced in the primary winding, due to the change of main flux, which is given by,

$$e_1 = -N_1 \frac{d\phi}{dt} \quad (1)$$

$$\phi = \phi_m \cos \omega t \quad (2)$$

$$e_1 = \frac{-N_1 d(\phi_m \cos \omega t)}{dt} = N_1 \omega \phi_m \sin \omega t$$

$$E_1 = 4.44 f N_1 \phi_m \text{ volts} \quad (3)$$

$$E_1 = 4.44 f N_1 B_m A_i \text{ (where } \phi_m = B_m A_i) \quad (4)$$

Induced e.m.f. in secondary winding,

$$E_2 = 4.44 f N_2 B_m A_i \text{ volts} \quad (5)$$

e.m.f. per turn,

$$E_t = 4.44 f B_m A_i \quad (6)$$

For E.M.F per Turn,

$$E_t = 4.44 f \phi_m \quad (7)$$

K.V.A rating per phase,

$$E_t = V \times I \times 10^{-3} = \frac{V}{N} \times IN \times 10^{-3} \\ = E_t \times IN \times 10^{-3} \quad (8)$$

The ratio of cross-sectional area of the core and the copper area of the windings will be constant for a particular transformer i.e.

$$\frac{A_i}{A_c} = \text{constant} \quad (9)$$

Cross sectional area of core,

$$A_i = \frac{\phi_m}{B_m} \text{ or} \quad (10)$$

$$A_i = \frac{\sqrt{P}}{5.58} \text{ sq in} \quad (11)$$

Copper area of the windings,

$$A_c = a N = \frac{I}{\delta} \times N$$

$$\frac{A_i}{A_c} = \frac{\phi_m}{IN} \times \frac{\delta}{B_m}$$

As current density, δ and flux density, B_m is nearly constant,

$$\frac{\phi_m}{IN} = \text{constant} = r \quad (12)$$

Substituting for IN from Equation 12 into Equation 8,

$$\frac{\text{kVA}}{\text{phase}} = E_t \times \frac{\phi_m}{r} \times 10^{-3} \text{ (or)} \\ \phi_m = \frac{(\frac{\text{kVA}}{\text{phase}}) \times r}{E_t} \times 10^3 \quad (13)$$

Substituting for ϕ_m from Equation 13 into Equation 7,

$$E_t = 4.44 f \times \frac{(\frac{\text{kVA}}{\text{phase}}) \times r}{E_t} \times 10^3$$

$$E_t^2 = (4.44 f r \times 10^3) \times \frac{\text{kVA}}{\text{phase}}$$

e.m.f. per turn,

$$E_t = \frac{4.44 B_m N_e f A_i}{10^8} \text{ volt} \quad (14)$$

$$E_t = K \sqrt{\text{kVA/phase}}$$

$$\text{Where } K = \sqrt{4.44 f r \times 10^3} \quad (15)$$

In order to utilize equation 12, for finding out the e.m.f. per turn, the value of the factor, K is needed. And then, the turns per volt will be got.

$$\text{Turns per volt, } N_e = \frac{E_t \times 10^8}{4.44 B_m f A_i} \quad (16)$$

C. Factor K

Factor, K which basically depends upon the ratio of cross sectional area of core to the copper section of the windings, will be different for two types of transformers i.e. core and shell. The value of factor K with respect to transformer type is shown in Table I.

TABLE I. CONSTANT K WITH RESPECT TO TRANSFORMER TYPE

Type	K (Factor)
(1) Single phase core	0.75-0.8
(2) Single phase shell	1.0-1.1
(3) Three phase core (power)	0.6-0.65
(4) Three phase core (distribution)	0.45-0.5
(5) Three phase shell	1.2-1.3

D. Stacking Factor

To get the required core section, the transformer core is prepared by stacking together thin sheets of laminations. These laminations are insulated on both sides usually by spray of varnish. That, the assembled core includes the area of insulation as well. The gross core section A_{gi} , is related with the net core section, A_i , by a factor K_s called stacking factor.

$$\text{Thus, } A_i = K_s A_{gi} \quad (17)$$

K_s = stacking factor, usually value is 0.85 ~ 0.9.

E. Flux Density (B_m)

The voltage equation as well as output equation indicates that the higher value of flux density B_m is chosen, the core area A_i reduces. This will reduce the diameter of circumference thereby reducing the length of mean turn. The choice of B_m will also depends upon the type, service conditions of the transformer. It has already been pointed out that a distribution transformer should be designed for lower iron losses giving good all-day efficiency. Therefore, for distribution transformer comparatively lower flux density is assumed.

Using hot rolled silicon steel

- Power transformers - 1.2 to 1.4 Tesla
- Distribution transformers - 1.1 to 1.3 Tesla

Using cold rolled grain oriented silicon steel

- Power transformers - 1.5 to 1.7 Tesla
- Distribution transformers - 1.4 to 1.5 Tesla

Lower values should be used for small rating transformers.

III. CALCULATION OF TOROIDAL TRANSFORMER

According to Equation 1 to Equation 17, 15 kVA rating of the variable transformer is designed in this research.

Core Design of Toroidal Transformer

$$\begin{aligned} \text{Cross section area of iron core, } &= \frac{\sqrt{15 \times 10^3}}{5.58} \\ &= 21.949 \text{ in}^2 \\ &= 141.606 \text{ cm}^2 \end{aligned}$$

Assume stacking factor (k_s) = 0.9

$$\begin{aligned} \text{Net-cross sectional area of iron core, } &= \frac{141.606}{0.9} \\ &= 157.34 \text{ cm}^2 \end{aligned}$$

For cold rolled grained oriented silicon steel,

Flux density, $B_m = 1.4 \sim 1.5 \text{ Wb/m}^2$

Assume flux density, $B_m = 1.4 \text{ Wb/m}^2$

Turns per volt,

At $K = 0.8$,

$$E_t = 0.8 \sqrt{15} = 3.098$$

$$\text{Turns per volt, } N_e = \frac{10}{21.949} = 0.5 \text{ turns/volt}$$

Since the form of the toroidal type transformer is a circular ring, the circumference condition, the inner diameter, the outer diameter, height of the core and the width place take by the winding will be considered first.

Width of the ring face, $A = \sqrt{157.34} = 12.543 \text{ cm}$

The ratio of the B/A must have 1.5~2 times. In 15 kVA autotransformer design, if $A = 9 \text{ cm}$, the height of the core, B , must be 17.483 cm.

Assume inner diameter (d_i) = 12 cm

Inner radius (r_i) = 6 cm

Outer radius (r_o) = $r_i + A = 15 \text{ cm}$

So, outer diameter (d_o) = $2r_o = 30 \text{ cm}$

Section view of toroidal autotransformer is shown in Fig. 1.

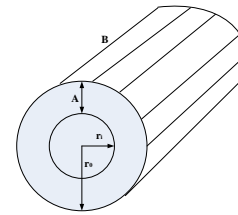


Figure 1. Section View of Toroidal Autotransformer

Winding Design of Toroidal Transformer

In winding design,

$S = 15 \text{ kVA}$

$V = 250 \text{ V}$

$f = 50 \text{ Hz}$

Assume Efficiency, $\eta = 0.9$ (90%)

Maximum current rating of the transformer,

$$I = \frac{15 \times 10^3}{250 \times 0.9} = 66.67 \text{ A}$$

So, S.W.G (6) will be chosen.

From standard wire gauge table,

Net cross-section area = 109.092 mm²

Diameter of bare conductor = 11.7856 mm

Length for a turn = 2 (A + B)

= 2 (9 + 17.483)

= 52.966 cm \approx 53 cm

Total length for a winding = mean length for a turn \times number of turns
 = 53 \times 125 = 6625 cm

From standard wire gauge table,

For S.W.G (6),

1000 ft – 111.6lbs

30480 cm – 111.6 lbs

6625 cm – ?

= 24.25 lbs \approx 25 lbs

Therefore, 25 lbs of the winding will be needed for the SWG (6) of the toroidal transformer. Wiring diagram of toroidal autotransformer is shown in Fig. 2.

Number of winding turns from P to N = 250 \times 0.5 = 125 turns

Number of winding turns from A to N = 220 \times 0.5 = 110

Number of winding turns from A to P = 15 turns

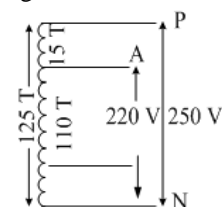


Figure 2. Wiring Diagram of Toroidal Autotransformer

$$\text{Current rating of each winding, } I_{\text{each}} = \frac{66.67}{125} = 0.533$$

$$\text{Current density, } \delta = 2.00 \text{ to } 2.5 \text{ A/mm}^2$$

$$\text{Assume, current density, } \delta = 2 \text{ A/mm}^2$$

Cross sectional area of each winding,

$$A = \frac{0.533}{2} = 0.2665 \text{ mm}^2$$

$$\pi r^2 = 0.2665$$

$$r = 0.287 \text{ mm}$$

$$\begin{aligned} \text{Diameter of each winding, } d &= 2 \times r \\ &= 0.574 \text{ mm} \end{aligned}$$

$$\begin{aligned} \text{Diameter of all winding, } d_1 &= 0.574 \times 125 \\ &= 71.75 \text{ mm} \end{aligned}$$

$$\text{Circumference of all winding} = \pi \times d_1 = 225 \text{ mm}$$

$$\text{Diameter of core, } d_2 = 9 \text{ cm} = 90 \text{ mm}$$

$$\text{Circumference of core} = \pi \times d_2 = 282.74 \text{ mm}$$

$$\begin{aligned} \text{Spacing of winding} &= 282.74 - 225 \\ &= 57.74 \text{ mm} \end{aligned}$$

$$\text{Spacing of each winding} = \frac{57.74}{125} = 0.462 \text{ mm}$$

$$\text{Spacing of each winding} = \frac{0.462}{\pi} = 0.15 \text{ mm}$$

The calculated values of toroidal autotransformer are shown in Table II.

TABLE II. DETAILED DESIGN SHEET FOR TOROIDAL AUTOTRANSFORMER

Description	Symbol	Unit	Designed values
kVA Rating	P (or) S	kVA	15
Cross sectional area	A_i	cm^2	141.606
Net cross sectional area	A_{gi}	cm^2	157.34
Turn per volt	N_e	T/V	0.5
Width of ring face of core	A	cm	9
Height of core	B	cm	17.483
Inner diameter	d_i	cm	12
Inner radius	r_i	cm	6
Outer diameter	d_o	cm	30
Outer radius	r_o	cm	15
Current	I	A	66.67
Number of turns	N	-	125
Conductor area	a	mm^2	109.092
Bare diameter	b	mm	11.7856
Length for a turn	-	cm/turn	53
Total length for a winding	-	cm	6625
Pounds of the winding	-	lbs	25
Current of each winding	I_{each}	A	0.533
Cross sectional area of each winding	A	mm^2	0.2665
Diameter of each winding	d	mm	0.574
Diameter of all winding	d_1	mm	71.75
Circumference of all winding	-	mm	225
Circumference of core	-	mm	282.74
Spacing of winding	-	mm	57.74
Spacing of each winding	-	mm	0.15

IV. ROTATIONAL TESTS

During the fluctuation of -40% , $+10\%$ servomotor automatic voltage stabilizer will give the following tables. In this region, this stabilizer will produce the stable output voltage 220 V. The variable autotransformer is arranged 0.5 turns per voltage and 180 circular is taken due to the limit switch position. Variable autotransformer with forward condition and reverse condition are shown in Fig. 3 and Fig. 4.

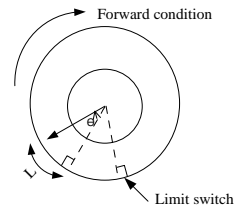


Figure 3. Variable Autotransformer with Forward Condition

When the supply voltage is lower than the output voltage, the variable autotransformer of brush will rotate the clockwise condition.

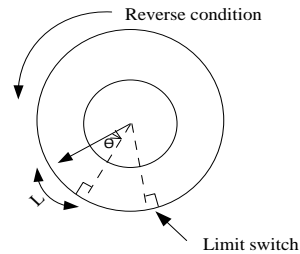


Figure 4. Variable Autotransformer with Reverse Condition

Where; Θ = rotational angle

L = linear displacement

When the supply voltage is higher than the output voltage, the variable autotransformer of brush will rotate the anticlockwise condition.

V. MODE OF OPERATION

During the fluctuation of -40% , $+10\%$ servomotor automatic voltage stabilizer will give the following result. The AVS will produce the stable output voltage 220 V. If the supply voltage is equal the output voltage of automatic voltage stabilizer, the servo motor does not run in this condition. Figure 5 shows the output result of servo motor when the input voltage is stable by using Proteus Software. In this figure, the input voltage of microcontroller is 4.34 V for phase R, Y and B.

During the under voltage condition, the input voltage of the stabilizer is lower than output voltage. In this condition, the motor drives in forward direction as to increase the stabilizer output voltage to the 220 V. Figure 6 shows the simulation result of under voltage condition. In this figure, the input voltage of microcontroller is

2.55 V for phase R, 3.73 V for phase Y and 2.96 V for phase B.

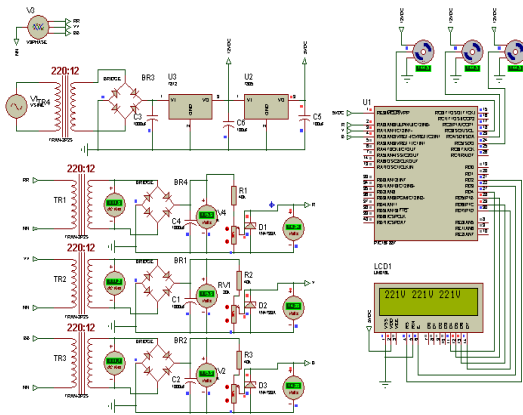


Figure 5. Simulation Result of AVS Controller in Stable Condition

During the over voltage condition, the input voltage of the stabilizer is higher than output voltage. In this condition, the motor drive in reverse direction as to decrease the stabilizer output voltage to the 220 V. Figure 7 shows over voltage condition of servo control system by using Proteus Software. In this figure, the input voltage of microcontroller is 4.52 V for phase R, 4.69 V for phase Y and 4.89 V for phase B.

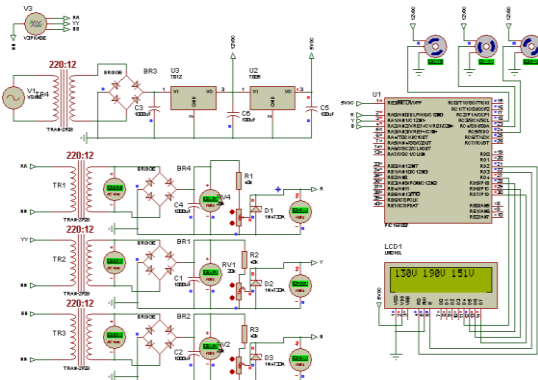


Figure 6. Simulation Result of AVS Controller in Under Voltage Condition

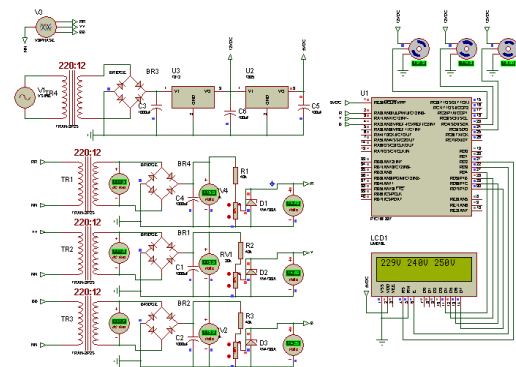


Figure 7. Simulation Result of AVS Controller in Over Voltage Condition

VI. TEST RESULTS OF STABILIZER OUTPUT AT DIFFERENT INPUT VOLTAGES

Table II shows the direction of servo motor depending on the variable input voltage to get nearly the stable output voltage 220 V.

TABLE II. FOR LOW VOLTAGE UP TO -40% AND HIGH VOLTAGE UP TO +10%, ANGLE DISPLACEMENT WITH RESPECT TO VOLTAGE FLUCTUATION

Input voltage	Different voltage	Number of turns	Clockwise direction	Output voltage
130	-90	45	164°	218.31
140	-80	40	148°	218.43
150	-70	35	133°	218.53
160	-60	30	127°	218.63
170	-50	25	111°	218.71
180	-40	20	94.5°	218.78
190	-30	15	85.8°	218.84
200	-20	10	68.4°	218.90
210	-10	5	53.3°	221.05
220	-	-	45.1°	221.00
230	+10	5	31.8°	221.05
240	+20	10	14.7°	221.09
250	+30	15	6.72°	221.14

In this research, when the voltage fluctuation is lower than 130 V and higher than 250 V, the servo control automatic voltage stabilizer is automatically shut down and does not operate in this situation. The servo motor automatic voltage stabilizer will nearly produce the stable output voltage 220 V.

CONCLUSIONS

Test outcome shows that the output voltage remains virtually constant at varying input voltage. However, at extremely low voltages below 130V there was no output voltage because the switching device is not even activated. On the other hand, at voltages beyond 250V the system protection is activated and no output voltage. Therefore the research has made it possible for the device to operate from as low as 130 V. The primary objective of this work which was to improve the performance of conventional AC voltage stabilizer was achieved. The work was designed in consideration with some factors such as economy, availability of components, efficiency, compatibility, portability and durability.

ACKNOWLEDGMENT

The author greatly expresses to his thanks to all persons whom will concern to support in preparing this research.

REFERENCES

- [1] BartloiejBelko, M. C.: The Conception and Implementation of Control System for Servo Motor with Application of Local Area Network, Cracow, (2010).
- [2] Metrel: Single-phase Built-in Variable Transformer, Three-phase Built-in Variable Transformer, Motor

- Driven Variable Transformer, Desk top Variable Transformer, (2009). <http://www.netrel.si>
- [3] Hans Beijher: Output Transformers and Magnetic Formulas, Prentice-Hall, Noord-Holland, Netherlands, (2004).
- [4] Matt Ruff: Servomotor Control Application, Freescal Semiconductor Inc., Japan, (2004).
- [5] Biswanath Paul: Industrial Electronics and Control, Prentice-Hall of Private Limited, India, (2001).
- [6] Chuck McManis: Servo Basic, Omron Asia Pacific Pte, Ltd., Korea, (2000).
- [7] Mark Readman: Motors, Seimens Company, London, (1997).
- [8] Bhopal: Design of Electrical Machines, Standard Publisher Distributors, 4th Ed., 1705-E, NalSarak, DELHI-110006, (1996).
- [9] Patchett, G.N.: Automatic Voltage Regulators and Stabilizers, Sir Isaac Pitman and Sons Ltd., 2nd Ed., Canada, (1954).

Comparison of Power Output from Solar Panel with Reflector and without Reflector

Thet Naung Win

Department of Electrical Power Engineering
Mandalay Technological University
Myanmar

Abstract- Energy consumption is one of the indices in determining the levels of development of a nation. Therefore, availability of energy supply to all sectors of life in any country is crucial for its development. There exists shortage of all kinds of energy, particularly electricity which is badly needed for economic development. Electricity from the sun which is quite abundant in most of the developing countries is used in rural areas to meet basic electricity needs of a rural community. Today's electricity supply in Myanmar is generated by fuel generators and hydroelectric power plants. However, far-flung areas which are away from National Grids cannot enjoy the electricity generated by these sources. Since Myanmar is a land of plentiful sunshine, especially in central and southern regions of the country, the first form of energy- solar energy could hopefully become the final solution to its energy supply problem. The direct conversion of solar energy into electricity using photovoltaic system has been receiving intensive installation not only in developed countries but also in developing countries. It is mainly intended to present solar energy potential and application in Myanmar. In this journal, have discussed the techniques to increase the light gathering ability of a solar panel in the morning and late afternoon by using multiple fixed directed mirrors as a reflector instead of ordinary costly tracking system. In this research have shown the comparison table and figure that depicts how much extra power the panel can add to the system by using mirror with a minimum cost.

Keywords - Photovoltaic (PV) system, Electricity supply national grids, Energy, Site condition; Annual radiation, PV Cell, Received Power, Reflector, Tilt Angle.

I. INTRODUCTION

The provision of electricity to rural areas derives important social and economic benefits to remove communities throughout the world. The potential for PV-powered rural applications is enormous.

The geographical location of Myanmar is between latitude $9^{\circ} 58' N$ and $28^{\circ} 29' N$ and longitude $92^{\circ} 10' E$ and $101^{\circ} 10' E$. Myanmar has a tropical monsoon climate. The cooler, dry season lasts from November to April and the hotter, wet season from May to September or October. Differences of altitude within the country, and the extent of exposure to the rainy southwest monsoon, are the main factors responsible for differences of climate within Myanmar. The weather is hottest from March-May, before the onset of the heaviest rains. Temperatures are cooler in the mountains, but the weather at places below 4000ft (1200m) is hot and tropical in most of the year. In coastal areas, conditions can be uncomfortable because of high humidity. Sunshine is plentiful during the dry season, averaging 7 to 10 hours a day. During the rainy season the weather is cloudier and daily sunshine amounts average only 3 to 4 hours a day. Total area or total square miles of Myanmar is 261228. The radiated heat energy from the sun on to the earth converted to horse power is 469×10^{11} . Therefore, total approximate horse power on total area of Myanmar is calculated to be 123×10^{10} , that is the sun's radiated heat power.

The following solar energy technologies can be successfully propagated: solar cookers; solar water

heating systems for industrial application; solar distillation units for battery charging; solar photovoltaic systems for water pumping, battery charging, and power supply to children's hospitals for operating vital equipment. Solar air driers can be used for agricultural and industrial products [1].

The objective of this paper is improving the solar energy by using mirror reflection. By using solar tracking the generation of solar energy is less compare to the mirror reflection. So, we can generate more solar energy by using mirror reflection. The improvement of the output power using plane mirror reflector is even higher than that of sun tracking and secondly these reflectors are very cheap and are easily available in market. The average power output during mid day as increased substantially using mirrors, the solar panels equipped with such mirrors can also be utilized for loads/equipments requiring higher power inputs during that period of the day.

II. SOLAR RADIATION DATA OF MYANMAR

The MEPE (Myanma Electric Power Enterprise) experimental measurements indicate that irradiation intensity of more than $5 \text{ kWh/m}^2/\text{day}$ was observed during the dry season. Since the reliability of these systems is paramount, the sizing method used is based on radiation data for the worst month of the year rather than on the average daily irradiation over the year. In addition to ensure system operation even over periods of lower solar radiation than predicted from the average yearly

values, the sizing often uses data for the worst year in ten [2].

In practical applications, solar cells do not operate under standard conditions. The two most important effects that must be allowed for are due to the variable temperature and irradiance. Temperature has an important effect on the power output from the cell. Irradiance is directly proportional to the short-circuit current of a solar cell [2].

Solar radiation data corresponding to the selected cities in Myanmar is shown in Figure 1.

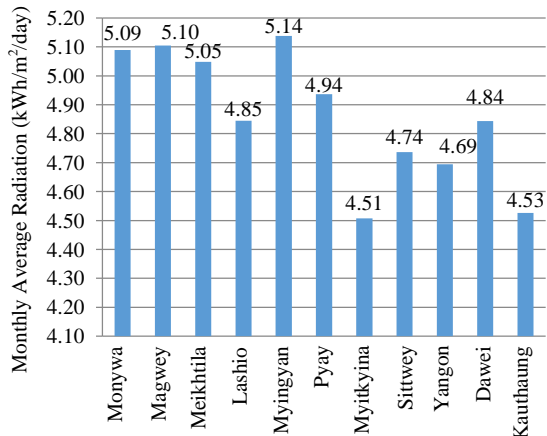


Figure 1. Monthly average radiation (kwh/m²/day) records of selected cities [NASA]

III. RESOURCES OF A SOLAR ENERGY IN SHINTAWKONE VILLAGE MYANMAR

Shintawkone village is saturated in Patheingyi township of Mandalay division. It is located between 21° and 22° north latitude and 96° and 97° east longitude. For area of an estimation of potential of solar power for regions where are absent Hydrometeorological service, world databases “NASA” can be used. Figure 2 shows monthly average incoming solar radiation on a horizontal surface.

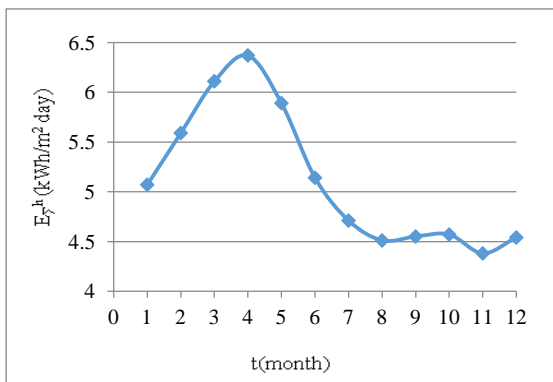


Figure 2. Monthly average incoming solar radiation on a horizontal surface

IV. CALCULATING TILT ANGLE OF A RECEIVING SURFACE ON ARRIVAL SOLAR RADIATION

The earth revolves around the sun in an elliptical orbit, making one revolution every 365.25 days. The related angles between the sun and the earth are as shown in Figure 3. Table I shows the day numbers for the first day of each month.

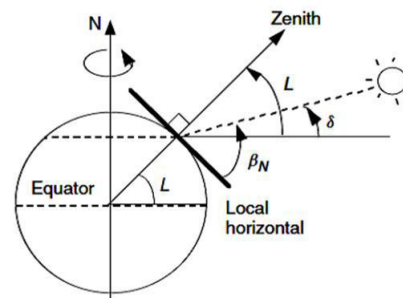


Figure 3. Related angles between the sun and the earth

TABLE I
THE DAY NUMBERS FOR THE FIRST DAY OF EACH MONTH

Months	Number (n)
January	1
February	32
March	60
April	91
May	121
June	152
July	182
August	213
September	244
October	274
November	305
December	335

A. Tilt Angle of a Receiving Surface on Arrival Solar Radiation

$$\text{Array tilt angle for selected location} = 90 - \beta_N \quad (1)$$

$$\beta_N = 90 - L + \delta \quad (2)$$

$$\delta = 23.45^\circ \sin \frac{360}{365} (n - 81) \quad (3)$$

where,

δ = the angle between the plane of the equator and a line drawn from the centre of the sun and centre of the earth (varies between extremes of $\pm 23.45^\circ$)

n = day number for the first day of each months (the spring equinox condition is 81 that is day number)

β_N = altitude angle of the sun at noon

L = latitude angle of the selected location [12]

B. Theory of Angle between PV and Reflectors

By mounting reflectors to sides of module, augmentation of radiation on surface of module was takes place. This modified system was able to produce more PV power. The sunlight hitting on the surface of the solar panel can be intensified by the use of parabolic shaped reflectors and flat panel reflectors. Since the manufacturing cost of curved reflectors are higher than that of flat panel reflectors. And since the solar intensifier only works at a certain spot in a certain direction the solar

panels and the reflectors are in need of a solar tracker system. Although implementing such a system to focus the sunlight on to a smaller area will cause a rise in the temperature and a separate cooling system will also be needed. The intensity of sunlight is very much higher with the reflection of sun light from the mirror than the ordinary sunlight intensity.

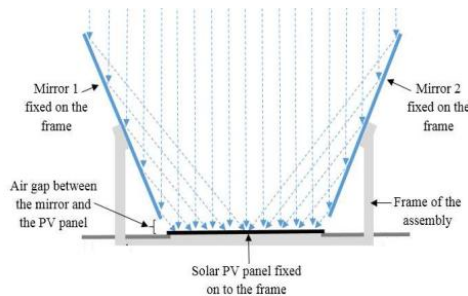


Figure 4. Design of PV panel with reflectors as mirror [6]

The amount of produced energy will also depend on the angle between the reflectors and the photovoltaic modules. The concept will utilize two mirrors which will be at fixed angles and they each would reflect additional sunlight on to a half of the solar PV panel. As illustrated in Figure 4 mirrors will be fixed on to the frame leaving a small gap between the solar panel and itself.

A. Angles between Solar PV and Reflectors

The first step of the design is to add the mirrors to focus additional sunlight on to the solar panel. In this design two mirrors will be used, each reflecting sunlight on to a half of the PV panel. The original area that the sunlight can be collected is only 104cm×66cm. Following are the diagram illustrates the utilization of the mirrors to maximize the solar panel output at a mirror angle of θ° . Following are the calculations carried out to find the angles between the PV panel and the mirror and the required length of the mirror, and to select the best angle, considering the cost of the mirror and additional effective width that the mirror creates. The sunlight hitting the additional effective area will be reflected on to a half of the PV panel. The panels are made out of polycrystalline solar cells which have an efficiency of 11-14% [3].

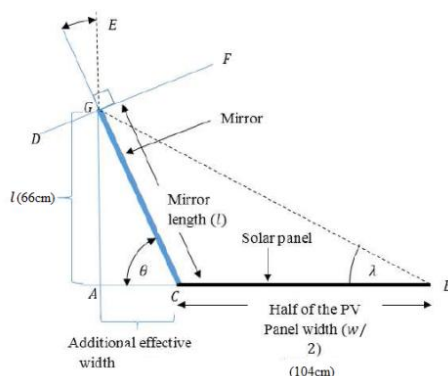


Figure 5. Illustration for the geometrical calculation [6]

For equation of angle between PV and reflectors:

From Figure 5,

$$\text{Since } \hat{A}CG = \theta, \hat{D}GC = 90^\circ, \hat{D}GA = \theta$$

$$\text{Since } \hat{D}GA \text{ and } \hat{E}GF \text{ are opposing angles}$$

$$\hat{E}GF = \theta$$

Since $\hat{E}GF$ and $\hat{F}GB$ are angles of the reflecting sunrays they also have to be equal

$$\text{Therefore } \hat{F}GB = \theta$$

$$\hat{F}GB + \hat{B}GC = 90^\circ$$

$$\hat{B}GC = 90^\circ - \theta \quad (4)$$

Considering the triangle of CGB;

$$\hat{B}GC + \hat{GCB} + \hat{CBG} = 180^\circ \quad (5)$$

$$\text{Since } \hat{B}GC = (90^\circ - \theta),$$

$$\text{And } \hat{GCB} = (180^\circ - \theta)$$

$$(90^\circ - \theta) + (180^\circ - \theta) + \hat{CBG} = 180^\circ$$

$$\hat{CBG} = \lambda = 2\theta - 90^\circ \quad (6)$$

V. CALCULATION RESULTS

For the research calculated the optimum tilt angle of PV solar panel by using Equation 1 to Equation 3 and angles between solar PV and reflectors by using Equation 4 to Equation 5.

A. For Filt Angle of PV Solar Panel

The optimum tilt angle is a south-facing PV module in Patheingyi Township, Mandalay Division (Latitude 22 degree) at solar noon on March 1. March 1 is the sixtieth day of the year so the solar declination is:

According to Equation: (3)

$$\delta = 23.45^\circ \sin \frac{360}{365} (60 - 81) = -8.29^\circ$$

According to Equation: (2)

$$\beta_n = 90^\circ - 22^\circ + (-8.29^\circ) = 59.9^\circ$$

According to Equation: (1),

$$\begin{aligned} \text{Array tilt angle for selected location} &= 90 - \beta_n \\ &= 30.3^\circ \end{aligned}$$

Therefore, we placed solar panel towards south at a tilt angle of around 30° ($\approx 30.3^\circ$) for selected location.

B. For Angles between Solar PV and Reflectors

From Figure 5,

And using the law of sines for the same triangle,

$$\frac{\text{mirror length}(l)}{\sin(2\theta - 90^\circ)} = \frac{\text{half of the PV panel width}(\frac{w}{2})}{\sin(90^\circ - \theta)}$$

$$\text{mirror length}(l) = \frac{-w \cos(2\theta)}{2 \cos \theta}$$

$$\frac{-\cos 2\theta}{2 \cos \theta} = \frac{1}{w}$$

$$\frac{-2\cos^2\theta + 1}{2\cos\theta} = \frac{104}{66} = 1.576$$

$$-2\cos^2\theta - 3.152\cos\theta + 1 = 0$$

$$\cos\theta = 0.2707 \text{ or } -1.847$$

$$\theta = 74.29^\circ$$

According to Equation: (5),

$$B\hat{G}C + GCB + CBG = 180^\circ$$

From (4) and (5),

$$90^\circ - \theta + GCB + 2\theta - 90^\circ = 180^\circ$$

$$GCB + \theta = 180^\circ$$

$$GCB = 180^\circ - \theta$$

$$= 180^\circ - 74.29^\circ = 105.71^\circ$$

Therefore GCB (105.71°) is the angle between reflectors and solar panel. For the experiment used a solar panel, which has the following features in Table II.

TABLE II
SPECIFICATIONS OF POLY-CRYSTALLINE SOLAR PANEL

Module Type		SYM 90P
Cell Material		Poly Crystalline
Maximum Power	P _{max}	90 W
Maximum Power Voltage	V _{pmax}	18.37 V
Maximum Power Current	I _{pmax}	4.9 A
Open Circuit Voltage	V _{oc}	22.05 V
Short Circuit Current	I _{sc}	5.15 A

VI. MATHEMATICAL MODEL OF PV SOLAR PANEL USING MIRROR AS REFLECTOR AND WITHOUT USING REFLECTOR

Solar panel towards north-south at a tilt angle of around 30° (≈ 30.3°) and taken data by using multi-meter for a 2th in July 2018 in the same weather and temperature. We used both mirror as reflector and without using reflector to concentrate sunlight onto the panel from the morning to the late afternoon. Using multimeter took both open circuit voltage and short circuit current and then calculates the power received by the panel.

$$\text{Power (W)} = \text{Open Circuit Voltage} \times \text{Short Circuit Current} \quad (7)$$

These values from 7.00 AM to 5.00 PM. Panels are observed that in the early morning and late afternoon the panel gives minimum power both by using reflector and without reflector as shown in Figure 6 and Figure 7. Table III shows the variation of current, voltage and power of a photovoltaic solar panel using mirror as reflector and without using reflector.



Figure 6. A solar PV panel without using reflector



Figure 7. A solar PV panel using mirror as reflectors

TABLE III
RECEIVED DATA OF A PV SOLAR PANEL USING MIRROR AS REFLECTOR AND WITHOUT USING REFLECTOR

Time	Open circuit voltage(V)		Short circuit current (A)		No load output Power (W)	
	No Mirror	Using Mirror	No Mirror	Using Mirror	No Mirror	Using Mirror
7:00 AM	1.65	1.02	1.81	1.85	1.68	3.55
7:30 AM	5.63	1.06	15.59	1.87	5.97	29.15
8:00 AM	13.38	1.78	17.16	2.06	23.82	35.35
8:30 AM	16.53	1.96	13.32	3.59	32.40	47.82
9:00 AM	16.67	2.12	13.65	3.35	35.34	45.73
9:30 AM	10.98	3.22	14.05	3.67	35.36	51.56
10:00 AM	13.46	3.46	14.41	3.71	46.57	53.46
10:30 AM	13.66	3.59	14.36	3.75	49.04	53.85
11:00 AM	14.12	3.65	14.33	3.78	51.54	54.17
11:30 AM	14.15	3.65	14.21	3.68	51.65	52.29
12:00 AM	14.21	3.68	14.75	3.72	52.29	54.87
12:30 PM	14.08	3.70	14.09	3.59	51.91	51.99
1:00 PM	13.32	3.58	14.16	3.68	47.69	52.11
1:30 PM	12.51	3.42	14.06	3.6	42.78	50.62
2:00 PM	12.78	3.19	14.26	3.64	40.77	51.91
2:30 PM	16.6	1.98	12.13	3.24	32.87	39.30
3:00 PM	16.22	1.96	12.7	3.46	31.79	43.94
3:30 PM	11.76	1.64	11.59	3.26	19.29	37.78
4:00 PM	8.87	1.32	11.6	3.29	11.71	38.16
4:30 PM	5.62	1	16.38	2.01	5.62	32.92
5:00 PM	2.14	0.66	12.74	1.82	1.41	23.19
Total					651.56	895.97

VII. COMPARISON OF PV SOLAR PANEL USING MIRROR AS REFLECTOR AND WITHOUT USING REFLECTOR RESULTS

The solar panel received maximum 52.29 W and minimum 1.68 W using without reflectors and maximum 54.87 W and minimum 3.55 W using reflectors.

Comparison efficiency of PV solar panel using mirror as reflector and without reflector are

$$\eta = \frac{\sum p_2 - \sum p_1}{\sum p_1} \times 100\% \quad (8)$$

$$\eta = \frac{895.97 - 651.56}{651.56} \times 100\%$$

$$\eta = 37.51\%$$

In this research that solar panel using mirror as reflector gives some extra power in the early morning and it is gradually increased at around 8.30 am. At that time panel received additional using mirror as a reflector. If we consider 10 hours' period from 7.00 AM to 5.00 PM, the panel without using reflector receives average power of 52.29 W which is 72.11% of the panel power. Whereas using reflector (mirror) the panel receives average power of 54.87 W which is 64.02% of the panel power. Therefore, the panel receives extra 37.51% power using mirror as a reflector. In Figure 8, the panel receives 72.11% without using reflector and 64.02% using reflector (mirror) of the panel capacity.

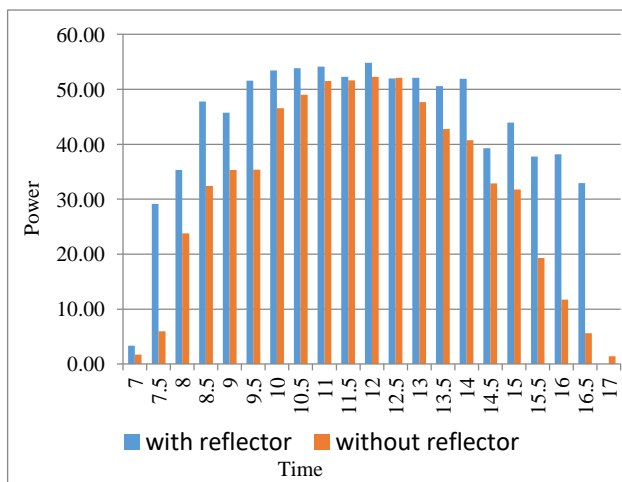


Figure 8. Receive power comparison using reflector (mirror) and without using reflector

CONCLUSIONS

From the research of the received power comparison using reflector and without using reflector; we can conclude that reflector plays a vital role in a solar power system. Photovoltaic solar panel using reflectors increases received power efficiency all day long specially in the morning and late afternoon. Using this technique the rural people can efficiently use their solar panel all the year.

ACKNOWLEDGMENT

The author greatly expresses to his thanks to all persons whom will concern to support in preparing this paper.

REFERENCES

- [1] [1] S.K. Sharma, "Alternate Energy Utilization in Myanmar," A Unicef
- [2] Myanmar Publication, March, 1992, University of Southampton, UK.
- [3] Himangshu Bhowmik and Ruhul Amin, Efficiency Improvement of Flat Plate Solar Collector Using Reflector, Dhaka University of Engineering & Technology, Department of Mechanical Engineering, Gazipur, Bangladesh, 2017.
- [4] GDM pathmika and MV Gamage, Efficiency Improvement of a Typical Solar Panel with the Use of Reflectors, Department of Mechanical Engineering, Faculty of Engineering, University of Sunderland, UK mihiran.g@slit.edu.lk, 2016.
- [5] Ionel L. Alboteanu, Cornelia A. Bulucea and Sonia Degeratu, Estimating Solar Irradiation Absorbed by Photovoltaic Panels with Low Concentration Located in Craiova, Romania, Department of Electromechanics, Environment and Industrial Informatics, Faculty of Electrical Engineering, University of Craiova 200440, Romania, 2015.
- [6] S Ahmed, More Efficient use of Photovoltaic Solar Panel Using Multiple Fixed Directed Mirrors or Aluminium Foils Instead of Solar Trackers in Rural Perspective of Bangladesh, International Journal of Scientific and Technology Research, 2014, 3(4).
- [7] V.N. Palasker and S.P. Deshmukh, Design and Performance Analysis of Reflectors Attached to Commercial PV Module, Veermata Jijabai Technological Institute Matunga Mumbai, India, 2014.
- [8] Potuganti Prudhvi and Ponnappalli Chaitanya Sai, Efficiency Improvement of Solar PV Panels Using Active Cooling, Dept of EEE and Department of Mechanical engineering at NIT Warangal, 2012.
- [9] G. C. Jain, Development and manufacture of photovoltaic system in developing countries, National physics laboratory, New Delhi, 1981.
- [10] J. Rizk, and Y. Chaiko, —Solar Tracking System: More Efficient Use of Solar Panels, World Academy of Science, Engineering and Technology 41 (2008)
- [11] Faisal Ahammed, Dilder Ahmed Taufiq, —Applications of Solar PV On Rural Development in Bangladesh, Journal of Rural Community Development 3 (2008) 93–103

- [12] Shakir-ul-haque Khan, Towfiq-ur-Rahman, and Shahadat Hossain, —A Brief Study of the Prospect of Solar Energy in Generation of Electricity in Bangladesh, Journal of Selected Areas in Renewable and Sustainable Energy (JRSE), June Edition, 2012

Design of Robot Arm imitating Human Arm system using PID Controller

Pan Myat Phyu
Department of Electronic
Engineering
Technological University
Thanlyin, Myanmar

Dr. Yin Yin Soe
Department of Electronic
Engineering
Technological University
Thanlyin, Myanmar

Daw May Thu Aung
Department of Electronic
Engineering
Technological University
Thanlyin, Myanmar

Abstract: The purpose system is to connect humans and robots in order to reproduce operator action at a distance. An inexpensive, a lightweight and easily controlled robotic arm with human interface is developed. The developed robotic arm is fully functional and accurately reacts to the movements from the human arm. The purpose system consist of a ‘master’, a human arm, and a ‘slave’, robot arm, located at a remote site. The human arm is given position force and the slave receives a position reference from the human. The human user wears 2 sensors on his/her arm. These sensors relay position information to the robotic arm. This can be achieved with the help of simple Gyro sensor at the joints of the user arm. The Position-force is designed and implemented using a PID controller. PID controllers are most popular and most often used controllers in industry. Popularity of the PID controllers are due to their wide range of operating conditions and functional simplicity. Different types of tuning rules have proposed which can fine tune the system to get desired response. In this, manual tuning method of PID controller is used to control of position of DC motor using Arduino microcontroller. Overall aim is to make the microcontroller understand human body language, thereby bridging the gap between machine and human. This thesis presents a PID controller method by using MATLAB R2017a simulation and experiment result to accurate robot action is similar to human arm action. According to the result, the robot action is similar human arm action to 98%.

Keywords: gyro sensor; Arduino; PID controller; master; slave.

1. INTRODUCTION

As technology becomes more advanced, machines become more complex and intelligent. Now a days , robots are able to carry heavy objects and operate with a precision which is below the range of human hand . Other applications again require the operation in human-unfriendly or hazardous environments. Thus, at present, typical application fields for robots can be found in areas where human physical abilities are exceeded or the usage in human-inaccessible or unfriendly environments is necessary.

In technical terms a system consists of a human arm is embedded Gyro sensor and a slave robot arm and a communication channel which controls the transfer position information . The angle can be read easily with the help of a sensors embedded human arm and this angle is transmitted to the robot arm [1].

This technique is very useful since it takes real time of human arm and tracks it to get interface with robotic arm. Tracking of such hand will interface the controller with robotic arm. The main aim behind this approach to program a robotic arm, so that it should be controlled by human hand and will reach the locations where human will not be able to reach and do the given task by direct interfacing with human arm. In this we can see the real time movement of robotic arm [2].The hardware setup consists of two Pololu-75:1 Metal Gearmotor 37D×52L mm with 48 CPR Encoder ,two Gyro sensors and Arduino Mega board .Gyro sensors is embedded in human arm and sensors are read human arm position and then control the robot arm to same human arm action using PID controller.

The implementation of a proportional integral derivative (PID) controller was used in this system. They controlled the

position of the DC motors with pulse width modulation using Arduino Mega Board. This system is shown in Figure 1.

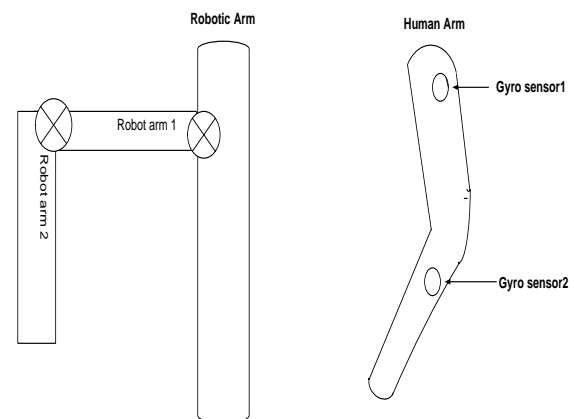


Figure 1. The Diagram of the Purpose System

2. RELATED WORK

2.1 Arduino Mega Board

The microcontroller board used in the robotic arm system is Arduino Mega, which is shown in Figure 2. The board is sufficient for our design, and there are enough input and output pins for the project.



Figure 2. Arduino Mega Board

2.2 Gyro Sensor

This IMU 10DOF is a motion tracking module. Its design is based on the sensor MPU6050, HMC5883L and BMP085. The sensor MPU6050 which is the world's first integrated 6-axis Motion Tracking device, that combines a 3-axis gyroscope, 3-axis accelerometer, and a Digital Motion Processor™ (DMP). The Honeywell's HMC5883L which is a 3-axis digital compass. The BMP085 is a high-accuracy chip to detect barometric pressure and temperature.



Figure 3. Gyro Sensor

2.3 POLOLU – 75:1 Metal Gearmotor

POLOLU -75:1 Metal Gearmotor is a powerful brushed DC motor with metal gearbox intended for operation at 12 V. These units have a 16mm-long, 6mm-diameter D-shaped output shaft. This gearmotor is also available with integrated encoder.

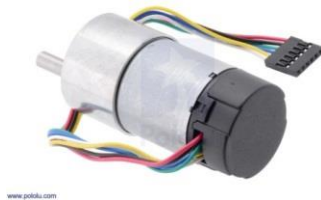


Figure 4. Pololu Gear motor

2.4 Pin Connection of Purpose System

The circuit diagram of the system is shown in Figure 5.

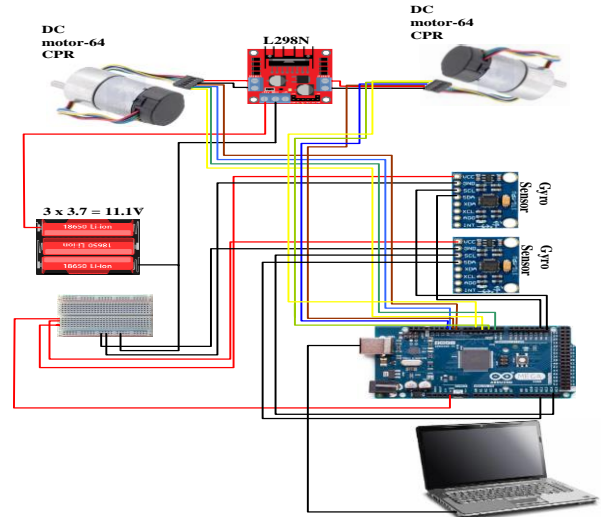


Figure 5. Connection of circuit diagram

3. TEST AND RESULTS

The Controller in any system plays very significant role and helps in taking remedial control action. The essential function of controller is to maintain the output at that level so that there is no difference between the measured output and set point value. PID controllers are the predominant type of controllers which are used in almost every process industry [3]. PID controller is widely used in industries due to its simplicity and easy to implement. A PID controller calculates an “error” and tries to minimize it by adjusting the control inputs. It improves the transient response of the system by reducing overshoot and by shortening the settling time and also has the ability to eliminate steady state offset through integral action. The transfer function for the PID controller can be written as,

$$u(t) = MV(t) = K_p e(t) + K_i \int e(t) dt + K_d \frac{de(t)}{dt} \quad (1)$$

Equivalently, the transfer function in the Laplace domain of the PID Controller

$$L(s) = K_p + K_i / s + K_d s \quad (2)$$

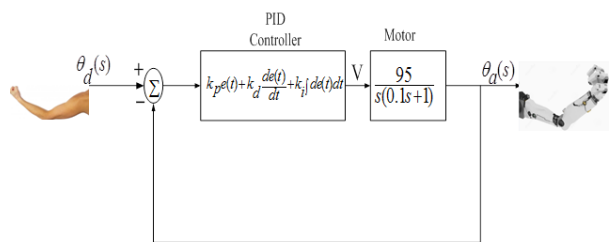


Figure 6. Diagram of PID Controller with motor

The Manual tuning method is used in the system. Because Manual tuning method can be relatively time consuming, particularly for system with long loop time. The various tuning steps of control gain is shown in Table 1. The system have been decided the gain result of $K_p = 0.3$, $K_i = 0.01$ and $K_d = 0.02$. Because the motor's actual angle is acceptably reached to its desired angle after a load disturbance.

Results, Steady State Error $= e_{ss} = 0$, Rise Time $= t_r = 0.3$ (no significant change), Setting Time $= t_s = 0.5$ (no significant change) and slightly overshoot remained.

Table 1. The Tuning Step of PID controller gains using Manual tuning Method

Tuning Step	K_p	K_i	K_d
1 st	0.1	0	0
2 nd	0.2	0	0
3 rd	0.3	0	0
4 th	0.3	0.01	0
5 th	0.3	0.01	0.01
6 th	0.3	0.01	0.02

The simulation result of PID controller using set point 90 is shown in Figure 7 and the simulation result of the system is shown in Figure 8 and the experiment test for motor position is shown in Figure 9.

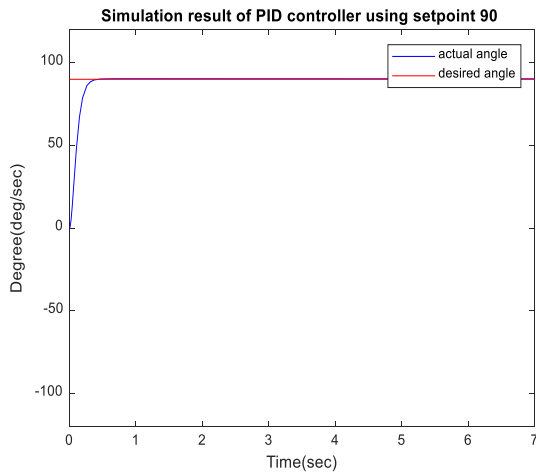


Figure 7. The Simulation result of PID Controller using set point 90

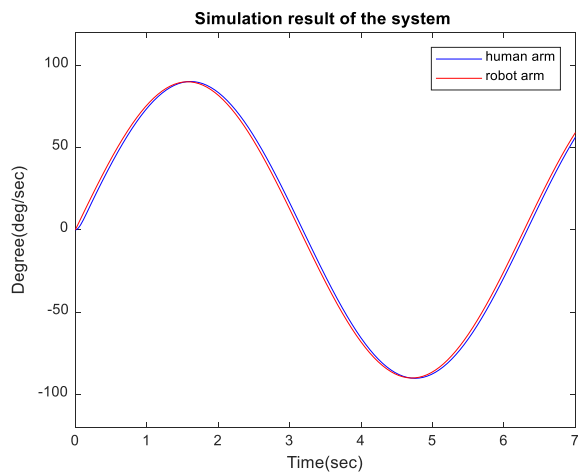


Figure 8. The Simulation result of Robot Arm Imitate Human Arm

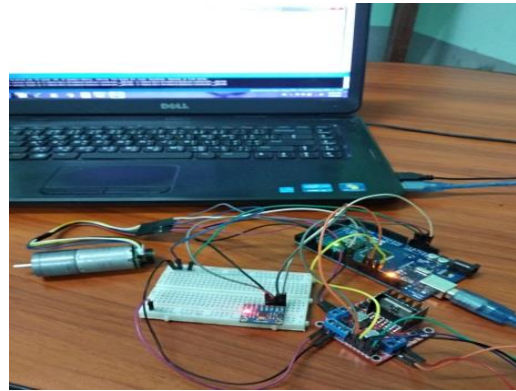


Figure 9. Experiment test for motor position .

The implementation of robot arm is shown in Figure 10 and the experiment test of robotic arm imitating human arm system is shown in figure 11 and the experiment result of overall system is shown in Figure 12.



Figure 10. The implementation of robot arm



Figure 11. The experiment test of overall system

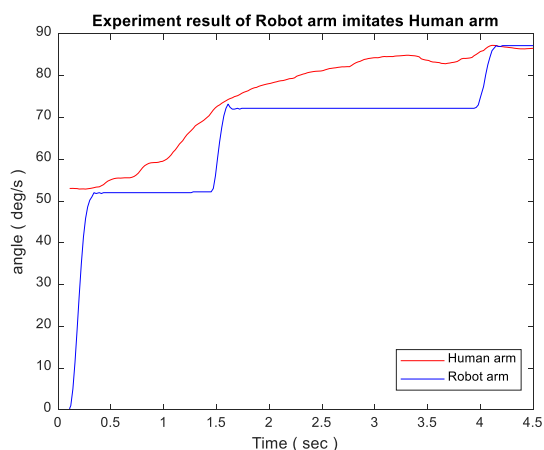


Figure 12 . The Experiment result of robot arm imitate human Arm

4. FUTURE WORK

In order to develop the efficiency of the robotic arm, the wireless sensors can be employed to enhance interface between the human arm and robotic arm [4]. Different sensors such as electromyography (EMG), accelerometer, and air-pressure sensors [5]–[6] can be incorporated; and corresponding algorithms can be investigated. In order to improve the response accuracy, the machine learning algorithms such as the artificial neural network (ANN) classifier and fuzzy logic classifier can be applied.

5. CONCLUSION

The system are going to develop is a device which is efficient ,light weight, comprising less machinery, and has applications in various domestic and industrial purposes. According to the result, the robot action is similar as 98% accuracy to human arm action. From observation that has been made, it clearly shows that its movement is precise, accurate, and is easy to control and user friendly to use. This robotic arm control method is expected to overcome the problem such as placing or picking object that away from the user, pick and place hazardous object in a very fast and easy manner.

6. ACKNOWLEDGEMENTS

Firstly, the author would like to acknowledge Dr. Thein Gi, Rector of Technological University (Thanlyin), for her kind permission to carry out this research work. The authors would like to thank many colleagues from digital image processing research group of Department of Electronic Engineering of Technological University (Thanlyin). The author particularly wishes to acknowledge all the teachers from Department of Electronic Engineering, Technological University (Thanlyin), for their support, encouragement and invaluable guidance in preparation of this research. The authors would like to express their thanks to all persons who have given support during the preparation period of this research work.

7. REFERENCES

[1] Rajesh Kannan Megalingam, Sricharan Boddupalli, K G S Apuroop K . 2017. “ Robotic Arm Control through Mimicking of Miniature Robotic arm”, 2017 International Conference on Advanced Computing and Communication Systems (ICACCS -2017).

[2] PANKAJ S LENGARE, MILIND E RANE” HUMAN HAND TRACKING USING MATLAB TO CONTROL ARDUINO BASED ROBOTIC ARM”, 2015 INTERNATIONAL CONFERENCE ON PERVASIVE COMPUTING (ICPC).

[3] N.S. Rathore, D.P.S. Chauhan, V.P. Singh. 2015. “ Tuning of PID Controller for Position Control of DC Servo Motor using Luus-Jaakola Optimization”, IEEE International Conference on Computer, Communication and Control (IC4- 2015).

[4] R. Sekhar, R. Musalay, Y. Krishnamurthy, B. Shreenivas. 2012. “Inertial sensor based wireless control of a robotic arm,” IEEE International Conference on Emerging Signal Processing Applications, pp. 87-90, Las Vegas, NV.

[5] M. Georgi, C. Amma, T. Schultz. 2015. “Recognizing hand and finger gestures with IMU based motion and EMG based muscle activity sensing,” Proceedings of the International Conference on Bioinspired Systems and Signal Processing, pp. 99- 108, Lisbon, Portugal.

[6] P. Jung, G. Lim, S. Kim, K. Kong. 2015. “A wearable gesture recognition device for detecting muscular activities based on air-pressure sensors,” IEEE Transactions on Industrial Informatics, 11(2), pp. 485-494.

Results Analysis of Real-Time Edge Detection Techniques using LabView

Htoo Le' Win
Department of Electronic
Engineering
Technological University
Thanlyin, Myanmar

Dr. Yin Yin Soe
Department of Electronic
Engineering
Technological University
Thanlyin, Myanmar

Daw Yi Yi Lwin
Department of Electronic
Engineering
Technological University
Thanlyin, Myanmar

Abstract: Edge detection is the process of finding information of meaningful transition in an image. The purpose of edge detection is to identify basic properties of image like area and shape. The edge detection operators such as canny, sobel, prewitt operators detects the wide range of edges in image. Edge detection is needed to discover the information about the edge and hiding the background data of the video such as the discontinuities in surface orientation and in depth, changes in material properties and variations in scene illuminations. Edge detection is an important basis and significance tasks of image analysis such as boundary detection, image segmentation, motion detection/estimation, texture analysis, object identification, object recognition and stereo matching. Structural Similarity Index (SSIM) is used as a standard among image quality metrics. In this research work, presents the implementation of edge detection of real time video using various edge detection operators (Sobel, Prewitt, Robert, Canny and Mathematical Morphology) with LabView Software, and compares the results with various parameters. The comparisons of experimental results demonstrate the effectiveness of the purposed method.

Keywords: SSIM; edge detection; edge detection operators; Mathematical Morphology; LabView

1. INTRODUCTION

Edge detection features will include as the important role of object segmentation in machine vision and image processing. Edges are important hints to split region within an object or to identify changes in illumination or color. Edge detection is an initial step in image enhancement procedures to identify the edge of the object, the sudden change in gray level intensity values of neighbor pixel will be an edge, therefore when there is highest difference between two neighbor pixels then there will be an edge is detected. Image edges correspond to points in an image where the gray value changes significantly. In gray scale image each pixel is represented by 8 bit, hence gray level values vary from 0 to 255, where 0 value stands for black color and 255 value stands for white color [1]. The main purpose of edge detector is to detect both strong as well as weak edges in order to do so various methods. In this research work various edge detector techniques has studied for detecting the edge of objects with SSIM values. SSIM is one of the parameter to evaluate the performance of edge detection method in real time application. Structural Similarity Index is used to assess the similarity between the reference video frame and the test (processed) video frame.

2. EDGE DETECTION OPERATORS

2.1 Mathematical Morphology

Imperfections may be present in binary images. In particular, the noise and texture will cause distortion to the binary images to the regions produced by simple thresholding. Morphology is nothing but the study of the structure of an object. Morphological filters will simplify the segmented image by smoothing out the outlines of an object using filling small holes and eliminating small projections. Mathematical morphology is a new mathematical technique which is used to process and analyze the images.

One of the applications of Mathematical Morphology is to filter the images; it is a well-known nonlinear filter for image enhancement. It will not use mathematical modeling instead it

used set theory to analyze the images. Mathematical Morphology will be well suited for processing binary images because the method will rely on only on the relative ordering of the pixel values not on their numerical values [2]. Morphological operations are generally neighborhood based. The new value for the pixel under inspection (PUI) is determined from the values of its neighboring pixels as shown in Fig. 1. The two main types of binary morphological operations are as follow.

- Erosion: Shrinking the foreground.
- Dilation: Expanding the foreground.

NW	N	NE
W	x	E
SW	S	SE

Figure 1. Pixel Under Inspection (PUI) with Neighboring Pixels

Erosion wears away the edges of image features, decreasing its size, and potentially opening up holes in the object. Dilation refers to the spatial expansion of an object with the potential of increasing its size, filling holes and connecting neighboring objects. Consider the image with the Fig. 1. Simple erosion occurs when the following is applied: if the PUI is 0, then it retains its value; if it is 1 and all of its cardinal neighbors are also 1, then set the new pixel value to 1 (otherwise set it to 0). This is shown in Equation (1).

$$x_{new} = \begin{cases} 0 & x_{old} \text{ otherwise} \\ 1 & x_{old} = 1 \text{ and } \wedge (N, E, S, W) = 1 \end{cases} \quad (1)$$

An erosion example is shown in Fig. 2.

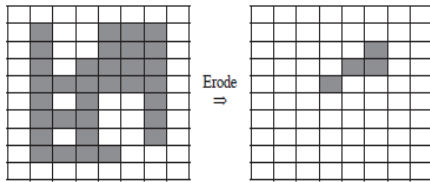


Figure 2. Example of Erosion

Simple dilation occurs when the following procedure is applied: if the PUI is 1, then it retains its value; if it is 0, it becomes the logical OR of its cardinal (North, South, East and West) neighbors. This is also present in Equation (2).

$$x_{new} = \begin{cases} 0 & x_{old} = 1, \exists (N, E, S, W) = 1 \\ 1 & x_{old} \text{ otherwise} \end{cases} \quad (2)$$

An example is shown in Fig. 3. Note that any PUIs with an original value of 1 are retained, small holes are filled and boundaries are retained [3].

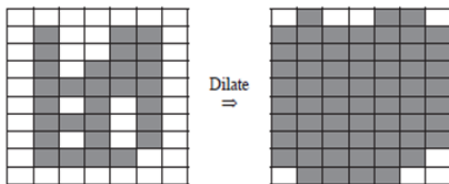


Figure 3. Example of Dilation

2.2 Traditional Operators

Some traditional operators are as follow.

- First order derivative/ gradient methods:
 - Sobel
 - Prewitt
 - Robert
- Second order derivative:
 - Laplacian
 - Laplacian of Gaussian
 - Difference of Gaussian
- Optimal edge detection:
 - Canny edge detection

Edge is a basic feature of an image. Edges define the boundaries between regions in an image and basic step for segmentation and object recognition. An image defined as two dimensional function $f(x, y)$, where x and y are spatial coordinates and amplitude of f at any pair of coordinates (x, y) defines the light intensity at that point. Edge detection is a process of identifying edges, the sharp change in image pixel intensity. In real world image edges are blurred and have ramp profile, in such cases position of edges are thicker because of blurring effect. Derivative of ramp function is step function, first order derivative is zero at constant gray level and non-zero value along entire ramp region hence magnitude of first order derivative can be used to detect an edge [1].

A gradient based edge detector method includes Roberts, Prewitt and Sobel operator. First order derivative in image processing are implemented using magnitude of gradient. For a function $f(x, y)$ the gradient of f at coordinates (x, y) is defined as two dimensional column vectors in Equation (3).

$$\nabla f = grad(f) = \begin{bmatrix} g_x \\ g_y \end{bmatrix} = \begin{bmatrix} \frac{\partial f}{\partial x} \\ \frac{\partial f}{\partial y} \end{bmatrix} \quad (3)$$

This vector points the direction of great rate of change of f at location (x, y) value at (x, y) is given by Equation 4.

$$mag(\nabla f) = \sqrt{g_x^2 + g_y^2} \quad (4)$$

It is more suitable computationally to approximate the square and square root operation by absolute values [1]. In digital image processing filter masks or operators used to approximate the derivative. Filter masks are convolved with entire image to obtain the edge detected image [4]. 3×3 filter mask is as shown in Fig. 4.

Z_1	Z_2	Z_3
Z_4	Z_5	Z_6
Z_7	Z_8	Z_9

Figure 4. 3×3 region of an image

The Robert edge detection is introduced by Lawrence Roberts in 1965. It performs a simple, quick to compute, 2-D spatial gradient measurement on an image. The operator consists of a pair of 2×2 convolution kernels as shown in Fig. 5 and Fig. 6. One kernel is simply the other rotated by 90° . This is very similar to the Sobel operator. Horizontal and vertical masks are used to convolve with the entire image to give edge detected image in x and y direction respectively.

Z_1	Z_2
Z_3	Z_3

Figure 5. 2×2 region of an image

+1	0	0	+1
0	-1	-1	0
G_x		G_y	

Figure 6. Robert masks

Robert masks of size 2×2 matrix are obtained by following equations:

$$G_x = (Z_1 - Z_4) \quad (5)$$

$$G_y = (Z_2 - Z_3) \quad (6)$$

-1	-2	-1	-1	0	+1
0	0	0	-2	0	+2
+1	+2	+1	-1	0	+1

$$G_x \qquad G_y$$

Figure 7. Sobel Operator

Horizontal derivative approximate as Equation 7 and vertical derivative approximate as Equation 8.

$$G_x = (Z_7 + 2Z_8 + Z_9) - (Z_1 + 2Z_2 + Z_3) \quad (7)$$

$$G_y = (Z_3 + 2Z_6 + Z_9) - (Z_1 + 2Z_4 + Z_7) \quad (8)$$

The Sobel edge detection method is introduced by Sobel in 1970. The Sobel method of edge detection for image segmentation finds edges using the Sobel approximation to the derivative. It precedes the edges at those points where the gradient is highest. In conjecture at least the operator consists of a pair of 3x3 complication kernels as given away in under table. One kernel is simply the other rotated by 90 degree. This operator is shown in Fig. 7.

The Prewitt edge detection is proposed by Prewitt in 1970. Prewitt mask is a discrete differentiation operator. This gradient based edge detector is estimated in the 3x3 neighborhood for eight directions. All the eight convolution masks are calculated. One complication mask is then selected, namely with the purpose of the largest module. Prewitt detection is slightly simpler to implement computationally than the Sobel detection and is used for detecting vertical and horizontal edges in images, but it tends to produce somewhat noisier results [5]. Prewitt operator is shown in Fig. 8.

-1	-1	-1
0	0	0
+1	+1	+1

$$G_x$$

-1	0	+1
-1	0	+1
-1	0	+1

$$G_y$$

Figure 8. Prewitt Operator

Horizontal derivative approximate as Equation 9 and vertical derivative approximate as Equation 10.

$$G_x = (Z_7 + Z_8 + Z_9) - (Z_1 + Z_2 + Z_3) \quad (9)$$

$$G_y = (Z_3 + Z_6 + Z_9) - (Z_1 + Z_4 + Z_7) \quad (10)$$

Canny edge detection method was developed in 1986 by John Canny. The Canny edge detector is an edge detection operator that uses a multi-stage algorithm to detect a wide range of edges in images. The algorithm consists of 4 main stages. The first step involves removing noise with the use of a Gaussian filter. As a result, the obtained image is slightly blurred, without any noises. The next stage features finding the intensity of the image gradient. Considering the fact that edges can be directed in different directions, the algorithm uses four filters to detect the horizontal, vertical, and diagonal edges. Edge operators (e.g. Sobel operator) shall calculate the value of the first derivative of the horizontal and vertical directions. The angle of the edge detection is rounded to four cases representing the horizontal, the vertical and two diagonals (e.g. 0, 45, 90, 135°). The obtained contours are characterized by a certain width and it is not the width of one pixel. The third step consists in the elimination of non-maximal values of pixel intensity. Pixels constituting the orthogonal cross-section of the contour are analyzed, and those lacking maximum intensity values are turned off. The last step includes thresholding aimed at removing unnecessary

edges with inclinations below the set threshold. Canny's algorithm can be used in many different environments. Its parameters can be modified so as to enable the algorithm to recognize edges of various features [6].

3. LABVIEW PROGRAMMING

LabView is a graphical programming language. Programmers work with two views: front-panel view and a schematic diagram view. Since the front panel view is a necessary part of the integrated Development Environment (IDE), developing human machine Interfaces (HMI) is practically automatic. In fact, it actually is automatic, but the automatically generated HMIs are badly organized. Much of the programming effort goes into “prettying up” the HMI to make it communicate better to humans. Advantages of LabView are as follow.

- Reduced time to discovery – get results faster.
- Reduced time to prototype – create a functional prototype in less time.
- Reduced time to market – productize an idea in less Time.
- Smoother technology transfer process – use the same tools as industry to help achieve a smoother and more efficient technology transfer process.
- Protection of intellectual property – using embedded, field-programmable gate array (FPGA)-based technology.
- Multidisciplinary development – encourage researchers from different disciplines to contribute to the project using the same development tools.
- Improved simulations – achieve better/faster prototyping, hardware-in-the-loop (HIL) simulations, and proofs of concept (POCs) [7][8].

4. STRUCTURAL SIMILARITY INDEX (SSIM)

The Structural Similarity (SSIM) index is a method for evaluating the perceived quality of digital images and videos. SSIM is the perceptual metric that quantifies image quality degradation caused by processing. SSIM is easy and well linked with subject evaluation. Due to its popularity, it is often perceptual image and video quality metrics. An early variant was developed in the Laboratory for Image and Video Engineering (LIVE) at the University of Texas at Austin and the full algorithm was developed jointly with the Laboratory for Computational Vision (LCV) at New York University. Structural Similarity is used for measuring the similarity between two images [9]. The Structural Similarity index is a measurement or prediction of image quality based distortion-free image as reference. Peak signal-to-noise ratio (PSNR) and mean squared error (MSE) have proven to be inconsistent with human visual perception. Mean squared error (MSE) and Peak signal-to-noise ratio (PSNR) estimates absolute errors, whereas SSIM is a perception-based model that considers image degradation as perceived change in structural information by incorporating important perceptual phenomena, including both luminance masking and contrast masking. Structural information is the design that the pixels have strong inter-dependencies when they are spatially close. These dependencies carry significant information about the structure of the objects in the visual scene. Luminance masking is a phenomenon whereby image distortions tend to be less visible in bright regions, whereas contrast masking is a

phenomenon whereby distortions become less visible where there is texture in the image. The SSIM index is calculated on various windows of a frame. The measure between two windows and of common size $N \times N$ is

$$SSIM(x, y) = \frac{(2\mu_x\mu_y + C_1)(2\sigma_{xy} + C_2)}{(\mu_x^2 + \mu_y^2 + C_1)(\sigma_x^2 + \sigma_y^2 + C_2)} \quad (11)$$

Where,

- $\mu_x, \mu_y, \sigma_x, \sigma_y, \sigma_{xy}$ are the local mean, standard deviations and cross-covariance of image x, y .
- $C_1 = (k_1l)^2, C_2 = (k_2l)^2$ two variables to stabilize the division with weak denominator
- l is the dynamic range of the pixel-values
- $k_1 = 0.01$ and $k_2 = 0.03$ by default

Similarity condition of SSIM index is defined as;

$$SSIM(x, y) = SSIM(y, x) \quad (12)$$

In order to assess the image quality, this formula is generally applied on luma, color values or chromatic values. The resultant SSIM index is a decimal value between 0 and 1[10].

5. PROPOSED SYSTEM

5.1 Software requirements

Software Tool

- LabVIEW 2015

Software modules

- Vision Acquisition Software
- Vision Development Module

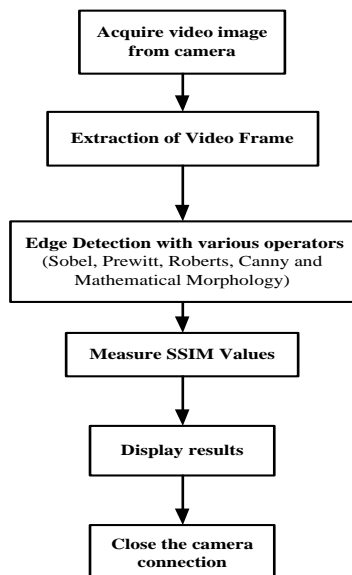


Figure 9. Block Diagram of Proposed system

5.2 Proposed work

Opens a camera with Open IMAQdx VI, queries the camera for its capabilities, loads a camera configuration file, and creates a unique reference to the camera. Configures a low-level acquisition previously opened with IMAQdx Open

Camera VI. Specify the acquisition type with the Continuous and Number of Buffers parameter and then starts an acquisition. Allocate memory space for acquired images as well as copied images for processing using IMAQ create VI. Images for every loop iteration will be got from specified camera. IMAQ ExtractColorPlanes VI to extract luminance color plane of a color image into an 8-bit image. Edge is detected by using different detection operators. The SSIM values and other parameters are measured. When stop button is hit or an error occurs, running program will be stopped. IMAQ Dispose VI is used to destroy an image, close camera connection and free the space it occupied in memory. Merges error is performed from different functions. After running the algorithm, compare the result between edge detection methods. The block diagram of labVIEW VI for proposed algorithm is shown in Fig. 10.

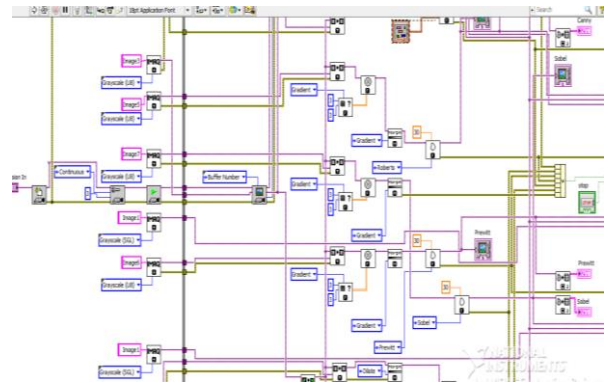


Figure 10. Block Diagram of Proposed Algorithm in LabView

6. EXPERIMENTAL RESULTS

This research work describes the relative performance of various edge detection techniques such as traditional edge detection methods (Robert edge detector, Sobel edge detector, Prewitt edge detector), morphological edge detection method (Dilation-Erosion), and optimal edge detection method (Canny edge detector). The edge detection techniques were implemented using LabView 2015, and tested with real time camera image.



Figure 11. Results of Different Edge Detection (Canny, Morphological, Prewitt, Roberts, Sobel)

In many computer vision and image processing systems the edge detection and corner detection are important tasks. The objective is extracted the principal edge features of the image to produce a clean edge map. It is important to know the differences between edge detection techniques, since edge

detection is the primary step in object recognition. The intensity of the pixels at the borders of a shadow also translates from a low to a high value. Due to this, any edge detection technique detects this outline of shadows as edges. The original image and the result image obtained by using different edge detection techniques are shown in Fig. 11.

Table 1. Mean SSIM values for Different Operators with other parameters

	SSIM	Maximum Pixel Intensity Value	Mean	Variance
Mathematical Morphology	0.047	103	2.79	4.73
Canny	0.0054	255	2.97	27.36
Sobel	0.0048	142	0.41	4.92
Prewitt	0.0047	139	0.40	4.85
Robert	0.0036	155	0.26	3.79

Mean Structural Similarity Index measurement (SSIM) values are calculated and tabulated in Table. 1 by applying Sobel, Robert, Prewitt, Mathematical Morphology and Canny operators at frame buffer number 100 and described the other parameters. Structural similarity index (SSIM) is able to provide a good approximation of perceived image quality. They are maximum pixel intensity value of edge, the mean and variance of the pixels. An increase in maximum intensity value indicated the enhanced edge. After analysing the results, Suitable edge detection method can be chosen for different purposed works.

7. CONCLUSION

A standard webcam and the LabVIEW programme were applied. NI Vision Development tools were used. The programme output was compared during the application of several methods of edge detection. In this research, the most commonly used edge detection techniques of traditional edge detection, morphological edge detection, and optimal edge detection methods. The relative performance of various edge detection techniques is carried out with an image and compared the results under a variety of situations to determine which detector was preferable under different sets of conditions. According to the implement result, the edge detection using mathematical morphology is more efficient than the traditional methods (Canny, Robert, Prewitt and Sobel). Canny's edge detection algorithm performs better than all these operators under almost all scenarios and under noisy conditions, but it is computationally more expensive compared to Sobel, Prewitt and Robert's operator. The Prewitt filter is very sensitive to noise which is a major drawback of it.

8. ACKNOWLEDGEMENTS

Firstly, the author would like to acknowledge Dr. Thein Gi, Rector of Technological University (Thanlyin), for her kind permission to carry out this research work. The authors would like to thank many colleagues from digital image processing research group of Department of Electronic Engineering of Technological University (Thanlyin). The author particularly wishes to acknowledge all the teachers from Department of Electronic Engineering, Technological University (Thanlyin), for their support, encouragement and invaluable guidance in

preparation of this research. The authors would like to express their thanks to all persons who have given support during the preparation period of this research work.

7. REFERENCES

- [1] R. C. Gonzalez, R. E. Woods, Digital Image Processing. 3rd ed, Prectice Hall, 2007, pp. 187-190.
- [2] Panchami S V, Dr. M V Sathyanarayana, Senthilkumar S, "Continuous Image Acquisition and Edge Detection Using Morphological Filters and Classical Edge Detection Algorithms in Labview", International Journal of Engineering Research & Technology, vol. 6, no. 12, 2017, pp. 242-245.
- [3] Christopher G. Relf, " Image Acquisition and Processing with LabVIEW", ch. 6.
- [4] Girish N. Chaple, R. D. Daruwala, Manoj S. Gofane, "Comparisons of Robert, Prewitt, Sobel operator based edge detection methods for real time uses on FPGA", International Conference on Technologies for Sustainable Development, February 2015, pp. 04-06.
- [5] Muthukrishnan.R, M.Radha, "edge detection techniques for Image segmentation", International Journal of Computer Science & Information Technology, vol. 3, no. 6, 2011, pp. 259-267.
- [6] Kamil Sidor, Anna Szlachta, "The Impact of the Implementation of Edge Detection Methods on the Accuracy of Automatic Voltage Reading", Measurement Science Review, vol.17, no. 2, 2017, pp. 93-99.
- [7] NI Vision for LabVIEW User Manual.
- [8] Ravi Kumar A.V, Nataraj K.R, "Result Analysis of LabVIEW and MatLab in Application of Image Edge Detection", International Journal of Computer Applications, vol. 48, no. 9, 2012, pp. 6-10.
- [9] Journal of Advanced Research in Computer and Communication Engineering, vol. 2, no. 1, January 2013.
- [10] S.Dutta and BB.Chudhuri, "A color edge detection algorithm in RGB color space," Internal conference on Advances in Recent Technologies in communication and computing, 2009, pp.337-340.

Stress Analysis on Spur Gears Using ANSYS Workbench 16.0

May Phyoe Thu
Dept. of Mechanical Engg.
Technological University
Hmawbi, Myanmar

Nwe Lin Min
Dept. of Mechanical Engg.
Technological University
Hmawbi, Myanmar

Abstract: Gear is one of the most important machine elements in mechanical power transmission system. It is a rotating machine part having cut tooth which meshes with another tooth part in order to transmit torque. The application of gears has a wide range starting from tiny wrist watch to huge heavy machinery such as automobile, aerospace industry and marine engines due to its high degree of reliability and compactness. Spur gears have straight tooth and are parallel to the axis of the wheel. The bending stress and total deformation of gear tooth is considered to be the paramount objective of for modern gear design. A pair of spur gear tooth in action is generally subjected to two types of cyclic stress, contact stress and bending stress including fatigue. In this paper, the contact stress analysis of stainless steel spur gear by theoretical method using Hertz equation and Finite element analysis using ANSYS 16.0 workbench. The present work is an attempt to find root bending stress distribution, maximum allowable contact stress and total deformation of a stainless steel spur gear tooth.

Keywords: Stainless Steel Spur Gear, Static load, Contact Stress, Bending Stress, Total Deformation, ANSYS Workbench 16.0

1. INTRODUCTION

Gears are used in most types of machinery. Like nuts and bolts, gears are common machine elements that will be needed from time to time by almost all machine designers. They are mostly used to transmit torque and angular velocity. It would be appropriate to say that because of compactness and high degree of reliability, gears will predominate in future industrial machines as the most effective means of power transmission. Furthermore, refinement in the application of gear technology is necessary due to the sudden shift from heavy industry such as shipbuilding to automobile manufacturing and office automation tools.

As there is always a demand for enhanced service life of gears in industry, more efficient, reliable and light-weight gears needed to be designed and manufactured. Designing gear is highly complicated and intellectual field. For decades, several measures have been adopted to enhance the service life of gears such as heat treatment, adjusting micro geometry. Many physical factors accumulate to cause a gear failure, including the material of the gear. Selecting different materials for gears plays an important role in gear technology. Material selected for making a gear must satisfy two conditions: (1) manufacturability and processing requirement; (2) achieving required service life. Manufacturability requirement includes its forgeability and its response to heat treatment. Whereas, to achieve required service life, gears should transmit power to a satisfactory level when working in loading conditions as well as fulfilling mechanical property requirement such as fatigue, strength and response to heat treatment.

In industry, gear designers have been working hard for years to achieve precise gearing without error and to produce maximum service life. To reach the most refined level of gear design, designers refer to the standard such as DIN, AGMA, IS, ISO. These standards are strongly influenced by several safety factors. To reduce the cost of actual prototypes and field testing of gears, analysis software was introduced. Analysis software such as ANSYS is capable of performing finite element analysis (FEA) over not only gear teeth but each part of the gear body such as the rim. This software also provides information of bending stresses, contact stresses along with transmission error. To minimize the modeling time, preprocessor software that helps to create the geometry required for FEA, such as Solidworks could be used.

Solidworks generates the three-dimensional spur gears easily. After designing and saving the geometry in solidworks, it is easy to import the same file into ANSYS. Advances in software development have opened a new era of gear analysis simulation. Computer simulation results have helped to achieve more accurate gear tooth profiles before manufacturing a practical prototype of a gear.

2. FINITE ELEMENT METHOD

The finite element method is numerical analysis technical of optioning approximate solution to a wide variety of engineering problems. Because of its diversity and flexibility as an analysis tool, it is receiving much attention in engineering school and industries in more and more engineering situation today, we find that it is necessary to obtain approximate solution to problems rather than exact close from solution it is not possible to obtain analytical mathematical solutions are many engineering's problems. An analytical solution is a mathematical expression that gives value of the desire unknown quantity at any location in the body, as consequence it is valid for infinite number of location in the body. For problem involving complex material properties and boundary condition, the engineer resource to numerical method that provide approximate that eatable solution.

2.1 Terms used in Gear

The pitch circle of a gear is the circle that represents the size of the corresponding friction roller that could replace the gear. As two gears mate, their pitch circles are tangent, with a point of contact on the line that connects the center of both circles. The pitch point is the point of contact of the two pitch circles. The pitch diameter, d , of a gear is simply the diameter of the pitch circle. Because the kinematics of a spur gear are identical to an analogous friction roller, the pitch diameter is a widely referenced gear parameter. However, because the pitch circle is located near the middle of the gear teeth, the pitch diameter cannot be measured directly from a gear. The number of teeth, N , is simply the total number of teeth on the gear. Obviously, this value must be an integer because fractional teeth cannot be used. The circular pitch can be calculated from the number of teeth and the pitch diameter of a gear.

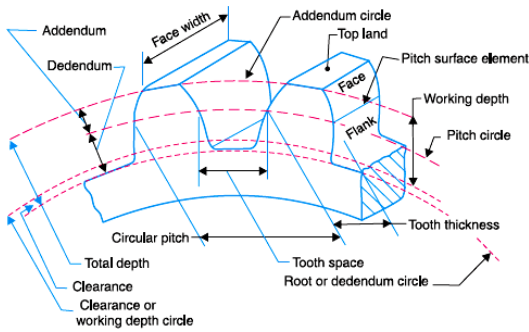


Figure 1. Terms used in Gears

The circular pitch, p_c is the distance measured along the pitch circle from a point on one tooth to the corresponding point on the adjacent tooth of the gear.

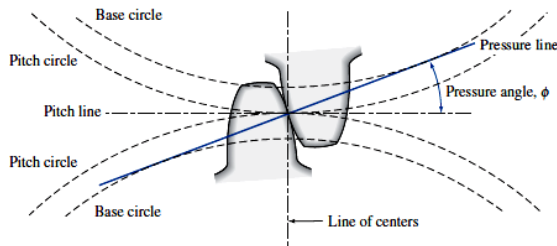


Figure 2. Pressure angle

The pressure angle, ϕ , is the angle between a line tangent to both pitch circles of mating gears and a line perpendicular to the surfaces of the teeth at the contact point.

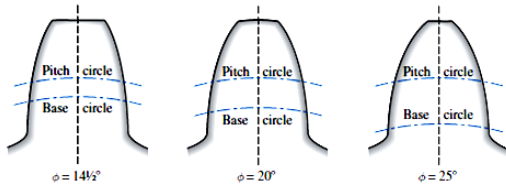


Figure 3. Pressure angle influence on tooth shape

The line tangent to the pitch circles is termed the pitch line. The line perpendicular to the surfaces of the teeth at the contact point is termed the pressure line or line of contact.

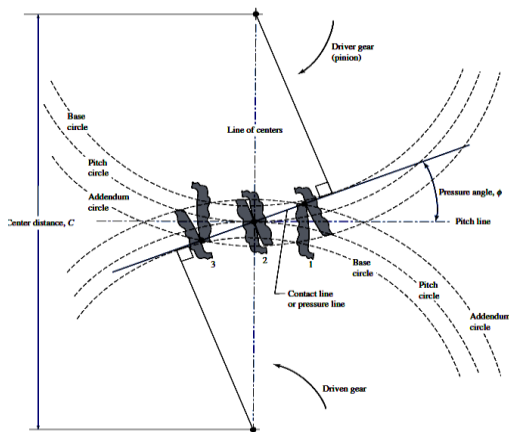


Figure 4. Gear Mating Process

Therefore, the pressure angle is measured between the pitch line and the pressure line. The pressure angle is illustrated in Figure 2. The pressure angle affects the relative shape of a

gear tooth. Although gears can be manufactured in a wide range of pressure angles, most gears are standardized at 20° and 25°. Gears with 14.5° pressure angles were widely used but are now considered obsolete. They are still manufactured as replacements for older gear trains still in use. Because the pressure angle affects the shape of a tooth, two mating gears must also have the same pressure angle. Recall that forces are transmitted perpendicular to the surfaces in contact. Therefore, the force acting on a tooth is along the pressure line.

2.2 Standard Proportions of Gear Systems

The following table shows the standard proportions in module(m) for the four gear systems.

Table.1 Standard proportions of Gear systems

S. No.	Particulars	14½° composite or full depth involute system	20° full depth involute system	20° stub involute system
1.	Addendum	1 m	1 m	0.8 m
2.	Dedendum	1.25 m	1.25 m	1 m
3.	Working depth	2 m	2 m	1.60 m
4.	Minimum total depth	2.25 m	2.25 m	1.80 m
5.	Tooth thickness	1.5708 m	1.5708 m	1.5708 m
6.	Minimum clearance	0.25 m	0.25 m	0.2 m
7.	Fillet radius at root	0.4 m	0.4 m	0.4 m

2.3 Arc of Contact

The arc of contact is the path traced by a point on the pitch circle from the beginning to the end of engagement of a given pair of teeth. The arc GP is known as arc of approach and the arc PH is called arc of recess. The angles subtended by these arcs at O1 are called angle of approach and angle of recess respectively.

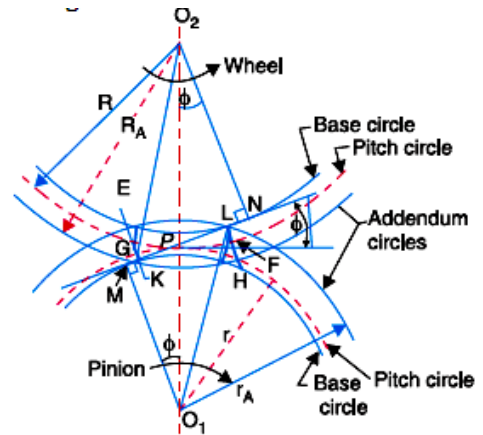


Figure 5. Path of contact

$$\text{Length of the arc of contact} = \frac{\text{length of path of contact}}{\cos \phi}$$

2.4 Contact Ratio

The contact ratio or the number of pairs of teeth in contact is defined as the ratio of the length of arc of contact to the circular pitch. Mathematically;

$$\text{Contact ratio} = \frac{\text{length of arc of contact}}{p_c}$$

Where p_c = circular pitch = πm ; m = module

3. DESIGN SPECIFICATION

For calculating bending stress, contact stress and total deformation we have taken a standard model for designing the spur gear tooth. The following data is given for the design of

20° full depth spur gear made of stainless steel transmitting torque at 10 kW power with 3000rpm.

Table 2. Specification of Spur Gear Tooth

Description	Units	Symbol	Value
No. of teeth on pinion	-	N_p	20
No. of teeth on gear	-	N_g	20
Pressure angle	degree	ϕ	20
Module	mm	m	6
Addendum	mm	h_a	$m = 6$
Dedendum	mm	h_d	$1.25m = 7.5$
Pitch circle diameter	mm	d_p	$mN = 120$
Pitch circle radius	mm	r_p	60
Base circle diameter	mm	d_b	$d_p \cos \phi = 112.76$
Addendum circle diameter	mm	d_a	$d_p + 2m = 132$
Dedendum circle diameter	mm	d_d	$d_p - (2 + \pi/N)m = 107.06$
Face width	mm	b	54
Tooth thickness	mm	t	$1.5808m = 9.485$
Fillet radius	mm	r_f	$0.4m = 2.4$

Specification of Spur Gear Tooth and Material Properties of Stainless Steel are described in Table 2 and 3.

Table 3. Material Properties of Stainless Steel

Property	Value	Unit
Density	7750	kg/m ³
Coeff. of thermal expansion	1.7e-05	C ⁻¹
Young's Modulus	1.93e+11	Pa
Poisson's ratio	0.31	Pa
Bulk Modulus	1.69e+11	Pa
Shear Modulus	7.3664e+10	Pa
Tensile Yield Strength	2.07e+08	Pa
Compressive Yield Strength	2.07e+08	Pa
Ultimate tensile Strength	5.86e+08	pa

3.1 Theoretical Calculation

3.1.1 Contact stress calculation using Hertz Equation

Earle Buckingham(1926) used the Hertz theory to determine the contact stress between a pair of teeth while transmitting power by treating the pair of teeth in contact as cylinders of radii equal to the radii of curvature of the mating involutes at the pitch point. According to Hertz theory, when the two cylinders are pressed together, the contact stress is given by,

$$\sigma_c = \frac{2F}{\pi B L} \quad (i)$$

$$B = \sqrt{\left[\frac{2F \left(\frac{1-\mu_1^2}{E_1} + \frac{1-\mu_2^2}{E_2} \right)}{\pi L \left(\frac{1}{d_1} + \frac{1}{d_2} \right)} \right]} \quad (ii)$$

where σ_c = maximum value of contact stress (N/mm²)
 F = force pressing two cylinders together (N)
 B = half width of deformation (mm)
 L = axial length of cylinders (mm)
 d_1, d_2 = diameters of two cylinders (mm)
 E_1, E_2 = moduli of elasticity of two cylinder materials (N/mm²)
 μ_1, μ_2 = poisson's ratio of materials

Substituting the value of half width of deformation B in equation(i) and squaring both sides,

$$\sigma_c^2 = \frac{F}{\pi L} \left[\frac{\left(\frac{1}{r_1} + \frac{1}{r_2} \right)}{\left(\frac{1-\mu_1}{E_1} + \frac{1-\mu_2}{E_2} \right)} \right] \quad (iii)$$

If the material of both cylinders are the same, then the moduli of elasticity and poisson's ratio will be equal. Substituting $E_1 = E_2 = E$ and $\mu_1 = \mu_2 = \mu$ in eq.(iii),

$$\sigma_c^2 = \frac{F}{2\pi L} \left[\frac{\left(\frac{1}{r_1} + \frac{1}{r_2} \right)}{\left(\frac{1-\mu}{E} \right)} \right]$$

(iv)

Now applying this equation to a pair of spur gear teeth in contact, replacing the radii r_1 and r_2 by the radii of curvature at the pitch point.

$$r_1 = \frac{d_{pp} \sin \phi}{2} \quad \text{and} \quad r_2 = \frac{d_{pg} \sin \phi}{2}$$

where d_{pp} = pitch circle diameter of pinion

d_{pg} = pitch circle diameter of gear

Since the pinion and gear have equal geometry in all respects as given in table 2, therefore

$$d_{pp} = d_{pg} = d_p,$$

$$r_1 = \frac{d_p \sin \phi}{2} \quad \text{and} \quad r_2 = \frac{d_p \sin \phi}{2}$$

$$\Rightarrow r_1 = r_2 = r = \frac{d_p \sin \phi}{2}$$

(v)

\Rightarrow substitute in eq.(iv) we get

$$\sigma_c^2 = \frac{1}{\pi(1-\mu)} \left[\frac{FE}{Lr} \right]$$

(vi)

For both materials as stainless steel, from table 3 poisson's ratio $\mu = 0.31$ and substitute in eq.(vi) and solving;

$$\sigma_c = 0.6792 \left(\frac{FE}{Lr} \right)^{\frac{1}{2}}$$

(vii)

From table 3 modulus of elasticity $E = 193000$ MPa and substitute in (vii),

$$\sigma_c = 0.6792 \left(\frac{F \times 193000}{Lr} \right)^{\frac{1}{2}}$$

$$\sigma_c = 298.386 \left(\frac{F}{Lr} \right)^{\frac{1}{2}}$$

(viii)

from (v)
$$r = \frac{d_p \sin \phi}{2} = \frac{r_p \sin \phi}{2}$$

Therefore
$$\sigma_c = 298.386 \left(\frac{F}{Lr_p \sin \phi} \right)^{\frac{1}{2}}$$

(ix)

Now, $F = \frac{F_t}{\cos \phi}$ where F_t is the tangential component of the resultant force F between two meshing teeth. Substitute this value in (ix),

$$\sigma_c = 298.386 \left(\frac{F_t}{Lr_p \sin \phi \cos \phi} \right)^{\frac{1}{2}}$$

(x)

Also the axial length L is equal to the face width b of spur gears, therefore replacing L by b in (x),

$$\sigma_c = 298.386 \left(\frac{F_t}{br_p \sin \phi \cos \phi} \right)^{\frac{1}{2}}$$

(xi)

Equation (xi) is the general mathematical model for evaluating the contact stress for a pair of stainless steel spur gear teeth in contact, for the equal geometry and dimensions of pinion and gear in mesh.

Considering the power to be transmitted $P = 10$ kW and the rotational speed of the pinion $n_p = 3000$ rpm, the tangential component of force can be obtained from;

$$P = \frac{2\pi n_p T}{60 \times 10^6} \quad (xii)$$

Where T is transmitting torque in N-mm.
 $\Rightarrow T = 31831$ N-mm

Also $F_t = \frac{2T}{d_p}$ and from table 2, $d_p = 120$ mm

$\Rightarrow F_t = 530.517$ N

Again $b = 54$ mm, $\phi = 20^\circ$ and $r_p = 60$ mm are substituted in

$$(xi) \quad \sigma_c = 212.98 \text{ MPa}$$

Allowable maximum contact stress,

$$\sigma_{c,all} = \frac{\sigma_c}{S.F} \text{ where } S.F \text{ is safety factor.}$$

Taking $S.F$ as 2.736,

$$\sigma_{c,all} = 77.84 \text{ MPa}$$

Again from eq.(xi)

$$\sigma_c = 298.386 \left(\frac{F_t}{b r_p \sin \phi \cos \phi} \right)^{\frac{1}{2}}$$

$$F_t = b r_p \sin \phi \cos \phi \left(\frac{\sigma_c}{298.386} \right)^2$$

(xiii)

Replacing σ_c by the maximum allowable Hertz stress σ_H in(xii), the tooth surface strength of pinion is;

$$F_{ts} = b r_p \sin \phi \cos \phi \left(\frac{\sigma_H}{298.386} \right)^2$$

(xiv)

The maximum allowable Hertz stress for stainless steel spur gears is 405.015 N/mm².

$$F_{ts} = 1918.527 \text{ N}$$

For the design to be safe, the tooth surface strength F_{ts} must be greater than the dynamic load on gear tooth F_d . The dynamic load on gear tooth is given by;

$$F_d = \frac{21v(Ceb + F_t)}{21v + \sqrt{Ceb + F_t}}$$

(xv)

Where v = pitch line velocity (m/s)

C = deformation factor (N/mm²)

e = sum of error between two meshing teeth (mm)

b = face width of tooth (mm)

F_t = tangential component of force (N)

The deformation factor C_k is given by,

$$C = \frac{1}{\left[\frac{1}{E_1} + \frac{1}{E_2} \right]}$$

where $k = 0.111$ constant depending on form of tooth

$$\Rightarrow C = 10711.5 \text{ N/mm}^2$$

Pitch line velocity $v = \frac{\pi d_p n}{60 \times 10^3}$; $n = 3000$ rpm and

$d_p = 120$ mm,

$$v = 18.84 \text{ m/s}$$

The error e is a function of the quality of the gear and the method of manufacturing. There are twelve different grades of gears as listed in table 4.

Table 4. Tolerances on the adjacent pitch

Grade	e (microns)
1	$0.80 + 0.06\phi$
2	$1.25 + 0.10\phi$
3	$2.00 + 0.16\phi$
4	$3.20 + 0.25\phi$
5	$5.00 + 0.40\phi$
6	$8.00 + 0.63\phi$
7	$11.00 + 0.90\phi$
8	$16.00 + 1.25\phi$
9	$22.00 + 1.80\phi$
10	$32.00 + 2.50\phi$
11	$45.00 + 3.55\phi$
12	$63.00 + 5.00\phi$

The tolerance factor ϕ is given by,

$$\phi = m + 0.25\sqrt{d_p}$$

where m = module, d_p = pitch circle diameter

\Rightarrow for top precision as grade 1;

$$e = 2e_p = 2e_g = 2(0.8 + 0.06\phi) = 2.6486 \times 10^{-3} \text{ mm}$$

from eq.(xv) the dynamic load $F_d = 1850.15$ N

$$F_{ts} = 1918.517 \text{ N} > F_d = 1850.15 \text{ N}$$

Therefore, the design is safe from surface durability consideration.

3.2 Assumption of Lewis Equation

The analysis of bending stress in gear tooth was done by Mr. Wilfred Lewis in his paper, 'The investigation of the strength of gear tooth' submitted at the Engineers club of Philadelphia in 1892. Even today, the Lewis equation is considered as the basic equation in the design of gears. Lewis considered gear tooth as a cantilever beam with static normal force F applied at the tip. Assumptions made in the derivation are:

1. The full load is applied to the tip of a single tooth in static condition.
2. The radial component is negligible.
3. The load is distributed uniformly across the full face width.
4. Forces due to tooth sliding friction are negligible.
5. Stress concentration in the tooth fillet is negligible.

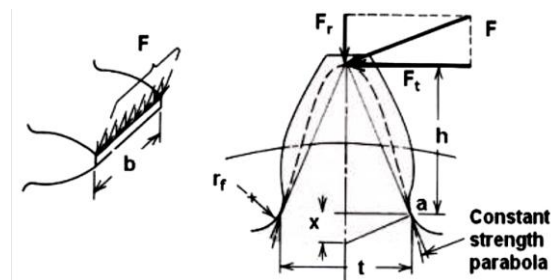


Figure 6. Force on a gear tooth

In the above Figure 3.1, the following notations are used: F is the Full load, F_r and F_t are the Radial and Tangential component of the full load, h , b and t are the height, face-width and thickness of the tooth at critical section respectively.

3.2.1 Calculation of Bending Stress

In calculation of bending stress of tooth we consider the Lewis assumption as discussed above in 3.2. From the Figure 3 at point 'a'

$$\text{Bending moment } M_b = F_t * h \quad (1)$$

$$\text{Area moment of inertia } I = \frac{bt^3}{12} \quad (2)$$

$$\text{Then the bending stress is given by } \sigma_b = \frac{6hF_t}{bt^2}$$

from the Eq. (1) and Eq. (2). After the rearranging we have

$$F_t = b * \sigma_b * \frac{t^2}{6h} \quad (3)$$

Multiplying numerator and denominator by module (m) from the Eq. (3) we have the tangential component of the force is

$$\text{given by } F_t = m * b * \sigma_b * \frac{t^2}{6hm} \quad (4)$$

$Y = \frac{t^2}{6hm}$ is known as Lewis form factor. Equation (4) can be

$$\text{rewritten as } F_t = m * b * \sigma * Y \quad (5)$$

When the tangential force increased the stress also increases. When the stress reaches the permissible magnitude of bending

stress the corresponding force F_t is known as Beam strength and denoted by S_b . So replacing F_t in the Eq. (5) we have

$$S_b = m * b * \sigma * Y. \quad (6)$$

Consider torque $T = 31831$ N-mm at 3000 rpm. The tangential load F_t can be found as

$$F_t = 2 * T / d_p; \quad F_t = 530.517 \text{ N},$$

The value of bending stress is given from Eq.(5) if form factor $Y = 0.32$, $\sigma_b = 5.117$ MPa.

Ultimate tensile strength of gear material is 586 MPa.

Consider safety factor as 3, the allowable bending stress is 195.33 MPa > 5.117 MPa.

So the design is satisfactory.

As the gear and pinion are identical there is no need to check the following relation i.e. strength of gear $<$ strength of pinion.

3.2.2 Calculation of Total Deformation

It is observed that the cross section of the gear tooth varies from free end to the fixed end. Lewis has assumed it as a constant strength parabola. Using Castigliano's Theorem total deformation of the tooth can be found with minor error. For linearly elastic structure, where external forces only cause deformations, the complementary energy is equal to the strain energy. For such structures, the Castigliano's first theorem may be stated as the first partial derivative of the strain energy of the structure with respect to any particular force gives the displacement of the point of application of that force in the direction of its line of action. The theory applies to both linear and rotational deflection $\delta = \frac{\partial U}{\partial F}$. It should be clear that Castigliano's theorem finds the deflection at the point of application of the load in the direction of the load.

Here U is the strain energy given by $U = \int_0^l \frac{M^2}{2EI} dx$, where M is the moment due to the load. Consider the parabolic tooth of height h and thickness t . The equation of parabola $y^2 = 4 * a * x$, the boundary condition at $x = h$, $y = t/2$. After substitution

$$y^2 = (t^2 x / 4 h) \text{ and } y^3 = (t / 2)^3 (x / h)^{1.5}$$

Putting $M = F_t * x$, $I = (2/3) * b * y^3$, the strain energy will be

$$U = \frac{8h^3 F_t}{Ebt^3}$$

(7)

Again deflection is given by $\delta = \frac{16F_t h^3}{Ebt^3}$

(8)

4. STATIC ANALYSIS

4.1 Meshing

Meshing is basically the division of the entire model into small cell so that at each and every cell the equations are solved. It gives the accurate solution and also improves the quality of solution. Here the element size of 1 mm with medium smoothing is considered for mesh generation.

4.2 Boundary Conditions

Based on the assumptions of Lewis equation, the boundary conditions are set in ANSYS Workbench. The fixed support is used at the root end of the tooth and the force is applied on the face having components in Y and Z directions.

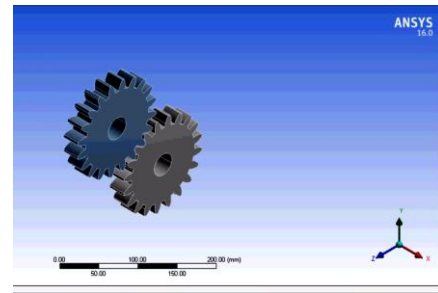


Figure 7. Gear Geometry

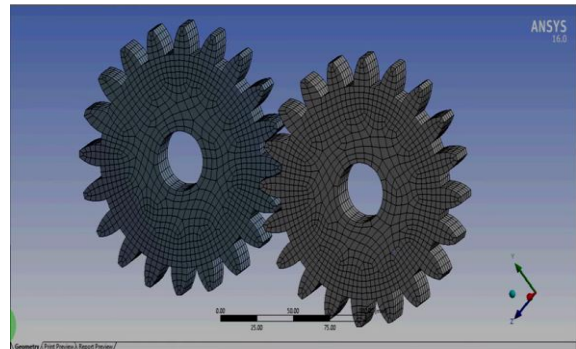


Figure 8. Meshing of Gears

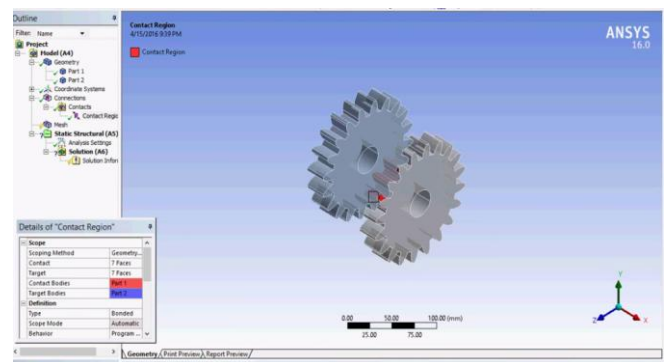


Figure 9. Contact region

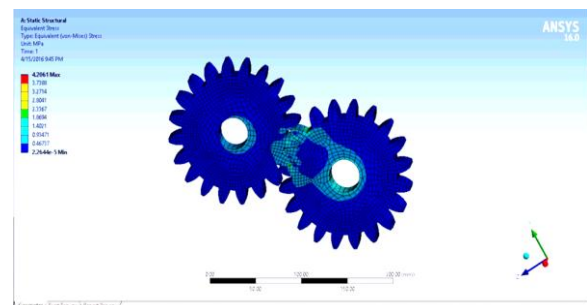


Figure 10. Distribution of Equivalent (Von Mises) stress

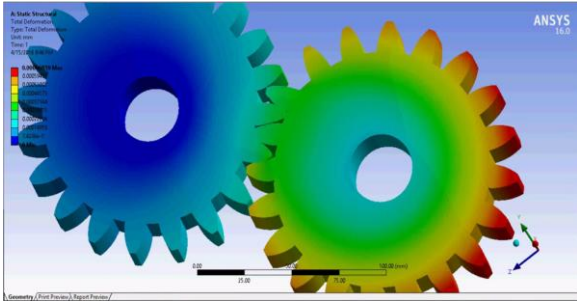


Figure 11. Total Deformation

FEA provides results that are comparable with theoretical analysis results as was in the contact stress analysis of spur gears in the present study. FEA can predict whether a product will break, wear out, or work the way it was designed. Hence, FEA can prove very helpful in the product development process by forecasting its behavior in operation. A number of research studies have been carried out in the context of spur gear using different types of materials. An extended version of the above work based on the same software can also be carried out for the analysis of shear stress between two mating gears.

6. ACKNOWLEDGMENTS

Special deep thanks to teacher Dr. Theingi (Rector) for encouraging me to make this paper and her kind support and valuable suggestions. We also wish to thank HOD and all the faculty members of mechanical engineering department for their constant help and patient understanding.

7. REFERENCES

- [1] Gitin M Maitra, Spur gear, Handbook of Gear Design, 2nd ed. New Delhi, India, McGraw Hill Education, ISBN: 0-07-460237-3, 2010, Ch. 02, sec.2.25, pp.2.99-2.100.
- [2] Bhandari, V. B. *Design of machine elements*. Tata McGraw-Hill Education, 2010
- [3] http://nptel.ac.in/courses/112106137/pdf/2_7.pdf.
- [4] <http://www.gizmology.net/gears.htm>.
- [5] Kailash.C.Bhosale, Analysis of bending strength of the helical gear by fem, The international institute for science, technology and education (iiste), Volume 2, No 4, 2011, ISSN 2222-1727(Paper) ISSN 2222-2871
- [6] Khurmi, R.S., 1997. "Theory of machine". Khanna publication.
- [7] Rattan, S.S., 1998. "theory of machines". Dhanpat rai publication.
- [8] R.S. Khurmi, J.K. Gupta, Spur gear, A Text Book of Machine Design, S. Chand, Eurasia Publishing House (pvt.) ltd., 2005.
- [9] S. Baud, P.Velex, Static and dynamic tooth loading in spur and helical geared systems experiments and model validation, Journal of Mechanical Design, 124(2), 2002, pp. 334–346.
- [10] Shubham A. Badkas and NimishAjmera, Static and dynamic analysis of spur gear, International Journal of Mechanical Engineering & Technology (IJMET), Volume 7, Issue 4, July–Aug 2016, pp.8–21.
- [11] Sunil Kumar, K.K. Mishra, JatinderMadan, Stress analysis of spur gear using fem method, National Conference of Advancements and Futuristic Trends in Mechanical and Material Engineering, Feb 19-20.2010.
- [12] V.Rajaprabakaran, Mr.R.Ashokraj, Spur gear tooth stress analysis and stress reduction, IOSR Journal of Mechanical and Civil Engineering (IOSR-JMCE), e-ISSN: 2278-1684, ISSN: 2320-334X, pp.38-48.

5. RESULTS AND CONCLUSION

In the present work, the spur gear tooth is modeled and is analyzed in the static structural domain of ANSYS software. The results found in the above figures are the maximum equivalent stress is 4.206 MPa and total deformation is 0.0006689 mm. It is concluded that for the given specification, the maximum bending stress and total deformation can be found for a torque specification.

Analysis of Forging Processes for Machine Building Industry Modeling

New Lin Min
Department of Mechanical Engineering,
Technological University
Hmawbi, Myanmar

May Phyoe Thu
Department of Mechanical Engineering,
Technological University
Hmawbi, Myanmar

Abstract: This paper presents the efforts of forging process. As new uses for various metals multiplied, and the superior quantities imported to metals by forging came to be more positively recognized, the forging industry accelerated its efforts to produce more and better products at diminishing cost. During the production of a crankshaft weighing 17 kilograms from a bar of rolled steel, up to 31.5 kilograms are irretrievably lost as chips in machining. When the same weight of crankshaft is manufactured by the forging process, only 13.7 kilograms of steel are lost in chips. i.e. the loss is 56.6 percent less. When the temperatures increase, it is found that forging load decreases. Forging load is directly proportional to the percentage of reduction. Low carbon steels are easy to forge and super alloys are difficult to forge. In this paper, three different types of materials namely, 1020 carbon steel (crankshaft), A-286 alloy (turbine disc) and 6061 alloy (aircraft housing) are analyzed to determine the relationship between the forging temperature, forging loads and percentages of reduction. There were made at the laboratory, Department of Metallurgical Engineering and Materials Science, Yangon Technological University.

Keywords: Hammer Forging, 1020 Carbon Steel, A-286 Alloy, 6061 Alloy.

1. INTRODUCTION

Forging processes are extremely important in the machine building industry. No machine, whether simple or complicated can be built without the use of forging. There are seven forging methods. These are hand forging, hammer forging, smith forging, drop forging, press forging, upset forging and roll forging. Among them, hammer forging method is the most suitable for any materials and it is the easiest to do. It is particularly wide spread in the tractor, automobile, agricultural machinery, ship building, locomotive building and other industries.

For instance, in the railway car building industry up to 70 percent of all the parts which go to make a car are forging. Selection of a basic process of forging is determined by two chief requirements—first, production of an object of a specified shape, and second, improvement of the physical properties of the metal. [1]

Important advantages of the forging are as follows,

1. When designing the required part, the engineer has considerable freedom because of a wider range of materials at his disposal to meet specific demands in service.
2. Since forged parts have ample strength to resist external forces, the use of parts of lighter sectional thickness is permitted, thus considerably reducing the dead weight of these parts.
3. Forging a part to the required shape also produces in the part the desired combination of physical properties in the correct proportion, thus insuring maximum strength and toughness, properties so vital in service.
4. Thoughtful and careful design of proper tools results in accurate shaping of parts with the least amount of allowance for finishing, thereby reducing substantially the cost of final machining. [1]

2. MAJOR REQUIREMENTS IN FORGING

It is understood without specific mention that are excess metal or flash of forgings shall be removed by trimming and that forgings shall be free from injurious defects. Standard specification for forgings are quantity, size, coining or sizing, surface conditions, special requirements, dies, and tolerances. [2]

Combining Forging Operations

In some cases, forgings are completed using more than one type of forging operation. [2]

Forging Defects

Faults in the original metal, incorrect die design, improper heating, or improper forging operation are some of the reasons for forging defects. Samples of incoming metal should be given a careful metallurgical inspection before the lot is accepted. [2]

Forging Design

When the production-design engineer specifies a forging or metalworking process, he is usually trying to design a product with more attractive mechanical characteristics, such as greater strength, or else to economize on the weight of the finished part, thus saving on material cost. [2]

Inspection and Acceptance of Forgings

All finished forgings are inspected for quality. The aim of quality inspection is to ascertain whether the strength of the forging meets the conditions for which it is designed. [3]

Hammer Forging

Heavy machine parts cannot be forged by hand, since the comparatively light blows of a hand or sledge hammer are unable to produce a great degree of deformation in the metal being forged.

Moreover, hand forging is a lengthy process and requires repeated heating of the metal. For this reason, hammer forging, sometimes also called power, machine forging, is used for the manufacture of heavy forging.

3. MATERIALS PROPERTIES UNDERFORGING CONDITIONS

Practically all metals of industrial importance can be forged successfully, but there is some difference between metals in the ease with which this can be done.

1. steel
2. Alloy steels
3. heat resisting steels and stainless steels
4. Iron
5. copper, brasses and bronzes
6. Nickel and nickel-copper alloys
7. light alloys
8. titanium alloys [4]

Steels

Low carbon steels are the easiest of their class of forge. They also have better transverse properties than the harder alloys. Fine grained ingots produce better transverse properties than coarse grained; thus, high quality forgings are made generally from killed, ladle-deoxidized steel showing a minimum of segregation. C1020, C1030, C1035 are for small forgings and C1040 are used for medium forgings. Temperature range is from 1500 to 2500°F. [4]

Alloys

Forging temperatures for aluminum and its alloys ranges are from 650°F to 900°F.

Effect of Temperature on Material

The forging processes work material cold or hot, depending upon the nature of the material and its size. The ability to work cold material depends upon its ductility and malleability. The ability to work hot material depends on its range of plasticity at higher temperatures. The greatest ductility is near the melting point. The forming properties of any metal or alloy depend on the temperature of the material. [5]

Hot Working

The product of such hot-working is operations are called wrought metals and are important engineering materials because they are worked under pressure to:

1. Obtain the desired size and shape from the original ingot, thereby saving time, material, and machining costs.
2. Improve the mechanical properties of the metal through refinement of the grain structure, development of directional "flow lines" and breakup and distribute unavoidable inclusions, particularly in steel.
3. Permit large changes in shape at low power inputs, per unit volume.

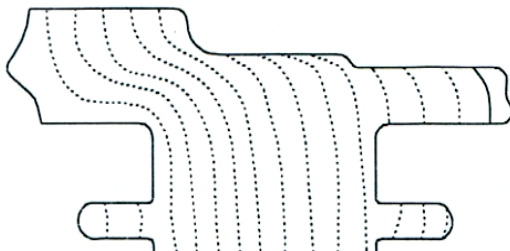


Figure 1. A cross section of a forging for a crank shaft.

Hot Working Processes

1. Rolling
2. Forging
3. Extruding
4. Upsetting

Forging

Forging is the forming of metal, mostly hot, in the early dawn of civilization, man discovered that a heated piece of metal was more easily hammered to desired shapes.

Steps in Forging a Crankshaft

The various steps in forging a single-throw crankshaft are:

1. Form flange and draw tong hold stock in turned in the dies between hammer strokes, to gather flange metal.
2. Flatten. Done between plain flat dies.
3. Bend. Done to make stock fit into die impressions.
4. Forge in crankshaft impression. Stock is forged until chilled flash prevents further metal flow.
5. Trim flash.
6. Reheat.
7. Forge again in crankshaft impression. Continue if necessary until shaft is reduced to drawing size.
8. Trim flash again.
9. Restrike in crankshaft impression for final straightening and sizing.
10. Saw off tong hold.
11. Heat treat.

4. RESULTS AND DISCUSSIONS

A case study is made at the laboratory of Department of Metallurgical Engineering and Materials Science, Yangon Technological University.

This paper studies hammer forging method.

The different results are used for different materials. In this paper, three different types of materials are analyzed to determine the relationship between the forging temperatures, loads and percentage of reduction [6]

Low carbon steel is easy to forge and super alloy is difficult to forge. If the temperatures increase, the forging loads decrease. The forging load is directly proportional to the percentage of reduction. The varying forging temperatures results the varying forging loads and pressures.

The different temperatures of three materials are described in Table 1.

Table 1. Calculated results for gears

No	Material	Maximum Temperature	Minimum Temperature
1	1020 carbon steel	2300°F	1300°F
2	A-286 alloy	2100°F	1600°F
3	6061 alloy	900°F	600°F

The collected datas for this paper are shown below. The experimental datas are done on the basic of hammer forging method.

Crankshaft will depend on its design, on the dimensions and on the grade of material. The selection of forging temperature for carbon steel is based on (1) the carbon content, (2) the alloy composition, (3) the temperature range for optimum plasticity, (4) the amount of reduction.

Table 2. Effect of temperature on load, pressure and percentage of reduction for Crankshaft Steel

No: of Step	Material Used	Forging Temperature	For- ging load	Frog- ing pres- sure	% of red- uct- ion
1.	1020carbon steel (Crankshaft steel)	1800°F	60 lb	21psi	60%
2.			50 lb	20psi	50%
3.			42 lb	19psi	40%
4.			40lb	18psi	30%
5.			39lb	17psi	20%
1.	1020carbon steel (Crankshaft steel)	2000°F	35 lb	12psi	50%
2.			30lb	12psi	40%
3.			25lb	12psi	30%
4.			22lb	11psi	20%
5.			20lb	10psi	10%
1.	1020carbon steel (Crankshaft steel)	2200°F	30lb	10psi	60%
2.			25lb	10psi	50%
3.			22lb	10psi	40%
4.			20lb	10psi	30%
5.			19lb	10psi	20%

According to the results, it is noticed that the varying temperatures result varying forging loads and pressures .At 1800 °F, forging load is from 60lb to 39 lb and forging pressure is from 21 psi to 17 psi .The higher the temperatures , the lower forging loads, forging pressures and percentage of reduction.

A-286 alloy is iron base alloy. Iron bases super alloys are widely used in the manufacture of turbine discs for turbo-jet engine application. The control of grain flow and grain size during forging depend on the sequence of forging operations as well as forging temperature and reduction. [6]

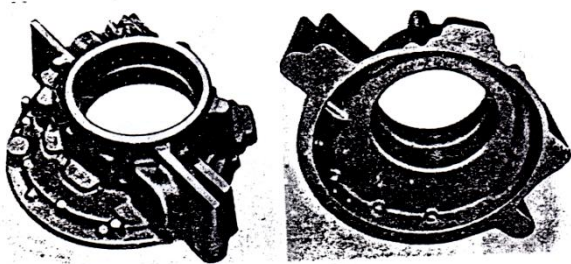


Figure 2. Two Views of Finished Aluminium Housing forging

Table 3. Effect of temperature on load, pressure and percentage of reduction for Turbine Disc Material

No: of Step	Material Used	Forging Temperature	For- ging load	Frog- ing pres- sure	% of red- uct- ion
1.	A-286 alloy Turbine Disc Material	1800°F	130lb	49psi	50%
2.			110lb	48psi	40%
3.			100lb	47psi	30%
4.			90lb	47psi	20%
5.			80lb	44psi	10%
1.	A-286 alloy Turbine Disc Material	2000°F	100lb	35psi	50%
2.			80lb	30psi	40%
3.			65lb	30psi	30%
4.			60lb	29psi	20%
5.			53lb	28psi	10%
1.	A-286 alloy Turbine Disc Material	2200°F	80lb	30psi	50%
2.			65lb	25psi	40%
3.			58lb	24psi	30%
4.			50lb	23psi	20%
5.			40lb	20psi	10%

Production of an Aluminium-alloy Housing

A large number of aircraft parts are forgings made of strong and light aluminium alloys. The finished housing is approximately 14.25 inches in diameter and 5.5 inches in height. Aluminium alloys have excellent forge ability and have higher strength to weight ratio compared to steel forgings. Aluminium alloys are used where temperature environment does not exceed 200°C. Besides the advantages high strength to weight ratio and lightness, aluminium alloys are quite ductile and forgeable to be readily formed to precise, intricate shapes.

The most significant reasons for these are, (1) alloys are ductile due to its basic F.C.C. structure, (2) they can be isothermally forged, (3) they do not develop scale during heating, (4) they require low forging pressures. A significant problem with heat treatable Aluminium alloy forgings is associated with the residual stresses imposed by quenching and sometimes by straightening just to adequately remove the residual stresses. [6]

Three different temperatures are described in table II. The study also shows percentage of reduction depends of forging temperature and forging load .At 2200°Fforging load is 80lb and forging pressure is 30psi give percentage of reduction of 50%. At 2000°F forging load is 80lb and forging pressure is

30psi. The percentage of reduction is 40%. So, the study also shows the same load and pressure .The higher the temperature, the less the percentage of reduction.

Table 4. Effect of temperature on load, pressure and percentage of reduction for Aircraft Housing

No: of Step	Material Used	Forging Temperature	Forging load	Forging pressure	% of reduction
1.	6061 alloy (Aircraft housing)	900°F	30lb	11psi	60%
2.			24lb	10psi	50%
3.			22lb	10psi	40%
4.			20lb	10psi	30%
5.			18lb	10psi	20%
1.	6061 alloy (Aircraft housing)	750°F	58lb	20psi	60%
2.			45lb	19psi	50%
3.			39lb	18psi	40%
4.			35lb	17psi	30%
5.			30lb	16psi	20%
1.	6061 alloy (Aircraft housing)	600°F	70lb	25psi	60%
2.			62lb	24.5psi	50%
3.			55lb	24psi	40%
4.			48lb	23psi	30%
5.			42lb	20psi	20%

Table 3 and 4 show the same percentage of reduction but higher temperatures give lower forging loads and pressures.

5. CONCLUSIONS

Low carbon steels are easy to forge and super alloys are difficult and have higher strength. After forging process, metals are stronger than other metals which are manufactured by other processes and also the forged metals have more shock and fatigue resistant and more durable than other un-forged products. Because of the forged metals have fine grain size and fibrous structure with highest strength, they may provide required properties with less weight. On the other hand, a forging process offers the cheapest mean for producing a component. The hammer forging method can be done at this Department. In this paper, three different types of materials are analyzed to determine the relationship between the forging temperature, forging loads and percentages of reduction. Forging process touch the industrial lives everyday. Industrial developments have direct effect on the standard of living today.

6. ACKNOWLEDGMENTS

Special thanks to Dr. Theingi, Rector, Technological University (Thanlyin), for her kind support and suggestions. The author is very thankful to staffs, Mechanical Engineering Department, Technological University (Hmawbi), Dr. Swe Zin Nyunt from , Technological University (Thanlyin) and Dr. Khin Mar Zaw, Lecturer, Engineering Science Department, for their encouragements to do the research paper.

7. REFERENCES

- [1] Begeman, Mynon, L., Manufacturing Process 4thEdition., John Willey & Sons, Inc., New York, 1957.
- [2] Campbell, Janes, S., Principles of Manufacturing Materials and Processes, Mc Graw-Hill Publishing Co. Ltd., New York, 1978.
- [3] Draper, Alan. B., Niebel, Benjamin, W.Wysk, Richard. A., Modern Manufacturing Process Engineering, Mc Graw-Hill Publishing Co. Ltd., New York, 1989.
- [4] G. Johnson, C., Forging Handbook, Am. Tech. SOC., Chicago, 1938.
- [5] Nwe Lin Min, Daw . M.E Thesis, 2000. Analysis Of Metal Forging Processes.
- [6] Sharan, R., S. N. Prasad., N. P. Saksena, Forging Die Design and Practice, S. Chand & Company Ltd., New Delhi, 1982.

GLCM and LTP Based Classification of Food Types

Wint Myat Thu
Department of Electronic
Engineering
Technological University
Thanlyin, Myanmar

Dr. Pann Ei San
Department of Electronic
Engineering
Technological University
Thanlyin, Myanmar

Daw Win Thandar Tun
Department of Electronic
Engineering
Technological University
Thanlyin, Myanmar

Abstract: Food is an essential part of life from the beginning of civilization. People need food every day. Food is an indispensable need to being healthy and living a long life. But, consuming more food than the body needs is unhealthy habit. So, evaluation the amount of food is becoming an interest topic nowadays. Thus, a food detection and classification algorithm is proposed. In this research work, a food detection and classification algorithm is based on image processing technique. With this technique, the types of food can be classified automatically by a computer system. The purpose of the research work is to classify the food images. Food detection and classification system is useful for calories measurements and other applications. The proposed system uses the food images dataset to detect and classify the food types by using image processing technique. The image processing techniques consist of image preprocessing, image segmentation and image classification. The k-means clustering method is used to get the region of interest image (ROI). After that, the features from the ROI image are extracted by using Gray-Level Co-occurrence Matrix (GLCM), Local Ternary Patterns (LTP) and both. Then, the food types are classified by using Support Vector Machine (SVM). Finally, the percentage of accuracy and the processing time are calculated. This result shows that the accuracy is 93% and useful to examine the food types.

Keywords: classification; image segmentation; gray-level co-occurrence matrix (glcm); local ternary patterns (ltp); support vector machine

1. INTRODUCTION

The detection and classification of food types is a major part in many applications for various purposes. Healthy foods support a person in the mental well-being and physical developing. Food is divided into the groups based on healthy eating. A healthy diet can prevent diseases. Some people think that the burning off a ton of calories at the gym is a way of eating whatever food types. There are many reasons why eating healthy is important. Having too much body weight means obesity. Obesity is one of the hot problems in the world. A person whose Body Mass Index is higher than or equal to $30(\text{kg}/\text{m}^2)$, is considered as obesity [1]. Most obese people are suffered medical conditions such as hypertension, irregular heart rate, diabetes, colon cancer and so on. The research work uses image processing techniques to classify food types such a French Fried, Fried Chicken, Pizza, Cooked Rice and Hamburger. Nowadays most Myanmar people consume these types of food daily. The research work is organized as follows; Section 2 covers related work in this area, while Section 3 presents a brief background of image detection and classification method. In Section 4, analyses the research work. Finally, section 5 concludes this research work and a brief discussion of future works.

2. LITERATURE REVIEW

In the area of image processing, many food detection and classification methods are the active research topics. Researchers have introduced various algorithms to improve the accuracy. The first step is to detect the images which contain food items [2]. The main purpose of this research work is to detect images that contain food and to classify the types of food. Many research works of food detection and classification assume that only one food item is present in one image. Researchers had been testing on food detection and classification using conventional approaches based on various image features and machine learning for many years. In some

analysis, researchers created a private Japanese food dataset with 50 classes. They proposed a Multiple Kernel Learning (MKL) method using combined features including SIFT-based bag-of-features, color histogram and Gabor Texture features [3]. Some researchers defined eight basic food materials and learned spatial relationships between these ingredients in a food image using pairwise features [4]. Other researchers classified the food types by using only Gray-Level Co-occurrence Matrix (GLCM) [5]. In this research work, the experiment is conducted on a special image dataset of 553 food images created with controlled environment. The L^*a^*b color space and k-mean clustering is used for image segmentation in this research work. SVM classifier is used to train images and to classify food types. The experimental results show that the accuracy of detection and classification is over 90%.

3. METHODOLOGY

The block diagram of the proposed work is shown in Figure 1.

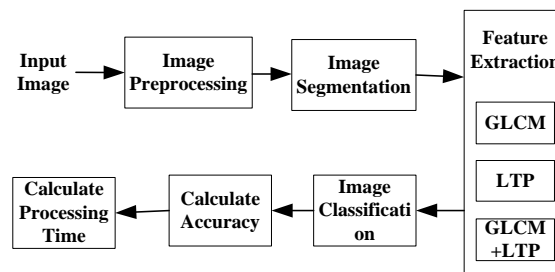


Figure 1. Block Diagram of the System

The flow chart of the food detection and classification system is shown in Figure 2.

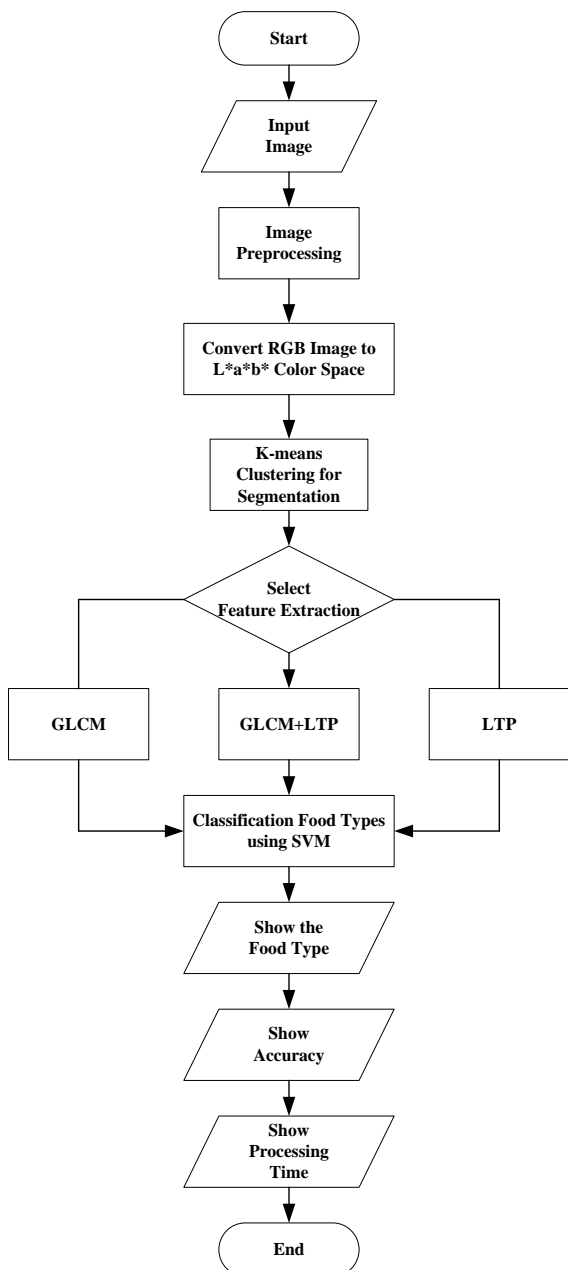


Figure 2. Flow Chart of the proposed system

The methodology of the research work can be divided into six steps. The image reading, image resizing and contrast enhanced image is the first step. The $L^*a^*b^*$ color space method and k-mean clustering method are used in image segmentation. The next step is feature extraction by using Gray-Level Co-occurrence Matrix (GLCM), Local Ternary Patterns (LTP) and both. The SVM classifier is used to detect and classify food types. Then calculate the accuracy and processing time. The procedure of food detection and classification system is as follow:

- Read input image
- Resize image
- Enhance contrast for the resized image
- Convert RGB color space to Lab color space

- Apply k-means clustering operation
- Extract the features from the segmented image
- Classify the types of food using SVM
- Calculate the accuracy
- Compute the processing time

3.1 $L^*a^*b^*$ Color Space

Coloring information is referred to the color of the white point of the system. The $L^*a^*b^*$ color model is based on the color model that the “Commission Internationale de l’Eclairage” (CIE) declared in 1931 to be the international norm for measuring colors.

This model was improved in 1976 and named CIE Lab. Then, $L^*a^*b^*$ colors are device independent; that is, they create constant colors independently from certain devices like monitors, printers, or computers that are used to create and print images. Moreover, $L^*a^*b^*$ colors are built by a luminosity or brightness component (L), and two chromatic components: the a-component ranges from green to red; the b-component from blue to yellow.

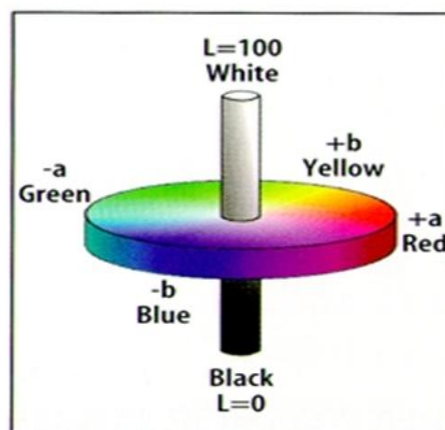


Figure 3. $L^*a^*b^*$ Color Model

The $L^*a^*b^*$ components are Luminosity L, and color components a^* and b^* which specify color hue and saturation along green-red and blue-yellow axes. $L^*a^*b^*$ color model determines the color depending on its position in a 3D color space, the L^* component is the lightness of the color (when $L^*=0$ means black and when $L^*=100$ refers to white) and the Chroma a^* (positive values indicate red and negative values indicate green) and the hue b^* (positive values refer to yellow while negative values refer to blue) as illustrated in Figure 3 [6]. CIELAB is device independent and considered very important for desktop color [7].

3.2 Gray-Level Co-occurrence Matrix

Feature extraction is the process of generating some quantifiable property to enable image classification. The image features can be classified into three types such as color, shape and texture. The color feature is extracted from the image by color histogram or color co-occurrence matrix. The color histogram can be assessed using three different color spaces including RGB, normalized RGB and HSI color spaces [8]. On the other hand, color co-occurrence matrix can be calculated using the four neighbouring pixels or eight

neighbouring pixels present in the image. The shape feature is extracted using two methods; region based and contour based.

The region-based method utilizes the entire area of the particle for shape description while the contour based method detects the information present in the contour of the particle. The third type of extracting features using texture is categorized into structural, statistical, model-based and transform-based. The statistical method measures the spatial interaction of image pixels and is further classified according to the number of pixels defining the local features such as first order, second-order and higher-order statistics. Histogram based method follows the first-order statistics and is widely used for feature extraction since they are fast and simple methods.

Features derived from this approach include moments such as mean, standard deviation, average energy, etc. The GLCM method following the second-order statistics determines the spatial relationship between the pixels by calculating the difference in intensities between the centre pixel and its neighbours. In texture classification, Gray level co-occurrence matrix is a great basis for use. The gray level co-occurrence matrix helps to get the details about the overall image content from various textural parameters [9].

3.3 Local Ternary Patterns (LTP)

Local Ternary Patterns are resistant to lighting effects in the sense that they are invariant to monotonic gray-level transformations, and they have been shown to have high discriminative power for texture classification. However because they threshold at exactly the value of the central pixel, i.e. they tend to be sensitive to noise, especially in near-uniform image regions. Given that many facial regions are relatively uniform, it is potentially useful to improve the robustness of the underlying descriptors in these areas. This section extends LBP to 3-valued codes, Local Ternary Patterns, in which gray levels in a zone of width $\pm t$ around i_c are quantized to zero, ones above this are quantized to +1 and ones below it to -1, i.e. the indicator $s(u)$ is replaced by a 3-valued function:

$$s'(u, i_c, t) = \begin{cases} 1, & u \geq i_c + t \\ 0, & |u - i_c| < t \\ -1, & u \leq i_c - t \end{cases} \quad (1)$$

and the binary LBP code is replaced by a ternary LTP code. Here t is a user-specified threshold (so LTP codes more resistant to noise, but no longer strictly invariant to gray level transformations). The LTP encoding procedure is illustrated in Figure 4. Here the threshold t was set to 5, so the tolerance interval is [10].

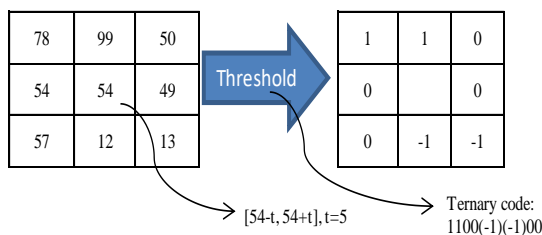


Figure 4. Illustration of the basic LTP operator

3.4 Support Vector Machine (SVM)

Machine Learning is an ability to enable the computer to learn. It uses algorithm and techniques which perform different tasks and activities to provide efficient learning. Our main problem is that how to represent complex patterns and how to exclude bogus patterns. Support Vector Machine is a machine learning tool used for classification and regression. It is based on supervised learning which classifies points to one of two disjoint half-spaces. It uses nonlinear mapping to convert the original data into higher dimension. Its objective is to construct a function which will correctly predict the class to which the new point belongs and the old points belong. With an appropriate nonlinear mapping, two datasets can always be divided by hyper plane.

Hyper plane separates the tuples of one class from another and defines decision boundary. There are many hyper planes that separate the data but only one will achieve maximum separation. The main reason behind maximum margin or separation is to classify a boundary, it may end up nearer to one set of datasets compared to others. This was the case when data is linear but mostly to find data is non-linear and data set is inseparable then kernels are used.

The core purpose of SVM is to separate the data with decision boundary and extends it to non-linear boundaries using kernel trick. Major benefit of SVM is versatile means different Kernel functions can be specified for the decision function. General kernels are provided, but it is also possible to specify custom kernels. SVM becomes prominent when using pixel maps as input; it gives accuracy equivalent to neural networks with elaborated features in a handwriting recognition task. Support vector machine is used for many applications such as text categorization, pattern recognition, face recognition, handwriting analysis but especially for classification and regression applications. The perceptron learning algorithms (e.g. gradient descent) are slower than SVM learning. SVM has been found to be unbeaten when used for pattern classification problems.

One of the major challenge is that of choosing a suitable kernel for given application. But there are many standard or default choices such as Gaussian or polynomial kernel but if these prove worthless then more elaborate kernels are needed. Traditional Classification approaches perform weakly when working directly because of high dimensionality of data but support vector machine can avoid the pitfalls of very high dimensionality representations. Support vector machine is the most promising technique and approach as compared to others. It scales fairly well to high dimensional data and the trade-off between classifier complexity and error can be controlled explicitly.

Another benefit of SVMs and kernel methods is that one can design and use a kernel for a particular problem that could be applied directly to the data without the need for a feature extraction process. It is particularly important in problems where a lot of structure of the data is lost by the feature extraction process.

Example is text processing. Limitations of SVM are speed, size both in training and testing. Discrete data presents another problem. Most severe difficulty with SVMs is the high algorithmic complexity and extensive memory requirements. In short, it can be said that the development of SVM is an utterly different from standard algorithms used for learning and provides a fresh insight into this learning [11].

4. TEST AND RESULTS

The test and result of food detection and classification are expressed in this section. Firstly, the image is resized into standard 256×256 pixels for simplicity. Large images or small images will be reshaped to this size before accomplishment of any image-processing technique. In the next step, the resized image is made contrast enhancement. And then, the RGB image is converted into L*a*b color space. The image is then segmented to separate the object and background by using k-means clustering algorithm. And then, select the segmented image. The results are shown in Figure 5, Figure 6 and Figure 7.

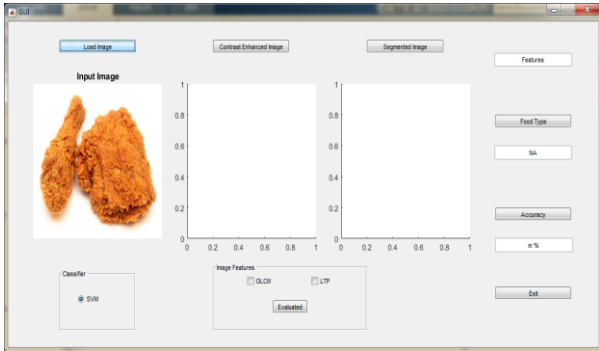


Figure 5. Load Image

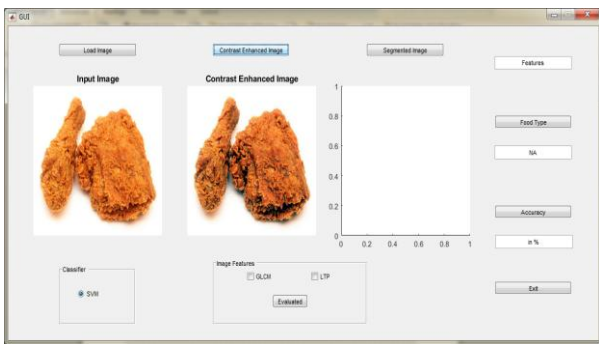


Figure 6. Contrast Enhancement Image

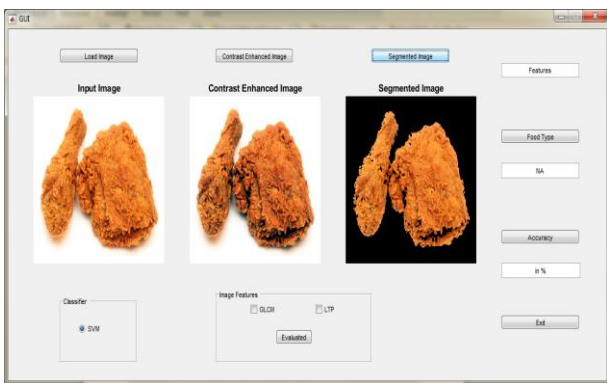


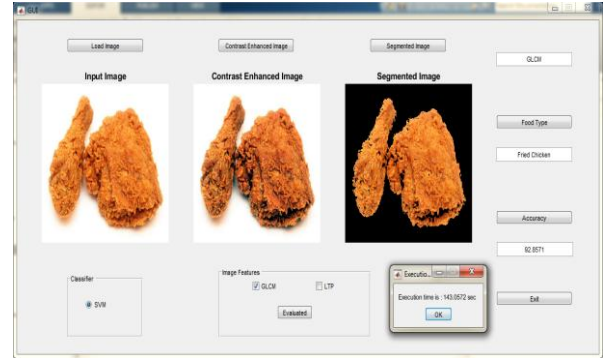
Figure 7. Segmented Image

The features are obtained by using Gray-Level Co-occurrence Matrix (GLCM), Local Ternary Patterns (LTP) and both. The food type can be classified by using Support Vector Machine (SVM). Then the percentage of accuracy is calculated [12].

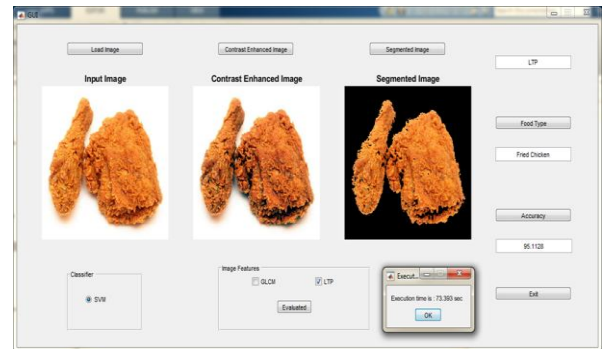
The overall accuracy of the food images can be calculated by using equation (2).

$$\text{Accuracy} = \frac{\text{The number of correctly recognized samples}}{\text{Total number of test symbol}} \times 100\% \quad (2)$$

In some cases especially for higher number of iterations, higher accuracy is achieved. In this research work, the maximum number of iteration is 500. Finally, compute the processing time. The results are shown in Figure 8(a), (b) and (c).



(a)



(b)



(c)

Figure 8. The Results for French Fried (a) GLCM, (b) LTP and (c) GLCM+LTP

The table shows that the result of processing time and accuracy by comparing different features. According to the table, the accuracy of the LTP method is the highest. Also, the

processing time is faster than others. So, a method combining the GLCM and LTP features is proposed. By experiments, the proposed method can be classified correctly almost all types of images in this research work. By combining these two features the accuracy and processing time are acceptable to calculate calories of food as the future work.

Table 1. Comparison of the proposed system in terms of processing time and accuracy

No	Input Images	Feature Extraction methods	Processing Time	Accuracy
1		GLCM	112.9sec	91.72%
		LTP	62.5sec	95.11%
		GLCM+		
		LTP	148.5sec	93.98%
2		GLCM	135.7 sec	92.85%
		LTP	67.2 sec	95.11%
		GLCM+		
		LTP	120.2 sec	93.60%
3		GLCM	143.1 sec	92.86%
		LTP	73.4 sec	95.11%
		GLCM+		
		LTP	124.9 sec	93.61%
4		GLCM	115.7 sec	92.48%
		LTP	88.9 sec	95.11%
		GLCM+		
		LTP	120.9 sec	94.18%
5		GLCM	109.6 sec	90.97%
		LTP	63.7 sec	95.11%
		GLCM+		
		LTP	123.9 sec	93.42%

5. CONCLUSION

This research work offers the detection and classification of food types. It concentrates on classification of food images by using image acquisition, image segmentation, feature extraction and image classification. The GLCM, LTP and GLCM+LTP feature extraction methods are used in the research. According to the result, the percentage of accuracy is enough to calculate food calories. This system can be used to help the overweight people without worrying about overeating and weight gain. To sum up, the proposed method is used for measuring calories and nutrition from food images.

6. ACKNOWLEDGEMENT

Firstly, the authors would like to acknowledge Dr. Thein Gi, Rector of Technological University (Thanlyin), for her kind permission to carry out this research work. The author particularly wishes to acknowledge all the teachers from Department of Electronic Engineering, Technological

University (Thanlyin), for their support, encouragement and invaluable guidance in preparation of this research. The authors would like to express their thanks to all persons who have given support during the preparation period of this research work.

7. REFERENCES

- [1] P. Pouladzadeh, S. Shirmohammadia, R. Almaghrabi, "Measuring Calories and Nutrition from Food Image," Distributed and Collaborative Virtual Environment Research Laboratory.
- [2] A. Singla, L.Yuan, T. Ebrahimi, "Food/Non-Food Image Classification and Food Categorization using Pre-Trained GoogLeNet Model," Multimedia Signal Processing Group, 2016.
- [3] T. Joutou, K. Yanai, "A food image recognition system with multiple kernel learning," In 2009 16th IEEE International Conference on Image Processing (ICIP), 2009, pp. 285-288.
- [4] M. Chen, K. Dhingra, W. Wu, L. Yang, R. Sukthankar, and J. Yang. P_d: Pittsburgh fast-food image dataset. In 2009 16th IEEE International Conference on Image Processing (ICIP),2009 , pp. 289-292.
- [5] Wint Myat Thu, Pann Ei San, and Win Thandar Tun. 2018. "A Cost Effective way of Food Detection And Classification Using Image Processing Techniques", 11th National Conference on Science and Engineering, YTU, Yangon, Myanmar.
- [6] Jayaraman,S., Esakkirajan S., and Veerakumar, T. 2009. Digital Image Processing. U.S.A.: McGraw Hill Co.
- [7] Myo Myo Han, "Anaiysis on Detection Improvement of Textile Fabric Defects using Gray Level Co-occurrence Matrix for automatic system," M.E .thesis, Dept , Electronic Eng., Yangon Technological University., Yangon, Myanmar, 2017.
- [8] S. Jayaraman, S. Esakkirajan , and T.Veerakumar, Digital Image Processing. U.s.a. :McGraw Hill Co.,2009.
- [9] Dhanashree Gadkari, B.S.E.E. University of Pune, 2000, " IMAGE QUALITY ANALYSIS USING GLCM " , Master Thesis, The College of Arts and Sciences at the University of Central Florida Orlando, Florida.
- [10] Xiaoyang Tan and Bill Triggs. 2007. "Enhanced Local Texture Feature Sets for Face Recognition Under Difficult Lighting Conditions", INRIA & Laboratoire Jean Kuntzmann, 655 avenue de l'Europe, Montbonnot 38330, France, pp. 168–182.
- [11] Yashima Ahuja and Sumit Kumar Yadav. 2012 . Multiclass Classification and Support VectorMachine , Global Journal of Computer Science and Technology Interdisciplinary ,Volume 12, Issue 11 Version 1.0
- [12] S.S. Patki and G. S. Sable. 2016. "Cotton Leaf Disease Detection & Classification using Multi SVM", International Journal of Advanced Research in Computer and Communication Engineering, Vol. 5, Issue 10,pp. 165-168.

Human Machine Interface System for Filling and Capping Process

Su Yadanar
Department of Mechatronic
Engineering
Mandalay Technological
University
Mandalay, Myanmar

Theingi
Rector
Technological University
Thanlyin, Myanmar

Wutyi Win
Department of Mechatronic
Engineering
Mandalay Technological
University
Mandalay, Myanmar

Abstract: In this research, bottle filling and capping processes are performed simultaneously in the pharmaceutical factory by using the PC based human machine interface (HMI) control system. In the traditional method of bottle filling process, the bottles are placed onto a conveyor and only one bottle is filled at a time. So, this method is time consuming and expensive as wide working place and many human labors is required. In this research, the proposed design can solve this problem without any complex control by using the HMI automation control system. The monitoring and running conditions in the packaging system are shown on the monitor of computer by using the composed of Visual Basic.Net and Mikro C. It also includes the volume of medical powder is limited by changing the size of filling funnel which is set up of shutter at the top and bottom of funnel. The entire system is more flexible and time saving. A prototype is implemented by using the DC motor, sensing devices; limit switches, peripheral interface controller (PIC) device and serial port communication. These control systems is very flexible, cost effective, space efficient and reduce complexity. PC based HMI control is used for monitoring the process.

Keywords: Bottle filling and capping process; Serial Interfacing; Motor Driver; HMI Control System; Manufacturing System

1. INTRODUCTION

As Myanmar is developing country; many pharmaceutical industries are being improved in health care sector by using the automation control system. For these kinds of applications, the trend is moving away from the individual devices or machine toward continuous automation solution. The filling and capping operation is implemented for packaging the medical powder and this can be used other system of various industries. Nowadays, most of the modern industrial plants have applied the automation control system. Automation is the use of control systems and information technologies to reduce the need for the human labours in the production of goods and services [2].

Among many industries, the pharmaceutical factory is one of the powerful players in the developing countries. In the manufacturing process of pharmaceutical products, the many steps are needed for companies and individuals to gain a complete process. In many production steps, packaging is a critical tool in the pharmaceutical industry for the product delivery. Packaging is composed of primary and secondary packaging processes. The primary packaging components (e.g. bottles, vials, closures, blisters) are in direct physical contact with the product, whereas the secondary components are not (e.g. carton, cardboard, boxes) contact with the product [3]. In this research, primary packaging system is emphasized for the medical powder filling and capping processes of bottles.

The packaging of a pharmaceutical product is aimed that the medicines arrive safely in the hands of the vendees. In the qualities of the pharmaceutical products, the quality of the packaging of pharmaceutical products plays a very important role [1]. So, this research is mainly aimed on the integration of primary packaging system in which filling and capping operation is done simultaneously at the same place by using the human machine interface in the industries. The advantages of this system are that taking low space, saving labors cost due to one or two operators is needed and reducing the time consuming.

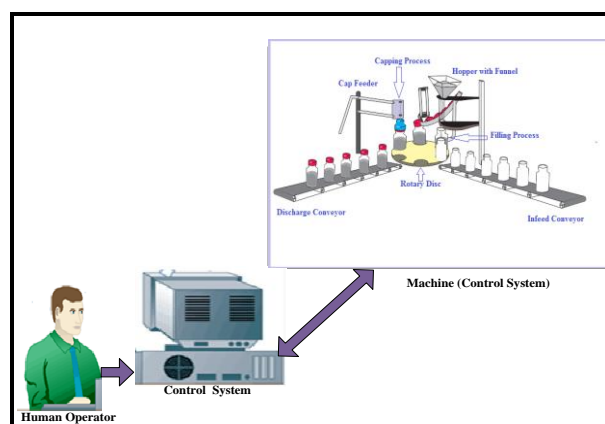


Figure 1. Sketch diagram of PC based Monitoring System for Primary Packaging System

This system allows the user to control the process, monitoring production data and correct malfunction. This user-friendly interface minimizes system complexity, operator training and troubleshooting time. The real-time monitoring for the primary packaging system is designed with the signal sensing by using the controller and interfacing programs. The sketch diagram for the packaging operation is shown in Figure 1.

2. METHODOLOGY

This research is emphasized on the PC based HMI control system for the primary packaging process in which the automation of filling and capping processes. In this system, belt conveyor is used for carrying the bottles to the rotary disc which is used for the bottles filling and capping processes simultaneously.

DC motors are used to control the motion of conveyors and capping processes. Peripheral interface controller 16F887 microcontroller is used because of providing the serial communication interface and controlling the motor motion. LDR sensors are used for the position sensing circuit. In the firmware sector, Mikro C and VB.Net programming language is used. Personal Computer (PC) is used as human machine interface (HMI) system and provided the series of episode for monitoring and controlling the process. Visual Basic.Net programming is provided in the implementation and displaying of packaging processes for the monitoring system. The block diagram of this system is shown in Figure 2.

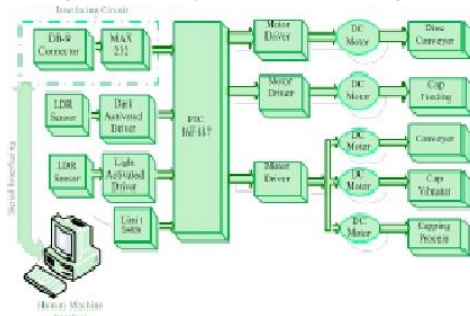


Figure 2. Overall Block Diagram of Primary Packaging System

3. CONTROL SYSTEM AND ELECTRICAL SETUP

This system is composed of four portions; interfacing system, control unit, position sensor input portion and output motors driving circuits. The pin connections of the PIC16F887 are very important to control the processes and it is also a brain of a whole process [4]. These connections of the PIC16F887 are described in Figure.3.

In this interface controller, port D is assigned as input pins and port B is used as output pins. RD0, RD1 and RD2 from port D are used to sense from the position sensors of the rotary disc. RB0, RB1 and RB2 from port B are used as output pins to drive the motors for the conveyor, disc and capping processes. RC6 and RC7 are used as interface ports between the PIC and PC.

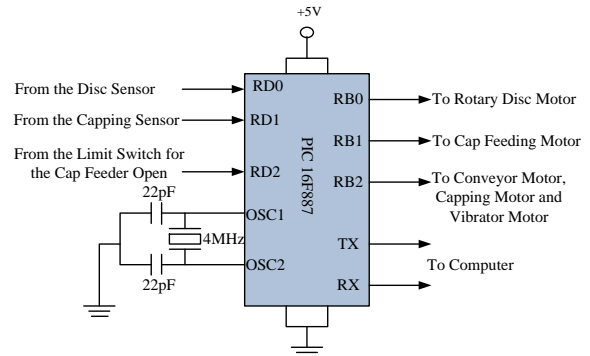


Figure 3. Pin Connection of PIC 16F887

3.1 Interfacing System

In the interfacing system, serial communication method is used in which DB 9 connector and RS232 protocol is implemented. In the serial interfacing system, MAX 232 level converter is needed to convert the voltage level between the PC and PIC controller. It is used to convert RS232 logic level into the TTL logic level because microcontroller is compactable with TTL logic. In TTL, logic '1' is used +5V and logic '0' is +0V. In RS232, logic '1' is -12V and logic '0' is +12V [5]. The pin connection of MAX 232 is shown in Figure 4.

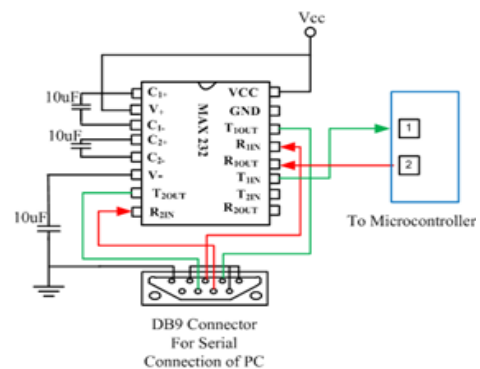


Figure 4. Pin Connection of MAX 232

3.2 Position sensor Input Portion

The position sensor circuit is used to know the arrival of the medical powder bottle. LDR (Light Dependent Resistor) sensor is designed as dark active circuit. The signal is sent when the bottle passes through the sensor. The output signal of the position sensor circuit must be 0V all the time and nearly 5V output is sent to the PIC when the bottle is passed.

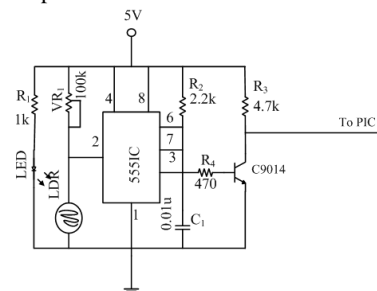


Figure 5. Position Sensor Drive Circuit

Two LDR sensor or positions sensors are placed on the disc conveyor for the filling and capping process. The counter starts counting at the cap feeding position. When the bottle reaches in the light of the LED, the resistance of the LDR will be taken $1M\Omega$. In Figure 5, the output waveform of the circuit is low pulse signal. To generate this signal, the 555 timer monostable circuit is used to generate the required input voltage for microcontroller.

3.3 Motor Driver Circuit

The DC motor driver is needed to control the magnitude of supply voltage for controlling the speed of DC motor. Moreover DC motors cannot be driven directly with a microcontroller as they require high current and high voltage than a microcontroller can handle. The DC motor driver circuits that will be used in this research are a relay driver, and the SG3525 pulse width modulator control circuit that offers improved performance and lower external parts count when implemented for controlling all types of switching power supplies [7]. The conveyor, rotary disc, cap holder, capping process and cap feeder are driven by DC motors. In this driven system, relay driver with transistor C9014 switching circuit is used as shown in Figure 6.

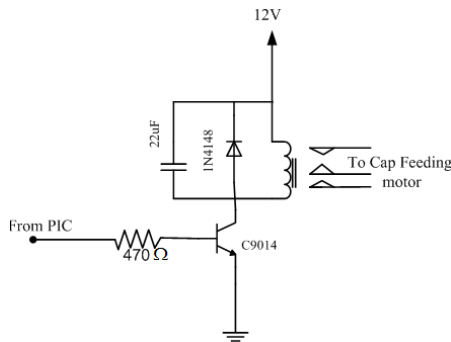


Figure 6. Relay motor drive Circuit

Transistor C9014 is being used to control the relay with a 12V coil, operating from a +12V supply. Series base resistor 470Ω is used to set the base current for the transistor, so that the transistor is driven into saturation (fully turn on) when the relay is to be energized [8]. That way, the transistor will have minimal voltage drop, and hence dissipate very little power as well as delivering most of the 12V to the relay coil.



Figure 7. (a)Electrical Setup and (b) Control box

A power diode IN4148 is connected across the relay coil, to protect the relay coil from damage due to the back-EMF pulse generated in the relay coil's inductance when the transistor turns off. Electrical setup and control box of this system is shown in Figure 7(a) and (b).

4. HARDWARE COMPONENT OF THE SYSTEM

The filling and capping operation is implemented in a sequential manner. In this system, it is composed of the conveyor which is used for transporting, cap slide and cap feeder for capping process, rotary disc and hopper for filling process.

4.1 Belt Conveyor and Rotary Disc Conveyor

Belt conveyor which is constructed by rubber belt and its guide way which is made up of fiber plastic is used to carry the bottles. Its length is 16inches and its width is 2 inches. Photo of belt conveyor is shown in Figure 8(a). Disc conveyor is used for the filling and capping process and is constructed by fiber plastic. It is composed of six plots and its diameter is 11inches. Photo of rotary disc is shown in Figure 8(b).

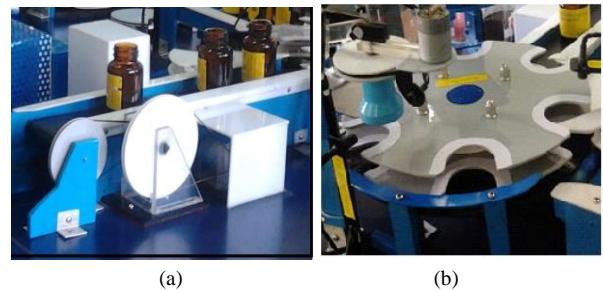


Figure 8. (a) Belt Conveyor and (b) Rotary Disc

4.2 Hopper for Filling Process

Hopper is used for filling process where hopper is set up with the funnel to drop the medical powder. This is made up of the fiber plastic which is lightweight and cheap to build the prototype. Funnel is designed with its length is 3.5 inches and its area is 0.5625 sq.-inches. Filling process is controlled by placing the shuttle valves at the top and bottom of the funnel. Photo of hopper with funnel is shown in Figure 9.

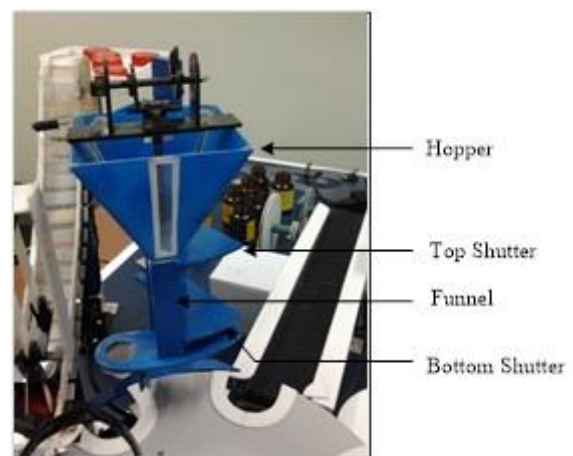


Figure 9. Hopper for Filling Process

The top shuttle valve is set up between the bottom of the hopper and the top of the funnel. When the filling process

start, the top shuttle valve is closed and the bottom shuttle valve is opened by rotating the disc with carrying the bottle. If the bottle don't present at the filling position on the disc, the filling process will not start. If the filling process doesn't start, the top shuttle valve is opened and the bottom shuttle is closed. The filling process is constructed by the mechanically design and control.

4.3 Capping Mechanism

A cap is applied to a bottle at station two on the rotary disc, which is a pre-tightening station. The capping mechanism consists of a caps holder, a stationary arm and a capping arm/head. There is a vibrator motor is employed to vibrate the cap holder for moving the caps to the cap slide. The cap feeder is applied for tightening the capping process. The capping head can move up and down in a controlled manner. Whenever the cap feeder sensor gets the signal from detecting the bottle, the cap feeder moves down and tightens the cap against the bottle. The limit switch is used to move up the cap feeder. Capping Mechanism is shown in Figure 10.

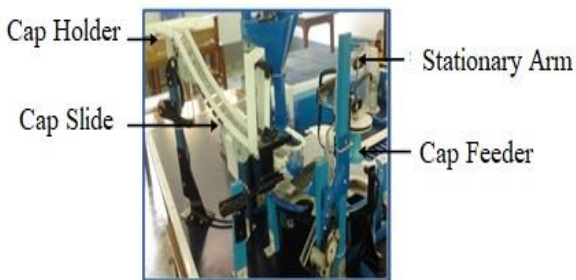


Figure 10. Capping Mechanism

4.4 Cap Feeding Process

In the cap feeding system, DC motor is used for the cap feeding process. At this position, LDR sensor is used as the position sensor. When the bottle reaches at the cap feeding position, the disc conveyor will stop as the position sensor gets the signal. At that time, the capping motor come down and operates the cap feeding process. The capping time is limited by the limit switch. Cap feeding photo is shown in Figure 11.



Figure 11. Cap Feeding Process

4.5 Position Sensor

The position sensor circuit is used to know the arrival of the medical powder bottle. LDR (Light Dependent Resistor) sensor is designed as dark active circuit. The signal is sent when the bottle passes through the sensor. The output signal of the position sensor circuit must be 0V all the time and nearly 5V output is sent to the PIC when the bottle is passed. Two LDR sensor or positions sensors are placed on the rotary disc for the filling and capping process. The counter starts counting at the cap feeding position. The counter is used to show how many bottles have been filled and capped during the operation process. Position sensor 1 is used for filling process and position sensor 2 is used for capping process. Position sensor design is shown in Figure 12.

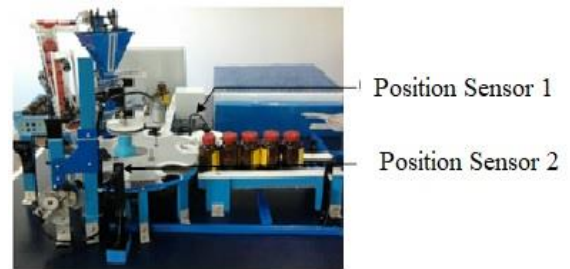


Figure 12. Position Sensor Design

5. SOFTWARE DEVELOPMENT OF THE SYSTEM

Human machine interface (HMI) control system is a computer control software application. HMI Systems provide the automation control system. PC based HMI system is divided into two major portions; the first one is to interface the control unit with PC and the next portion is to monitor the whole process. The VB.Net programming from Visual Studio 2010 IDE is utilized as the monitoring program. Micro C programming language is used as controlling software for the PIC controller. Block Diagram of linking window for control and simulation is shown in Figure 13.

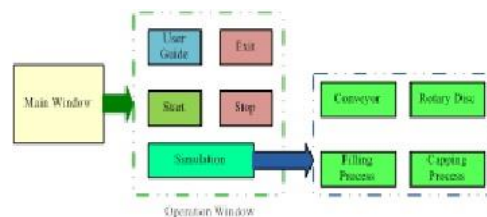


Figure.13. Block Diagram of Linking Window for Control and Simulation

In HMI applications with a graphical interface, the complex operations in the real time system can be monitored and controlled by commanding from the PC. In this research, the implementation and displaying of filling and capping process for the monitoring and control system use Visual Basic.Net programming language as HMI software. The serial communication method is used as the interfacing system between the PC for the monitoring and hardware system [9].

To start the serial communication, initialize the UART module and assigned the baud rate as 9600. The interfacing component for the serial communication method is very simple. It has to use only MAX 232 level converter to convert the voltage level between PIC and PC. The flow chart of the system is shown in Figure 14.

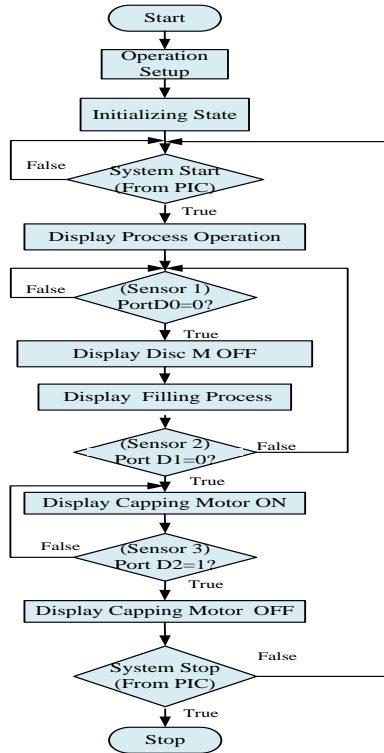


Figure .14.VB.Net Programming Flow Chart of the System

4.5 Linking Window System for the Process

The operation of the filling process can be run and stopped from main page by the operator.

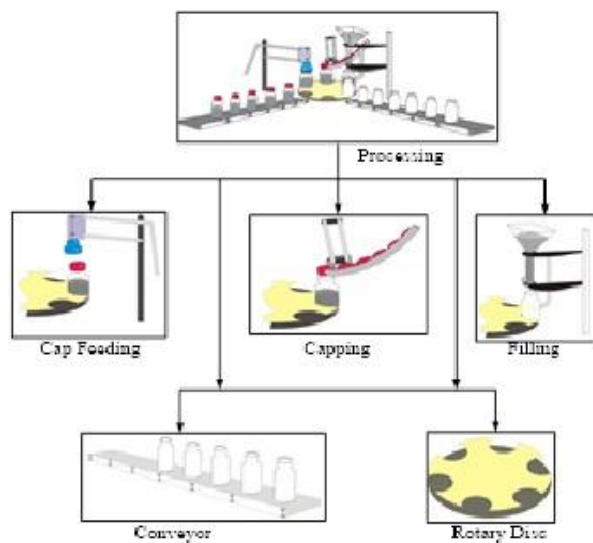
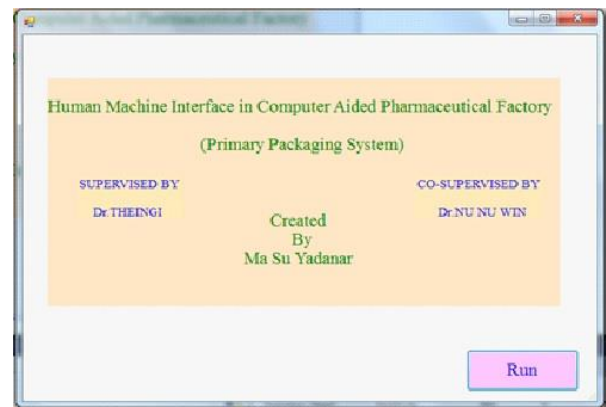


Figure 15. Linking Window Pages with Operation Page (Processing)

The main page serves to collect data from the operation window and to display in real-time running condition. When the main window is shutdown, the processing is shutdown all process except receiving command from the main window. So, the application software can be viewed in window frames, linking windows with processing page are shown in Figure 15.

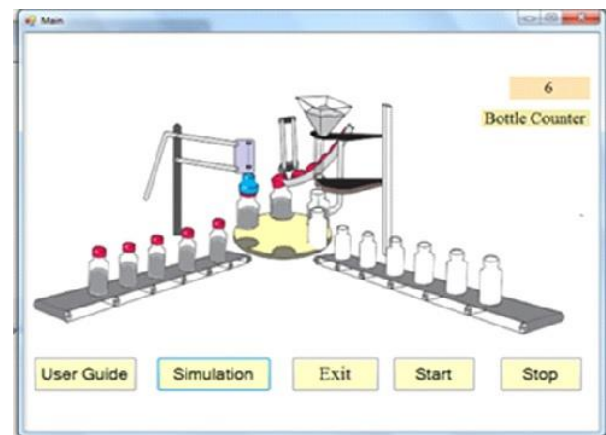
4.6 Displaying the System

The display system only intends to monitor and control for the process. For the overall system, the hardware devices for control unit are connected to the computer including window application software using the serial port connector. Serial communication method is used to communicate between the operating system and the displaying system. The monitoring software is implemented by the seven pages. They are the main page, simulation page, instruction page, filling page, capping page, cap feeding page and disc page. The first page is the title name of the project and also includes run button which is linked to the main page. The title page is shown in Figure 16.



. Figure 16. Simulation Result of the Title Page

The title page can firstly be seen when the software is run. The name of the research is expressed in this page. By pressing the run button on this page, the main page will be appeared.



. Figure 17. Simulation Result of the Main Page

The main page which links other pages is composed of user guide, simulation (operating) which links the devices operations, start, stop and exit buttons. The main page also includes the bottle counter box. This bottle counter shows the number (quantity) of bottles which are completed with filling and capping processes. The main page is shown in Figure 17.

The simulation page is the main process of the monitoring system to show for all operations. The simulation page is designed with the sample components for the real devices of packaging process by using the images of the devices. It shows the monitoring of the changing or moving of components. It uses I/O signal from serial port for the operation sequence by using each their signal. By clicking the simulation button on the main page, the running condition of the operation page is appeared as Figure 18.

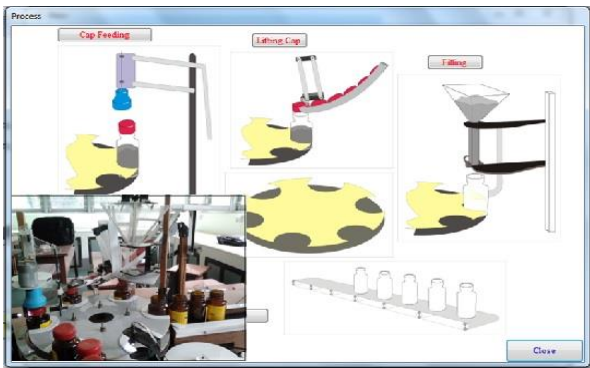
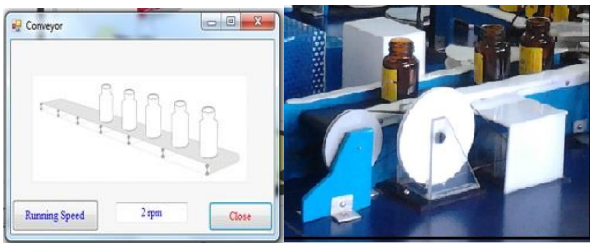


Figure 18. Displaying of the Simulation Page

The simulation of conveyor can be seen by clicking the figure of conveyor on the simulation page, is shown as Figure 19(a) and the photo of conveyor is shown in Figure 19(b).

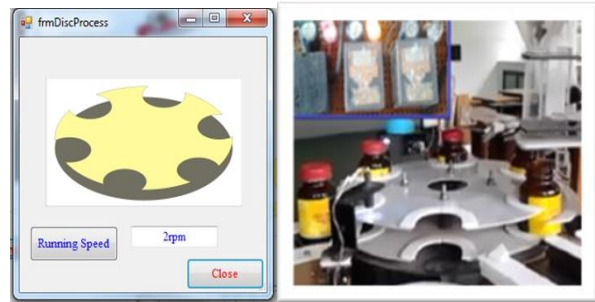


(a) (b)

Figure 19. Simulation and Photo of Conveyor

(a)Simulation of the Conveyor Page and (b) Photo of the Conveyor

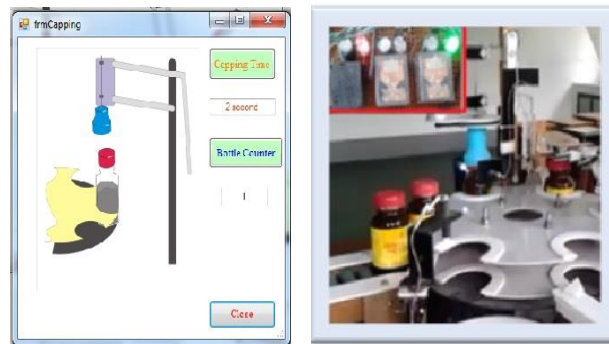
The text box contains in this page to define the moving speed of the conveyor motor. The close button is used to close the conveyor moving page and go back to the process simulation page. In the control circuit, three LEDs; red, yellow and green are used to show the running conditions of the process respectively. The red LEDs will be displayed when the conveyor is moved. The red LEDs will always be displayed as the conveyor will be ON as soon as the process start operates. The figure for the conveyor is implemented as the image of the real conveyor in the hardware design. Displaying of the rotary disc is shown in Figure 20(a). The figure for the rotary disc is implemented in the monitoring system as the image of the real disc in the hardware design. Photo of the rotary disc is shown in Figure 20(b).



(a) (b)

Figure 20. Simulation and Photo of the Rotary Disc
 (a) Simulation of the Rotary Disc Page and(b) Photo of the Rotary Disc

In the bottle filling page, the counter and timer tools are used to fill the medical powder into the bottle as the real filling process. Bottle filling page contains the text boxes to define the filling time and the amount of medical powder which is filled into the bottle. By clicking on the figure of cap feeding process on the simulation page, the cap feeding process will be shown as in Figure 21(a).



(a) (b)

Figure 21. Simulation Result and Running Condition of Cap Feeder

The cap feeder will operate when the signal is received from the PIC. The PIC will send this signal when the bottle reaches near the position sensor (light sensor). If the signal from the PIC is not received, the cap-feeder will not operate. The green LEDs will be lighted when the cap-feeder is running condition as shown in Figure 21(b).



Figure 22. PC Based HMI Packaging System

In this research, the operation conditions of the whole system are displayed by the PC based HMI system. This research aims to verify that the machine can fill and cap for six medical powder bottles in one minute. So the production rate is roughly 360 bottles per hour. The experimental results of the system is shown in Figure 22.

5. CONCLUSIONS

This research is a development of PC based HMI system for the packaging system. In this research, design and implementation of the filling and capping processes that used Visual Basic.Net programming for the monitoring and control of PC based HMI system have been studied. Serial interfacing system for this process which is used for communication between the PC and control system is designed and constructed and tested by connecting both hardware and software. PIC microcontroller is used in this system instead of PLC. Hardware of packaging process is designed with the prototype and tested by connecting hardware and software for monitoring of the running condition. This system provides a platform for further advancement in the field of industrial use of the filling process. It is possible to automate any system, improving the production time, saving cost, and the repeatability of the end product.

6. ACKNOWLEDGMENT

The author wishes to express deeply grateful thanks to Dr.Theingi, for guidance, help and sharing fruitful ideas. The author is deeply grateful to Dr. Nu Nu Win for willingness to share ideas, experience. I would like to express my sincere appreciation to Dr. Wutyi Win for their guidelines, encouragement and care for this research. The author wishes to acknowledge her teachers at Department of Mechatronic Engineering from Mandalay Technological University who

will concern to support in preparing this paper. Finally, I especially acknowledge my great special thanks to my parents.

7. REFERENCES

- [1] American Industrial Systems, Inc. (AIS), “Packaging Machinery Industry
- [2] S. David O’, “Industrial Automation ”, Course Notes, Universidade do Minho, May 2009.
- [3] WHO – Guidelines on packaging for pharmaceutical products, No.902, 2002
- [4] [http://msdn2.microsoft.com/library/30swa673\(en-us.vs.80\).aspx](http://msdn2.microsoft.com/library/30swa673(en-us.vs.80).aspx)
- [5] Craig Peacock, January 1998,“Interfacing the Serial/RS232 Port V5.0”
- [6] [http:// www.senet.com.au/cpeacock](http://www.senet.com.au/cpeacock).
- [7] Gary Cornell and Jonathan Morrison, “Programming VB.NET: A Guide for Experienced Programmers”, Copyright United State of America, 2002.
- [8] <http://onsemi.com>, DC Motor Driver Fundamentals.
- [9] Gary Cornell and Jonathan Morrison, “Programming VB.NET: A Guide for Experienced Programmers”, Copyright United State of America, 2002.
- [10] Microchip Technology,2001,“PIC 1687x DATA sheet 28/40 pin -8bit CMOS FLASH microcontrollers,” inUSA.
- [11] Aung Naing Myint, Hla Soe, Theingi, Win Khaing Moe ‘Implementation of control unit using SCADA system for filling system’, World Academy of Science, Engineering and Technology, 2008.

Design, Analysis and Evaluation of the Sun Simulator Mechanism

Farhad Fani Saberi
Institute of Space science and
Technology
Amirkabir University of
Technology (AUT)
Tehran, Iran

Ali Kasiri
Department of Aerospace
Engineering
Amirkabir University of
Technology (AUT)
Tehran, Iran

Hashem Bazrafshan
Iranian Space Research Center
(ISRC) Tehran, Iran

Hossein Rostami Barooji
Department of Mechanical
Engineering
Amirkabir University of
Technology (AUT)
Tehran, Iran

Mehdi Zandieh
Institute of Space science and
Technology
Amirkabir University of
Technology (AUT)
Tehran, Iran

Farshid Parhizgar
Department of Mechanical
Engineering
k. N. Toosi University of
Technology
Tehran, Iran

Abstract: In the satellite laboratories, sun simulator is one of the most important equipment in order to test satellite sun sensors. The behaviour of sun sensors is strongly influenced by the angle of sunshine. Therefore, increasing the accuracy in the testing mechanism of these elements is essential for their overall monitoring of their performance before launching to space. Sun simulator includes electronics and control units, structures, motion mechanisms, heat control, optics and light sources. In the design of the motion mechanism and the structure of this simulator, the considerations of the instruments such as the material of the structure, the type of joints, the structural components, motion mechanism of the projector, the static and dynamic loads applied to the structure and the thermal considerations caused by the projector heaters are very important. The purpose of this study is to design and analyse the loading, dynamical and thermal properties of the solar system simulator with precision positioning. Therefore, at the first, plans are proposed and the proper design is selected and preliminary design and partial design are done. Finally, after selecting the components of the system, various analyses and the correct operation of the device will be approved in order to evaluate the system's resistance to static and dynamic loads as well as vibrational and thermal loads.

Keywords: Sun simulator design; Attitude determination and control sub-system; Satellite; Vibrational and thermal analysis;

1. INTRODUCTION

In recent decade, the aerospace industry and its discoveries are the fields which have been very dynamic activities. Activities in this area require the growth of science and technology in the control and guidance field of aerospace systems. Space environment, due to unpredictable behavior of things and obstacles and also lack of precise knowledge of equipment workspace specifications are serious problem in this area. In order to exploratory and research travel to the space, spacecrafts and satellites are used. Therefore, in order to have accurate navigation for spacecraft or satellite in the environment of outside the atmosphere, one of the suitable guide is the sun and its light.



a



b

Fig. 1 Two samples of the device made for the sun simulator: a) a stimulus sample with a manual winch of Astofein; and b) a sun simulator with manual positioning of ADCS TB.

For this purpose, most of space crafts and satellites are equipped for measuring the angle of sunshine to make a detailed adjustment and reported information about the position of the spacecraft. The main challenge of space systems, the lack of access near and low cost to the real working space which are made for that space. For example, if needed check and verify one-stage of sensor angle which is mounted on the spacecraft from a functional point of view, It is necessary to test in the outside the atmosphere which is not feasible and has much costs. Therefore, designing and manufacturing equipment to simulate the work space of spacecrafts and satellites is necessary in the laboratory environment.

Satellite attitude and determination control laboratory system(ADCS) is designed to test satellites in order to guide and navigate equipment and their verification. Very precise equipment which two of them are shown in figure 1, have many different components, like test table system which has very sensitive degrees of freedom, sun simulator and etc.

In existing sample of this test device, adjustment system for projector positioning of sun simulator which simulates inversely the behavior of the sun. driven manually and there is

no possibility to accurately adjust the position of the projector to prove correct operation of angle sun sensors.

The aims of this work are dynamic and thermal loading of sun simulator and positioning satellite test device with precise positioning. Therefore, at first proposed proposals are introduced and suitable proposal will be selected. In the following details of design are called and fully designed will be completed. Finally, render various analysis to evaluate the systems resistance to static and dynamic loads and also vibrating and thermal loads, and the correct operation of the device is confirmed.

2. CONCEPTUAL DESIGNS FOR THE MOVABLE PART OF SUN SIMULATOR

2.1 Introduction

In order to design a sun simulator, it is necessary to consider possible schemes for drive system. In this section, first, a few possible plans to fitting suitable system location and system actuation mechanism are investigated. The main challenges of the system and optimal solutions will be mentioned and the final design will be presented.

Existing challenges and design goals are as follows:

- 1.the structure must be non-magnetic
2. reduce the cost of construction as much as possible
3. ability to position the device
4. possibility to accurately position of the projector and mirror assembly
5. the presence of curvature of the path and the motion
6. high occupancy space
7. high thermal temperature of projector lamp
8. reduction of dynamic forces on the structure
9. possibility of changing the angle of reflection of light on the satellite
10. resistance of the structure for possible transverse load
11. resistance Of the structure to dynamic load from the actuating system.
12. resistance to earthquakes and vibrational motion of the environment
13. low maintenance costs and optimal safety.

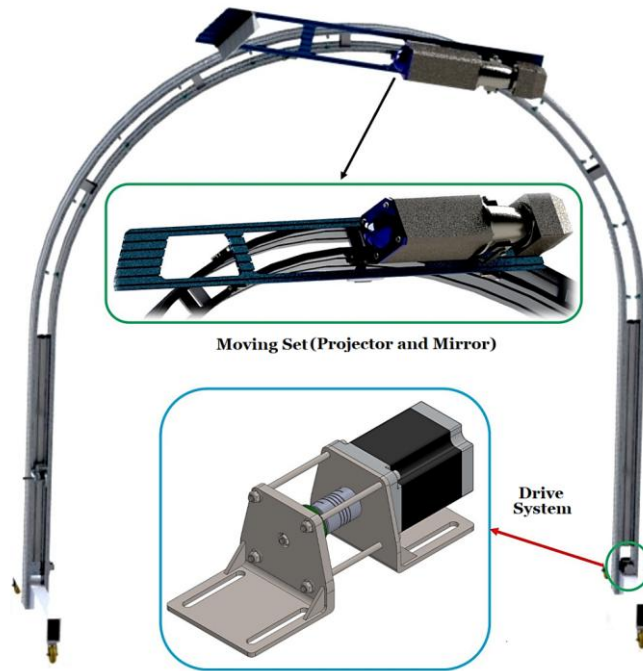


Fig. 2 Outline and main components of the sun simulator.

By considering all of these, the proposed scheme is presented in figure 2 which in following will be focused on design details and analysis.

2.2 First concept design: put the motor on the drive system

One of the plans is to put a flat-small-motor on aluminum base of lamp and pass a path of cable over the Pulley. In this plan only needs a cable path and by passing a few cables through pulley of motor and providing sufficient friction, the moving of base on the constant cable is guaranteed. In addition, the range of this system for adjustment sufficient preload on the cable is so important.

Using only one motor and a cable path is an advantage, because the cost of segment will be reduced and easier control. In return, the obligation to use a mechanism for passing the motor and accessories of motor over the rollers, increases the complexity of the system. In addition, by increasing the weight of moving set in the system and consequently the dynamic forces are important factors. As another disadvantages, the reliability of the system due to the possibility of damage to the moving set and also mention maintenance problems which all of these, together offer a partly weak design. The idea of this kind of moving set is taken from telecabin which is shown an example in figure 3.

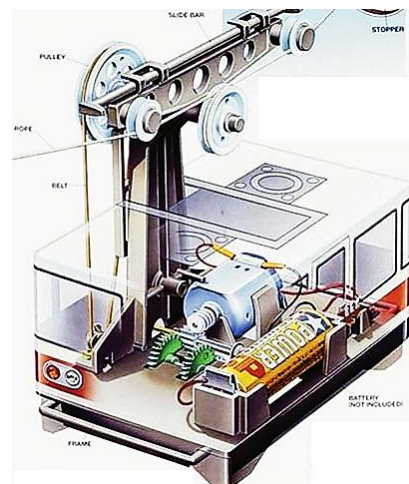


Fig. 3 Cable car (tele cabin) self-contained drive system [3].

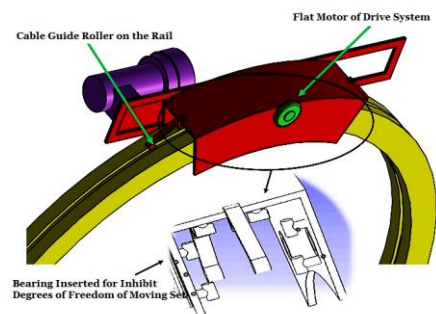


Fig. 4 First conceptual design for locating the motor of the driving system, bearings, rollers, and how to insert and direct the cable.

An overview of the conceptual plan 1 is presented in figure 4. In this figure, the green disk is a schematic of motor, the bulb is shown in purple, and as shown in the figure there is a mechanism to keep the cable in the middle to cross the roller over the motor and Pulley should be located which has a little space for guide cable on to the roller. the cable movement on the rail is also inside the groove on the path which this idea although dose not use the conductor roller, but versus power drop due to slipping cable connection and path will happen which is the disadvantage of cabling of this project.

2.3 Second conceptual design: Fitting the fixed motor next to the base

One of the **most** reasonable plans is to use a fixed motor on the base. The mechanism of this design is quite similar to the plans which is used in the telecabin figure4. There is a going round path and the base of the lamp is fixed and connected to the cable.



Fig. 5 Cable car rail drive unit in terminal [4].

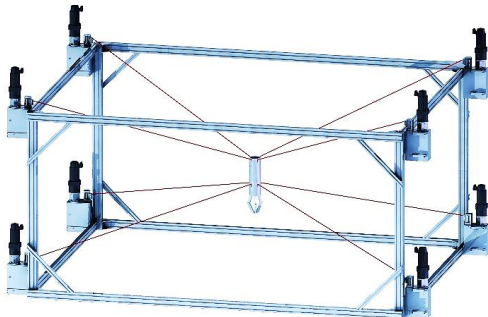


Fig. 6 Cable-Driven Parallel Robot [6].

In going round path for guide the rollers of cable must be inserted, additionally to adjust the preload inside the cable can tighten the strap which a Pulley is used outside the cable line.

The clear advantage of this design is, its simplicity, additionally the mass of movable has been reduced and does not require range.

One of the disadvantages of this project is cable stretching. In this type of mechanism, the cable is rotated over pulley many rounds and then crossed, according to direction of pulley rotation, always, one side of the cable is under more force, this is possible to effect the positioning of the movable and do not provide enough precision. This error is found when movable set is coming down from the opposite site and in this case if the movable set does not have stretch, there is a possibility of falling to the front.

2.4 use two fixed motors on both sides

Another plan which is exist, put two motors on both sides of the base, in this plan, the problem of freedom of cable on one side will not exist, because only one cable path is required. Like that rotation side of the two motors must be opposite of each other until one motor collect cable and opposite motor open the cable. this design is the same as the cable robots which controlled by the cable. In this system , to move the clamp in different direction, are used separate operators.

The important advantages of this project than previous project is resolving the problem of positioning accuracy because in this project always two movable side of cable are under stretch. Also, in this project is used one cable path too.

Perhaps paying for another motor can be the defect of this plan. Of course it is important to mentioning which in this plan, on the way back there were a number of rollers which were eliminated. And for this reason the cost of cable and roller is also saved, although in comparison with movable system it is not so important.

2.5 Conclusion

According to the description and complexity . slow acceleration, possibility of construction and maintenance costs, the second plan can be the optimum . in the following details of plan are selected and will be introduced and designed.

In the final section, dynamic analysis , tension and thermal analysis due to the operating condition of the machine happened and plan will be evaluated

3. REVIEW DETAILS OF MOVABLE MOTOR

3.1 Text Structure

As shown in figure 7 the middle part of the main structure is made of two semi-circular profiles which connected together by several small spacers, bending is the reason why two semi-circular profiles are used; if the thickness of the profile be high the possibility of bending will be discarded even there is a chance for bending, using a single piece of profile with high thickness will have a high mass which is not suitable for use.

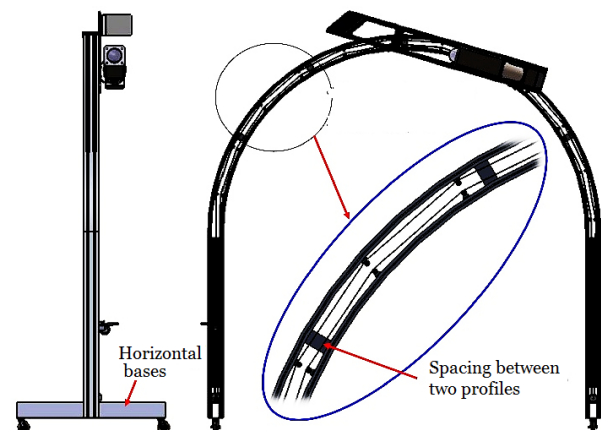


Fig. 7 Structure of the Sun Simulator.

In figure 7 is clear that in the lower part of structure for more stability is used an aluminum profile on both sides as a horizontal base.

3.2 Motor driven system

3.2.1 Motor

To select the right motor, the power required for the system must be calculated. Mass of the simulator system is considered 20 KG. Because this speed will not be high, therefore the stair motors can be used. The advantages of these motors are, produce more torque at low speed than high speed. Due to the mass of the simulator system amount of power which is required to be provided by the motor is calculated as follows. It is important to mention which maximum required force is where the simulator system is located vertically.

There for the motor without considering dynamic force must be able to apply force equal to 200N.m, the dynamic force is checked to ensure which is negligible.

The speed of slider movement of the lamp is approximating of distance traveled and time calculation , 0.2m/s will be obtained as a result , the acceleration should be about 0.15m/s² so: it was ensured which the amount of this force is negligible against the weight force and it will be discarded.

To find motor power the Pulley of motor must be selected so the torque of arm can be obtained, similarly, to choose the right size of Pulley, at first the appropriate cable must be selected. There for at first must be discussed about cable. For now, for pass this stage radius of Pulley must be assumed 5cm. as result the motor torque is calculated as follows :

$$\tau = F * R = 200 * 0.05 = 10 \text{ N.M} \quad (1)$$

3.2.2 Cable

The cable should be able to withstand 200N.m , by selecting the confidence coefficient 7, can choose a suitable cable. Referring to the cables which are used in the industry, 19*1 cable is suitable cable for using , diameter of selected cable is 2mm.

3.2.3. Pulley

There are several choice for the Pulley system:

- A) The first plan is passing a few rounds on Pulley and then the cable is going back, in this plan, friction between Pulley and cable is the reason for moving the movable and the slider (on the rails) figure 8 shows schematic of the first plan.

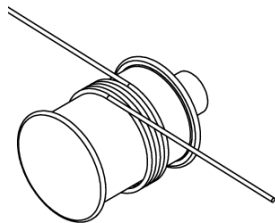


Fig. 8 Schematic of the first solution of cable twisting on drum.

One of the problem of this plan is the possibility of slip cable on the Pulley which , in spite of this, positioning will be in trouble. To avoid this, another plan will be presented

- B) There is a solution to ensure non-slip which the cable are connected to the drum , so that, at first one side of cable is tightened to the drum and passed

from rollers, then it is passed on the drum for one cable pass, and the other side of the cable will be tightened to the drum, figure 9 shows, cable closure to the drum, wrap cable on the drum for one path after passing cable from rollers causes to((results in)), when the cable is opening over drum from one side. From other side the cable will be wrapped over the drum , in this way movement of slipper is guranteed on the rails

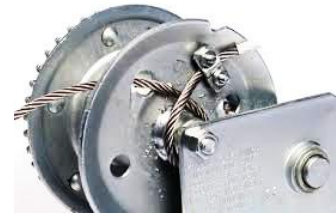


Fig. 9 Tightening of the cable end to the drum.

- C) Another design is using of timing belt and timing Pulley. In this design it is not necessary to wrapping belt around the Pulley and timing belt will ensure non-slipping.

Radius of the suns simulator is 2.5 meters so , the length of the path which is wrapped over Pulley is calculated as follows:

$$L = r * \pi = 2.5\pi = 7.85 \text{ m} \quad (2)$$

Now if a drum with a radius of 5cm is assumed and its length is 5cm. for maximum torque of motor, the number of rounds which the cable, is calculated as follows:

$$\theta = \frac{L}{r} = \frac{7.85}{0.05} = 157 \text{ rad} = 25 \text{ turns} \quad (3)$$

The length of drum is 5cm with 2cm thickness for 25 rounds of cable is suitable. Even its length can be decreases to half(and two rounds around it). In this case , maximum power will be equal to

$$\tau = 200 \text{ N} * ((50 + 4) * 0.01) \text{m} = 10.8 \text{ N.m} \quad (4)$$

The reason of motor torque correction is illustrated by figure 10.

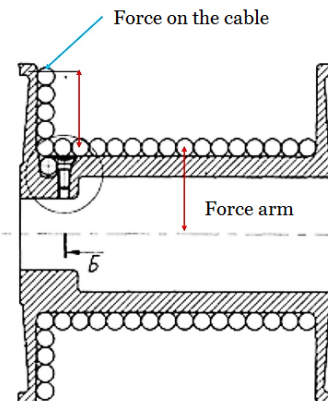


Fig. 10 Increase the power arm due to increasing the number of cable runs.

Now, by considering the torque and confidence factor of 1.5 , a motor with 15N.m torque should be selected but because the speed in the simulator of the sun is very slow, for reduce the

cost an motor with half of this torque with a 1 to 2 gear box looks more suitable. Stepping motor(Nema 34) with dimension and appearance of the QSH8616 is used(figure11). Due to the suitable dimension of motor it can be placed on horizontal legs which are between the section of elevation structure(figure12), and the Pulley and coupling sets will be connected to the motor, select a coupling for stepper motor is not so hard. Due to the diameter of the motor shaft and transmitting power and by considering the error topics, the suitable coupling will be selected.

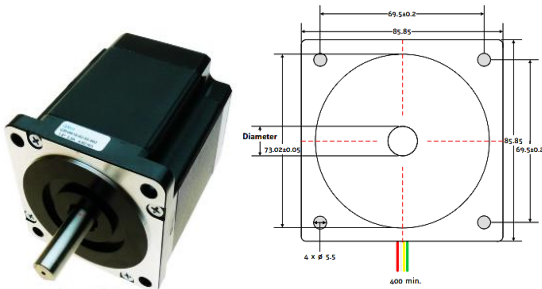


Fig. 11 Nema34 stepper motor



Fig. 12 Locating of a drive system.

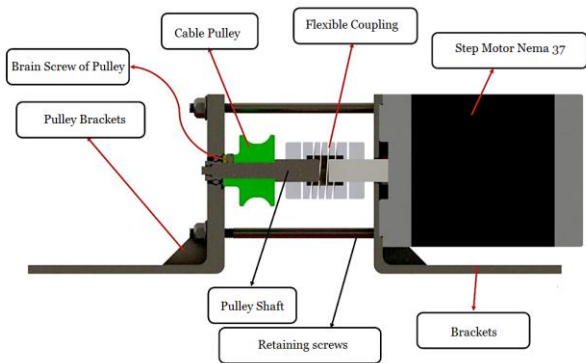


Fig. 13 Different parts of final power train design.

Movable part of motor and details of the bearing is shown in figure 13. Components and parts which are necessary to connect the horizontal base; by changing the position, to create bean grooves will be located.

3.3 Adjustment tension of cable

different designs can be used to adjust the preload inside the cable, in the following, different designs will be explained and eventually one design will be selected.

Use the weight of motor; a plan is to use the weight of motor set for preloading inside the cable, in this design the motor set is located on a plate and the plate will be hinged to the rest of the set until the weight of the motor stretches the cable or belt. figure 13 illustrates the explanation.

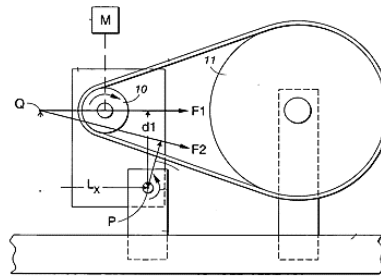


Fig. 14 Using motor weight to adjust the preload of the cable.

Using of this design is invalid, because by using of this design, repositioning and use another profile to pin in to the structure to place the motor on it, will be the problems.

Idler Pulley with additional weight: by using idler Pulley which is pinned on the rod which is mounted on the structure, can be adjusted the preload inside the cable, although looks simple and efficient but has disadvantages of the previous design. This design is shown in figure 15.

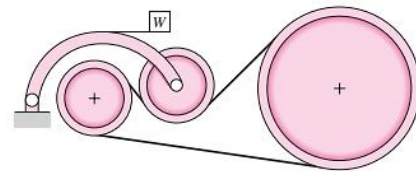


Fig. 15 Idler pulley with additional weight [7]

Idler Pulley with movable axis of rotation: in this design there should be a mechanism to take the axis of Pulley out of cable to be able to make enough load in cable. This design looks very simple and appropriate and there are no disadvantages of previous design. This design is shown in figure 16.

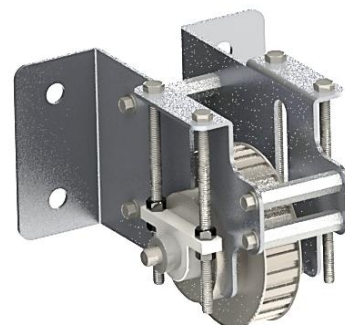


Fig. 16 Idler pulley with movable axis of rotation.

This mechanism is connected to the structure, then, by tightening the screws which move the axis of Pulley into the guide groove, can adjust the inside load of cable or trap. In order to three design which were introduced and advantages and disadvantages, the third design will be used as a tightening cable system in the intended device.

3.4 Cable guide rollers

It is necessary to use a conductive roller to guide the cable on the going round path. These rollers are located in the upper and lower rows (which these rows are between the two half-circle profile). The cable must be passed through the bottom of the lower roller and return from the top of the upper roller. Figure 17 is shown a piece designed to hold the cable guide

roller in its place. This piece is threaded by 2 bolts and it is designed in such way which it can be moved in to the groove by slightly opening the bolts so there is no necessary to drilling in a half-circle profile.



Fig. 17 Cable guide rollers.

Actually by tightening the bolts, T-section friction with groove will be increased and the piece is kept inside it.

Viewing the cross-section of this piece in figure 18 helps to understand better the problem.

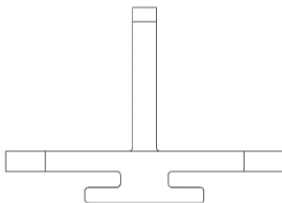


Fig. 18 Cross section of cable guide rollers holder.

How to connect the cable to the slider of lamp is a important point(figure19) which can be considered some plans. The simplest mode is use the hook which is attached to the slider of lamp.



Fig. 19 Cable connector hooks to moving bed.

3.5 Limiting system of movable on the path

One of the most important part of sun simulator system is designing constraints for slider inside the path. For this purpose there are different plans.

3.5.1 Circular rails

First plan is installing rails on an aluminum profile and using special sliders. in this design circular rails should be used. ‘Rollon’ company produce these rails(figure20). these rails which are produced by Rollon company are released in different radius. This should be ordered to the company for preparation. Using of such rails due to the limitation of its manufacturing companies and also unavailability seems very difficult but, instead, it does not have design problem and will have high confidence in the result. By the way, this design will not be used and suitable rollers will be design to constraint the slider on the path.



Fig. 20 ROLLON circular rails [7].

3.5.2 Designing a suitable roller

To design the roller to constraint the slider on the path, as it is clear, rollers in different parts to constraint and reduce the degree of freedom on the rails has been designed. On the four sides of the rails are such rollers which are as follows:

- a) Front rollers: the images of these rollers are shown in figure 21. Ball bearings are also used to provide rotational movement; which two ball bearings are placed in this plan. The reason is, these rollers are expected to endurance fairly large load. Contact between side surface of the semi-circle profile and movable set, by these rollers to routing mode is provided.

In figure 21, there is a thorn in the front roller to deprivation axial movement of pin, compared to the piece which is located on pin. At the end it has been worm threaded to prevent roller and bearing exits from their place.

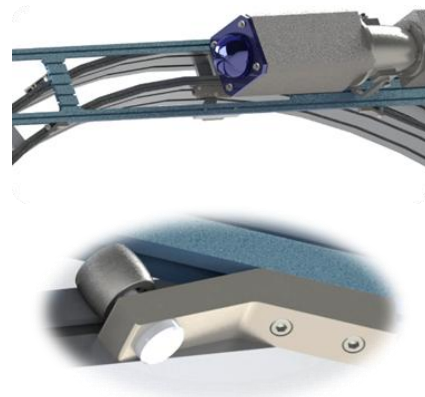


Fig. 21 Roller in the front and last of the moving bed.

- b) Rollers on the top side: rollers on the top side are shown in figure 22. In this design there are two rollers from above and there is one roller from the side. Some pins which are used on the top rollers, are shown in the below picture. To prevent collapse of the set and increase the structural reliability, is also used a roller on the opposite side. Two upper rollers just tolerate the vertical load. Rails of rollers are the groove of profiles. L-shaped piece which is roller inhibitor, by a pin which has the ability to rotate toward movable set is connected to it. To allow rotation toward structure during moving.

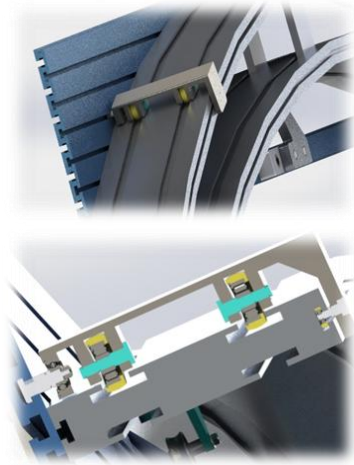


Fig. 22 Rollers on the top side of structure.

As mentioned, in this design there are two rollers on the top and a roller on the side; this design has been done conservatively and probably after design calculation only one roller will be required.

- D) Lower roller: as shown in figure 23, the lower roller made from some pieces, the rollers are located on the piece which is shown in figure 23, task of this part is allow the set to separate to upwards and increase accuracy of positioning.



Fig. 23 Inhibitor rollers from below.

according to this design and previous designs there are two thorn spring in figure 24(is shown cross section of roller) which is the reason of using thorn spring. As shown in two pictures, there are a step which is located in the middle of the roller, for separating ball bearing and the place of thorn spring, and there are grooves inside roller (as it is shown in figure 24) to tightens the axial movement.

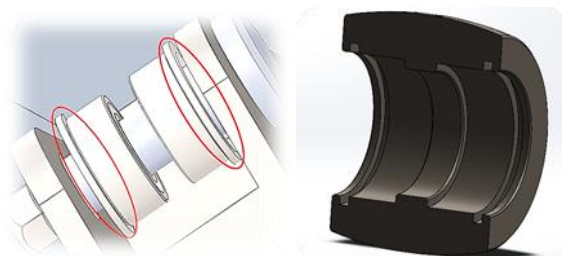


Fig. 24 Idler pulley with movable axis of rotation.

3-6- Mirror design system

The base of mirror is designed to change its angle and be fitted in the suitable place.



Fig. 25 Mirror design and its connections.

According to figure 25, screws which are used to connect the base of mirror to the slider profile, there are kind of screws which can be opened and closed by fingers easily. There is also a possibility to change the position on movable system.

3.7 Energy guide

To pass the wire of lamp, should be a suitable place. The gap between two grooves of profile seems to be a good place for guide energy. If the design of the upper rollers be corrected and one of the rollers be removed, inside the groove can also replace the guide energy (figure26 and figure27).



Fig. 26 Energy Guide.

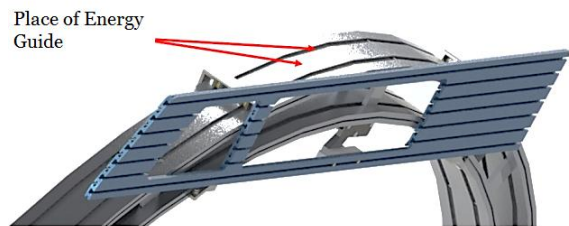


Fig. 27 Energy guide moving path.

3.8 Connect the cable to the movable set

In order to move the set by cable, it is necessary to connect the cable to the set by one or more points. On common cable connections, mostly there are hinges so leaping will be appearing which is not very suitable for precision of positioning.

From these designs, according to size of the cable ??? has been selected, which the location is also has been shown in the picture which there is no problem.]

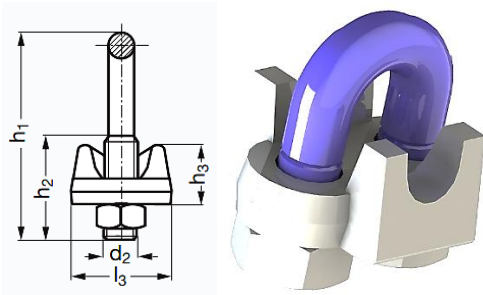


Fig. 28 Cable clamps used with different views.

As it is seen, by connecting the cable to the clamp, there is no touch when it is passing the lower roller and just there is a little movement of cable and there is no problem as view of astro company any more. So function of return pass will be continued easily (figure 29)

3.9 Summary and Conclusion

In this design, all possible problems are considered, surely, this is not the only plan and in the future, according to economical estimation and available facilities, there is possibility of changing some of details. Overall, this design can be introduced as the simplest, cheapest and the most accurate design. In the following, the details of this design will be designed and dynamic and tension analysis will be investigated.



Fig. 28 Locating and connecting the cable to the moving set.

4. DESIGNING AND FINAL FIXES FOR SENSITIVE COMPONENTS

In section 3, the initial design was presented for solar simulator. In this section final design will be specified.

4.1 Preliminary calculation of motor selection

Base on what was presented in conceptual design section, the final design of solar simulator system will be similar to figure 2. Generally, what was considered as movable system is a cable-driven-motor system. Different parts of this system are visible in the sectional view.

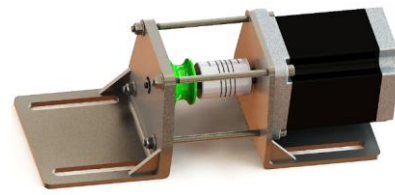


Fig.30 Overview of the actuator with the cable system.

Due to the mentioned problems, such as cable slip on the pulley (figure 30), the belt system is more appropriate than cable system. Actually instead of cable, timing belt drive will be used (figure31).

Now, analysis of the overall force on all components of system is necessary, in order to finish the initial design and then by software analysis, dimensions and geometry will be achieved.

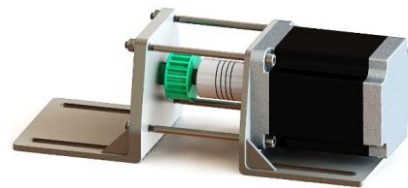


Fig. 31 Actuator system with time belt pulley

In the initial design, total mass of movable system is assumed 20Kg. load factor is assumed 2.5 for strike. Displacement of 50 Kg load will be the standard of designing; this force should be provided in all situation even in vertical direction by strain tension (figure 32).

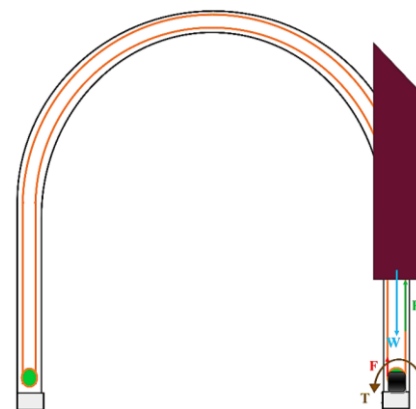


Fig. 32 The schematic of loading the actuator system in the worst possible mode (max necessary propulsion force).

According to the picture static equilibrium equations will be established. The motor torque will be obtained by specifying diameter of pulley (furmula1).

$$F = W = mg = 500 N \ \& \ T = F \cdot r \quad (5)$$

In this equation, radius of pulley is 'Y' and motor torque is 'T' in static situation. It should be noted, impact of dynamic forces due to acceleration and braking is so important which should be evaluated because of low speed of the solar simulator system, the effect of these forces will be very low. According to approximate calculations, velocity is assumed 0.2m/s and approximate acceleration time is 1 second which the acceleration is equal to 0.2m/s², the dynamic force will be calculated with mass of 20Kg. based on these calculations, influence of inertial forces(F_i) compared to static forces which is related to the weight, are less than 1% and is

negligible.(safety factor of these forces is included).(formula2)

$$F_I = ma = 20 \times 0.2 = 4 \text{ N} \ \& \ F_s = 500 \text{ N} \quad (6)$$

$$\Rightarrow \frac{F_I}{F_s} < 1\%$$

Now, if the rate of constant speed be 0.2 m/s and the force of belt be 500N , input power required with 85% efficiency will be 120W. if a timing belt is used with diameter of 40mm, required torque for the motor is calculated as follows: (formula3)

$$T = 500 \times 20 \times 10^{-3} = 10 \text{ N.m} \quad (7)$$

$$= 1000 \text{ N.cm}$$

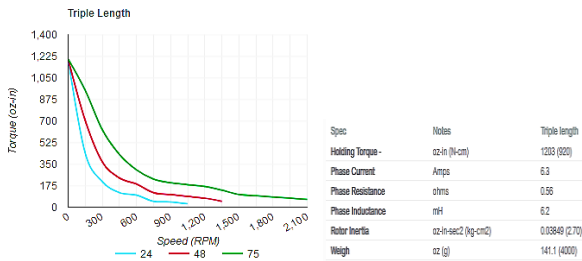


Fig. 33 Nema 34 with three Stacks features.

According to the load factor which is considered and manufactures catalogs, stepper motor ‘NEMA34 triple stack’ with maximum torque (920N.cm) is appropriate to choose. Curves of produced torque in different rounds and different voltages (12-24-48) are provided.

Alternative design of this type of motor is stepper motor with less length and step and has flexible gearbox. Since it does not require high speed, ability to reduce the speed and required torque will be possible.

According to the manufactures, sun gear box (4:1) can be used with dimensional and functional characteristics. In this situation, the torque of motor will be 250N.cm, so ‘NEMA34 single length motor’ can be used.

For compare the existing solutions, economic analysis will be useful.

Cost of motor which has torque of 250N.cm and lower is 40\$ and cost of 4:1 sun gear box is 53\$, therefore total cost will be 90\$. While, cost of motor which has torque of 13N.m is about 80\$ which is cheaper than the motor with gear box and in terms of construction, buy, assembly and maintenance are cheaper and easier.

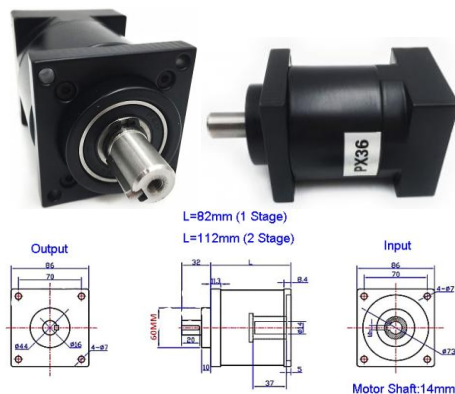


Fig. 34 Different views of 4:1 sun gearbox

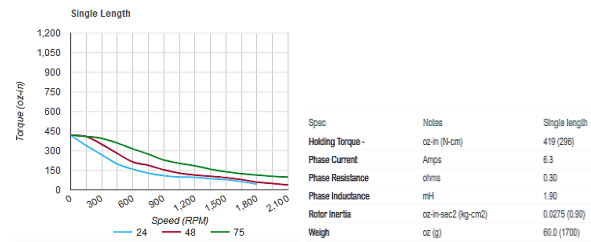


Fig.35 Nema 34 with three Stacks features

4.2 design and select timing Pulley and belt

In order to diameter which was 40mm in the previous section, by referring to different standards and catalogs, depending on the transmission power of 130W and the speed ratio of 1:1 the Pulley was selected from BBman company which is shown in figure 36. As it is shown, figure 36 has two adjustment screws for curb the axial movement. The width of the belt is about 15mm, and the diameter of pitch is about 40mm. shaft hole diameter is 6.5mm. the overall length of Pulley is also about 26mm. (figure 36)

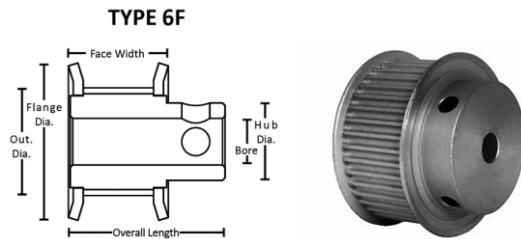


Fig. 36 The schematic of chosen pulley of BBman.

And the length of required belt is about 20m.

Because the rest of pulley set the path for movable set, they are similar to idler. So all of them will be chosen from same kind. In the route section which the belt passes above Pulley, exterior idler which has no gear will be used.

4.3 Designing and selection of flexible couplings

Flexible coupling is existed in different types with different applications. These kinds of coupling can tolerate the radial and angular axial asymmetry between the driving axis and movable axis.

Flexible couplings have four main tasks:

- . Transfer the torque and speed of the driving to the movable.
- . Neutralize the vibration
- . Compensation for unbalancing
- . Affection on the normal frequency of the system.

Generally, normal axial unevenness in small coupling is 0.055 inches and in large coupling is 0.03. Maximum angular misalignment is usually considered to be about $\pm 3^\circ$. Due to wide range of flexible coupling, there are no comprehensive categories for flexible coupling. So category of these coupling is not useful.

In stepper motor systems and servo systems, typically, there are two flexible coupling (rotex coupling and encoder coupling) (figure37).

Coupling is consist of two flexible pieces. Rotex coupling is made of high quality cast iron and all parts are machined to stop the vibration in high speed.

Spider of rotex coupling is made of high quality polyurethane materials(TPUS) rotex coupling is small and light but can tolerate high torque and is suitable for absorbing the vibrations and shocks of the system, operation temperature of rotex coupling is between 40 c- 90 c in normal mode and between 50 c-120 c in short periods. The material of rotex coupling are divided in to 3 categories: aluminum, cast iron and steel.



Fig. 37 Two common types of flexible couplings for control systems.

Encoder coupling are flexible, these couplings are made of aluminum, these kinds of coupling are suitable to control the situation. Encoder coupling can be used in CNC machines and servo motors.

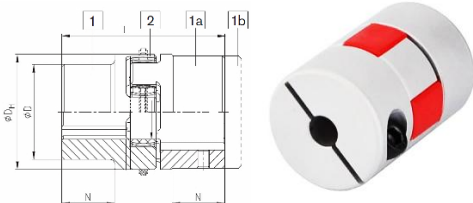


Fig. 38 Views of used Rotex coupling

According to the diameter of motor ‘NEMA 34’ which is 12.7mm so it is necessary the diameter of coupling hole be at least equal or smaller than this value, because it can reach this value by machining, in this condition, the outer diameter should be as large as possible to machining if rotex coupling is used(aluminum type), diameter of the shaft hole, 7.12mm are accessible for inlet and outlet. This coupling is a good choice but leaping is the main problem due to high load, so it is better to use encoder coupling.

By referring to the catalog, aluminum type with an outer diameter of 31.8 mm and inner diameter range of 5-15mm which maximum torque tolerable is 15N.m, is the suitable choice for this design.

So, both designs are partially usable, and base on market status and economic issues and positioning accurately best design can be chosen. in this paper encoder coupling will be used.

4.4 Designing and analyzing the main timing Pulley shaft

Figure 39 shows the shaft which is designed for Pulley. If assumed 10N.m torque is supposed to be applied in the middle of the thorn, which comes from 500N shear force, by assuming maximum bending in the location of thorn, with

coefficient of bending stress $k_t=2.15$, $k_{ts}=3$ with the following geometric dimension. Static analysis can be performed: (formula 4)

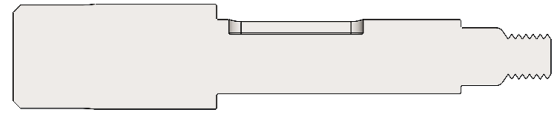


Fig. 39 Cross section of moving motor timing shaft.

$$\begin{aligned} \sigma_t &= K_t \frac{32FL}{2\pi d^3} = 262 \text{ Mpa} \quad \& \quad \tau_s = K_{ts} \frac{16T}{\pi d^3} \\ &= 210 \text{ Mpa} \rightarrow \sigma' \\ &= \sqrt{\sigma_t^2 + 3\tau_s^2} = 450 \text{ Mpa} \end{aligned} \quad (8)$$

Assuming a 10145CD steel, which yield stress is equal to $S_y=530$ Mpa, static safety factor on the set can be found(formula1)

$$n_s = \frac{S_y}{\sigma'} = \frac{530}{450} = 1.2 \quad (9)$$

The load factor is assumed 2.5, real safety factor will be $n=2.5*1.2=3$. in fact, because all loads are very slow, safety factor with impact loading also models fatigue behavior.



Fig. 40 Final actuating system pulley shaft.

So the safety factor of fatigue can be assumed 1.2. so the diameter of 9mm for the hole of pulley is safe. The final shape of the shaft is visible in figure40

5. TENSION ANALYSIS OF SENSITIVE COMPONENTS

To ensure resistance of system against static and dynamic loads, it is necessary some critical components of the system are carefully analyzed, which comes in the following.

5.1 Static Analysis of pulley Timing

First, pulley timing will be analyzed, because it is under high load. This sample has been considered steel due to magnetic conductivity problems. Second suitable material is aluminum 7000, which most of components are considered aluminum.

Due to the variety of dent for pulley timing, for pulley timing which has 40 gears, the analysis will be repeated again. In this case, they have the same material and mesh, with static loading, by assuming only 10% of gears will withstand all load, tension and displacement are shown in figure 41 and 42.

As it is shown in figure 41 maximum tension occurs at the root of the dent and it is equal to 8.5Mpa which in comparison to crushing strength which is 172Mpa, is very low. According to the maximum displacement on surrounding of dents and it is equal 0.6mm and it will happen. As static analysis, this design is appropriate and the type of 40 dents will be selected.

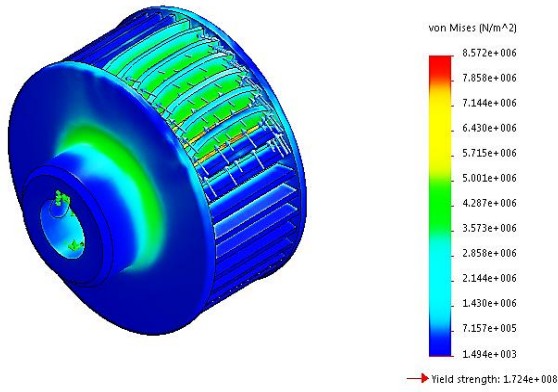


Fig. 41 Von Mises static analysis of a 40 teeth pulley.

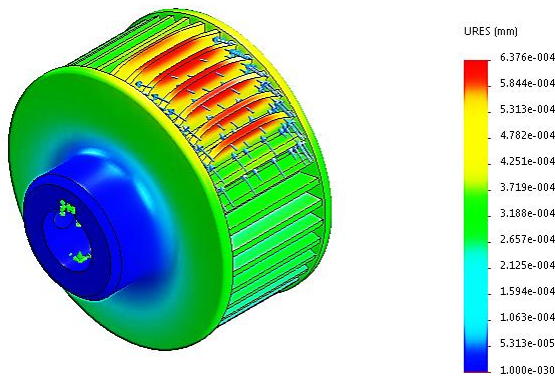


Fig. 42 Colorful curve of deflection of timing pulley with 40 teeth in static analysis.

5.2 Structural analysis with vertical and transverse force by SOLID WORKS

In this section, the main structure of the system ‘railing of projector’ will be analyzed. Due to aluminum and dimension of structure the total mass of the structure is calculated 500Kg.

The material is aluminum 7075-T6 which the yield stress is equal to 505Mpa and breaking strength is equal to 570Mpa. Density of the system to reduce the total weight of the system is less than steel and is equal to 2850Kg/m³. versus, modulus of elasticity is low and equal to 72Gpa. So deflection and displacements under the loading are so important.

First, it is necessary to determine the fixed positions and supports of structure, because the structure is located on the solid horizontal beams. connection between the rail and these horizontal beams which are connected by 8 screws, will be considered solid. So 16 internal surfaces of holes due to connection to the underlying structure will be assumed fixed.

Loading on the system has three separate parts:

- 1- Due to the size of the structure which is huge, and by considering gravity, the weight of structure which enters on the structure is considered
- 2- 500N vertical force which enters on the upper surface of the structure which comes from the weight of the system

- 3- 200N force as transverse unwanted forces and also bending force which enters to the structure.

After loading, next step is meshing. Meshing algorithm is four-point element with a size of 50mm.

Table 1 shows the reaction forces on the support, X direction and rail direction are the same which there is no force in this direction.

Table 1 Reaction forces on horizontal base.

Components	X	Y	Z	Resultant
Reaction force(N)	0.0367517	5430.81	199.973	5434.49
Reaction Moment(N.m)	0	0	0	0

Figure 43 shows equivalent static stresses on the structure. According to the graph, Maximum stress will be 12.3Mpa, which is very small compared to 505Mpa so the safety factor will be 41. Maximum and minimum structural stress values are visible. Minimum stress occurs in the side columns.

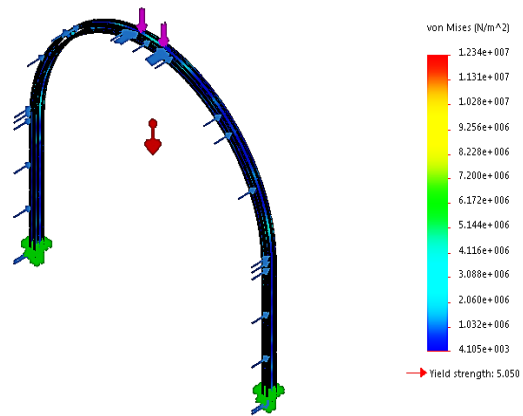
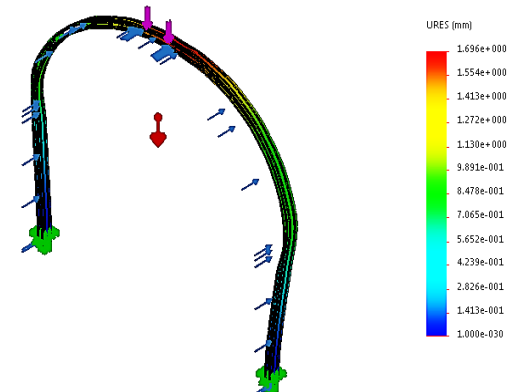


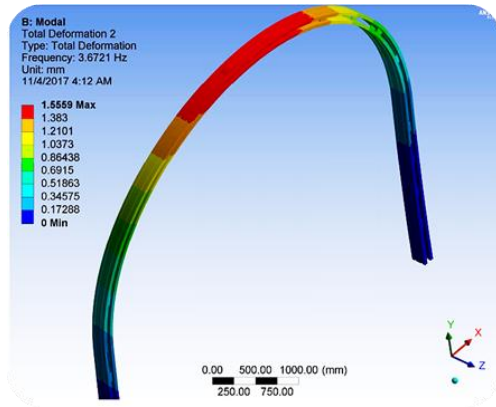
Fig. 43 Colorful curve of Von Mises stresses of the structure

Table 2 Modified static stress results

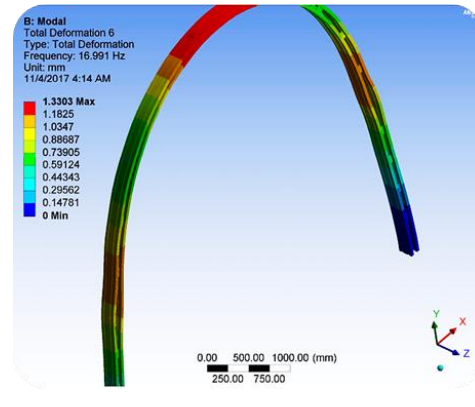
Name	Type	Min	Max
Stress1	VON: von Mises Stress	4.105e+003N/m ² Node: 118719	1.234e+007N/m ² Node: 19286

According to the figure 44, maximum displacement of the structure is approximately 1.7mm. according to the figure 44 this displacement is at the highest point of the structure and it is very small, so it does not occur an error in the system performance.

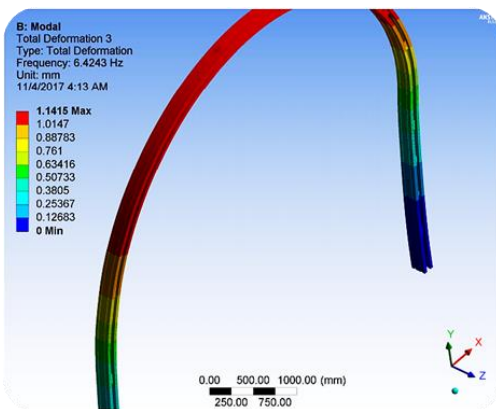




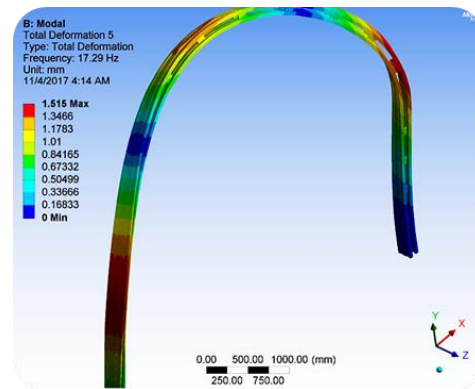
a) first natural modes 3.7Hz



b) first natural modes 17Hz



b) first natural modes 6.4Hz



c) first natural modes 17.3Hz

Fig. 44 Colorful curve of deflection of projector rail structure

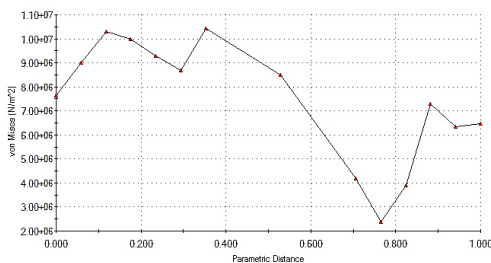
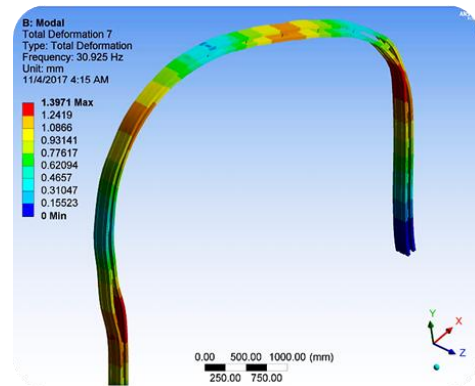


Fig. 45 Stress distribution around the hole of connection to the horizontal support structure



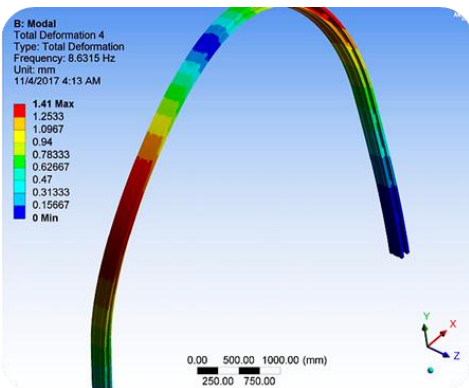
d) first natural modes 31Hz

Fig. 46 Projector rail final design natural modes in Ansys

One of the sensitive areas of the structure is the holes of horizontal base. For this reason, the variation curve of the stress around one of the holes is shown in figure 45. As it is known the maximum stress in these areas is not more than 10Mpa.so the safety factor is more than 50. So the structure design is safe (from the static loading view)

5.3 Modal analysis with ANSYS workbench

The result of model analysis which is dynamic, will be analyzed with ANSYS workbench software to prove results. Figure 46 shows different modes. Natural frequencies are shown in table 3.



a) first natural modes 8.6Hz

Table 3 Six first natural frequencies of the projector structure using the Ansys software

Mode	Frequency [Hz]
1.	3.6745
2.	6.4446
3.	8.6427
4.	17.046
5.	17.277
6.	31.026

The final results of the stress analysis are discussed in the following. Maximum displacement and maximum stresses in different vibrational directions are coming in the following table:

5.4 Frequency vibrations response of structural in vertical and lateral directions

Earthquake acceleration is 10mm/s^2 . The frequency response for the displacement of the highest point of the structure is plotted after the time analysis for the frequency range up to 50Hz. Details are shown in the following table.

To check in transverse direction, the input value is in the same value as before, and in Z direction.so, three natural frequencies are seen.

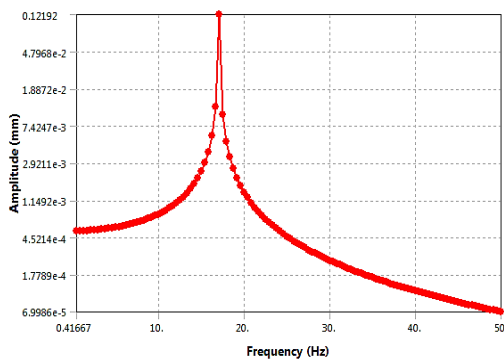


Fig. 47 Projector rail frequency response with vertical base excitation (Y direction)

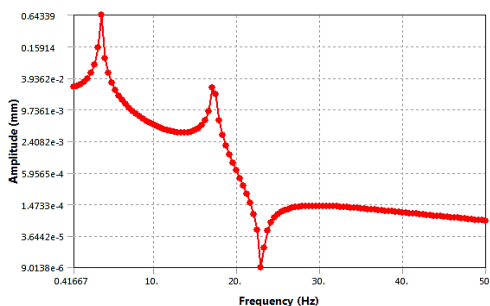


Fig.48 Projector rail frequency response with lateral base excitation

maximum displacement in this direction is 0.6mm which is very small and shows strength of the structure against dynamic and vibration loads.

5.5 Thermal analysis and effects of projector on ambient temperature

In order to modeling the thermal effects of the projector on the structure and environment, by assuming suitable air

conditioning at the place and ambient temperature of 22°C , thermal analysis has been done. In this analysis the upper surface is of the structure is the closest location to the projector and most sensitive location, temperature of this location is 100°C . between the other surfaces and air the heat transfer is assumed convection type and a steady thermal analysis has been done in ANSYS software. The analysis characteristics are presented in table 4.

Table 4 Thermal loading of the structure

Object Name	Temperature	Convection
State	Fully Defined	
Scope		
Scoping Method	Geometry Selection	
Geometry	1 Face	585 Faces
Definition		
Type	Temperature	Convection
Magnitude	100. °C (ramped)	
Suppressed	No	
Film Coefficient		Tabular Data
Coefficient Type		Average Temperature Film
Ambient Temperature	22. °C (ramped)	
Convection Matrix	Program Controlled	
Edit Data For	Film Coefficient	
Tabular Data		
Independent Variable		Temperature
Graph Controls		
X-Axis		Temperature

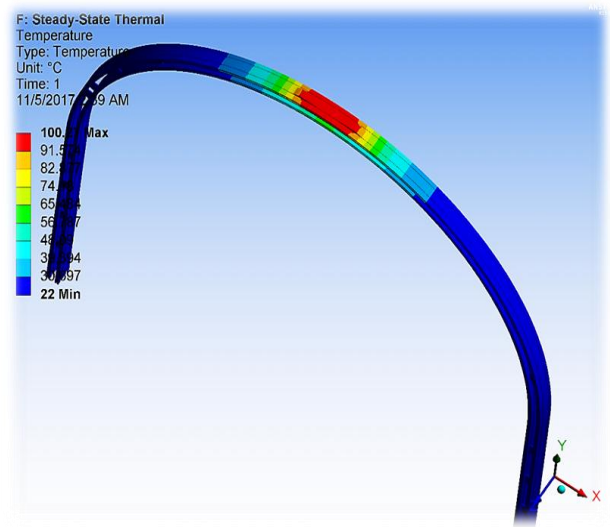


Fig. 49 Thermal distribution curve of the projector rail

After modeling and analyzing, temperature distribution of the structure will be determined. so the temperature reaches ambient temperature (22°C) at a distance of one meter above the surface.

6. TENSION ANALYSIS OF SENSITIVE COMPONENTS

By examining the system from dynamic, static, vibrational and thermal views, the structure and movable system have a suitable design, so it is possible to build this set up which has acceptable safety factor from fracture and deformation view. Dynamic analysis due to low acceleration in the system and

excessive complexity on the rails seemed irrational, this is shown in the calculations in the first section and it does not analysis by software and just effects on the structure are investigated and kinematic is considered as a results of the calculation.

7. REFERENCES

- [1] ACS test facility. (2010, December 21). Retrieved from <http://www.astrofein.com/astro-und-feinwerktechnik-adlershof/products/raumfahrt-eng/80/acs-teststand-eng/>
- [2] ADCS Test Facility, Hawaii univrsity, (n.d.). Retrieved from <https://www.hsfl.hawaii.edu/facilities/adcs/>
- [3] Catalog, “Tamiya Cable Car - WattsUp,” On the WWW, May. URL <http://www.wattsup.co.nz>
- [4] Gondola lift, Inside the terminal, Retrieved from. https://commons.wikimedia.org/wiki/Gondola_lift
- [5] Universität Duisburg-Essen. (n.d.). Retrieved from https://www.uni-due.de/mechatronik/forschung/european_robotic_forum.php
- [6] Shigley, J. E. (2011). Shigley's mechanical engineering design. Tata McGraw-Hill Education
- [7] Curvilinear guides, Online access: www.rollon.com/GB/en/-products/linear-line/5-curviline/

Performance Evaluation of Different Scheduling Schemes for Marcocell with MIMO Closed Loop Spatial Multiplexing (CLSM) 2x2 Antenna Configuration

Kyawt Kay Khaing
Department of Electronic
Engineering,
Technological University
Thanlyin, Myanmar

Zin Ma Ma Myo
Department of Electronic
Engineering,
Technological University
Thanlyin, Myanmar

Thae Hsu Thoung
Department of Electronic
Engineering,
Technological University
Thanlyin, Myanmar

Abstract: Nowadays, the usage of smart phones is very popular. More and more people access the Internet with their smart phones. This demands higher data rates from the mobile network operators. Every year the number of users and the amount of information is increasing dramatically. The wireless technology should ensure high data rates to be able to compete with the wire-based technology. The main advantage of the wireless system is the ability for user to be mobile. The 4G LTE system made it possible to gain very high peak data rates. The purpose of this paper was to investigate the improvement of the system performance for the downlink based on different antenna configurations and different scheduling algorithms. Moreover, the fairness between the users using different schedulers has been analyzed and evaluated.

Keywords: LTE, RR, PF, BCQI

1. INTRODUCTION

Long Term Evolution (LTE) is a broadband wireless access network offering a rich suite of multimedia applications such as 3D video conferencing, mobile HD TV and real time streaming videos at very high vehicular speeds. These applications have heterogeneous Quality of Service (QoS) requirements such as priority, transmission delay, jitter, packet loss rate, packet error rate etc., to provide better user experience. QoS provisioning offers a challenge for the LTE network designers to efficiently utilize the limited available radio resources in a highly fading wireless medium. In order to meet this challenge, LTE standard incorporates Radio Resource Management (RRM) mechanisms such as Call Admission Control (CAC), scheduling etc., which are open issues for designers. Scheduling is a crucial RRM mechanism which divides and allocates radio resources among different users while maintaining QoS to optimize system performance.

The scheduling in both downlink and uplink is carried out by scheduler present at the Medium Access Control (MAC) sublayer of eNodeB (eNB). Since scheduling algorithm for eNB MAC scheduler is not standardized, LTE network designers have proposed scheduling algorithms which results in significantly different levels of user and system performance [3, 4].

LTE technology presents a very challenging multiuser problem: Several User Equipments (UEs) in the same geographic area require high data rates in a finite bandwidth with low latency. Multiple access techniques allow UEs to share the available bandwidth by allocating to each UE a fraction of the total system resources. The strong motivation beyond the resource allocation algorithms for scheduling is the improvement of system performance by increasing the spectral efficiency at the wireless interface and consequently enhancing the system capacity. Other constraints such as fairness must also be improved. Hence, it is important to find away to performance effective trade-off between efficiency and fairness. To develop an efficient scheduler to reach this trade-off, several factors must be taken into account such as: Signal-to-Interference-plus-Noise Ratio (SINR), packet

delays, buffer status (queues length and packet delays), and type of service, fairness, channel conditions and complexity (time and computing) [2].

Hence in this paper an attempt has been made to evaluate the performance of Round Robin, Best CQI and Proportional Fair scheduling algorithms for Constant Bit Rate (CBR) traffic scenario using MATLAB based Vienna LTE Simulator.

2. LTE MIMO (MULTIPLE INPUT MULTIPLE OUTPUT)

The MIMO, Multiple Input Multiple Output is another of the LTE major technology innovations used to improve the performance of the system. This technology provides LTE with the ability to further improve its data throughput and spectral efficiency above that obtained by the use of OFDM. Although MIMO adds complexity to the system in terms of processing and the number of antennas required, it enables far high data rates to be achieved along with much improved spectral efficiency. As a result, MIMO has been included as an integral part of LTE.

2.1 LTE MIMO Basics

The basic concept of MIMO utilises the multipath signal propagation that is present in all terrestrial communications. Rather than providing interference, these paths can be used to advantage.

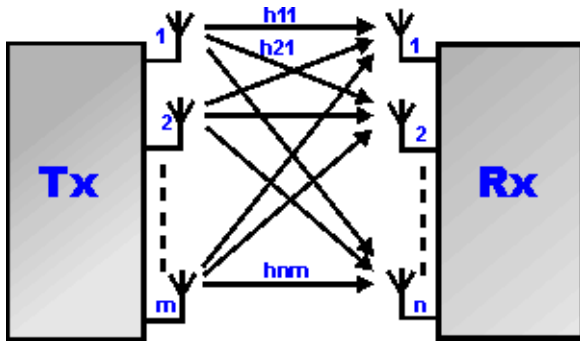


Figure 1. General Outline of MIMO system

The transmitter and receiver have more than one antenna and using the processing power available at either end of the link, they are able to utilise the different paths that exist between the two entities to provide improvements in data rate of signal to noise. MIMO is being used increasingly in many high data rate technologies including Wi-Fi and other wireless and cellular technologies to provide improved levels of efficiency. Essentially MIMO employs multiple antennas on the receiver and transmitter to utilise the multi-path effects that always exist to transmit additional data, rather than causing interference. The use of MIMO technology has been introduced successively over the different releases of the LTE standards. MIMO has been a cornerstone of the LTE standard, but initially, in releases 8 and 9 multiple transmit antennas on the UE was not supported because in the interested of power reduction, only a single RF power amplifier was assumed to be available.

3. LTE MIMO MODES

There are several ways in which MIMO is implemented in LTE. These vary according to the equipment used, the channel function and the equipment involved in the link.

3.1 Single Antenna

This is the form of wireless transmission used on most basic wireless links. A single data stream is transmitted on one antenna and received by one or more antennas. It may also be referred to as SISO: Single In Single Out or SIMO Single In Multiple Out dependent upon the antennas used. SIMO is also called receive diversity.

3.2 Transmit Diversity

This form of LTE MIMO scheme utilises the transmission of the same information stream from multiple antennas. LTE supports two or four for this technique.. The information is coded differently using Space Frequency Block Codes. This mode provides an improvement in signal quality at reception and does not improve the data rate. Accordingly this form of LTE MIMO is used on the Common Channels as well as the Control and Broadcast channels.

1.3 Open Loop Spatial Multiplexing

This form of MIMO used within the LTE system involves sending two information streams which can be transmitted over two or more antennas. However there is no feedback from the UE although a TRI, Transmit Rank Indicator transmitted from the UE can be used by the base station to determine the number of spatial layers.

3.4 Close Loop Spatial Multiplexing

This form of LTE MIMO is similar to the open loop version, but as the name indicates it has feedback incorporated to close the loop. A PMI, Pre-coding Matrix Indicator is fed back from the UE to the base station. This enables the transmitter to pre-code the data to optimise the transmission and enable the receiver to more easily separate the different data streams.

3.5 Closed Loop with Pre-Coding

This is another form of LTE MIMO, but where a single code word is transmitted over a single spatial layer. This can be used as a fall-back mode for closed loop spatial multiplexing and it may also be associated with beamforming as well.

3.6 Multi-User MIMO, MU-MIMO

This form of LTE MIMO enables the system to target different spatial streams to different users.

3.7 Beam-forming

This is the most complex of the MIMO modes and it is likely to use linear arrays that will enable the antenna to focus on a particular area. This will reduce interference, and increase capacity as the particular UE will have a beam formed in their particular direction. In this a single code word is transmitted over a single spatial layer. A dedicated reference signal is used for an additional port. The terminal estimates the channel quality from the common reference signals on the antenna.

4. LTE DOWNLINK SCHEDULING

The air interface of LTE technology is based on OFDMA and SC-FDMA in the downlink and uplink respectively to deliver the flexibility and increase data rate without additional bandwidth or increase transmit power. The base station (eNodeB) is the entity responsible for controlling the air interface between the network and user equipments. The data transmission in LTE system is organized as physical resources which are represented by a time-frequency resource grid consisting of Resources Blocks (RBs) which has a duration of 0.5 ms and a bandwidth of 180 kHz (12 subcarriers spaced with 15 kHz). It is a straight forward to see that each RB has $12 \times 7 = 84$ resource elements in the case of normal cyclic prefix and $12 \times 6 = 72$ resource elements in the case of extended cyclic prefix [8].

The scheduler entity have a role to assigns resources blocks every TTI, based on the channel condition feedback received from User Equipment in the form of Channel Quality Indicator (CQI) send by the UEs to the eNodeB, to indicate the data rate supported by the downlink channel. Every value of CQI, index in the range 1 to 15, corresponds to the highest Modulation and Coding Scheme (MCS) and the amount of redundancy included [2].

In LTE system, the resource allocation is done in time and frequency domain. In time domain, the downlink channel is divided into frame of 10ms each consists of 10 subframes of 1 ms each referred to as Transmission Time Interval (TTI). In frequency domain, the available system bandwidth is divided into sub-channels of 180 kHz, comprising of 12 consecutive equally spaced OFDM subcarriers of 15 kHz each. A time-frequency radio resource spanning over 0.5 ms slots in the time domain and over 180 kHz sub-channel in the frequency domain is called Resource Block (RB). The number of resource blocks in the available bandwidth is called Resource grid. Resource Element (RE) represents one OFDM subcarrier during one OFDM symbol interval. The number of RBs in a resource grid depends on the size of the bandwidth. The LTE operates in the bandwidth of 1.4 MHz up to 20 MHz, with number of RBs ranging from 6 to 100 respectively.

Figure 3 shows the various results that help in assessing the network operation based on network configuration. They show how the average throughput varies with the SINR and the spectral efficiency. The upper right corner displays the fairness index, average/peak and edge user throughput and also the total cell throughput. This network shows that the fairness index of the network is 0.72 which is as expected for the Round Robin as it serves all the users requesting service. Each user has average user throughput of 2.51 Mbps. The similar simulations are carried out for the Best CQI and Proportional Fair scheduling scheme and results are compared to evaluate best scheduling scheme under different network conditions with MIMO Closed Loop Spatial Multiplexing (CLSM) 2 × 2 antenna configuration. In Figure 4 to Figure 7, simulation is run by attaching each user to its corresponding sector and each sector using the Best CQI and Proportional Fair scheduling schemes.

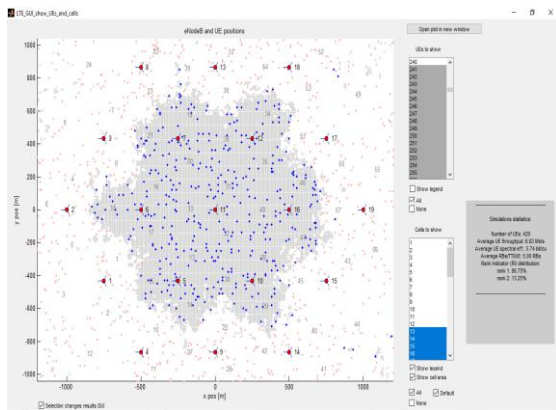


Figure 4. Network under Study of Best CQI Scheduling with 20 Users per Cell

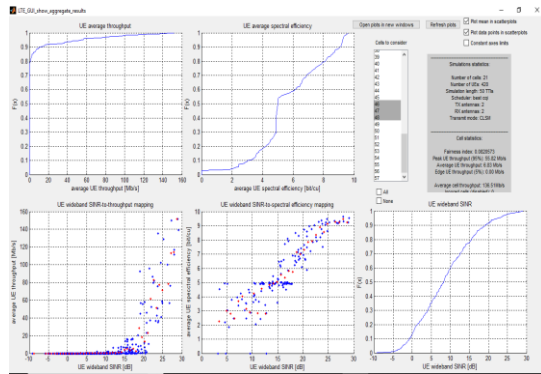


Figure 5. Simulation Results for Best CQI Scheme with 20 Users per Cell

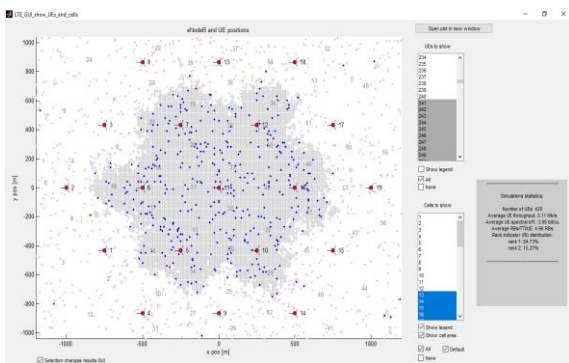


Figure 6. Network under Study of Proportional Fair Scheduling with 20 Users per Cell

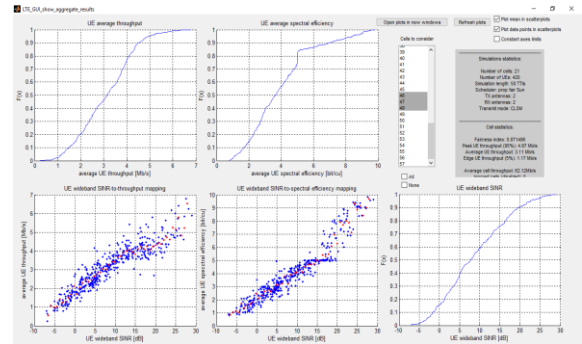


Figure 7. Simulation Results for Proportional Fair Scheme with 20 Users per Cell

The simulations were made with the LTE System Level Simulator 1.6. The LTE downlink OFDMA scenario is considered in the following simulations. Figure 8 illustrates the mean, edge and peak throughput.

Three different scheduling algorithms were chosen: Round Robin, Best Channel Quality Indicator and Proportional Fair. Closed Loop Spatial Multiplexing (CLSM) with 2 × 2 antenna configuration, 20 MHz bandwidth and 20 users in the cell. The simulation time is chosen equal to 50 TTI where TTI is equal to 1 ms. The pathloss model was chosen according to the 3GPP technical specification TS36.942. The scenario in the following simulation is done for the urban area model. The propagation model is the following:

$$L = 40 (1 - 4 \cdot 10^{-3} \cdot \text{Dhb}) \cdot \log_{10}(R) - 18 \cdot \log_{10}(\text{Dhb}) + 21 \cdot \log_{10}(f) + 80 \text{ dB}$$

where Dhb is the height of the base station antenna measured in metres from the average rooftop level, R is the base station UE separation in km, and f is the carrier frequency in MHz.

The carrier frequency was taken equal to the 2000 MHz and Dhb = 15 m above the average rooftop level according to the 3GPP technical specification TS36.942. Then the equation 10 will be in the following form:

$$L = 128.1 + 37.6 \log_{10}R$$

After L propagation factor is found the pathloss can be described by the following formula:

$$\text{Pathloss}_{\text{macro}} = L + \log F$$

where LogF is the log-normally distributed shadowing with the standard deviation of 10 dB.

For the first mean throughput it can be seen that the Best CQI has the maximum value and the Round Robin has the smallest one. The drawback of the Best CQI scheduler is a very low fairness among the users. It is happening because this scheduler gives the resources only to the user with the best channel conditions. The users that have all the time a bad channel quality will be not scheduled at all. In contrast, the Proportional Fair scheduler has the best fairness among the users. Despite on the very high peak throughput of Best CQI scheduler it is not serving the users that have a bad channel condition, the edge throughput is equal to 0.

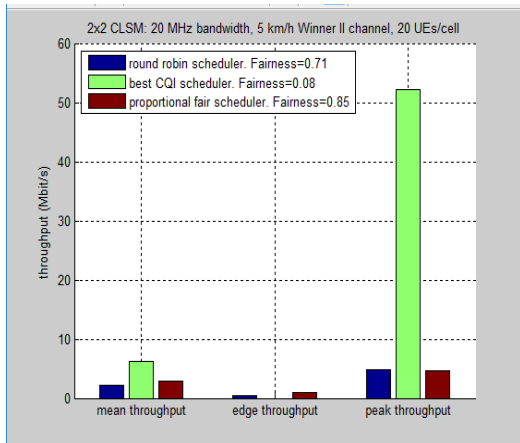


Figure 8. UE Throughput Comparison for Different Scheduling Algorithms

Figure 9 illustrates the empirical CDF of throughput of different scheduling algorithms. It can be seen that the probability of throughput to be equal to 0 for best CQI scheduler has the very big chances, the ECDF of it is about 0.64. But from the other side it can achieve the higher throughput than Proportional fair and Round Robin schedulers. The black dots on the graphs correspond to the mean value.

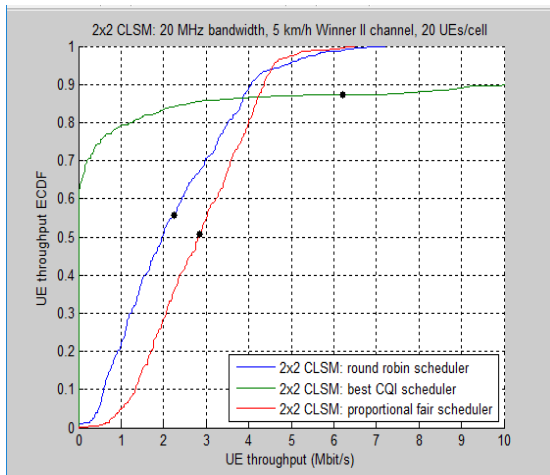


Figure 9. The Empirical CDF of the Throughput of Different Scheduling Algorithms

7. CONCLUSION

Long Term Evolution is the Fourth Generation that was developed in the 3GPP project. Long Term Evolution has improved the performance of the wireless communication significantly. It has the ability to achieve very high data rates using new technologies as OFDMA and MIMO.

The different scheduling algorithms of the downlink are simulated in this work. The Vienna LTE simulator which contains the LTE System Level Simulator is used. The results that were achieved demonstrate the multiple ways of how to improve the system performance.

The following results were collected after the simulation of different schemes:

The scheduling algorithm can improve the system performance. The right allocation of radio resources could increase the throughput of the system. Furthermore, the

fairness between users has to be taken into account. According to the simulation results the best scheduler between Round Robin, Proportional Fair and Max CQI in respect to the fairness, became the Proportional Fair algorithm. Though, the Max CQI gave the highest peak data rate.

The increased number of transmitter and receiver antenna made the system get a higher data rate than SISO would provide.

8. ACKNOWLEDGMENTS

The author would like to express her profound gratitude to Dr. Theingi, Rector, Technological University (Thanlyin), for her encouragement and managements and the author would like to express her thanks to thesis supervisor, Dr. Zin Ma Ma Myo, Professor and Head of Department of Electronic Engineering, for her motivation and encouragement to complete this research in time. After all, the author would like to express her thanks to all her teachers and her parents, for their supports and encouragements.

9. REFERENCES

- [1]. 3GPP TS 36.212 Version 10.0.0 Release 10, Evolved Universal Terrestrial Radio Access (E-UTRA): Multiplexing and channel coding, March, 2009.
- [2]. M. AMMAR, B. NSIRI, W. HAKIMI and M. ELJAMAI, "A comprehensive study of Open-loop Spatial Multiplexing and Transmit Diversity for Downlink LTE", International Journal of Computer Sciences and Telecommunication (IJCSST), volume 5 Issue 2, January 2014.
- [3]. Technical White paper: "Long Term Evolution (LTE): A Technical Overview," by Motorola.
- [4]. S. M. Chadchan, "A Fair Downlink Scheduling Algorithm for 3GPP LTE Networks", I. J. Computer Network and Information Security, 6, pp 34-41, 2013. [6] D. Talevski and Li. Gavrilovska, "Novel Scheduling Algorithms for LTE Downlink Transmission", Telfor Journal, Vol. 4, No. 1, February 2012.
- [5]. Dinesh Mannani, "Modeling and Simulation of Scheduling Algorithms in LTE Networks", Bachelor of Science Thesis report, Warsaw, January 2012.
- [6]. Al. Bahillo Martinez, "Evaluation of multiuser scheduling algorithm in OFDM for different services", Master of Science in Electronics report, June 2006.
- [7]. H. Seo and B. Gi Lee, "A Proportional Fair Power Allocation for Fair and Efficient Multiuser OFDM Systems", School of Electrical Engineering, Seoul National University, April 2004.
- [8]. E. L. Hahne, "Round-Robin Scheduling and Window Flow Control for Max-Min Fairness in Data Networks" IEEE, technical report, November 1987.
- [9]. Raymond H. Y. Louie, "Open-Loop Spatial Multiplexing and Diversity Communications in Ad Hoc Networks", Revised version. Submitted to IEEE Tr. Info Theory, 17 september 2010.

DC Motor Control System with PID Controller

Aung Ye Tun
 Department of Electrical
 Systems and Instrumentation,
 Myanmar Aerospace
 Engineering University,
 Meiktila Township,
 Mandalay Division, Myanmar

Abstract: With the rapid development of DC motor and computer technology, the DC motor control system is widely used in many industrial fields especially in aeronautic and astronautic application. With the high response, good adaptability and flexibility, DC motor has precise and fine control performance and a wide adjustable speed range. The aim of this paper is to study the dynamic performance of DC motor control system and provide the corresponding control law so as to improve its dynamic performance. In this paper establishes the mathematical model of DC motor control system, investigates the PID control algorithm to reach the high performance of whole system. Utilizing the Matlab Simulink, the simulation results indicate that the system modeling and controller are content to the system requirement.

Keywords: DC motor, PID controller, system simulation

1. INTRODUCTION

In control or robotic engineering, motor control plays a major role and is an unavoidable part, regardless of whether it is speed or position control. The effectiveness of a controller can be justified by performance objectives such as for high precision or rapid movement. Like other trade-off schemes, some control architecture has advantages over the others under certain real-application situations.

2. MODELLING OF DC MOTOR

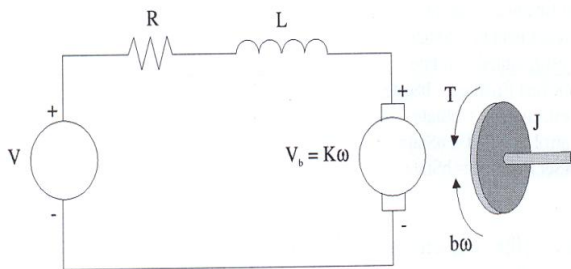


Figure 1. Electric circuit of the armature and the free body diagram of the rotor

The motor torque T is relative to the armature current, i by a constant factor K

$$T = Ki \quad (1)$$

The back electromotive force (emf), V_b , is related to the angular velocity by;

$$V_b = K\omega = K \frac{d\theta}{dt} \quad (2)$$

Following equation is derived by using the Newton's law and Kirchhoff's law

$$J \frac{d^2\theta}{dt^2} + b \frac{d\theta}{dt} = Ki \quad (3)$$

$$L \frac{di}{dt} + Ri = V - K \frac{d\theta}{dt} \quad (4)$$

Using the laplace transform equation (3) and (4)

$$(Js + b)s\theta(s) = KI(s) \quad (5)$$

$$I(s) = \frac{V(s) - Ks\theta(s)}{(Ls + R)} \quad (6)$$

According to Equation (5) and (6)

$$G_a(s) = \frac{\theta(s)}{V(s)} = \frac{K}{s[(Js + b)(Ls + R) + K^2]} \quad (7)$$

$$G_v(s) = \frac{\omega(s)}{V(s)} = \frac{K}{(Js + b)(Ls + R) + K^2} \quad (8)$$

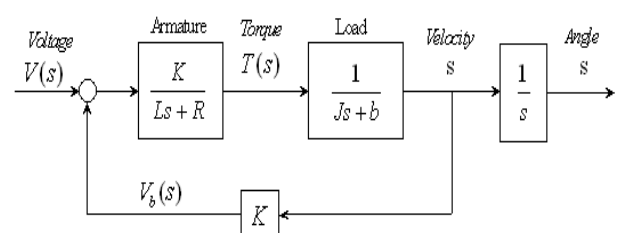


Figure 2. Block diagram of the DC motor

The DC motor parameters shown as follows.

Table 1. DC motor parameter

Symbol	Name	parameter
J	Inertia	0.01 Kg - m ² ?
L	Inductance	0.5H
R	Resistance	1 ohm
B	Damping coefficient	0.1 N-m-sec/rad
K _m	motor Constant	0.01 N-m/A
K _B	Back-EMF Constant	0.01 V-sec/rad

3. PID CONTROLLER

The traditional expressions for PI and PID controllers can be described by their transfer functions, relating error $E(s) = R(s) - Y(s)$ and controller output $U(s)$.

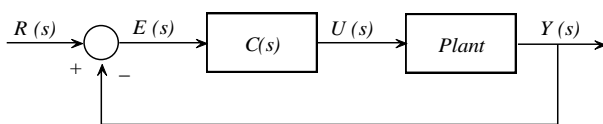


Figure 3. basic feedback control loop

For control over steady state and transient errors all the control strategies discussed so far should be combined to get proportional –integral-derivative (PID) control. Here the control signal is a linear combination of the error, the time integral of the error, and the time rate of change of the error. All three gain constants are adjustable.

The PID controller contains all three control components (proportional, derivative, and integral). Its transfer function model can be derived as follows:

$$U(y) = K_p e(t) + K_d \frac{de(t)}{dt} + K_i \int_0^t e(t) dt \quad (9)$$

4. SIMULATION OF DC MOTOR

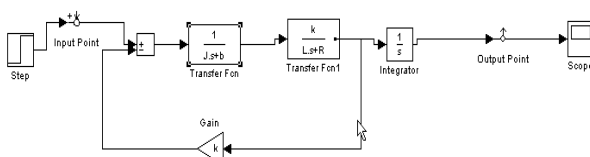


Figure 4. Simulink diagram of DC motor

According to figure 5, for time domain, response time is greater than 2.5 second. The system should get response time

is less than 0.1 second for good response. So the system has to combine with PID controller to reduce the response time.

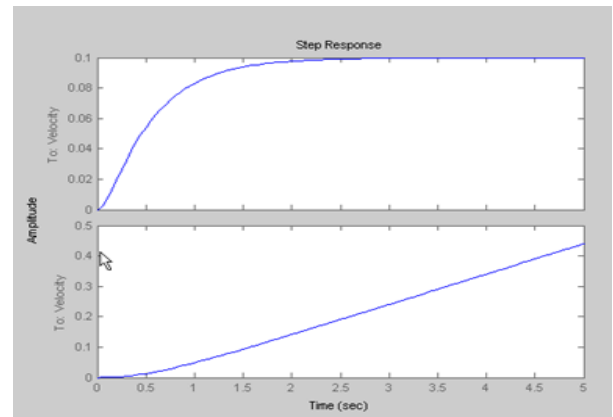


Figure 5. Step Response of DC motor

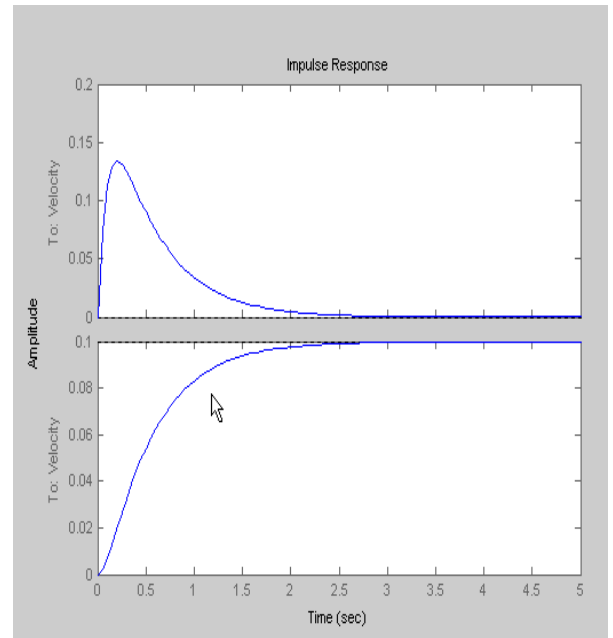


Figure 6. Impulse Response of DC motor

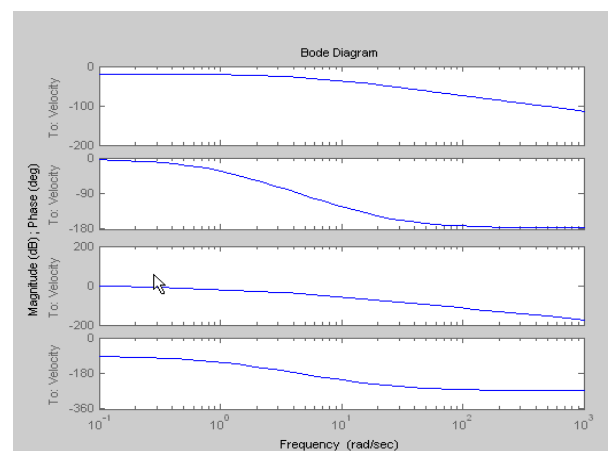


Figure 7. Bode diagram of DC motor

5. SIMULATION WITH PID CONTROLLER

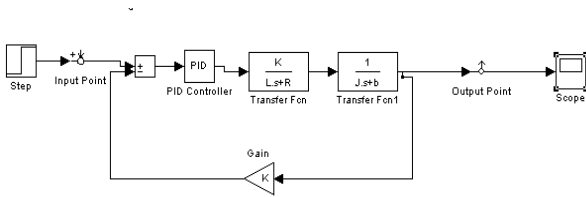


Figure8. simulink diagram of system

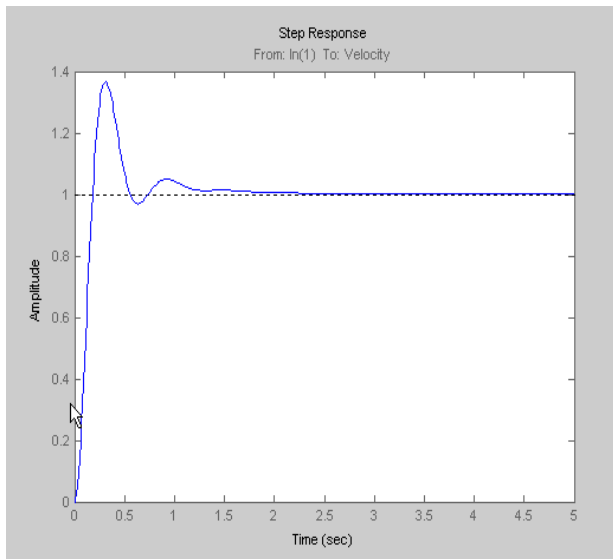


Figure 9. Close-loop step response with PID controller

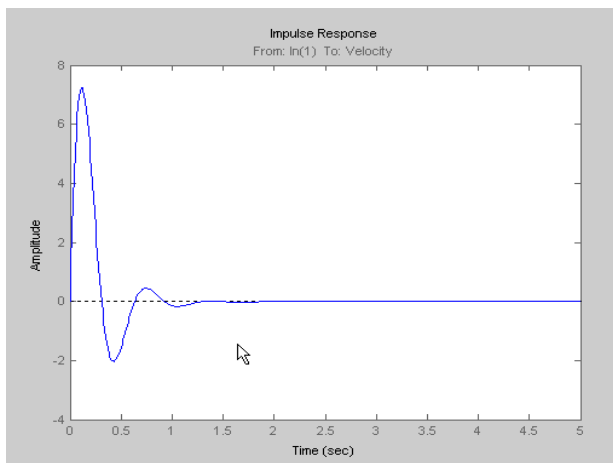


Figure 10. Close-loop impulse response with PID controller

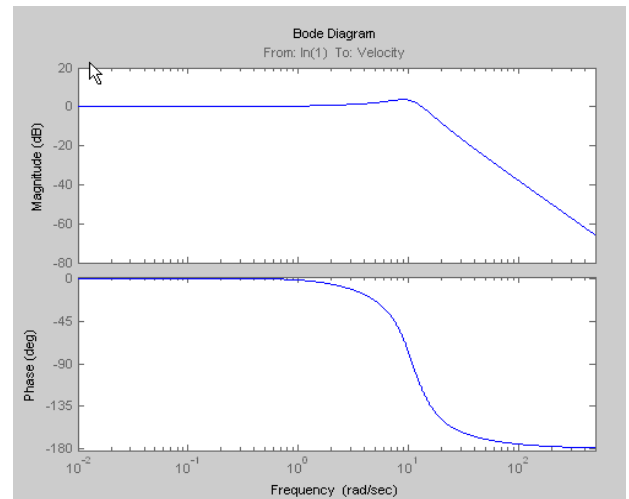
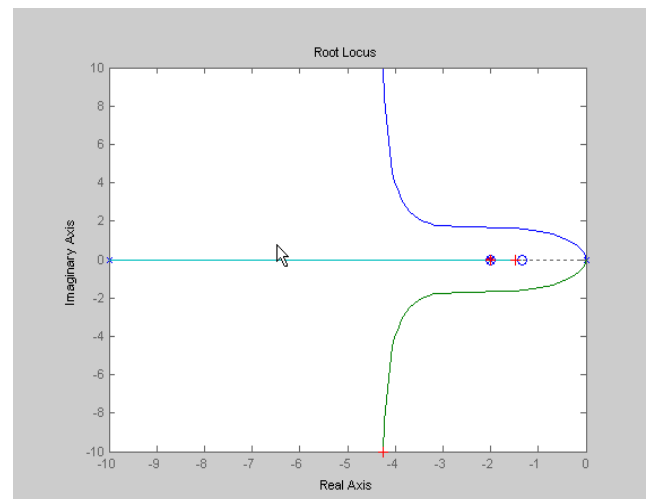


Figure 11. Close-loop bode diagram with PID controller



Selected point -9.8223+9.0994i

Figure 12. Root Locus diagram of PID controller

PID eliminates overshoot and decrease the rise time. To improve the settling time we try first to decrease K_d .

6. CONCLUSION

In this paper, basic technique for improvement by doing analysis and design of DC motor control system with PID controller is discussed. Therefore, we will learn how to develop a linear model for a DC motor, how to analyze the model under matlab (poles and zeros, frequency response, time-domain response, etc.), how to design a controller, and how to simulate the open-loop and closed-loop systems under simulink.

In my paper, DC motor system is modeled by summing torque acting on the inertia and integrating the acceleration to give the velocity, Kirchoff's Law is applied to the armature circuit and simulation for control system are discussed.

Simulation is today a very important part of engineering design. A lot of simulation software is available today for engineers.

In simulating the DC motor and controller is deriving its equations of motions. The second step is finding the transfer function. To get the transfer function, we have to apply the laplace transform.

PID controller is discussed in detail. We can determine the parameter of controller according to their response.

In the case of feed forward control, the system has no loop. So that the controller will measure the new torque (by measuring the current) and will increase or decrease the voltage. So, in feed forward control, the controller will not affect the system stability because there is no loop. So we must be use close loop system.

In paper program by using matlab for DC motor control system are discussed. The program enables the analysis of the control system in time and frequency domains, and also makes it possible to optimise the parameters of the control systems.

[15] J. F. Lindsay and M.H.Rashid' 'Electromechanics and Electrical Machinery'

7. REFERENCES

- [1] Encyclopedia Britannica, "Electricity and Magnetism," Macropedia, Vol. 18, pp. 193-194,1995.
- [2] T.C. Martin and J. Wetzler, "The Electric Motor and its Applications", book, W.J. Johnston,Publisher, 1887.
- [3] Nikolai Tesla, "A New System of Alternate Current Motors and Transformers," AIEE Transactions, 1888.
- [4] A. Blondel, "Synchronous motor and converter, Part III," book, McGraw-Hill, New York,1913.
- [5] R.H. Park, "Two reaction theory of synchronous machines- Part I," AIEE Transactions, Vol. 48, No. 2, 1929, pp.716-730.
- [6] F. Blaschke, "The principle of field orientation as applied to the new Transvektor closed-loop control system for rotating field machines," Siemens Review XXXIX, 1972, pp. 217-220.
- [7] Limei Wang and Robert D. Lorenz, 'Permanent Magnet Synchronous Motor Using Saliency-Tracking Self-Sensing Method'.
- [8] Todd D. Batzel and Kwang Y. Lee, ' Motor Slotless Permanent Magnet Synchronous Operation without a High Resolution Rotor Angle Sensor'
- [9] Hyung-Tae Moon, Hyun-Soo Kim, and Myung-Joong Youn, 'A Discrete-Time Predictive Current Control for PMSM'
- [10] Mo-Yuen Chow, Senior Member,IEEE and Yodyium Tipsuwan,Student Member, IEEE, 'Gain Adaptation of Networked DC motor Controllers Based on QOSVariations'
- [11] Chen , Analog and Digital Control System,S college Publishing, NY,1993
- [12] Li Yunhua, Shi Wei Xiang, an Introduction to Artificial Intelligent Control,BUAA, Beijing China 1998.
- [13] Earl Cox, the Fuzzy System Hand Book,ISBN AP Professional,1998
- [14] Bishop,R.,Modern Control Systems Analysis and Design using Matlab and Simulink , Addision Wesley Longman Inc, 1997.